UC Irvine

UC Irvine Electronic Theses and Dissertations

Title

Links of climate variability and change with regional hydroclimate: Predictability, trends, and physical mechanisms on seasonal to decadal scales

Permalink

https://escholarship.org/uc/item/3374c06s

Author

Mamalakis, Antonios

Publication Date

2020

Copyright Information

This work is made available under the terms of a Creative Commons Attribution License, availalbe at https://creativecommons.org/licenses/by/4.0/

Peer reviewed|Thesis/dissertation

eScholarship.org Powered by the California Digital Library
University of California

UNIVERSITY OF CALIFORNIA, IRVINE

Links of climate variability and change with regional hydroclimate: Predictability, trends, and physical mechanisms on seasonal to decadal scales

DISSERTATION

submitted in partial satisfaction of the requirements for the degree of

DOCTOR OF PHILOSOPHY

in Civil and Environmental Engineering

by

Antonios Mamalakis

Dissertation Committee:

Distinguished Professor Efi Foufoula-Georgiou, Chair
Professor Amir AghaKouchak
Ralph J. and Carol M. Cicerone Professor James T Randerson
Professor Jin-Yi Yu

2020

© 2020 Antonios Mamalakis

DEDICATION

To my parents, twin brother, and friends

a lesson

Seeking scientific truth is like a marathon rather than a sprint. It is surely about talent, but it is more about perseverance.

a hope

If the fool would persist in his folly, he would become wise.

William Blake
Proverbs of Hell

TABLE OF CONTENTS

	Page
LIST OF FIGURES	iii
LIST OF TABLES	vii
ACKNOWLEDGEMENTS	viii
VITA	ix
ABSTRACT OF THE DISSERTATION	x
INTRODUCTION	1
1. Climate teleconnections and predictability of winter precipitation over the southwestern US	5
1.1. A new interhemispheric teleconnection increases predictability of winter precipitation in southwestern US	6
1.2. The impact of El Niño-Southern Oscillation and external forcing on the identified teleconnection	38
1.3. Probabilistic assessment of predictive skill of extreme wet and dry years in southwestern US in observed and CMIP6 simulated climates	50
2. Future trends in the position of the Intertropical Convergence Zone	81
2.1. A multivariate probabilistic framework for tracking the intertropical convergence zone: Analysis of recent climatology and past trends	82
2.2. Zonally contrasting shifts of the intertropical convergence zone under climate change	106
CONCLUSIONS	143

LIST OF FIGURES

Page

Figure 1.1. Evidence for a new teleconnection in the southwestern Pacific. 9

Figure 1.2. NZI had a barotropic structure. 11

Figure 1.3. Time series of Niño 3.4, and NZI indices and precipitation anomaly. 13

Figure 1.4. Strengthening of NZI after the mid-1970s. 14

Figure 1.5. 30-year running averages of ENSO and NZI predictive skill for two different lead times indicated the strengthening of NZI after the mid-1970s. 15

Figure 1.6. During the last three decades, NZI associated more strongly with the average winter precipitation in the SWUS than Niño 3.4. 16

Figure 1.7. Comparison of ENSO and NZI teleconnection strengths. 17

Figure 1.8. Within-year evolution of the association of winter precipitation in SWUS with SSTs and GPHs revealed a northward interhemispheric cascade. 19

Figure 1.9. The NZI teleconnection depends on a western Pacific ocean-atmosphere pathway. 20

Figure 1.10. SSTs in the region of NZI were closely related with those in the region east of Philippines especially during late boreal summer and fall. 22

Figure 1.11. Positive SST anomalies in the NZI region weaken the southern Hadley circulation during late boreal summer. 23

Figure 1.12. During late boreal summer, the southern Hadley cell expands and connects the area of NZI with the northern hemisphere. 24

Figure 1.13. NZI anomalies are followed by a northward cascade of SST anomalies in the northern Pacific Ocean starting late summer and ending late winter. 25

Figure 1.14. NZI affects the upper zonal winds in the northeastern Pacific and modulates SWUS precipitation. 27

Figure 1.15. NZI was a driver of a dipole of precipitation anomalies along the west coast. 28

Figure 1.16. Southwestern Pacific SSTs were strongly correlated with the second principal component of winter precipitation in the western US. 29

Figure 1.17. Interhemispheric teleconnections between NZI and SST anomalies in the northwestern Pacific have significantly strengthened during the last three to four decades. 31

Figure 1.18. NZI interhemispheric connection when accounting for local SST memory and ENSO. 40

Figure 1.19. Time-lagged correlations between NZI and EPI in 1982–2015. 42

Figure 1.20. Changes in the strength of correlation between the NZI and EPI regions derived from the CESM-LENS project. 43

Figure 1.21. Composite differences between 5 warmest and 5 coldest NZI years during 1982-2015. 46

Figure 1.22. Jul-Sep correlation maps (1982-2014) between NZI and various atmospheric variables 47

Figure 1.23. Same as in Figure 1.22, using different datasets. 48

Figure 1.24. Correlation matrix for the 14 SST indices that were examined in this study (over the years from 1969-70 to 2018-2019). 54

Figure 1.25. The predictive PDF of SWUS precipitation for the year 1995-1996 and summary of all possible outcomes when predicting precipitation. 55

Figure 1.26. The empirical distribution of the considered statistical metrics under the null hypothesis H_0 of no predictive skill, for different sample sizes and for different definitions of extremes. 61

Figure 1.27. Series of the predictive PDF of SWUS winter precipitation from 1969-70 to 2018-19, using different predictive models. 63

Figure 1.28. Performance of different predictive models, as evaluated using the introduced statistical metrics and different definition of extremes. 65

Figure 1.29. Same as in Figure 1.28, but when SST in each grid point was used separately as a predictor. 67

Figure 1.30. Same as in Figure 1.29, but the results for No Drought Success, and categorical Log-likelihood are presented. 68

Figure 1.31. Application of the false discovery rate method for different significance levels, and for predicting different precipitation conditions. 69

Figure 1.32. Multi-year mean and standard deviation of the winter precipitation over the SWUS, as calculated using observations and individual CMIP6 model outputs. 70

Figure 1.33. Same as in Figure 1.28, but results from CMIP6 model outputs are also presented. 73

Figure 2.1. Probabilistic tracking of the ITCZ at longitude *l* = 175ºE, based on monthly precipitation. 86

Figure 2.2. Probabilistic tracking of the ITCZ at longitude *l* = 175ºE, based on the joint distribution of the monthly precipitation and OLR. 89

Figure 2.3. The location of the ITCZ around the globe in 1983-2012. 91

Figure 2.4. Location of the ITCZ in 1983-2012 as defined using multiple physical variables. 92

Figure 2.5. Same as Figure 2.4, but using monthly products from the 20CR dataset. 94

Figure 2.6. Same as Figure 2.5, but using monthly products from the NCEP/NCAR dataset. 95

Figure 2.7. Seasonal tracking of the ITCZ. 97

Figure 2.8. Same as Figure 2.7a-b, but using all 320 months in 1983-2012. 98

Figure 2.9. Changes in the location of the ITCZ. 100

Figure 2.10. Trends and changes in the distribution of the location of the ITCZ. 101

Figure 2.11. Application of a longitudinally explicit, multivariate probabilistic approach to track the ITCZ on annual scales. 111

Figure 2.12. The baseline climatology of the ITCZ in observations and CMIP6, as shown in average precipitation and OLR maps, and using a multivariate probabilistic tracking framework. 113

Figure 2.13. Climatological location of the ITCZ during 1983-2005 based on observations and CMIP6 models. 116

Figure 2.14. Double-ITCZ biases in CMIP6. 117

Figure 2.15. Future changes in the ITCZ location under climate change as predicted in CMIP6. 121

Figure 2.16. Future changes in the ITCZ location in CMIP6, as shown in changes of average precipitation and OLR maps, and using a multivariate probabilistic tracking framework. 122

Figure 2.17. 21st century series of ITCZ location as predicted in CMIP6. 124

Figure 2.18. The effect of the double-ITCZ bias on the sign of the projected ITCZ shift over the east Pacific and Atlantic Oceans. 125

Figure 2.19. Future changes in sea surface temperature and precipitation under climate change as predicted in CMIP6. 127

Figure 2.20. Atmospheric energy transport in base period 1983-2005, as predicted in CMIP6. 129

Figure 2.21. Future changes in the atmospheric energy input under climate change as predicted in CMIP6. 130

Figure 2.22. Future changes in the components of the atmospheric energy budget as predicted in CMIP6. 131

Figure 2.23. Future changes in the atmospheric energy transport (AET) over the tropics and the energy flux equator (EFE) under climate change, as predicted in CMIP6. 134

LIST OF TABLES

Page

Table 1.1. Effect of non-stationarity in the NZI/ENSO teleconnection strength on the precipitation prediction error. 32

Table 1.2. The skill scores based on the defined statistical metrics for different predictive models and for different extreme thresholds. 64

Table 1.3. CMIP6 models used in this study. 71

Table 1.4. Same as Table 1.2, but using multi-model mean of 27 CMIP6 model simulations. 72

Table 2.1. CMIP6 models used in this study and their double-ITCZ biases. 112

Table 2.2. Mean and standard deviation of the future ITCZ and EFE shifts and changes of the hemispheric energetic asymmetry over different longitudinal sectors, as obtained from 27 CMIP6 models outputs. 120

ACKNOWLEDGEMENTS

I would like to express the deepest appreciation to my advisor, Professor Efi Foufoula-Georgiou, who has been a constant source of inspiration and support for me over the course of my degree. She continually conveys a spirit of excitement for research and hard work to her students, and she has taught me the importance of perseverance when seeking scientific truth. Without her guidance and help this dissertation would not have been possible.

I would like to thank my committee members, Professor Jin-Yi Yu who introduced me to the basics of Earth System Science, and Professors James T Randerson and Amir AghaKouchak for their guidance and trust.

Financial support for my research was provided by the University of California, Irvine, and the National Science Foundation (NSF) under the EAGER program (grant ECCS-1839441) and the TRIPODS+CLIMATE program (grant DMS-1839336), as well as by NASA's Global Precipitation Measurement program (grant 80NSSC19K0684). The support by NSF (grant EAR-1928724) and NASA (grant 80NSSC19K0726) for the organization of the 12th International Precipitation Conference (IPC12) and production of the IPC12 special collection of papers is also gratefully acknowledged.

VITA

Antonios Mamalakis

EDUCATION

2020	Ph.D. in Civil and Environmental Engineering, University of California, Irvine
2016	M.Sc. in Water Resources and Environmental Engineering, University of Patras, Greece
2014	Diploma in Civil Engineering, University of Patras, Greece

PUBLICATIONS

- **Mamalakis, A.**, E. Foufoula-Georgiou, A. AghaKouchak and J.T. Randerson (2021) Probabilistic assessment of predictive skill of extreme wet and dry years in southwestern US in observed and CMIP6 simulated climates, *in preparation*
- Guilloteau, C., **A. Mamalakis**, L. Vulis, P. Le, T. Georgiou and E. Foufoula-Georgiou (2020) Rotated spectral principal component analysis (rsPCA) for identifying dynamical models of variability in climate systems, *J. Climate*, in revision.
- Stevens A., R. Willett, **A. Mamalakis**, E. Foufoula-Georgiou, J. Randerson, P. Smyth, S. Wright and A. Tejedor (2020) Graph-guided regularized regression of Pacific Ocean climate variables to increase predictive skill for southwestern US winter precipitation, *J. Climate*, in revision.
- **Mamalakis, A.**, J.T. Randerson, J.-Y. Yu, M.S. Pritchard, G. Magnusdottir, P. Smyth, P.A. Levine, S. Yu and E. Foufoula-Georgiou (2020) Zonally contrasting shifts of the tropical rainbelt in response to climate change, *Nature Climate Change*, in revision.
- **Mamalakis, A.**, J.-Y. Yu, J.T. Randerson, A. AghaKouchak, and E. Foufoula-Georgiou (2019) Reply to: A critical examination of a newly proposed interhemispheric teleconnection to Southwestern US winter precipitation, *Nature Communications*, https://doi.org/10.1038/s41467-019-10531-3
- **Mamalakis, A.** and V. Kaleris (2019) Estimation of seawater retreat timescales in homogeneous and confined coastal aquifers based on dimensional analysis, *Hydrological Sciences Journal*, doi:10.1080/02626667.2018.1552787
- **Mamalakis, A.** and E. Foufoula-Georgiou (2018) A multivariate probabilistic framework for tracking the intertropical convergence zone: Analysis of recent climatology and past changes, *Geophysical Research Letters*, doi:10.1029/2018GL079865
- **Mamalakis, A.**, J.-Y. Yu, J.T. Randerson, A. AghaKouchak, and E. Foufoula-Georgiou (2018) A new interhemispheric teleconnection increases predictability of winter precipitation in southwestern US, *Nature Communications*, doi: 10.1038/s41467-018-04722-7
- **Mamalakis A.**, A. Langousis, R. Deidda and M. Marrocu (2017) A parametric approach for simultaneous bias correction and high-resolution downscaling of climate model rainfall, *Water Resour. Res.*, doi: 10.1002/2016WR019578).
- Langousis A., **A. Mamalakis**, M. Puliga and R. Deidda (2016) Threshold detection for the generalized Pareto distribution: Review of representative methods and application to the NOAA NCDC daily rainfall database *Water Resour. Res.*, doi: 10.1002/2015WR018502.
- Langousis A., **A. Mamalakis**, R. Deidda and M. Marrocu (2016) Assessing the relative effectiveness of statistical downscaling and distribution mapping in reproducing rainfall statistics based on climate model results, *Water Resour. Res.*, doi:10.1002/2015WR017556.

ABSTRACT OF THE DISSERTATION

Links of climate variability and change with regional hydroclimate: Predictability, trends, and physical mechanisms on seasonal to decadal scales

by

Antonios Mamalakis

Doctor of Philosophy in Civil and Environmental Engineering

University of California, Irvine, 2020

Distinguish Professor Efi Foufoula-Georgiou, Chair

The mechanistic understanding and reliable prediction of regional hydroclimatic variability across scales remains a challenge, with important socioeconomic and environmental implications for many regions around the world. Despite the significant advances in earth system modeling during the recent decades, deterministic models show limited predictive skill of regional hydroclimate, mainly due to imperfect physical conceptualizations and inaccurate initial conditions. Statistical schemes that are based on empirically established climate teleconnections are not reliable due to the non-stationary nature of the system under climate change. In this dissertation, to gain physical insight on precipitation variability across scales, we explore a) the physical teleconnections and predictability of winter precipitation totals over the southwestern US (SWUS), and b) the future shifts in the position of the tropical rainbelt/intertropical convergence zone (ITCZ) in response to climate change. The hydroclimatic variability in these two cases is based on fundamentally different phenomena (mid latitude dynamics versus tropical circulation) and operates at largely different temporal scales (seasonal versus multidecadal timescales), thus offering great potential for physical insight and broadening the impact of this work.

We present evidence that new modes of sea surface temperature variability over the southwestern Pacific have been robustly connected to SWUS precipitation over the past four decades, providing improved prediction skill compared to traditionally used indices. We suggest that the revealed connection materializes through a western Pacific pathway

whereby temperature anomalies in the proximity of New Zealand propagate from the southern to the northern hemisphere during boreal summer and early fall. The importance of the revealed teleconnection and the skill of other predictive models in predicting extreme precipitation totals in SWUS is assessed via a new probabilistic framework that is also introduced in this work.

Regarding the future response of the tropical rainbelt to climate change, we propose a new multivariate approach to track its position as a function of longitude, and by using state-of-the-art climate model outputs, we report a robust, zonally contrasting shift of the ITCZ with climate change. Specifically, we document that the ITCZ will shift northward over eastern Africa and the Indian Ocean, and southward in the eastern Pacific and Atlantic Oceans by 2100, for the SSP3-7.0 scenario. We find that the revealed ITCZ response is consistent with future changes in the divergent atmospheric energy transport over the tropics, and sector-mean shifts of the energy flux equator. The shifts in the energy flux equator appear to be the result of zonally contrasting imbalances in the interhemispheric atmospheric heating over the two sectors, consisting of increases in atmospheric heating over Eurasia and cooling over the Southern Ocean, which contrast with atmospheric cooling over the North Atlantic Ocean due to a model-projected weakening of the Atlantic meridional overturning circulation.

The results of this dissertation highlight the need to understand the dynamic nature of the coupled ocean-atmosphere system and exploit climate information that goes beyond the traditionally used indices for improving future prediction skill of regional precipitation in a changing climate. Future research should focus on the development of new, data-driven methodologies that aim to integrate physics and machine learning, and predict seasonal precipitation variability in a setting where the predictors are not prescribed a priori, but rather emerge from the model fit to the data. For longer timescales (i.e. decadal and multi-decadal), our results provide new insights about the mechanisms that will influence the future position of the tropical rainbelt, and may allow for more robust projections of climate change impacts.

INTRODUCTION

Understanding the factors that determine regional precipitation variability across scales (i.e., sub-daily to interannual variability, and long-term future trends with climate change) as well as increasing its predictive skill is one of the most pressing and crucial problems for engineers and earth system scientists, with important implications for the economy, security and environmental sustainability of many regions around the globe. To address this challenge advanced physics-based modeling and data analytic methodologies are needed for investigating observations and state-of-the-art model simulations to enhance process-level understanding, diagnose changing modes of climate variability, and detect and attribute regional manifestations of climate change for improved precipitation prediction.

Despite the substantial progress that has been made in the recent decades in identifying and understanding physical drivers and climate teleconnections to regional hydroclimate, important challenges remain. At seasonal and interannual scales, climate models show no predictive skill, while commonly used climatic modes, like the El Niño-Southern Oscillation (ENSO), can explain only a fraction of precipitation variability, and only over specific regions where the signal is statistically significant. Moreover, the changing climate alters the empirically established teleconnections, with new climatic modes emerging or becoming more important. At decadal and multi-decadal scales, the effect of climate change on regional precipitation can only be explored based on outputs from state-of-the-art climate models, which, despite the great advances in climate modeling, still exhibit important systematic biases. Also, due to the different physical approximations of each model and the different scenarios of future climate change that are considered in the literature, future precipitation changes remain uncertain.

The above challenges limit our ability to understand and attribute past variability and/or improve prediction of future variability and change of regional hydroclimate across a range of timescales. In this dissertation, we investigate the mechanisms that determine winter precipitation variability over the southwestern US (in Chapter 1) and explore model consensus in the response of the intertropical convergence zone to climate change as a function of longitude (in Chapter 2). The hydroclimatic variability in these two cases is based on fundamentally different phenomena (mid latitude dynamics versus tropical circulation) and operates at largely different temporal scales (seasonal versus multidecadal timescales), thus, offering a great potential for gaining physical insights.

Despite the increasing attention that it has received over the years, early and accurate prediction of winter precipitation in SWUS remains a challenge, with significant implications for the region's population and economy. Traditional climatic drivers of SWUS precipitation (e.g. the ENSO) explain just a small fraction of the interannual variability of precipitation totals, which in some cases are determined by a small number of winter storms. Moreover, it is known that the ENSO relationship with SWUS climate undergoes multidecadal fluctuations, with many recent studies pointing out that it has been losing strength in the recent decades, while the western Pacific climatic state is gaining in importance. The special difficulty of this problem also arises because the SWUS lies within a transition zone between the subtropics and the mid-latitudes (i.e. 30°- 40° N). In fact, the latter is among the reasons that the effect of climate change on future precipitation trends over the SWUS is highly uncertain, with mid-latitude regions expected to become wetter and subtropical regions drier.

In our analysis, we start by highlighting a new emerging connection between southwestern Pacific sea surface temperature (SST) and SWUS precipitation, by also offering a possible mechanistic explanation of the revealed link. We then propose a probabilistic framework to assess prediction skill of extreme seasonal precipitation totals. As an application of this framework, we use the prediction problem of precipitation over SWUS and highlight the most predictive SST features in observed and model-simulated climates.

In Chapter 2 we explore the long-term effect of future climate change on the position of the tropical rainbelt/intertropical convergence zone (ITCZ). Future changes in the ITCZ position with climate change are of high interest since they could substantially alter precipitation patterns in the tropics and subtropics, and affect the livelihood and food security of billions of people. However, although climate models predict a future narrowing of the ITCZ during the 21st century in response to climate warming, uncertainties remain large regarding its future position, with most past work focusing on the zonal-mean ITCZ shifts. Thus, this problem offers a great case study for highlighting climate models' biases and uncertainty of their outputs, regarding the future response of tropical hydroclimate to global climate change.

We first introduce a new probabilistic framework to track the ITCZ position as a function of longitude. We then use projections from 27 state-of-the-art (CMIP6) climate models and document a robust zonally-varying ITCZ response to the SSP3-7.0 scenario by 2100, with a northward shift over eastern Africa and the Indian Ocean, and a southward shift in the eastern Pacific and Atlantic Oceans. The revealed zonally-varying response is consistent with changes in the divergent atmospheric energy transport, and sector-mean shifts of the energy flux equator.

Chapters 1 and 2 are written in stand-alone format based on already published or submitted work.

CHAPTER 1

Climate teleconnections and predictability of winter precipitation over the southwestern US

1.1. A new interhemispheric teleconnection increases predictability of winter precipitation in southwestern US

Part of this chapter has been published in Nature Communications

Citation: Mamalakis, A., J.-Y. Yu, J.T. Randerson, A. AghaKouchak, and E. Foufoula-Georgiou (2018) A new interhemispheric teleconnection increases predictability of winter precipitation in southwestern US, Nature Communications, doi: 10.1038/s41467-018-04722-7

Seasonal and sub-seasonal precipitation prediction typically relies on deterministic climate models or statistical methods[1]. However, both climate models (which represent the complex land-ocean-atmosphere interactions) and statistical models (that either harness empirical relationships between precipitation and large-scale ocean-atmosphere teleconnections or are persistence-based) have shown limited success for precipitation prediction[1-7]. As climate change is expected to modify precipitation patterns, the need for improved seasonal to sub-seasonal predictive skill becomes critical for sustainable management of ecosystems and water resources[8-12].

Traditional drivers of winter precipitation in the southwestern US (SWUS) are the El Niño-Southern Oscillation (ENSO), decadal oscillations of the sea surface temperature (SST) in the Pacific and Atlantic oceans (i.e. Pacific Decadal Oscillation; PDO, Interdecadal Pacific Oscillation; IPO, Atlantic Multidecadal Oscillation; AMO), and persistent high-pressure ridges over the Gulf of Alaska[13,17-25,46]. Although these teleconnections are physically established[38,39,42], their predictive power on seasonal scales is limited. For example, there have been several years where El Niño conditions did not coincide with positive precipitation anomaly in SWUS, while years of extreme precipitation anomalies corresponded to neutral ENSO conditions[23,25-27]. More generally, ENSO as well as other climate modes (e.g. PDO, AMO) exhibit weak statistical relationships with precipitation amounts, and even lower predictability as lead time increases[24-27].

In this study, we use historical records and reanalysis data to show that late-summer SST anomalies close to New Zealand strongly correlate with SWUS winter precipitation, outperforming all commonly used teleconnections, and enhancing the potential for earlier

and more accurate prediction of precipitation. We provide evidence that the strength of the discovered teleconnection has been increasing during the latest 3-4 decades, in contrast to ENSO indices, which have been losing predictive strength. The new teleconnection is linked to an interhemispheric atmospheric bridge which occurs over western Pacific and is proposed to be driven by the migration of the intertropical convergence zone to the northern hemisphere during late summer, and the accompanied expansion of the southern Hadley cell[55], which allows for SST anomalies in the south to affect the north Pacific.

Results

Evidence for a new teleconnection. Grounded on the hypothesis that still undiscovered relationships between large-scale atmosphere-ocean dynamics and SWUS precipitation might exist, we followed a diagnostic approach by which instead of restricting ourselves to the established teleconnections, we analyzed systematically the correlation of global SST and geopotential height (GPH) with winter precipitation amounts for all of the climatic divisions in SWUS. The premise was that if a coherent pattern emerged from such a data-analytic approach, it would warrant merit for further investigation of its physical/mechanistic underpinning and its possible relation with other climate modes known to influence SWUS precipitation. For our analysis, we used observations of winter precipitation amount (data source: https://www.ncdc.noaa.gov/cag/time-series/us, [40]), together with SST data from two different datasets (monthly SSTs on a 1º×1º grid, [34] and [36]) and GPH reanalysis data (monthly GPH on a 2º×2º grid, [33]). We assessed predictability based on global correlation maps between winter (Nov-Mar) precipitation amount in each climate division within SWUS (California, Nevada, Arizona, and Utah) and SST and GPH, averaged over 3-month periods corresponding to different lead times. We performed the analysis for the 66-yr period of 1950-2015, when higher quality SST and GPH observations are available. Specifically, for each grid cell on the globe, we calculated the correlation between P_m and $I^{k,l}_{i:i+dt}$, where P_m is the precipitation (Nov-Mar) in climate division m, $I^{k,l}_{i:i+dt}$ is the SST (or GPH) at latitude k and longitude l, while i indicates the starting month, and $i + dt$ the ending month of the period over which SST and GPH were averaged; here we considered i = 7 and 9 (Jul and Sep) and dt = 2, that is, we correlated P_m (Nov-Mar) to I(Jul-Sep) and I(Sep-Nov), i.e. late summer and fall

period. This analysis allowed us to examine the presence, and the strengthening or weakening of spatial correlation patterns with lead time.

The unexpected result of our investigation was the emergence of persistent SST and GPH patterns located in the southwestern Pacific, which exhibited strong negative correlation with precipitation in most SWUS climate regions. By examining the correlation maps for all climate divisions, the location and areal extent of the SST pattern was first qualitatively assessed to ensure its robustness. Then, by considering the SST anomalies enclosed within contours of statistically significant correlation, the location and size of the emergent teleconnection was formally defined as the 30° × 15° region of 170°E-200°E and 25°S-40°S (Figure 1.1g). We refer to the emergent teleconnection as the New Zealand Index (NZI; Figure 1.1g) because of its proximity to New Zealand.

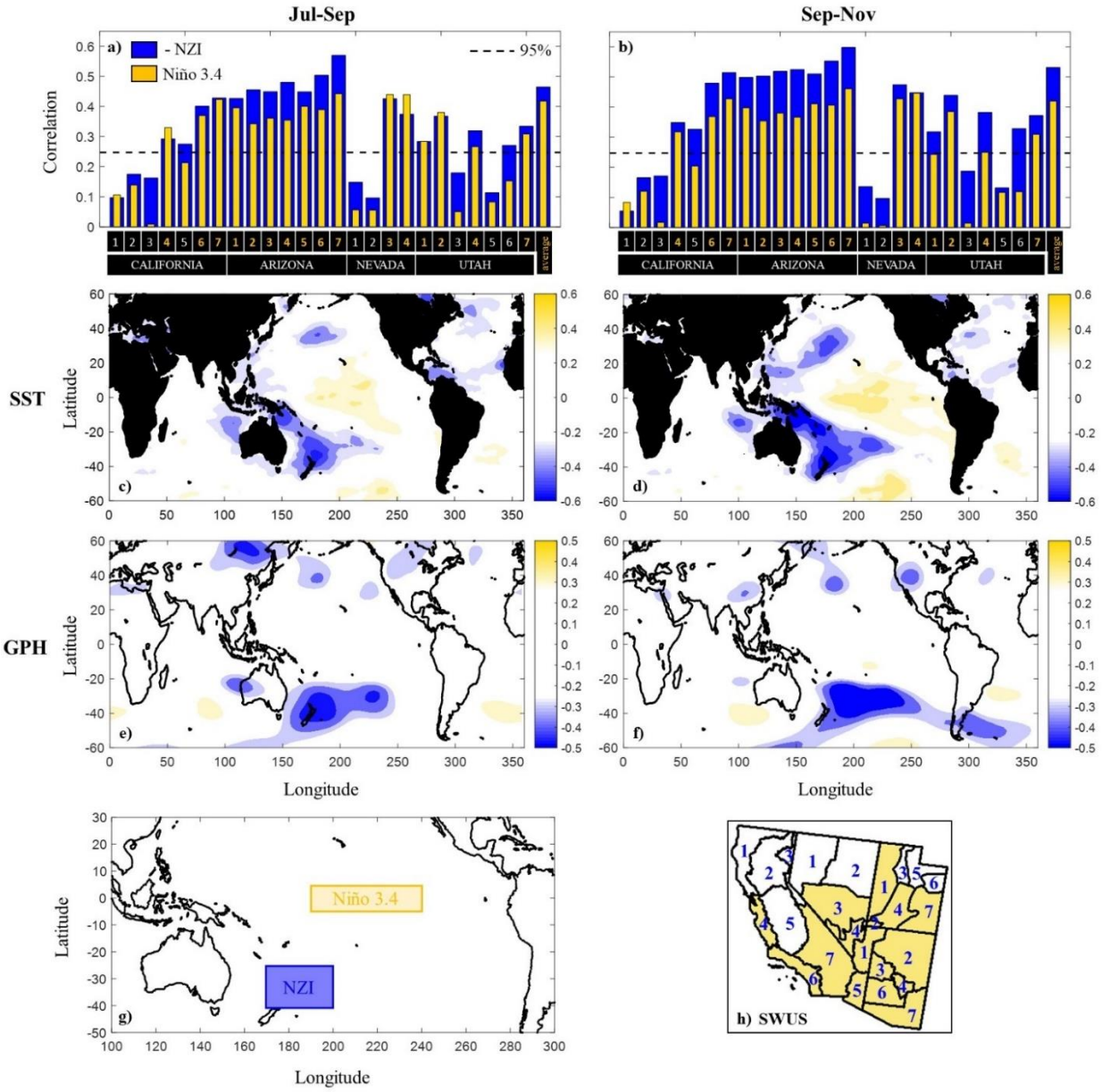

Figure 1.1: **Evidence for a new teleconnection in the southwestern Pacific.** (a)-(b) Correlation coefficients of –NZI and Niño 3.4 with winter precipitation (Nov-Mar) for all climate divisions of Southwestern US (SWUS) and for two different periods (Jul-Sep and Sep-Nov) for 1950-2015. Average precipitation is defined as the area-weighted average precipitation amount over climate divisions where Niño 3.4 exhibits statistically significant correlation (see colored numbers in panels a-b, and regions in panel h). (c) Correlation map between SST (Jul-Sep) and the average winter precipitation in SWUS for 1950-2015. White color indicates statistically insignificant correlations (α = 0.05 significance level); (d) Same as (c), but SST is averaged over Sep-Nov; (e)-(f) Correlation maps as in (c)-(d) but using GPH (400 mb). The emergence of a persistent correlation pattern in the southwestern Pacific (coined as the New Zealand Index, NZI) is robust for both SST and GPH; (g) the location and areal extent of NZI and Niño 3.4; (h) The selected climate divisions in SWUS (in color), for deriving the regionally averaged precipitation amount, based on their significant correlation with Niño 3.4.

Correlations between NZI (Jul-Sep and Sep-Nov) and winter precipitation (Nov-Mar) for each climate division within CA, AR, UT, and NV revealed two important properties of the teleconnection (Figure 1.1a-b). First, NZI correlations were stronger than Niño 3.4 correlations for most climate divisions, highlighting the potential for earlier and more accurate precipitation predictions than those afforded by ENSO. Second, correlations of NZI and ENSO exhibited similar variability among different regions, with precipitation amount over northern CA, NV, and UT showing lower correlation with both indices. This is not surprising, since precipitation in these regions is known to be less dependent on Pacific SSTs. Specifically, by modulating the latitude at which the jet stream prevails, Pacific SSTs influence the US climate over the northern and southern west coast, but not over regions in the central western US, which exhibit very different precipitation variability[13,16,17,19,46,57]. For the remainder of this study, we focused our analysis on the region where precipitation was significantly related to Pacific SST variability. We defined a regionally averaged SWUS precipitation time series as the area-weighted average precipitation amount over climate divisions for which ENSO (Niño 3.4) exhibited a statistically significant correlation (at a significance level of $\alpha = 0.05$; Figures 1.1a-b and 1h).

The spatial correlation patterns between SST and the area-weighted average SWUS precipitation are shown in Figure 1.1c-d, for two lead times. Pacific SSTs in ENSO region had correlation values that did not exceed 0.4, whereas the strongest dependencies occurred in the southwestern Pacific, where correlations were less than -0.6. Similar patterns were apparent when using GPH data (400 mb), where a correlation of -0.5 was observed over the NZI region (Figure 1.1e-f). The correlations with GPH did not depend on pressure level (Figure 1.2), revealing that the GPH pattern had a barotropic structure, a major characteristic of teleconnection patterns in the atmosphere[41].

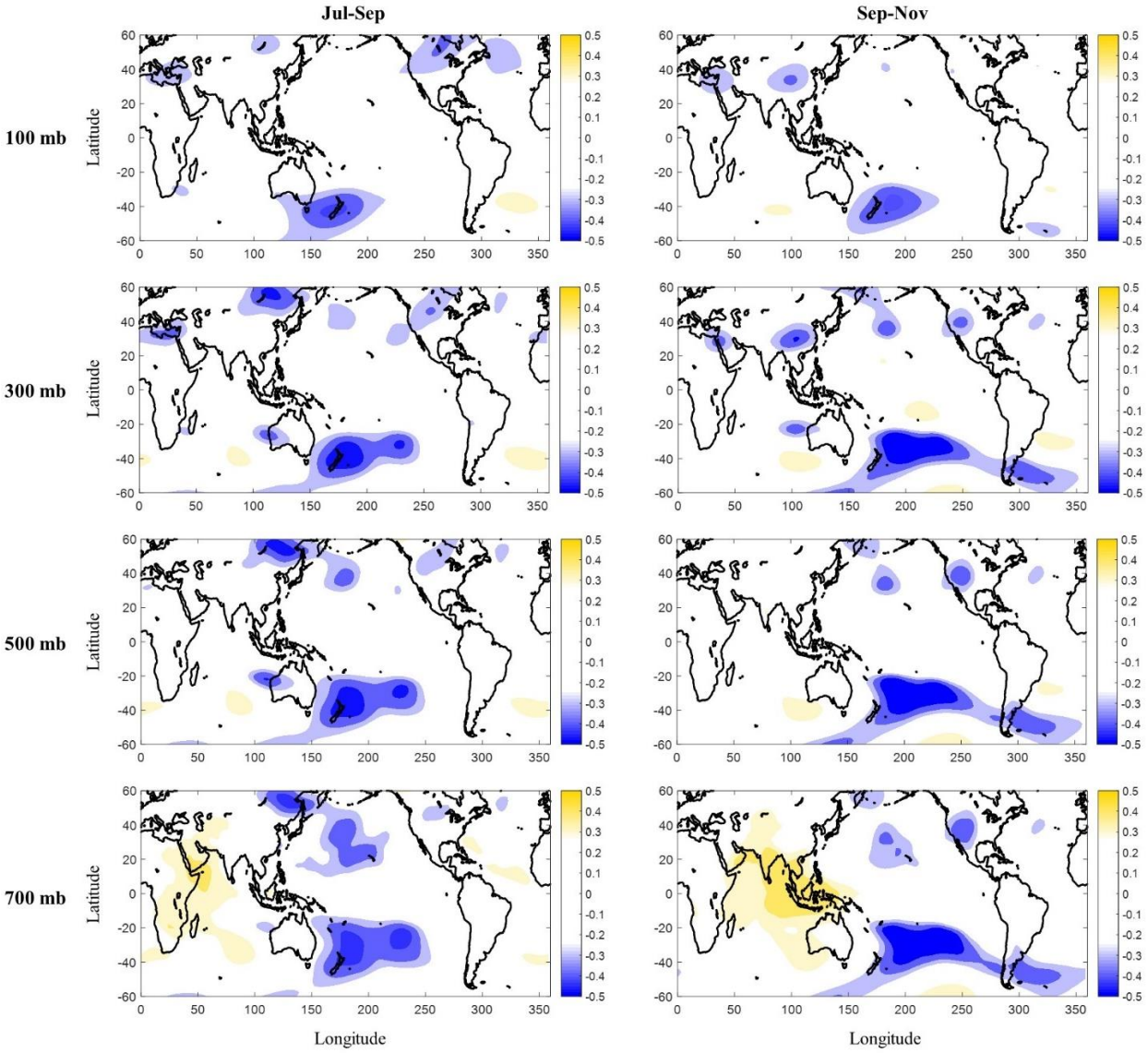

Figure 1.2: NZI had a barotropic structure. Correlation maps between GPH (Jul-Sep and Sep-Nov, at different pressure levels) and the average precipitation in SWUS (Nov-Mar), for 1950-2015 (same results as in Figure 1.1e-f, but for different pressure levels). White color indicates statistically insignificant correlations (α = 0.05 significance level).

Decadal variation of precipitation teleconnections. ENSO teleconnections to US precipitation have been shown to exhibit decadal and multidecadal variations in their strength[13-18]. These variations have been mainly attributed to natural climate variability[16-18] (e.g. PDO, AMO), and have been linked to the recurrence of persistent dry/wet periods in California and Arizona, with a periodicity of the order of 15 years[20,27](Figure 1.3). Here, to explore the decadal variations and trends of NZI and ENSO teleconnection with winter precipitation in SWUS, we considered a 30-yr moving window (starting in 1950), and calculated the correlation of NZI and ENSO indices averaged over periods of Jul-Sep and Sep-Nov with the regionally averaged winter precipitation amount. This analysis showed that the correlation of NZI with precipitation steadily increased over the duration of the time series, exceeding ENSO's correlation during the last 3-4 decades (Figure 1.4a-b). ENSO indices, in contrast, showed a declining teleconnection strength since the 1970s.

Although the ENSO teleconnections had a similar decadal structure of variability over the record, differences among the indices have important implications for seasonal prediction. Niño 3 exhibited statistically insignificant correlation for the Jul-Sep interval (at α =0.05 significance level), indicating that eastern Pacific SSTs may not be effective for SWUS precipitation prediction. SOI, in contrast, had the strongest correlation with winter precipitation of all the ENSO indices (Figure 1.4b), suggesting that atmospheric pressure variations across the tropical central/western Pacific may be more effective for prediction than SST-derived indices. ENSO teleconnection strength did not seem to be affected by the increased frequency of central-Pacific ENSO events relative to those of the eastern-Pacific, which has been reported recently[48,49,58]. Specifically, SST-based ENSO indices for different zonal regions (including Niño 3, Niño 3.4, and Niño 4) did not show diverging correlation patterns over the past several decades.

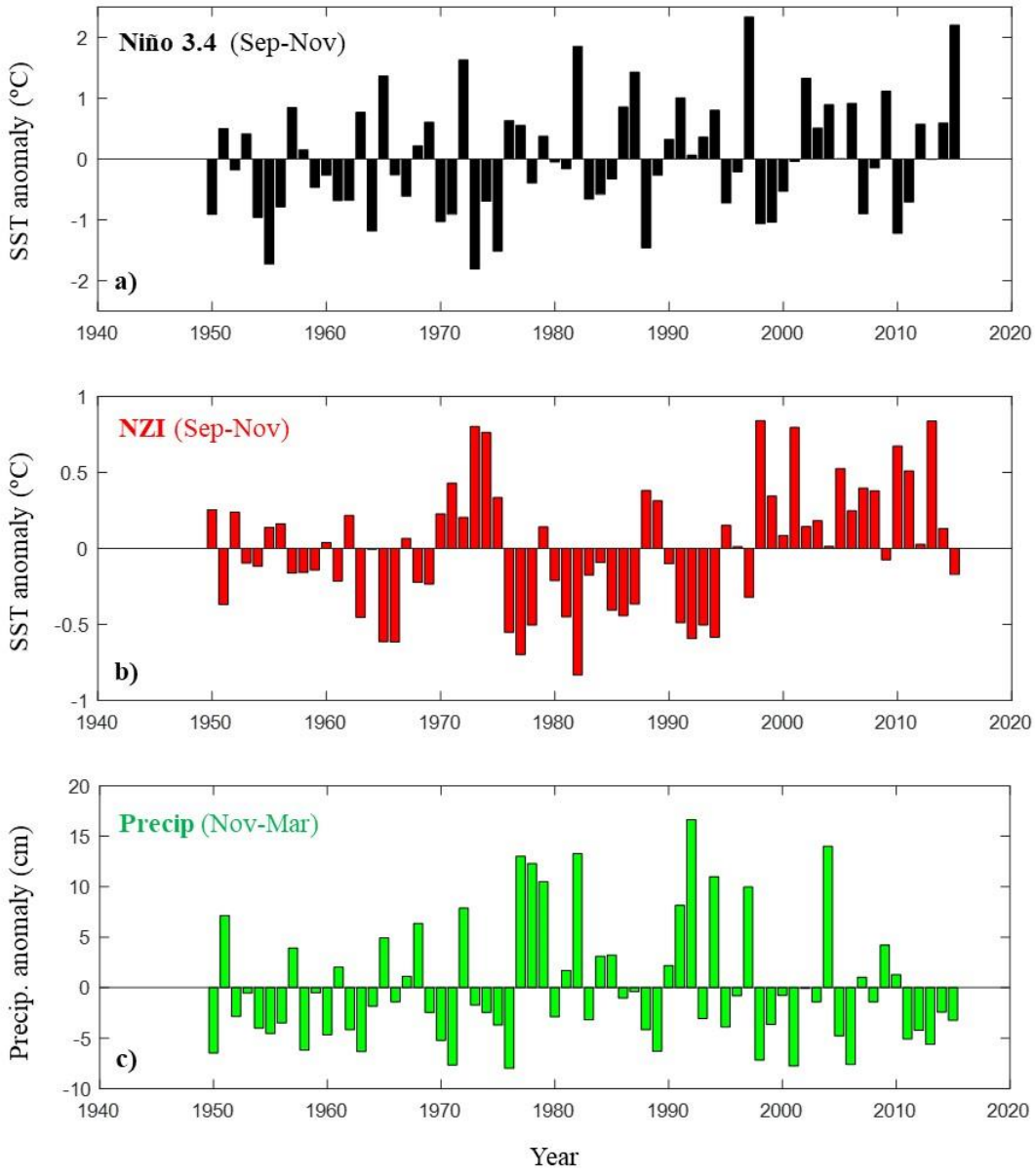

Figure 1.3. Time series of Niño 3.4, and NZI indices (both averaged over Sep-Nov) and precipitation anomaly (Nov-Mar). In (c), each year in horizontal axis refers to the beginning of Nov-Mar.

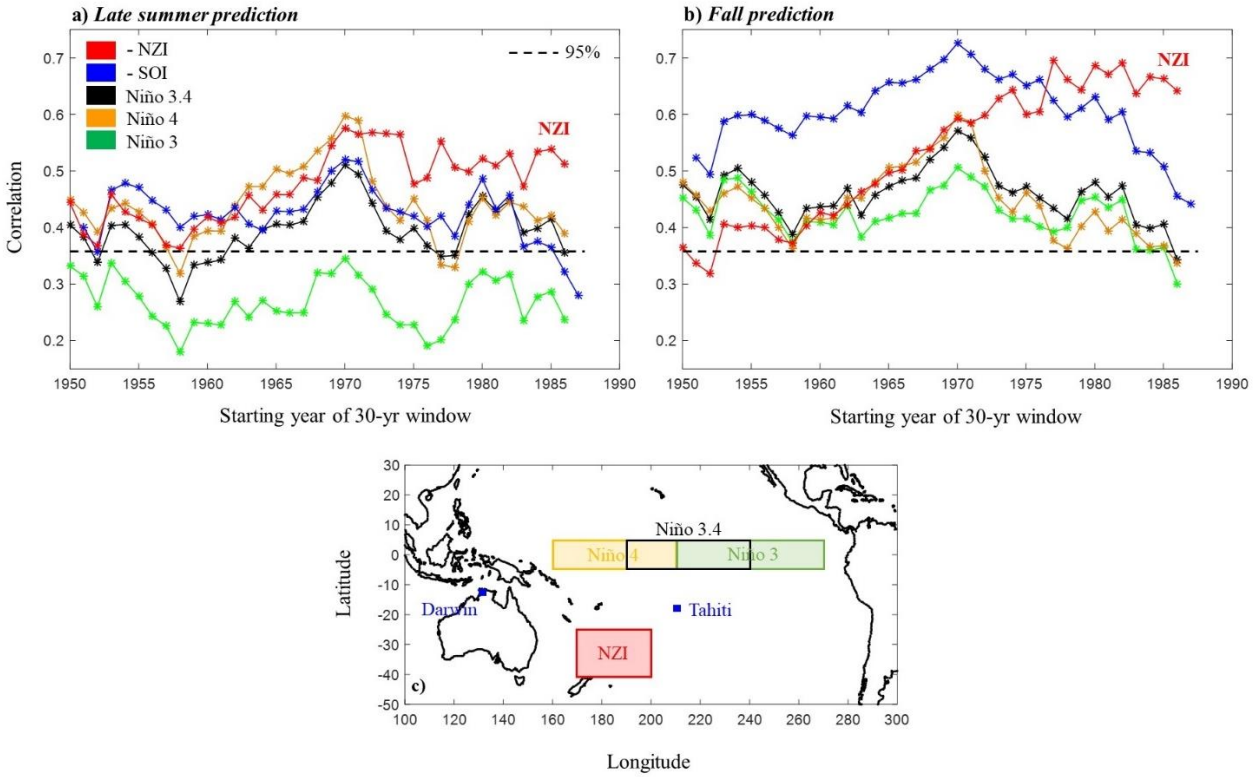

Figure 1.4: Strengthening of NZI after the mid-1970s. 30-year running averages of ENSO and NZI teleconnection strengths for two different lead times: (a) Correlation values for 30-yr moving windows between different climate indices (averaged over Jul-Sep) and winter precipitation in SWUS (Nov-Mar); (b) same as (a) but when climate indices are averaged over Sep-Nov. Dashed lines indicate the threshold below which correlations are statistically insignificant (α = 0.05 significance level); (c) the location and areal extent of NZI and ENSO indices. SOI (Southern Oscillation Index[17]) is defined as the standardized difference of the sea level pressure anomalies at Tahiti and Darwin (Australia).

To quantitatively compare the predictive skill of NZI and ENSO indices, we sequentially performed cross-validation analysis (over 30-yr running windows) using three linear prediction models based on NZI, SOI and Niño 3.4 time series. We assessed the predictive skill of each index based on the *RMSE* of the corresponding model prediction for regionally-averaged winter (Nov-Mar) precipitation; the percentage of precipitation variability each model explained (R^2); and the probability of each model to correctly predict dry or wet conditions in the SWUS, with the former referring to precipitation amounts below the 33% quantile, and the latter above the 66% quantile.

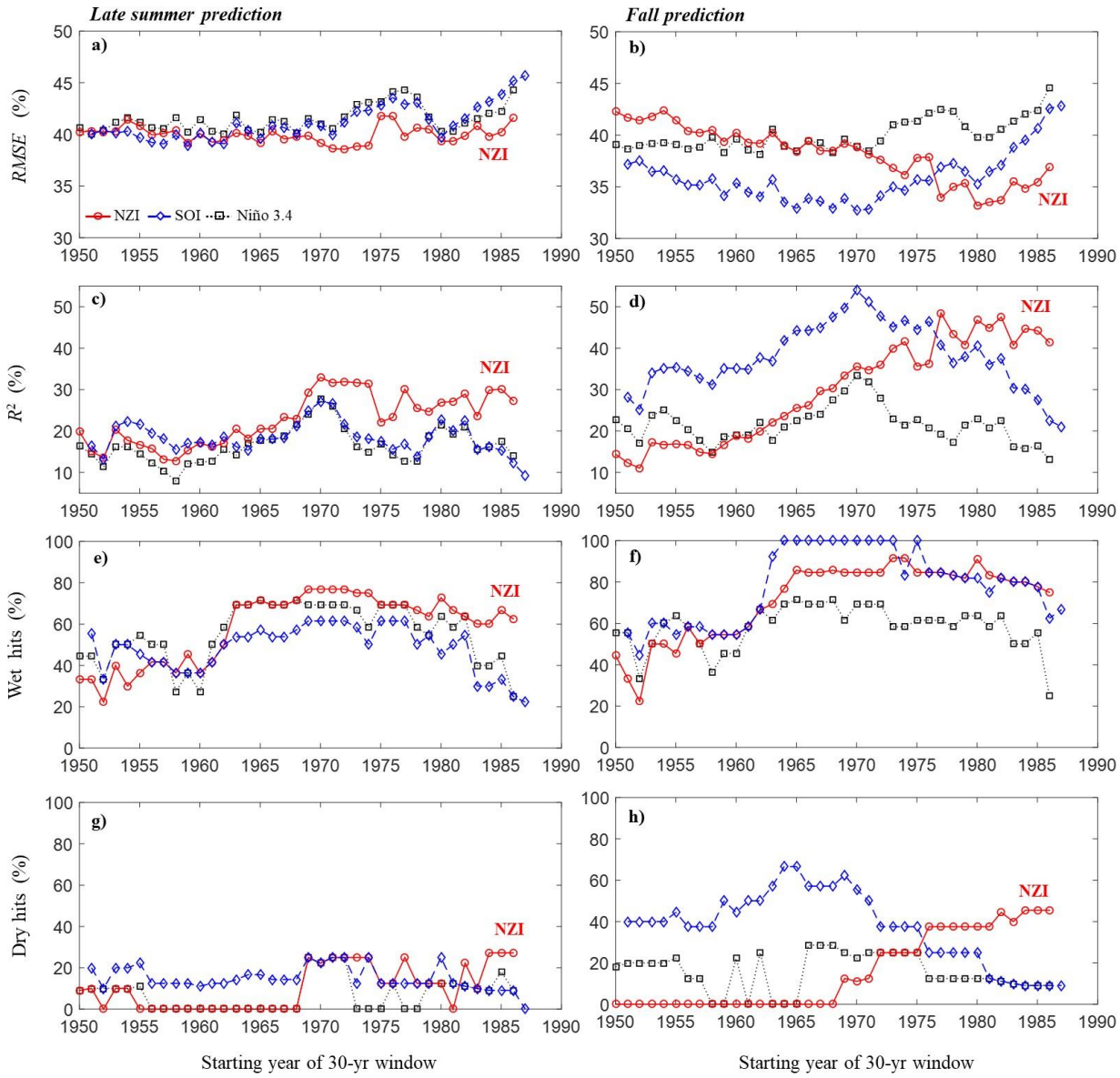

Figure 1.5: **30-year running averages of ENSO and NZI predictive skill for two different lead times indicated the strengthening of NZI after the mid-1970s.** Prediction metrics for 30-yr moving windows are established by comparing models' forecasts and average precipitation amount in SWUS (Nov-Mar): (a)-(b) Standardized *RMSE*; (c)-(d) Coefficient of determination; (e)-(f) Probability of correctly predicting wet conditions; (g)-(h) Probability of correctly predicting dry conditions.

Based on all metrics, after the mid-1970s NZI's predictive skill increased, while ENSO indices lost predictability (see Figure 1.5). Specifically, in the past three decades, NZI's correlation to winter SWUS precipitation was about -0.7, while SSTs in the Niño 3.4 region exhibited almost statistically insignificant relationships (Figure 1.6). The correlation of NZI

with winter precipitation for each climate division and for each of the different time lags is shown in Figure 1.7, further establishing higher level of performance of NZI compared to the most commonly used ENSO indices. The correlation of winter precipitation and NZI in late summer (during Jul-Sep) was high (about -0.55), and increased more during Sep-Nov (about -0.7).

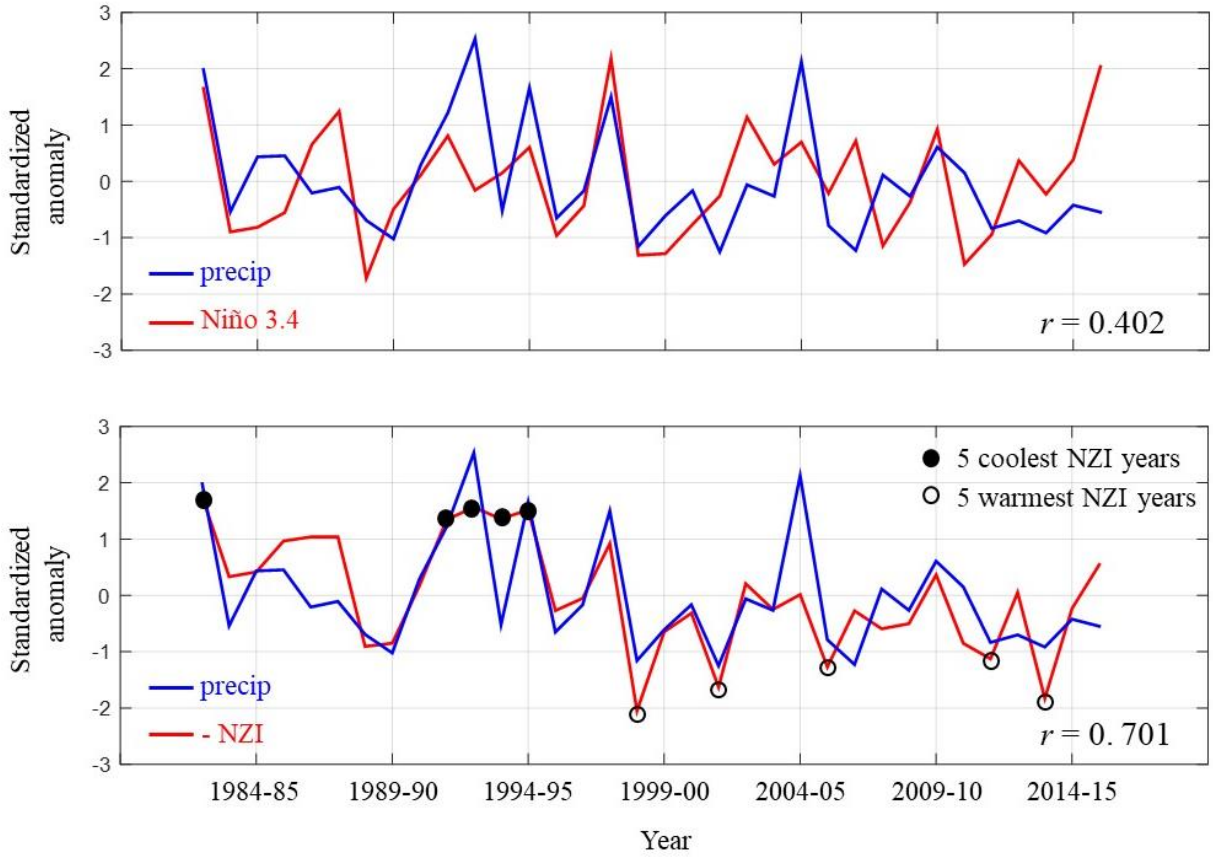

Figure 1.6: **During the last three decades, NZI associated more strongly with the average winter precipitation in the SWUS than Niño 3.4.** NZI and Niño 3.4 anomalies correspond to the Sep-Nov period, while average winter (Nov-Mar) precipitation is computed over climate divisions of significant correlation with Niño 3.4 (see caption of Figure 1.1). In the lower panel, the 5 coolest/warmest NZI years are indicated (lower/upper ~15%) as well, to be used in Figure 1.14 and in Figure 1.15.

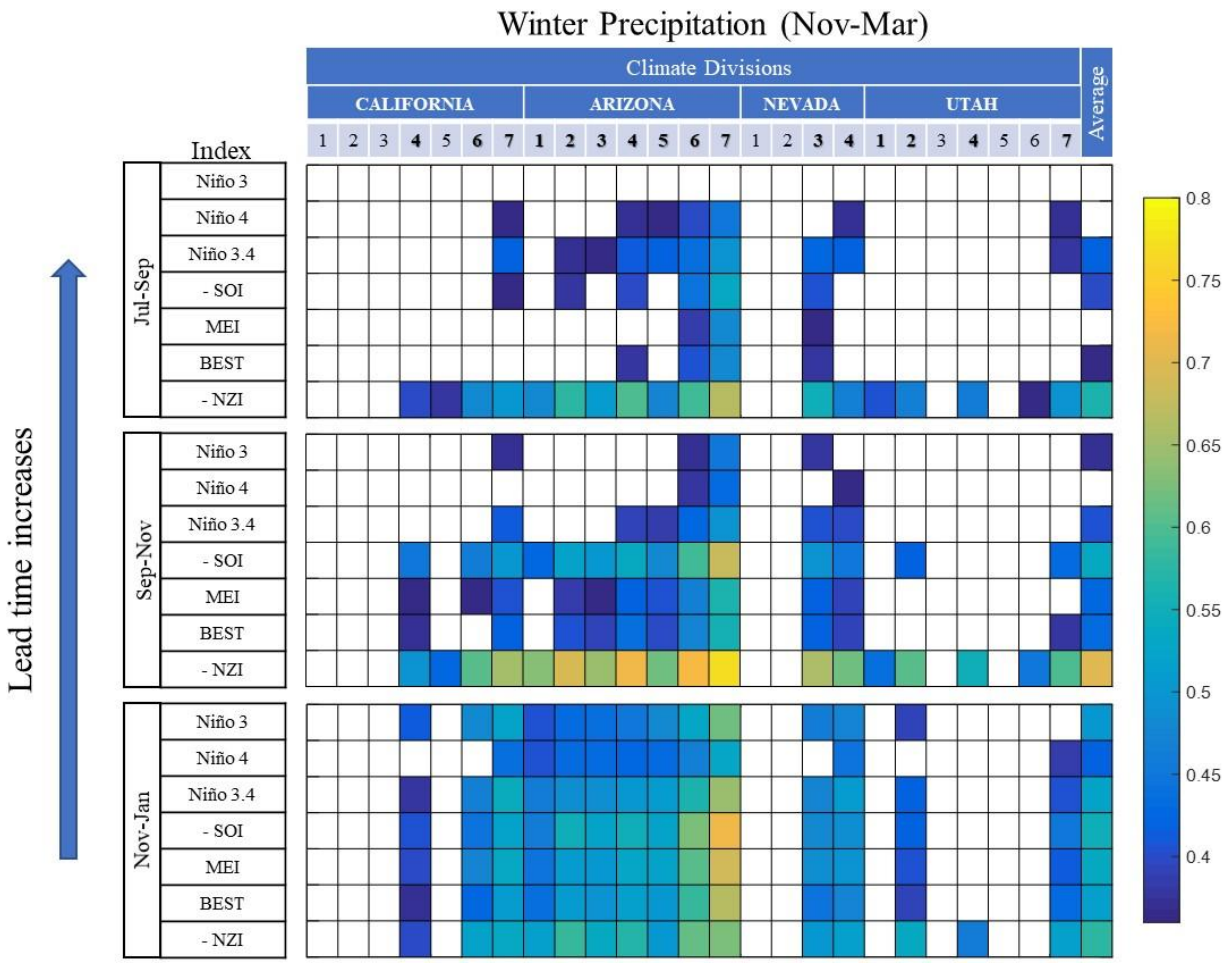

Figure 1.7: **Comparison of ENSO and NZI teleconnection strengths.** Colors illustrate correlation values between precipitation in different climate divisions over SWUS (Nov-Mar) and selected climatological indices corresponding to different 3-month periods, for 1982-2015. Colors denote statistically significant correlations (α = 0.05 significance level). Results in the last column were calculated using the regionally-averaged precipitation amount. NZI outperformed existing indices (correlation of -0.7 compared to 0.3-0.5) and provided statistically significant predictions with a 3-month lead time. Multivariate ENSO Index[5] (MEI) and Bivariate ENSO Timeseries[44] (BEST) are comprehensive indices consisting of multiple meteorological variables (SST, sea level pressure, surface wind, etc.) for determining ENSO state.

The western Pacific pathway. Important insight about the physical mechanism underpinning the NZI teleconnection is gained by exploring the dynamic evolution of the relationship between winter precipitation in the SWUS and ocean and atmosphere state variables in the Pacific basin during the preceding year. SSTs in the NZI region and SWUS precipitation exhibited statistically significant (α=0.05 significance level) correlations (Figure 1.8) during boreal spring (correlations of -0.5), which strengthened during boreal summer, and reached maximum values in fall (correlations of -0.7). Approaching winter, the association of precipitation with the SST and GPH in the NZI region decreased significantly; see also the decrease in the correlation of NZI in the lower panel of Figure 1.7. For zero lead time, precipitation was strongly correlated with SSTs in the northwestern Pacific and GPH directly to the west of SWUS[21-23,50,51], while correlations with ENSO regions emerged, but remained low (lower than 0.5). Two important conclusions were drawn from this analysis. First, climate information from the southwestern Pacific was critical for early prediction of the winter precipitation in the SWUS. Second, winter precipitation in SWUS was modulated by a northward cascade of SST and GPH anomalies through the year, starting in the southern hemisphere during late summer and fall, and cascading to the northwestern Pacific during fall and winter. We propose that this cascade was a key characteristic of the NZI teleconnection and worked through an atmospheric bridge in boreal summer, connecting SSTs in the southern hemisphere with those in the northern hemisphere. We present a mechanistic explanation of the NZI teleconnection in Figure 1.9, and elaborate on it below.

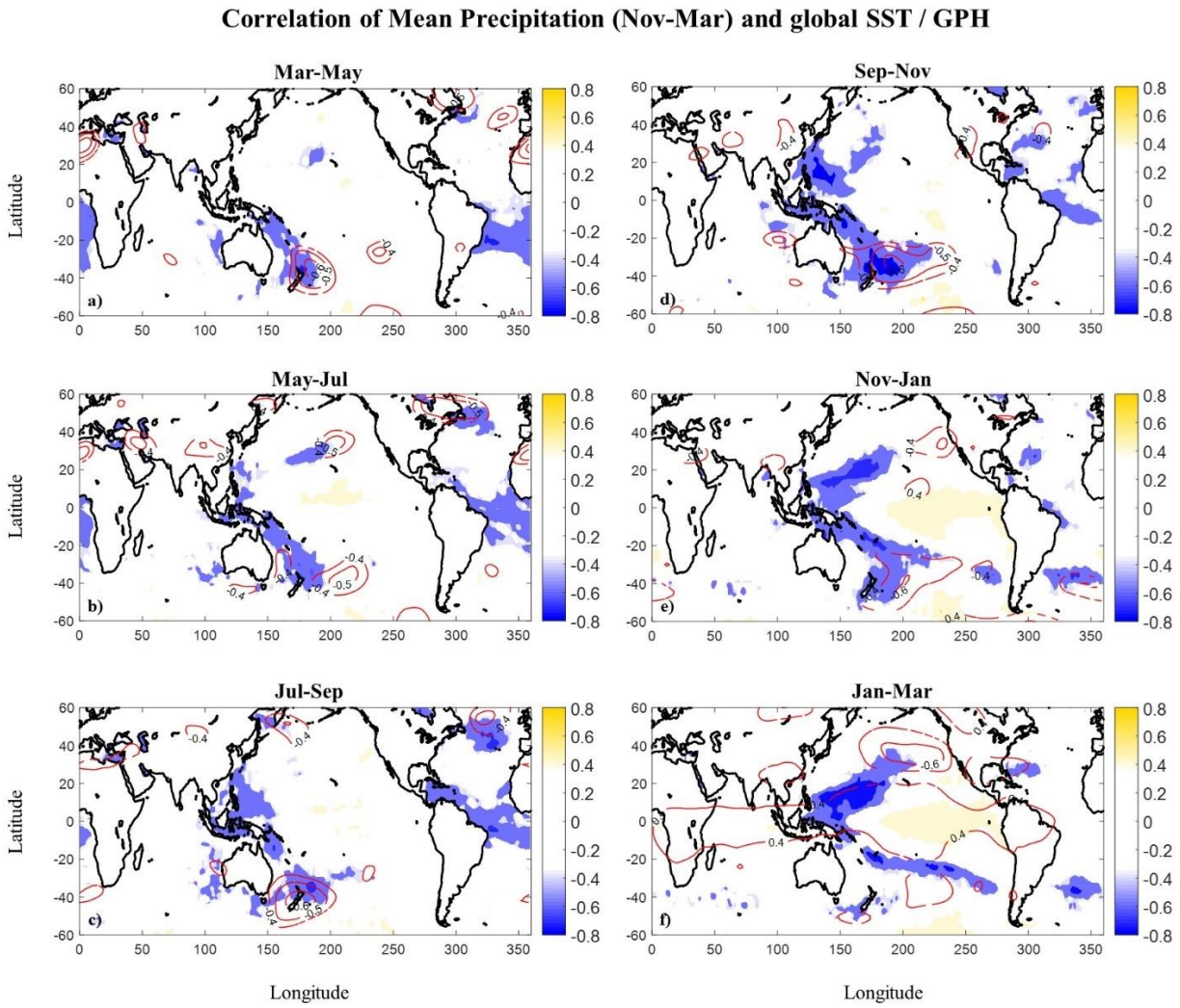

Figure 1.8: Within-year evolution of the association of winter precipitation in SWUS with SSTs and GPHs revealed a northward interhemispheric cascade. Correlation maps between average winter precipitation in SWUS (Nov-Mar) and global SST (shading) and GPH (400 mb; contours), for 1982-2015. SSTs and GPHs are averaged over different periods, starting Mar-May (previous spring) and ending Jan-Mar. Only statistically significant correlations are shown (α = 0.05 significance level).

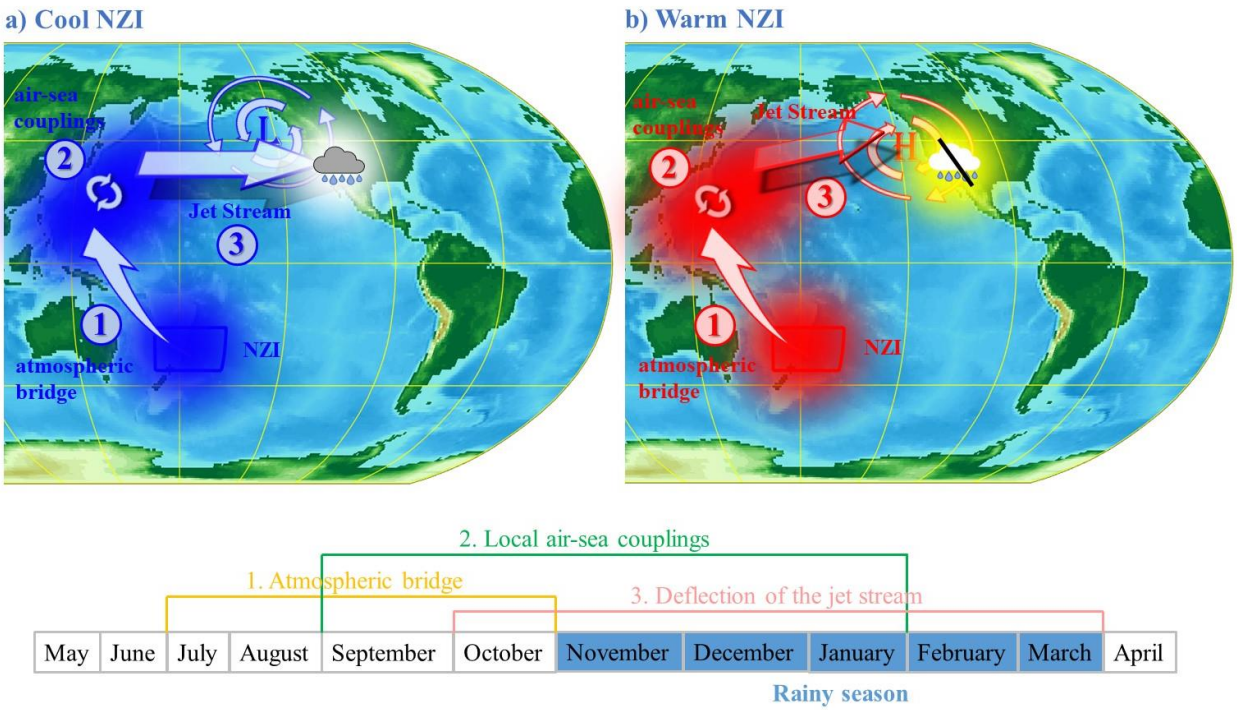

Figure 1.9: The NZI teleconnection depends on a western Pacific ocean-atmosphere pathway. (a) Negative SST anomalies (blue shading) in the NZI region cascade in the northern hemisphere through a late summer interhemispheric atmospheric bridge and are maintained by air-sea coupling until the following winter. The SST anomalies affect the atmospheric pressure in the US west coast and strengthen the regional jet stream which brings more winter storms in the SWUS; (b) Late-summer positive SST anomalies (red shading) in the NZI region deflect the jet stream to the north, leading to dry conditions over the SWUS.

SST anomalies in the NZI region exhibited strong correlation with time-concurrent SST and GPH anomalies near the Philippines, with statistically significant correlations throughout the year (order of 0.5 or less), which intensified during late boreal summer reaching values of 0.7 or higher (Figure 1.10). By analyzing the zonal average vertical velocity over the eastern Asia – western Pacific region of 70°E – 220°E (Figure 1.11), we found that positive SST anomalies in the NZI region induced an anomalous Hadley circulation that ascended from the southwestern Pacific and descended over the Philippines. Its descending motion produced adiabatic warming and increased downward shortwave radiation (likely by means of suppressing cloud formation) resulting in positive SST anomalies near the Philippines. The descending motion also produced positive GPH anomalies. This inter-hemispheric teleconnection was strongest during boreal summer (Figure 1.10), when the southern Hadley cell expands the most[55], connecting the two regions (Figure 1.12). The maximum correlation between late summer NZI and SSTs in the northern hemisphere occurred during late fall (see Figure 1.13) in the eastern side of the Philippines (as high as 0.85). This 3-4 months lag is a main characteristic of the atmospheric bridge and is associated with the time needed for ocean surface heat content and SSTs to respond to the cumulative atmospheric forcing[59]. A similar inter-hemispheric relation, connecting 500 mb GPH anomalies in the area east of Australia with those over the Philippines has been reported and described in the literature[52,53,54]. Specifically, past studies document that the latter teleconnection also takes place during late summer, and that the longitudinal zone around the globe where the most significant interhemispheric interaction occurs is the region of east Australia to east Asia[52,53].

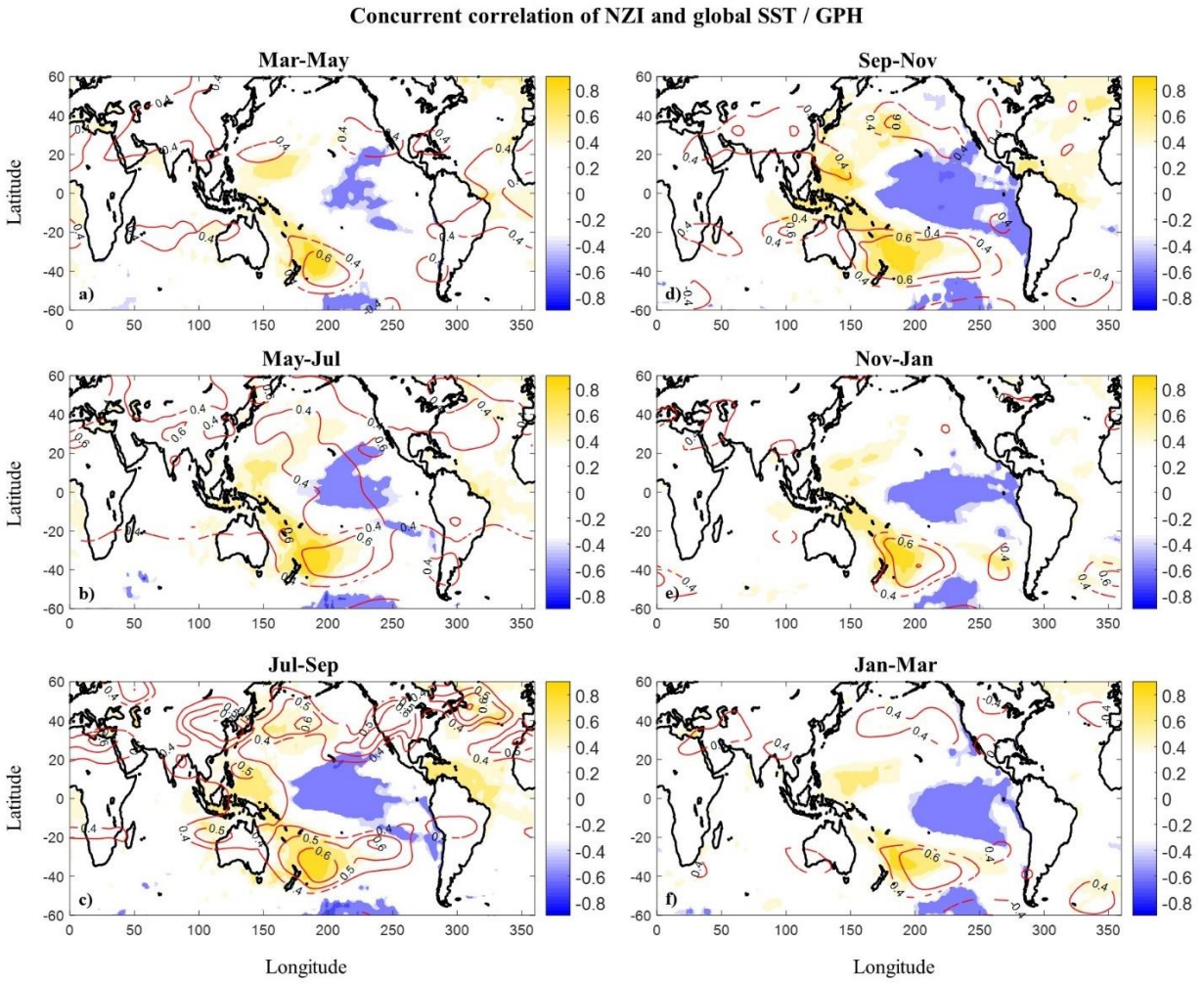

Figure 1.10: SSTs in the region of NZI were closely related with those in the region east of Philippines especially during late boreal summer and fall. Correlation maps between SSTs in the NZI region and global SSTs (shading) and GPHs (400 mb; contours), for 1982-2015. In each panel, NZI, and global SSTs and GPHs are averaged over the same time period, starting Mar-May (top left panel) and ending Jan-Mar (bottom right panel). Only statistically significant (α = 0.05 significance level) correlations are shown.

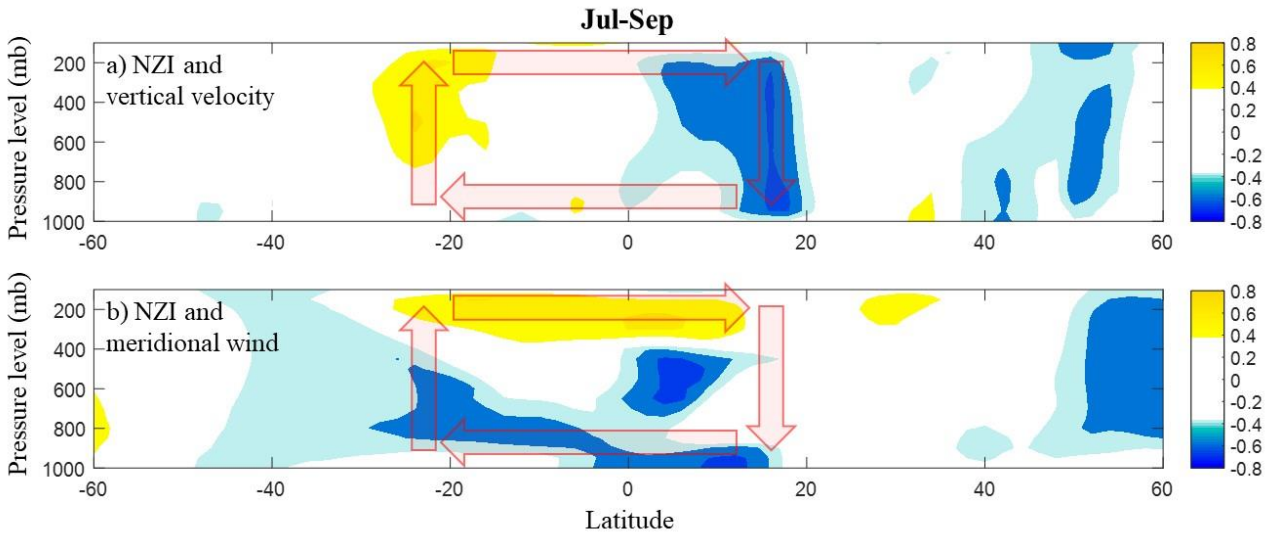

Figure 1.11: Positive SST anomalies in the NZI region weaken the southern Hadley circulation during late boreal summer. (a) Correlation between the NZI (Jul-Sep) and zonal average (70°E-220°E) vertical velocity in Jul-Sep, for 1982-2015 (here, vertical velocity is defined simply as the opposite of omega velocity). Only statistically significant (α = 0.05 significance level) correlations are shown; (b) Same as (a), but for the zonal average meridional wind. In both subplots, the anomalous Hadley circulation is indicated with transparent arrows.

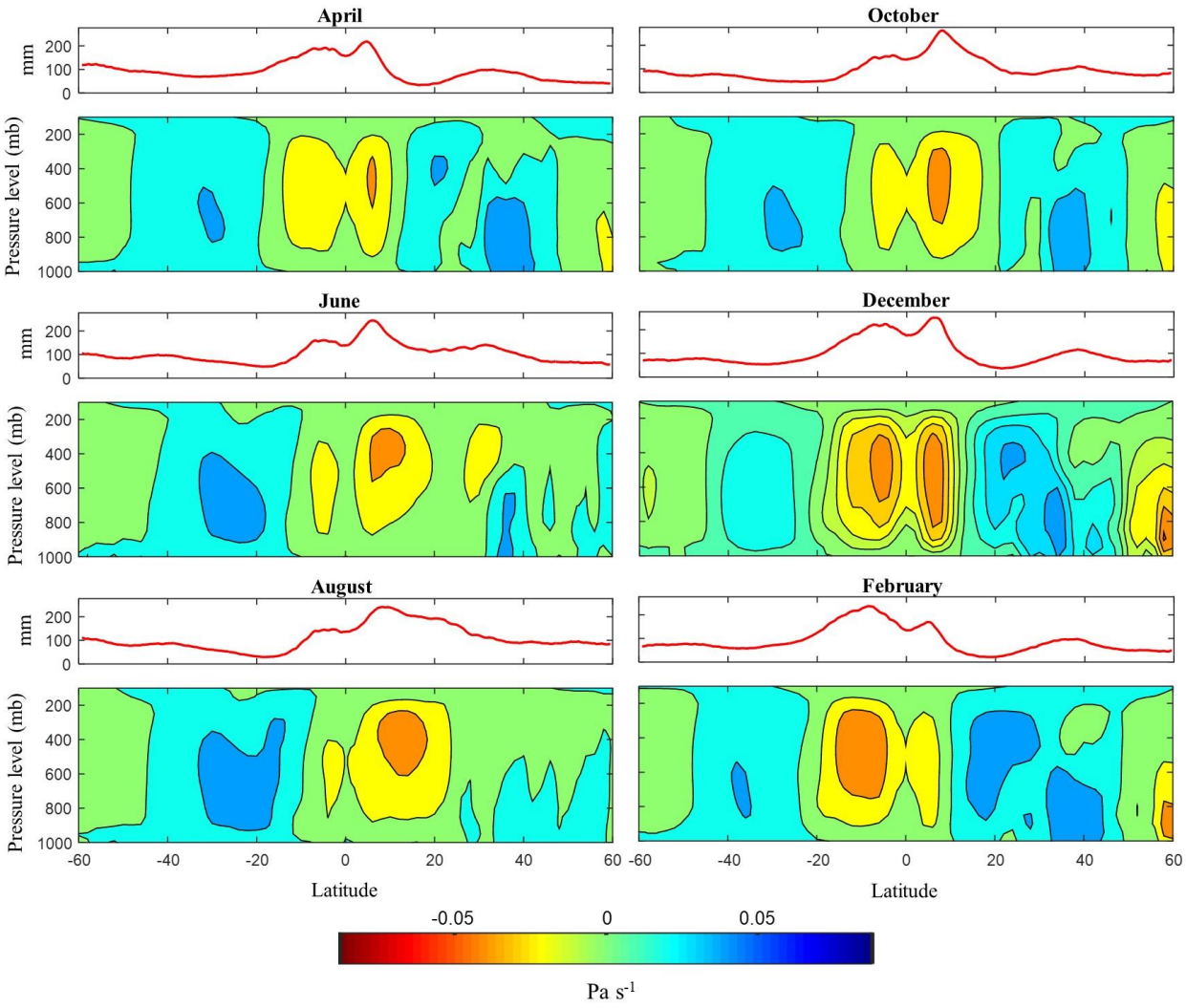

Figure 1.12: **During late boreal summer, the southern Hadley cell expands and connects the area of NZI with the northern hemisphere.** Upper panels: zonal average precipitation (mm) over eastern Asia - western Pacific region (70°E-220°E), for 1982-2015; bottom panels: zonal average omega velocity in Pa s^{-1}, over 70°E-220°E, for 1982-2015. Note that positive (negative) omega velocity corresponds to descending (ascending) motion.

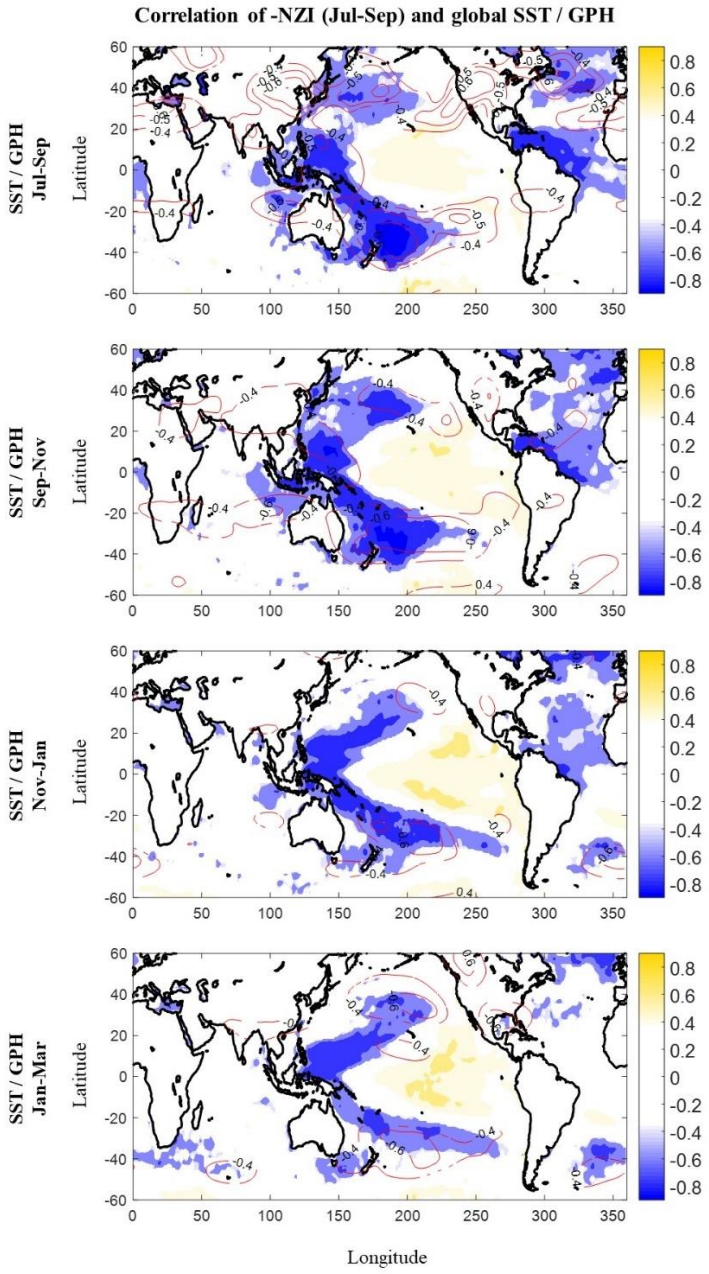

Figure 1.13: NZI anomalies are followed by a northward cascade of SST anomalies in the northern Pacific Ocean starting late summer and ending late winter. Correlation maps between –NZI (averaged over Jul-Sep) and global SST (shading) and GPH (400 mb; contours) in subsequent seasons, derived from reanalysis during 1982-2015. SSTs and GPHs are averaged over 3-month periods, starting Jul-Sep, and ending Jan-Mar. Only statistically significant ($\alpha = 0.05$ significance level) correlations are shown. We correlate SSTs and GPHs with –NZI, so this figure is directly comparable with results in Figure 1.8.

As soon as the cascade to the northern hemisphere has occurred, SST anomalies in the northwestern Pacific persist through boreal winter (see Figure 1.13) via local atmosphere-ocean couplings. Previous studies have shown that SST anomalies in this region interact with local mean trade winds to induce anomalous surface heat flux, and create a positive feedback loop between anticyclonic (cyclonic) activity and sea surface cooling (warming)[60]. This mechanism allows for maintenance and propagation of the SST anomalies from the northwestern Pacific to the northcentral Pacific (Figure 1.13). When the SST anomalies in the western and central north Pacific persist into the boreal winter, they alter the atmospheric pressure in the western US through a short-wave train which links the two areas[23,61], modifying the track and strength of the jet stream over the west US coast (220°E-260°E). These changes in the jet stream can steer more or fewer winter storms to impact SWUS precipitation (see Figures 1.8e,f and 1.9). Specifically, cool NZI conditions during late summer, after propagating into the northwestern Pacific and maintaining themselves during fall and winter, intensify the upper zonal winds at 30-35°N, and bring above average precipitation to SWUS (Figure 1.14). In contrast, warm SSTs in the NZI region excite positive anomalies in the northwestern Pacific, deflecting the jet stream northward (at 45°-50°N), and leading to wet conditions over the northwestern US, and dry conditions in SWUS. Accordingly, NZI is associated with a dipole pattern along the west coast of the US, which is evident in both zonal winds of the upper atmosphere, as well as in precipitation amounts (see Figure 1.15). Note that this behavior is well-known to be also associated with ENSO events[13,16,17,19,46,57], yet in the last three to four decades, ENSO did not correlate significantly with precipitation amount for many regions along the west coast (Figure 1.16).

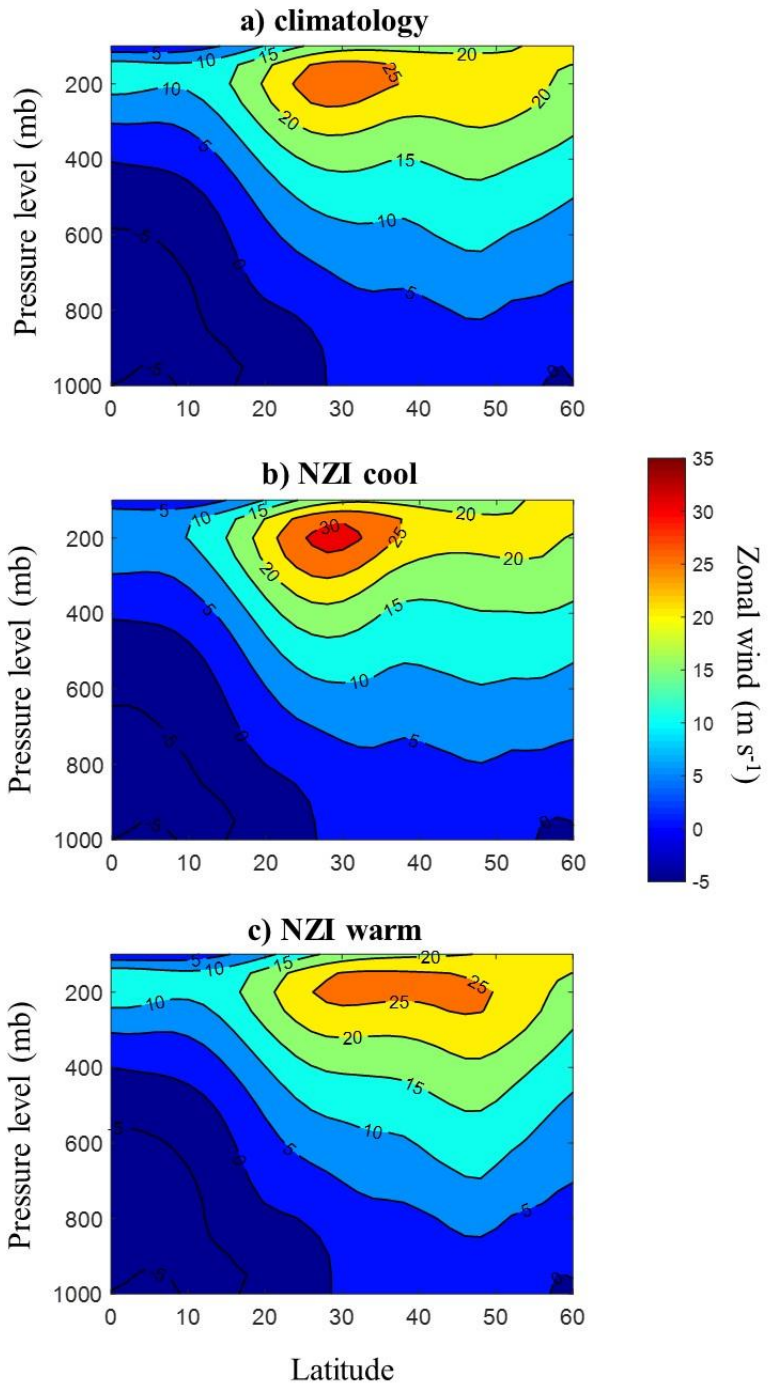

Figure 1.14: NZI affects the upper zonal winds in the northeastern Pacific and modulates SWUS precipitation. (a) Zonal average (220°E-260°E) of zonal wind in m s^{-1} for different latitude and pressure levels, during Nov-Mar, for 1982-2015; (b) Same as (a), but for the 5 coolest NZI years; see Figure 1.6; (c) Same as (a), but for the 5 warmest NZI years.

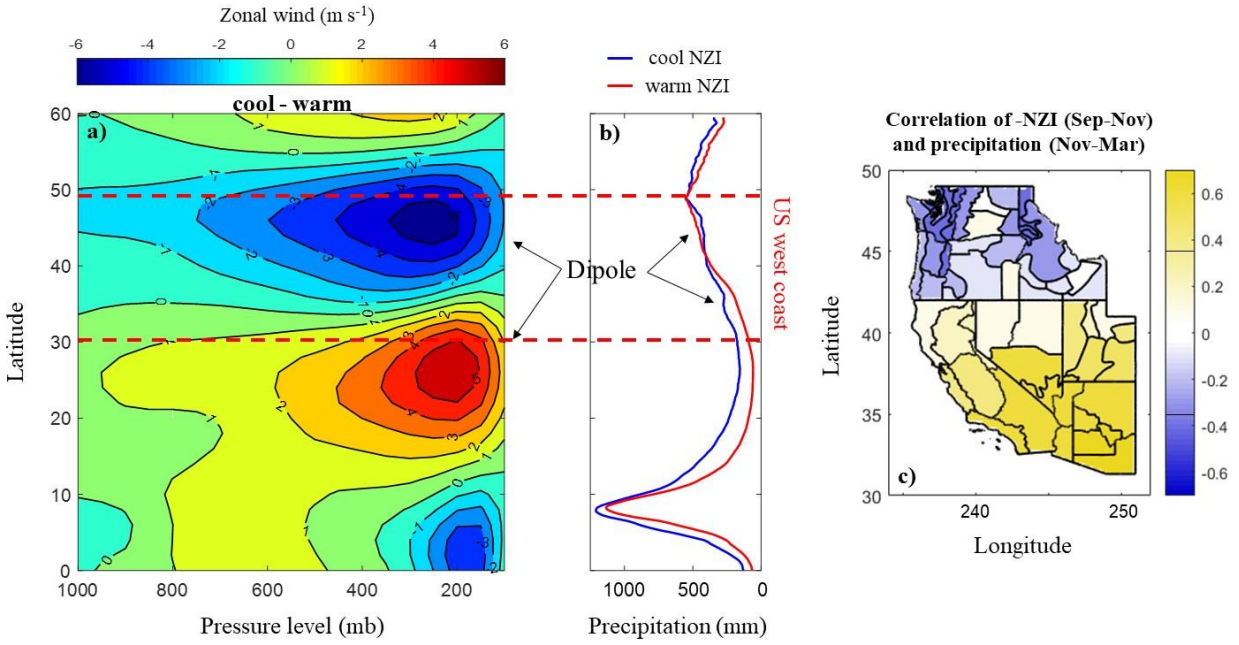

Figure 1.15: NZI was a driver of a dipole of precipitation anomalies along the west coast. (a) Difference of zonal average (220°E-260°E) zonal wind in cool and warm NZI conditions, in m s^{-1}, for Nov-Mar; (b) Zonal average winter precipitation in mm (Nov-Mar), corresponding to the 5 coolest (blue) and 5 warmest (red) NZI years; see Figure 1.6; (c) Correlation of –NZI (Sep-Nov) with winter precipitation (Nov-Mar) in all climate divisions over the west US coast, for 1982-2015. The area between the two solid black lines on the colorbar indicates statistically insignificant (α = 0.05 significance level) correlations.

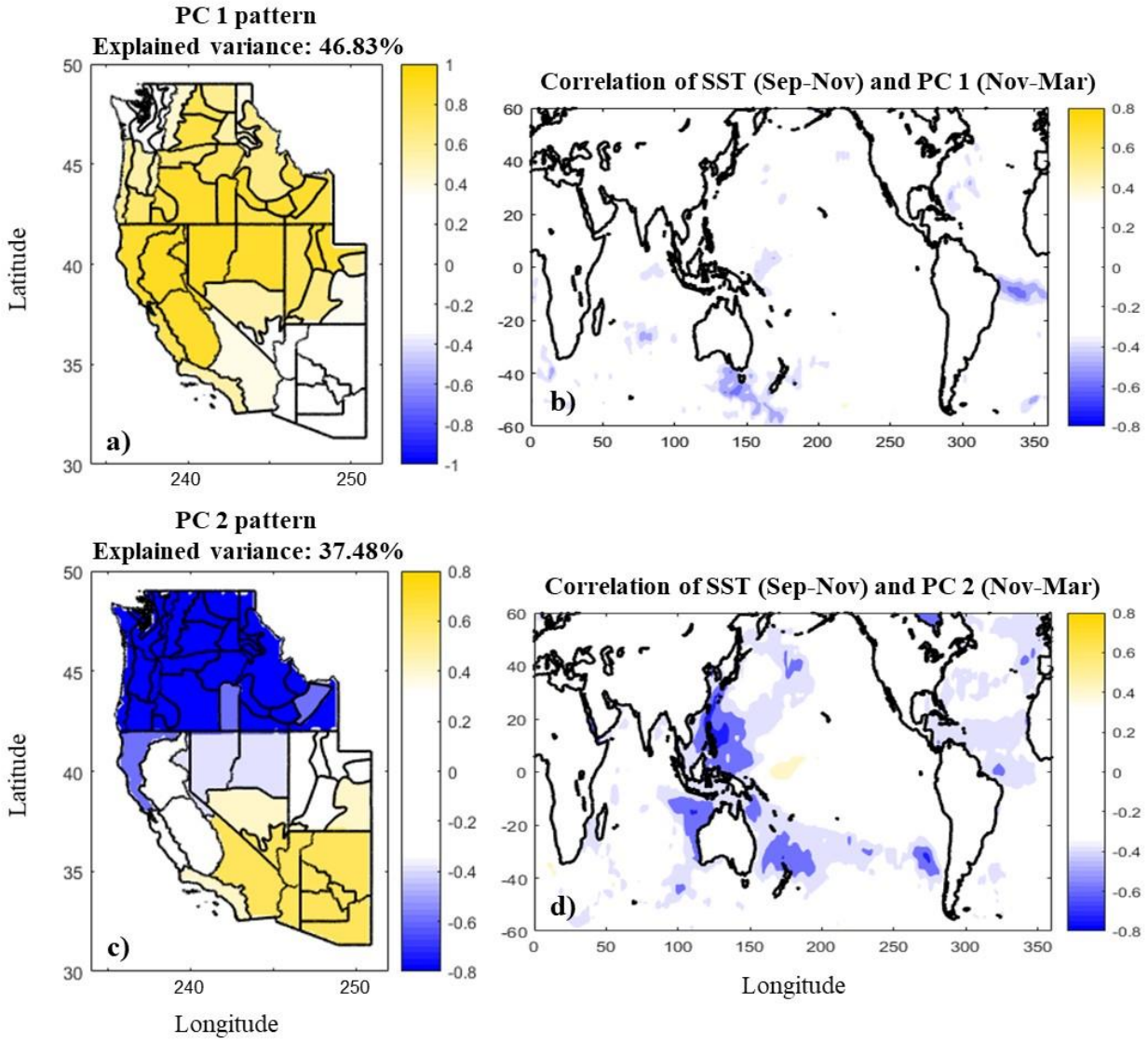

Figure 1.16: **Southwestern Pacific SSTs were strongly correlated with the second principal component of winter precipitation in the western US.** (a) The spatial pattern of the first principal component (PC) of winter (Nov-Mar) precipitation series of all climate divisions in the western US, as determined by its correlation with precipitation in each climate division. Only statistically significant (α = 0.05 significance level) correlations are shown; b) Correlation map between the first principal component and global SST (Sep-Nov), for 1982-2015; (c)-(d) same as (a)-(b), but for the second principal component. Note that PC1 is not related to SSTs, while PC2 exhibits strong statistical dependence with SSTs in the NZI region (correlation on the order of -0.6) but no statistical dependence with SSTs in the ENSO region.

The proposed mechanism of NZI reveals a western Pacific pathway and can be summarized by the following three sub-processes (Figure 1.9):

Late Summer: The expansion of the Southern Hadley cell creates an interhemispheric atmospheric bridge connecting geopotential heights (and SSTs) in the area close to New Zealand with those in the northwestern Pacific. Similar interhemispheric teleconnections have been described in previous studies[52,53,54].

Late Fall: Local air-sea coupling maintains atmospheric pressure and SST anomalies in the northwestern Pacific[60].

Winter: SSTs in the northwestern Pacific influence atmospheric pressure and upper zonal winds in the western US, which in turn change the positioning of storm tracks and precipitation amount in SWUS [21-23,50,51,61].

Changes in Pacific dynamics. By establishing similar analyses in the period before the 1980s, we determined that the correlation of NZI with SSTs in the region east of the Philippines (referred to as EPh: the areal average SSTs in the region of 5-15°N and 130-150°E), has not been stationary (Figure 1.17). During 1950 – 1983, the connection of NZI and EPh was weak (correlations did not exceed 0.45), whereas during the last 35 years, it was remarkably strong and robust, with correlations reaching 0.8 during boreal fall, and with NZI leading EPh by 3-4 months. The intensification of this connection between the two hemispheres was the primary reason for the increased correlation of NZI and SWUS precipitation observed during the last several decades (Figure 1.4). In contrast, during the earlier period where the NZI was only weakly connected to the northern hemisphere, its correlation with precipitation variability in SWUS was lower.

The time-evolving covariance of SSTs in the two regions highlights the non-stationary nature of ocean-atmosphere dynamics on decadal time scales, and its direct impact on regional hydroclimatic variability. The intensification of this northward interhemispheric cascade may be a result of the expansion of the tropics which has been observed after the 1980s[11,28-31,56], and allows SST or GPH variability at lower latitudes to more strongly affect the meridional atmospheric circulation at higher latitudes. However, it is still not known what exactly is the relative contribution of the natural variability (multi-decadal oscillations) and external (anthropogenic) forcing to the latter change[30,31], so it is not certain whether the strength of the NZI signal will continue to increase or undergo periodic fluctuations in the

future. The observed increase of the correlation of NZI with precipitation may also be influenced by changes in data quality after the late 1970s, when satellite data improved coverage, particularly in the southern hemisphere[37,38].

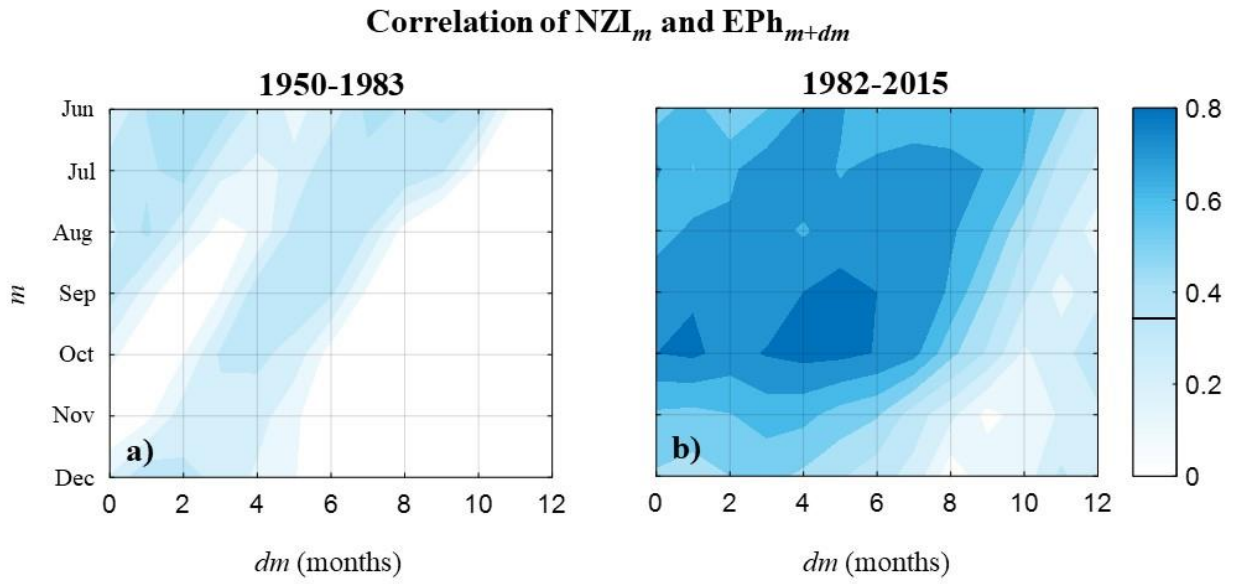

Figure 1.17: Interhemispheric teleconnections between NZI and SST anomalies in the northwestern Pacific have significantly strengthened during the last three to four decades. (a) Time-lagged correlation between NZI (averaged over the month indicated in the vertical axis) and SST in the region east of the Philippines (EPh) (box in 5-15°N and 130-150°E; lagged forward in time as indicated in the horizontal axis) in 1950-1983. Solid black line on the colorbar indicates the threshold below which correlations are statistically insignificant (α = 0.05 significance level); (b) Same as (a), but for the period 1982-2015.

Discussion

Non-stationary relationships between potential predictors (ENSO or NZI) and precipitation due to climate change or internal climate variability can significantly impact our ability to develop accurate seasonal forecasts[17,35,62]. The revealed changes in the strength of the NZI and ENSO signals to winter precipitation in SWUS is an example of such variation, offering the chance to quantify the effect of large-scale non-stationarity on regional precipitation predictability. To illustrate this point, we evaluated and compared the prediction error of an SST-based regression model in settings in which the calibration and prediction periods coincided versus settings that they did not (i.e., in-sample vs. out-of-sample predictions). Specifically, we predicted winter precipitation over two non-

overlapping periods (1951-1983 and 1983-2015) using a multiple regression model based on NZI, SOI and Niño 3.4 series. We quantified the effect of non-stationarity on the prediction skill as the relative increase of *RMSE* when the calibration and prediction periods did not overlap (e.g. prediction in 1983-2015, calibration in 1951-1983) relatively to the case that the calibration and prediction periods completely overlapped (e.g. prediction in 1983-2015, calibration in 1983-2015). If stationary conditions held, the increase of *RMSE* would be close to zero, since calibration in either period would result to almost identical regression functions (deviation from zero would be a result of sample variability). However, this analysis revealed that the relative increase of *RMSEs* can be as high as 400%-500% (Table 1.1), which means that our predictive skill is approximately 5-6 times lower than what it would have been if stationary relationships actually held. The latter analysis demonstrates the important effect of the stationarity assumption in a changing climate, and highlights the importance of understanding the multi-scale patterns of change from climate dynamics to regional precipitation.

Table 1.1: Effect of non-stationarity in the NZI/ENSO teleconnection strength on the precipitation prediction error. Computed *RMSE*s (cm) of precipitation prediction, when calibration and validation periods overlap (cross validation) and when they do not (***bold italics*** font).

prediction period		1951-1983			1983-2015		
averaging period of predictors		Jul-Sep	Sep-Nov	Nov-Jan	Jul-Sep	Sep-Nov	Nov-Jan
calibration period	1951-1983	5.85	5.39	5.48	***30.75***	***32.45***	***33.97***
	1983-2015	***31.26***	***32.25***	***32.31***	5.97	5.32	5.74
standardized difference (%)		434	498	490	415	510	492

In summary, we show that during the last several decades, SST anomalies in the southwestern Pacific Ocean have been closely related to precipitation in SWUS through a western Pacific pathway, and thus, they may be useful in increasing precipitation predictability. Idealized climate model experiments can be used to provide further evidence for our proposed teleconnection mechanism, by quantifying how prescribed SST anomalies in the southwestern Pacific influence the meridional circulation, north Pacific SSTs, and the western US precipitation. Further research is also needed to better understand the drivers of the decadal variability of the newly established teleconnection. Our work emphasizes the

need to understand the dynamic nature of the coupled atmosphere-ocean system in a changing climate, for improving future predictions of regional precipitation.

REFERENCES

1. National Academies of Sciences, Engineering, and Medicine (2016) *Next Generation Earth System Prediction: Strategies for Subseasonal to Seasonal Forecasts*, Washington, DC: The National Academies Press. doi:https://doi.org/10.17226/21873.

2. Becker, E., H. van den Dool, and Q. Zhang (2014) Predictability and Forecast Skill in NMME, *J. Clim.*, **27**, 5891–5906.

3. Chang, Y., S. D. Schubert, and M. J. Suarez (2000) Boreal winter predictions with the GEOS-2 GCM: The role of boundary forcing and initial conditions, *Quart. J. Roy. Meteor. Soc.*, **126**, 2293–2321, doi:10.1256/smsqj.56714.

4. Rajeevan, M., D. S. Pai, R. A. Kumar, and B. Lal (2007) New statistical models for long-range forecasting of southwest monsoon rainfall over India, *Clim. Dyn.*, **28**(7-8), 813-828.

5. Madadgar, S., A. AghaKouchak, S. Shukla, A. W. Wood, L. Cheng, K.-L. Hsu, and M. Svoboda (2016) A hybrid statistical-dynamical framework for meteorological drought prediction: Application to southwestern United States, *Water Resour. Res.*, **52**, 5095-5110.

6. Mamalakis, A., A. Langousis, R. Deidda, and M. Marrocu (2017) A parametric approach for simultaneous bias correction and high-resolution downscaling of climate model rainfall, *Water Resour. Res.*, **53**, 2149–2170.

7. Schubert, S., Y. Chang, H. Wang, R. Koster, and M. Suarez (2016), A Modeling Study of the Causes and Predictability of the Spring 2011 Extreme US Weather Activity, *Journal of Climate*, 29(21), 7869-7887.

8. AghaKouchak, A., D. Feldman, M. Hoerling, T. Huxman, and J. Lund (2015) Recognize Anthropogenic Drought, *Nature*, **524**(7566), 409-411.

9. Feng, S. and Q. Fu, (2013) Expansion of global drylands under a warming climate, *Atmospheric Chemistry and Physics,* **13,** 10081-10094, http://dx.doi.org/10.5194/acp-13-10081-2013

10. Overpeck, J. and Udall, B. (2010) Dry times ahead, *Science*, **328**, 1642–1643.

11. Seidel, D.J., Q. Fu, W.J. Randel, and T.J. Reichler, (2008) Widening of the tropical belt in a changing climate, *Nature Geosci.*, **1,** 21-24, http://dx.doi.org/10.1038/ngeo.2007.38

12. Seager, R., Ting, M., Held, I., Kushnir, Y., Lu, J., Vecchi, G., Huang, H. P., Harnik, N., Leetmaa, A., Lau, N. C., Li, C., Velez, J., and Naik, N. (2007) Model projections of an imminent transition to a more arid climate in southwestern North America, *Science*, **316**, 1181–1184.

13. Newman, M., *et al.* (2016) The Pacific Decadal Oscillation, Revisited, *J. Clim.*, 4399-4427.

14. Wang, S., J. Huang, Y. He, and Y. Guan, (2014) Combined effects of the Pacific decadal oscillation and El Niño–Southern Oscillation on global land dry–wet changes, *Sci. Rep.*, 4, 6651, doi:10.1038/srep06651.

15. Yu, J.-Y., Y. Zou, S. T. Kim, and T. Lee (2012) The Changing Impact of El Niño on US Winter Temperatures, *Geophysical Research Letters*, **39**, doi:10.1029/2012GL052483.

16. Brown, D. P., and A. C. Comrie (2004) A winter precipitation ''dipole'' in the western United States associated with multidecadal ENSO variability, *Geophys. Res. Lett.*, **31**, L09203, doi:10.1029/2003GL018726.

17. McCabe, G. J. and M. D. Dettinger (1999), Decadal variations in the strength of ENSO teleconnections with precipitation in the western United States, *Int. J. Climatology*, **19**, 1399-1410.

18. Enfield, D. B., A. M. Mestas-Nuñez (2001), The Atlantic multidecadal oscillation and its relation to rainfall and river flows in the continental U.S., *Geophys. Res. Lett.*, **28**(10), 2077-2080.

19. Schonher, T. and S. E. Nicholson (1989) The relationship between rainfall and ENSO events, *J. Clim.*, **2**, 1258–1269.

20. Dai, A. (2013) The influence of the inter-decadal Pacific oscillation on US precipitation during 1923-2010, *Clim. Dyn*., **41**, 633 - 646.

21. Seager, R., *et al.* (2015) Causes of the 2011-2014 California Drought, *J. Clim.*, **28**, 6997-7024.

22. Swain, Daniel L., Daniel E. Horton, Deepti Singh, and Noah S. Diffenbaugh. "Trends in atmospheric patterns conducive to seasonal precipitation and temperature extremes in California." *Science Advances* 2, no. 4 (2016): e1501344.

23. Wang, S. Y., L. Hipps, R. R. Gillies, and J. H. Yoon (2014) Probable causes of the abnormal ridge accompanying the 2013-2014 California drought: ENSO precursor and anthropogenic footprint, *Geophys. Res. Lett.*, **41**, 3220-3226.

24. McCabe, G. J., M. A. Palecki, amd J. L. Betancourt (2004), Pacific and Atlantic ocean influences on multidecadal drought frequence in the United States, *Proc. Natl. Acad. Sci. U. S. A.*, **101**(12), 4136-4141.

25. Baxter, S., and S. Nigam (2015) Key Role of the North Pacific Oscillation-West Pacific Pattern in Generating the Extreme 2013/14 North American Winter, *J. Clim.*, **28**, 8109–8117.

26. Teng, H., and G. Branstator (2017) Causes of extreme ridges that induce California droughts, *J. Clim.*, doi: 10.1175/JCLI-D-16-0524.1.

27. Dettinger, M. and D. Cayan, (2014), Drought and the California Delta – A matter of extremes, *San Francisco Estuary and Watershed Sci*., **12**(2).

28. Fu, Q., C. M. Johanson, J. M. Wallace, and T. Reichler, (2006) Enhanced mid-latitude tropospheric warming in satellite measurements. *Science*, **312**, 1179.

29. Adam, O., T. Schneider, and N. Harnik (2014) Role of changes in mean temperatures versus temperature gradients in the recent widening of the Hadley circulation, *J. Clim.*, **27**, 7450-7461.

30. Allen, R.J., J.R. Norris, and M. Kovilakam (2014) Influence of anthropogenic aerosols and the Pacific Decadal Oscillation on tropical belt width, *Nature Geoscience*, **7**, 270-274, doi: 10.1038/NGEO2091.

31. Garfinkel, C., I., D. W. Waugh, and L. M. Polvani (2015) Recent Hadley cell expansion: The role of internal atmospheric variability in reconciling modeled and observed trends, *Geophys. Res. Lett.*, **42**, 10824-10831.

32. Chen, X., and J. M. Wallace (2015) ENSO-Like Variability: 1900-2013, *J. Clim.*, **28**, 9623-9641.

33. Compo, G. P., *et al.* (2011) Review Article, The twentieth century reanalysis project, *Q. J. R. Meteorol. Soc.* **137**, 1–28.

34. Hirahara, S., M. Ishii, and Y. Fukuda (2014) Centennial-scale sea surface temperature analysis and its uncertainty, *J. Clim.*, **27**, 57-75.

35. Power, S., T. Casey, C. Folland, A. Colman, V. Mehta (1999) Inter-decadal modulation of the impact of ENSO on Australia, *Clim. Dynamics*, **15**, 319-324.

36. Reynolds, R. W., N. A. Rayner, T. M. Smith, D. C. Stokes, and W. Wang (2002) An improved in situ and satellite SST analysis for climate, *J. Clim.*, **15**, 1609-1625.

37. Seager, R., N. Harnik, Y. Kushnir, W. Robinson and J. Miller (2003) Mechanisms of hemispherically symmetric climate variability, *J. Clim.*, **16**(18), 2960-2978.

38. Seager, R., N. Harnik, W. A. Robinson, Y. Kushnir, M. Ting, H. Huang and J. Velez (2005) Mechanisms of ENSO-forcing of hemispherically symmetric precipitation variability, *Q. J. R. Meteorol. Soc.*, **131**, 1501-1527.

39. Seager, R., N.H. Naik, M.F. Ting, M.A. Cane, N. Harnik, Y. Kushnir (2010) Adjustment of the atmospheric circulation to tropical Pacific SST anomalies: Variability of transient eddy propagation in the Pacific-North America sector, *Q. J. R. Meteorol. Soc.*, **136**, 277-296.

40. Vose, R. S., *et al.* (2014) Improved Historical Temperature and Precipitation Time Series for U.S. Climate Divisions, *J. Appl. Meteor. Climatol.*, **53**, 1232-1251.

41. Wallace, J. M., and D. S. Gutzler, (1981) Teleconnections in the Geopotential Height Field during the Northern Hemisphere Winter, *Monthly Weather Review*, **109**, 784-812.

42. Wang, H. and M. Ting (2000) Covariabilities of winter U.S. precipitation and Pacific sea surface temperatures, *J. Clim.*, **13**, 3711-3719.

43. Webster, P. J., and S. Yang (1992) Monsoon and ENSO: Selectively interactive systems, *Q. J. R. Meteorol. Soc.*, **118**, 877 – 925.

44. Smith, C.A., and P. Sardeshmukh, (2000) The Effect of ENSO on the Intraseasonal Variance of Surface Temperature in Winter, *International J. of Climatology*, **20,** 1543-1557.

45. Wang, H., S. Schubert, M. Suarez, R. Koster (2010) The physical mechanisms by which the leading patterns of SST variability impact US precipitation, *J. Climate* **23**, 1815–1836.

46. Redmond, K.T., and R.W. Koch (1991) Surface climate and streamflow variability in the Western United States and their relationship to large-scale circulation indices, *Water Resources Research,* **27**(9) 2381-2399.

47. Ashouri, H., K.L. Hsu, S. Sorooshian, D.K. Braithwaite, K.R. Knapp, L.D. Cecil, B.R. Nelson, and O.P. Prat (2015) PERSIANN-CDR: Daily Precipitation Climate Studies Data Record from Multisatellite Observations for /Hydrological and Climate Studies, *Bull. Amer. Meteor. Soc.*, **96**, 69-83, doi: http://dx.doi.org/10.1175/BAMS-D-13-00068.1.

48. Johnson, N.C. (2013) How many ENSO flavors can we distinguish? *Journal of Climate*, **26**, 4816-4827.

49. Newman, M., S.-I. Shin, and M. A. Alexander (2011) Natural variation in ENSO flavors, *Geophys. Res. Lett.*, **38**, L14705, doi:10.1029/2011GL047658.

50. Cayan, D.R., Dettinger, M.D., Diaz, H.F., and Graham, N. (1998) Decadal variability of precipitation over western North America, *Journal of Climate*, **11**, 3148-3166.

51. Dettinger, M.D., Cayan, D.R., Diaz, H.F., and Meko, D. (1998) North-south precipitation patterns in western North America on interannual-to-decadal time scales, *Journal of Climate*, **11**, 3095-3111.

52. Liu, G., L. Ji, S. Sun, and Q. Zhang (2010) An inter-hemispheric teleconnection and a possible mechanism for its formation, *Advances in Atmospheric Sciences*, **27**(3), 629-638.

53. Wang, S. W., and Z. C. Zhao (1987) The interaction between the two hemispheres and long-term forecasting, *Foundation of Long-term Weather Forecasting*, Shanghai Science & Technology Press, Shanghai, 116–130. (in Chinese)

54. Tao, S. Y., and S. Y. Xu (1962) The characteristics of the zonal and meridional circulation over tropical and subtropical regions in eastern Asia in summer. *Acta Meteorologica Sinica*, **32**, 91–103. (in Chinese)

55. Oort, A.H., and J.J. Yienger (1996) Observed interannual variability in the Hadley circulation and it connection to ENSO, *J. Climate*, **9**, 2751–2767, doi:10.1175/1520-0442(1996)009.

56. Kang, S.M., J. Lu (2012) Expansion of Hadley Cell under Global Warming: Winter versus Summer, *J. Climate*, **25**, 8387–8393, doi:10.1175/JCLI-D-12-00323.1.

57. Lindsey, R., 2016: How El Niño and La Niña affect the winter jet stream and U.S. climate. Climate.gov. https://www.climate.gov/news-features/featured-images/how-el-ni%C3%B1o- and-la-ni%C3%B1a-affect-winter-jet-stream-and-us-climate.

58. Kao, H.-Y. and J.-Y. Yu, 2009: Contrasting Eastern-Pacific and Central-Pacific Types of ENSO. *Journal of Climate*, 22, 615-632, doi: 10.1175/2008JCLI2309.1.

59. Alexander, M. A., I. Bladé, M. Newman, J. R. Lanzante, N-C. Lau, and J. D. Scott, 2002: The atmospheric bridge: The influence of ENSO teleconnections on air–sea interaction over the global oceans. *J. Climate*, **15,** 2205–2231.

60. Wang, B., R.Wu, and X. Fu, 2000: Pacific–East Asian teleconnection: How does ENSO affect east Asian climate. *J. Climate,* **13,** 1517–1536.

61. Wang, S.-Y., R.R. Gillies, L.E. Hipps, and J. Jin, 2011: A transition-phase teleconnection of the Pacific quasi-decadal oscillation. *Clim. Dyn.,* **36,** 681–693.

62. Ramage, C., S., 1983: Teleconnections and the siege of time. *J. of Climatology,* **3,** 223–231.

1.2. The impact of El Niño-Southern Oscillation and external forcing on the identified teleconnection

Part of this chapter has been published in Nature Communications

Citation: Mamalakis, A., J.-Y. Yu, J.T. Randerson, A. AghaKouchak, and E. Foufoula-Georgiou (2019) Reply to: A critical examination of a newly proposed interhemispheric teleconnection to Southwestern US winter precipitation, Nature Communications, https://doi.org/10.1038/s41467-019-10531-3

Gibson et al. comment on the physical mechanism suggested by Mamalakis et al. (2018) (hereafter referred to as M18), and question the first step of the newly proposed interhemispheric teleconnection, i.e. the atmospheric bridge, whereby sea surface temperature (SST) close to New Zealand (termed as NZI; the New Zealand Index) modulates the SST in the northwestern Pacific. Specifically, they suggest that there is no direct causal relationship between these key areas since the observed high statistical correlations between the corresponding SST anomalies can be largely explained by local SST memory and the El Niño-Southern Oscillation (ENSO), and that the increase in the correlations over the past four decades, as reported in M18, is likely the result of internal variability alone, not caused by historical forcings. Gibson et al. also argue that warm NZI is not associated with decreased convective activity and cloud cover over the east of the Philippines region, as suggested by M18. We appreciate the opportunity to debate these issues. In principle, we agree that a combination of more than one contributors can drive climate (and SST) variability in the northwestern Pacific (i.e. M18 did not argue that NZI is the only driver). However, we disagree with the general suggestion by Gibson et al. that the atmospheric bridge, as proposed in M18, is not supported by the data (observations and models). Here, we present evidence that indeed NZI carries non-redundant information that cannot be dismissed, it cannot be explained by internal variability alone, and we provide further analysis that supports the causal mechanism of the proposed atmospheric bridge. We also point out some intricate limitations in the analysis of Gibson et al., that might have affected their conclusions.

One of the arguments of Gibson et al. in challenging the NZI lagged association with northwestern Pacific SST is that the statistical correlations between these key areas decrease when accounting for (using partial correlation) local SST memory or ENSO (specifically, the Southern Oscillation Index - SOI). However, their analysis exhibits some limitations. Firstly, M18 did not argue that NZI is the only driver of SST variability in the northwestern Pacific. In fact, M18 already invoked the local SST memory in their proposed teleconnection mechanism (see step 2 in Figure 5 of M18). M18 simply argued for the emergence of a new western Pacific interhemispheric teleconnection, which in the ocean-atmosphere coupled system can affect, among other contributors, the north Pacific climate and ultimately the precipitation in the southwestern US (SWUS). Having clarified this, the meaningful question is not whether correlations of NZI and SST in the northwestern Pacific decrease when considering additional predictors/mechanisms (this is to be expected), but whether there are still patterns of statistically significant relations not explained by other predictors. As Gibson et al.'s own results suggest, a consistent pattern of statistically significant (local hypothesis testing at $a = 0.05$) correlations is still evident after accounting for both local SST memory and SOI (see their Figure 1e,f), which means that NZI is not a redundant predictor of the SST in the northwestern Pacific. Thus, we do not think the results of Gibson et al. challenge our general suggestion. Note that although in the results of Gibson et al. (their Figure 1f) there is an entire pattern of local statistically significant correlations, the authors seem to assess correlation significance solely by using the results from the false discovery rate (FDR) method. This can be misleading, because FDR only controls the likelihood of the type I error (rejecting a true null hypothesis), yet without controlling the likelihood of the type II error (not rejecting a false null hypothesis), which is known to increase as the number of multiple hypotheses increases (known as cost of multiplicity control; Benjamini and Hochberg, 1995).

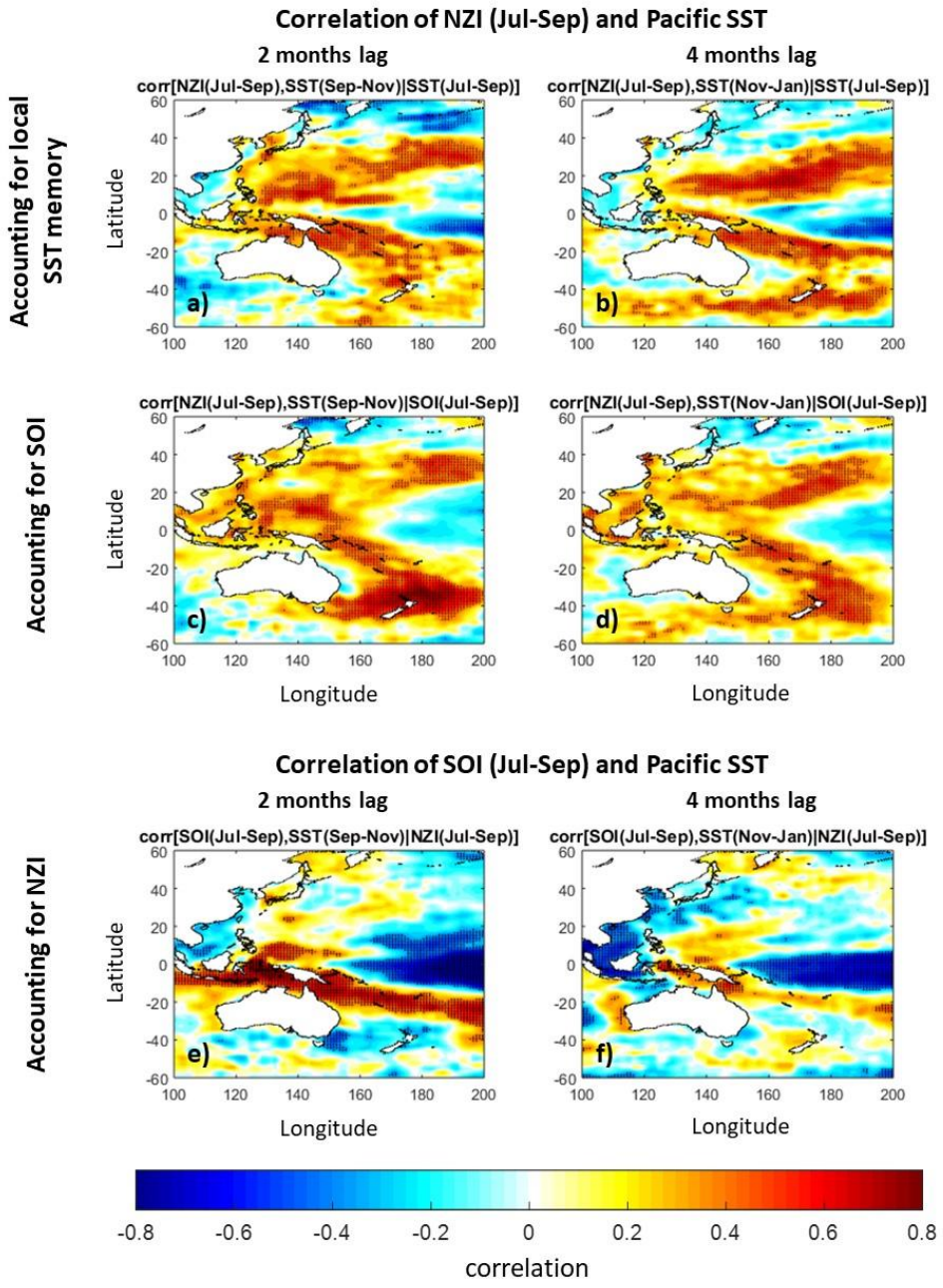

Figure 1.18: NZI interhemispheric connection when accounting for local SST memory and ENSO. a) Correlation map of NZI during Jul-Sep and Pacific SST during Sep-Nov, after accounting for the SST memory in each grid point. Before calculating correlations all series were detrended. Black dots indicate statistical significance at a = 0.05. b) Same as in (a), but using SST during Nov-Jan. c)-d) Same as in (a)-(b), but after accounting for the Southern Oscillation Index (SOI). e)-f) Same as in (c)-(d), but SOI is correlated with Pacific SST, after accounting for the NZI. It is evident that NZI correlations with SST in the northwestern Pacific remain high and statistically significant even after accounting for local SST memory and/or SOI. In contrast, when accounting for NZI, correlations of SOI with SST in the northwestern Pacific are not statistically significant.

Moreover, assessing the solidity of the atmospheric bridge mechanism by using only a small box (20° × 10°) to capture the SST variability in the northwestern Pacific can be misleading, especially when there is no investigation of how sensitive the general conclusions are to the choice of that box. The specific box east of the Philippines was tentatively used in our original study to summarize and compare the western Pacific dynamics before and after the 1980s (Figure 7 in M18); a very different context than the present investigation of causality and mechanism assessment. Thus, in order to rigorously assess the arguments of Gibson et al., we investigate herein the effect of local SST memory and SOI on the correlation between the late summer NZI and lagged SSTs over the entire western Pacific (not only over a specified box). We find that statistically significant correlation patterns are evident in the northwestern Pacific (with correlations reaching 0.7 in specific areas, see Figure 1.18), even after accounting for local SST memory (Figure 1.18a-b) or SOI (Figure 1.18c-d). When reproducing Figure 1 of Gibson et al. by considering a larger region in the northwestern Pacific (of comparable size to the NZI region and defined as the 30° × 15° box of 130°E-160°E and 5°N-20°N – we call the average SST in that box as the East of the Philippines Index, EPI), we find that NZI-EPI correlations remain high and statistically significant at a = 0.05, after accounting for the EPI memory (see Figure 1.19). Particularly in the summer period, correlations on the order of 0.6 are still evident, which means that NZI leads EPI SST in the following winter. Accordingly, our results show that when accounting for SOI, strong NZI-EPI correlation patterns are still evident (see Figure 1.19). All above results support that the lagged association between late summer-early fall NZI and northwestern Pacific SST is robust, and is not undermined by SOI or local SST persistence. Lastly, we note that if there was no direct causal relationship between NZI and EPI, and SOI was the driver of this interhemispheric connection (as implied by Gibson et al.), then following the reasoning by Gibson et al., one would expect that the correlation of SOI with the northwestern Pacific SSTs would be significant even after accounting for the NZI variability. However, our results indicate that this is not the case (not shown in Gibson et al.). Particularly, when accounting for the NZI variability, significant correlations of SOI and Pacific SST appear only in the tropics and do not extend to the northern Pacific (Figure 1.18e-f). Moreover, statistically significant SOI-EPI correlations are only found after November (see Figure 1.19f), which suggests that in late summer, NZI carries non-redundant information

for the fall-winter SST over the northwestern Pacific. In summary, although SOI and local SST memory are known to account for a fraction of SST variability in the northwestern Pacific, our results show that they do not undermine the robustness of the NZI-EPI statistical relationship.

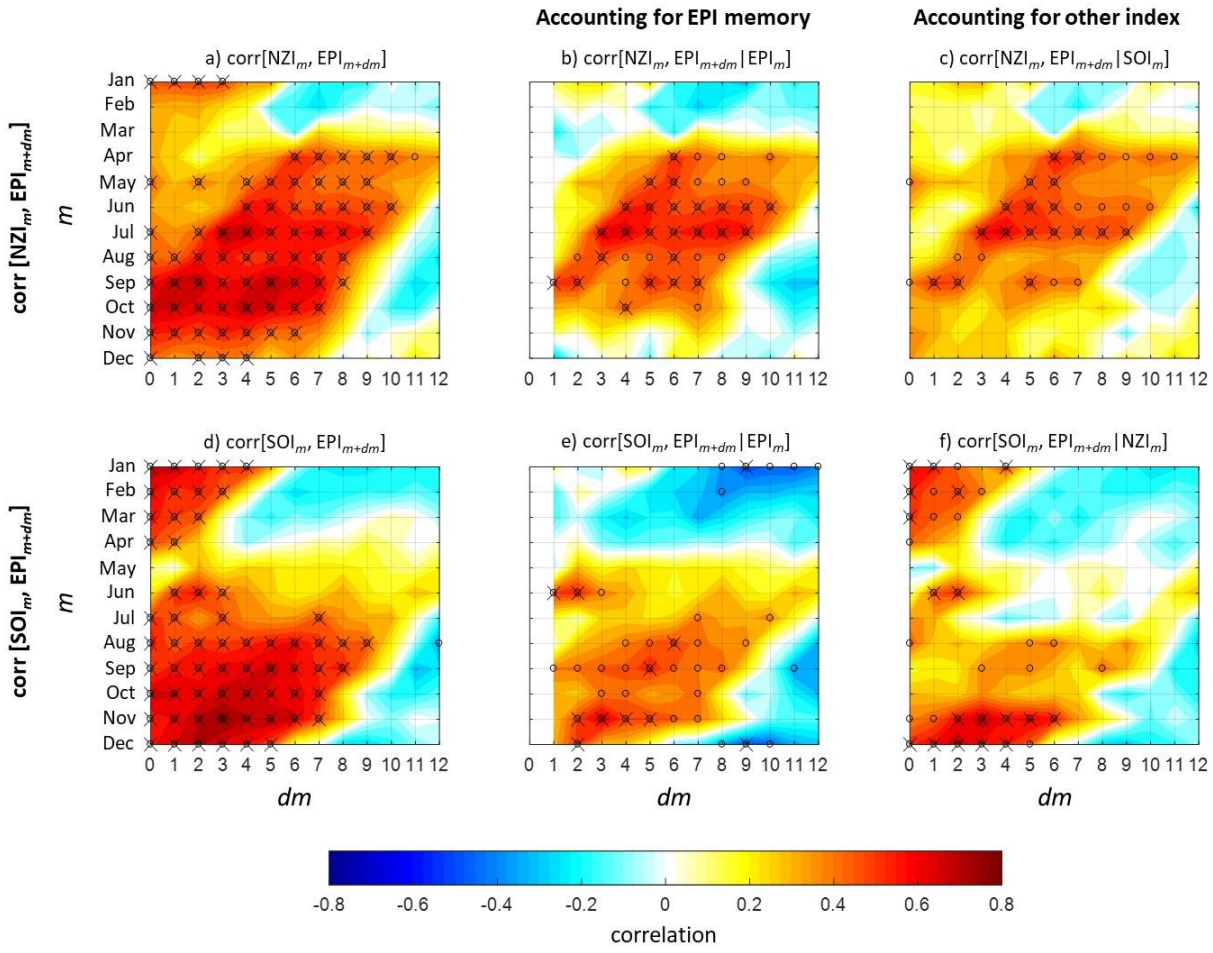

Figure 1.19: *Upper Panels:* a) Time-lagged correlations between NZI (averaged over the month indicated in the vertical axis) and SST in the region east of the Philippines (EPI) (box in 5–20°N and 130–160°E; lagged forward in time as indicated in the horizontal axis) in 1982–2015. Before calculating correlations all series were detrended. b) Same as in (a), but when the memory (monthly persistence) of EPI is taken into account. c) Same as in (a), but when the effect of SOI is taken into account. Black circles indicate statistical significance at a = 0.05, while black crosses indicate global significance at a_{global} = 0.05. For the latter, we have used the false discovery rate as in Gibson et al., with $a_{\text{FDR}} = 2a_{\text{global}}$ = 0.1, to account for dependence of the local tests, as suggested by Wilks (2016). *Bottom Panels:* Same as in upper panels, but using (d) SOI as predictor instead of NZI, and accounting for (e) EPI memory and (f) NZI variability. The coherent patterns of statistically significant NZI-EPI correlations when accounting for EPI memory and SOI establish the interhemispheric connection on its own right and not slaved to local SST memory or ENSO.

The second point raised by Gibson et al. concerns the decadal changes in the NZI-EPI relationship. Gibson et al. use SST data from the Community Earth System Model-Large ENSemble project (CESM-LENS, see Kay et al., 2015) and show that there are some ensemble members (realizations) where NZI-EPI are highly coupled and some where they are not statistically related. Based on this result, they cast doubt on the statement by M18 that the recent strengthening in the NZI-EPI relationship may be attributed, among others, to climate change. Specifically, Gibson et al. conclude that "*any apparent lagged correlations found between these regions are not likely a consistent or emerging feature of the climate system under historical forgings, but instead occasionally arise due to stochastic internal climate variability*".

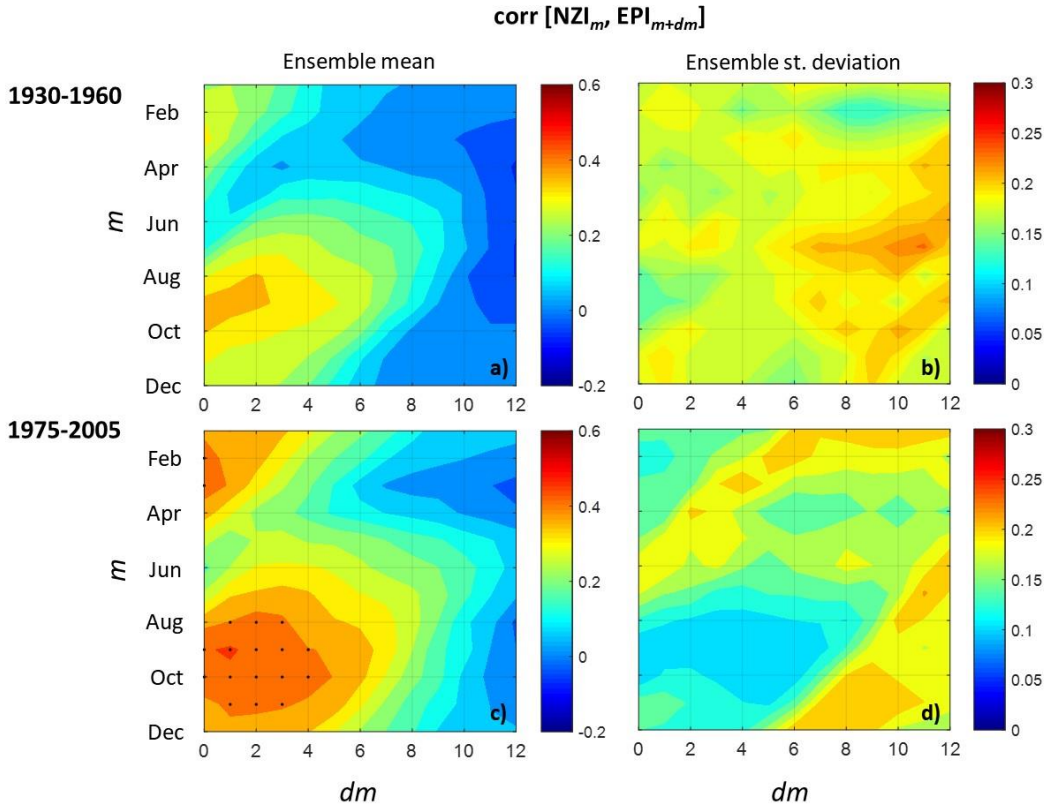

Figure 1.20: Changes in the strength of correlation between the NZI and EPI regions derived from the CESM-LENS project. Ensemble mean (a,c) and ensemble standard deviation (b,d) of time-lagged correlations between NZI (averaged over the month indicated in the vertical axis) and EPI (lagged forward in time as indicated in the horizontal axis) in 1930–1960 (a,b) and in 1975-2005 (c,d). Before calculating correlations all series were detrended. Black dots indicate statistical significance at $a = 0.05$. A higher level of agreement among ensembles and a clear increase in the NZI-EPI correlations is observed after 1975.

We respectfully disagree with this statement, since their results suggest that internal variability can indeed contribute in shaping the NZI-EPI relation (something that M18 did not argue against) but they cannot exclude historical forcings from being a contributor as well. To more extensively explore this, here we use the same set of LENS simulations that Gibson et al. use and compare the simulated NZI-EPI correlations before and after 1970s. Our results show that indeed there is a strengthening in the NZI-EPI relationship after the 1970s (see Figure 1.20), which is in accordance with the findings by M18. The latter is indicated not only by the increase of the ensemble mean correlations between NZI and EPI (especially in the late-summer season) but also by the decrease of the inter-ensemble variability in the recent decades, which indicates convergence of the ensembles. Thus, in accordance with M18, the LENS simulations suggest that the increased NZI-EPI correlations can be an emerging feature of the climate system under historical forcings, and cannot be solely explained by internal variability. Note that if stochastic internal variability was the only driver of the changes in the observed NZI-EPI correlations, then no changes should be apparent in the LENS ensemble mean correlations between the two periods, since changes in individual realizations would not be synchronized, and would cancel each other out.

The last claim by Gibson et al. is that warm NZI is not associated with decreased convective activity and cloud cover over the east of the Philippines region, as suggested by M18. Here, we show that this is not the case by performing composite and correlation analyses with multiple reanalysis and satellite datasets. When we consider the composite differences in the Jul-Nov SST, omega velocity, total cloud cover (TCC), and incoming solar radiation (ISR), between the five warmest and coldest NZI years, the mechanism suggested by M18 is supported (Figure 1.21). In late boreal summer, the intertropical convergence zone migrates close to the Philippines (see Mamalakis and Foufoula-Georgiou, 2018) and the southern Hadley cell expands the most (Lindzen and Hou 1988), dominating the atmospheric meridional circulation over the western tropical Pacific (see e.g. Trenberth et al., 2000 and supplementary Figure 7 in M18) and connecting the areas of NZI and EPI. In warm NZI years, both the descending motions over the southwestern Pacific (close to New Zealand) and ascending motions over the northwestern Pacific (close to the Philippines) weaken in all pressure levels, which translates to a weakened Hadley circulation (not reversed as Gibson

et al. imply) relatively to the cool NZI years (see the north-south dipole in Figure 1.21b). Accordingly, the suppressed cloud formation over EPI results in increased solar radiation reaching the surface (see Figure 1.21c-d), which can induce positive SST anomalies in this region (process 1 in Figure 5 of M18). In the Nov-Mar period, the cyclonic activity southwestward of the Philippines helps maintain the SST anomalies in the northwestern and central Pacific (process 2 in Figure 5 of M18), while a persistent high pressure ridge is evident off the coast of California, deflecting the jet stream to the north (process 3 in Figure 5 of M18) and introducing positive precipitation anomalies over the northwestern US and negative precipitation anomalies (drought) over the SWUS. Similar conclusions are obtained using correlation analysis and multiple other atmospheric variables (see Figures 1.22 and 1.23 of the present study). Particularly, a clear north-south dipole pattern is obtained over the western Pacific, which reveals the modulation effect of the NZI on the regional Hadley circulation. Finally, we note that the different findings of Gibson et al. regarding the effect of NZI on the convective activity over the northwestern Pacific might be attributed to the following reasons. First, Gibson et al. base their conclusions on the ERA-Interim dataset which, as shown in Figure 1.23 of the present study, exhibits the lowest level of agreement with other reanalysis and satellite datasets in reproducing the relationship of NZI and the convective activity over EPI. Second, their results presented in their Figure 2c,f,i are based on only 17 years of climatology (compared to our analysis based on 34 years, 1982-2015), which is not a sufficient size for statistical (correlation or composite) analysis.

In conclusion, we thank Gibson et al. for their careful analysis and exploration of the proposed physical mechanism of the NZI teleconnection, and for providing us with the opportunity to further examine and strengthen our original arguments. We believe their letter and our response advance the important topic of understanding sources of predictability of regional precipitation and their physical underpinnings in the western Pacific. As noted already by M18, given the short observational record that is available, whether NZI SST anomalies alone are sufficient to modulate the meridional circulation over the western Pacific demands extensive further testing, which will require the performance and analysis of a hierarchy of well-designed and targeted numerical simulations. We hope

that this undertaking will be the scope of future work in our group and others in the community.

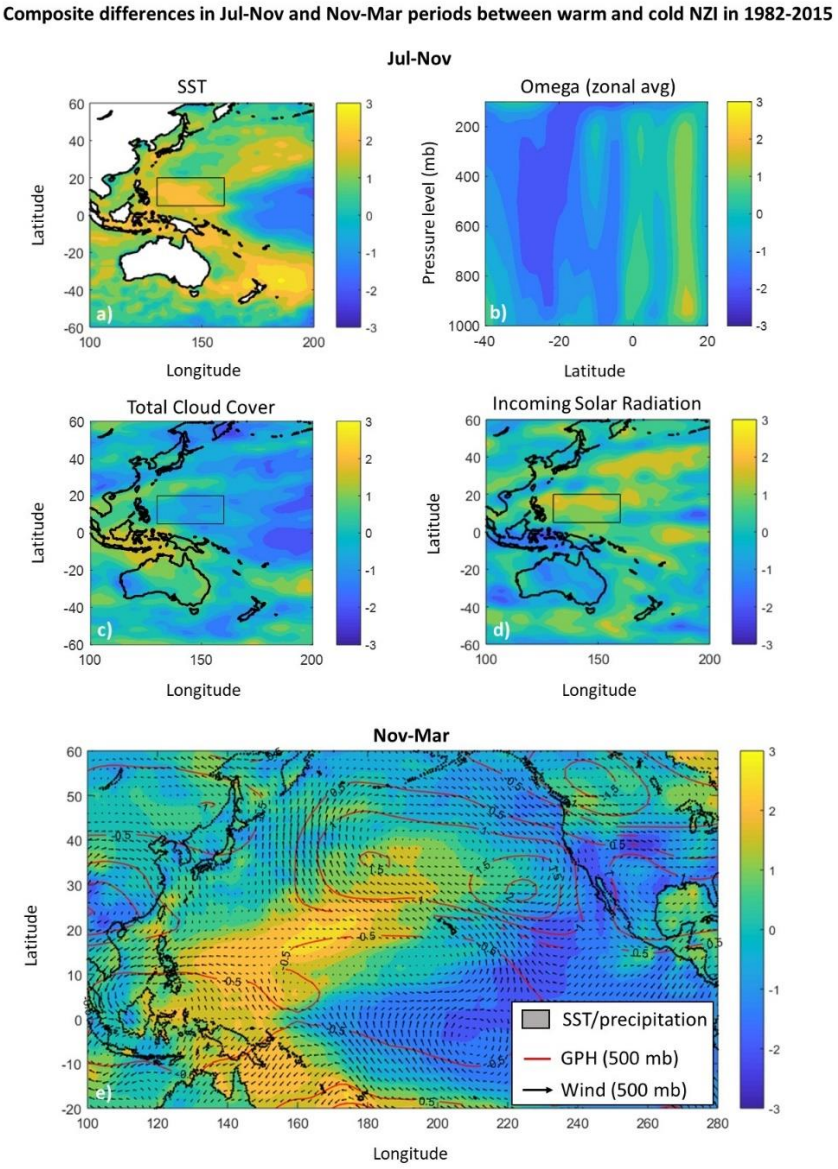

Figure 1.21: Composite differences between 5 warmest and 5 coldest NZI years during 1982-2015. a) Jul-Nov SST, b) Jul-Nov zonal average omega velocity over 100°E-200°E (positive sign corresponds to decreased ascending motion), c) Jul-Nov total cloud cover (TCC), d) Jul-Nov incoming solar radiation (ISR) at the surface, and e) Nov-Mar SST (shading over ocean), land precipitation (shading over land), geopotential height (GPH; contours) and horizontal wind (vectors) at 500 mb pressure level. All values have been standardized by dividing with the standard deviation of the respective series in 1982-2015. In (a),(c),(d), the EPI box is also shown. As suggested in M18, results support that warm NZI is associated with decreased convective activity and cloud cover, and increased incoming solar radiation over the east of the Philippines.

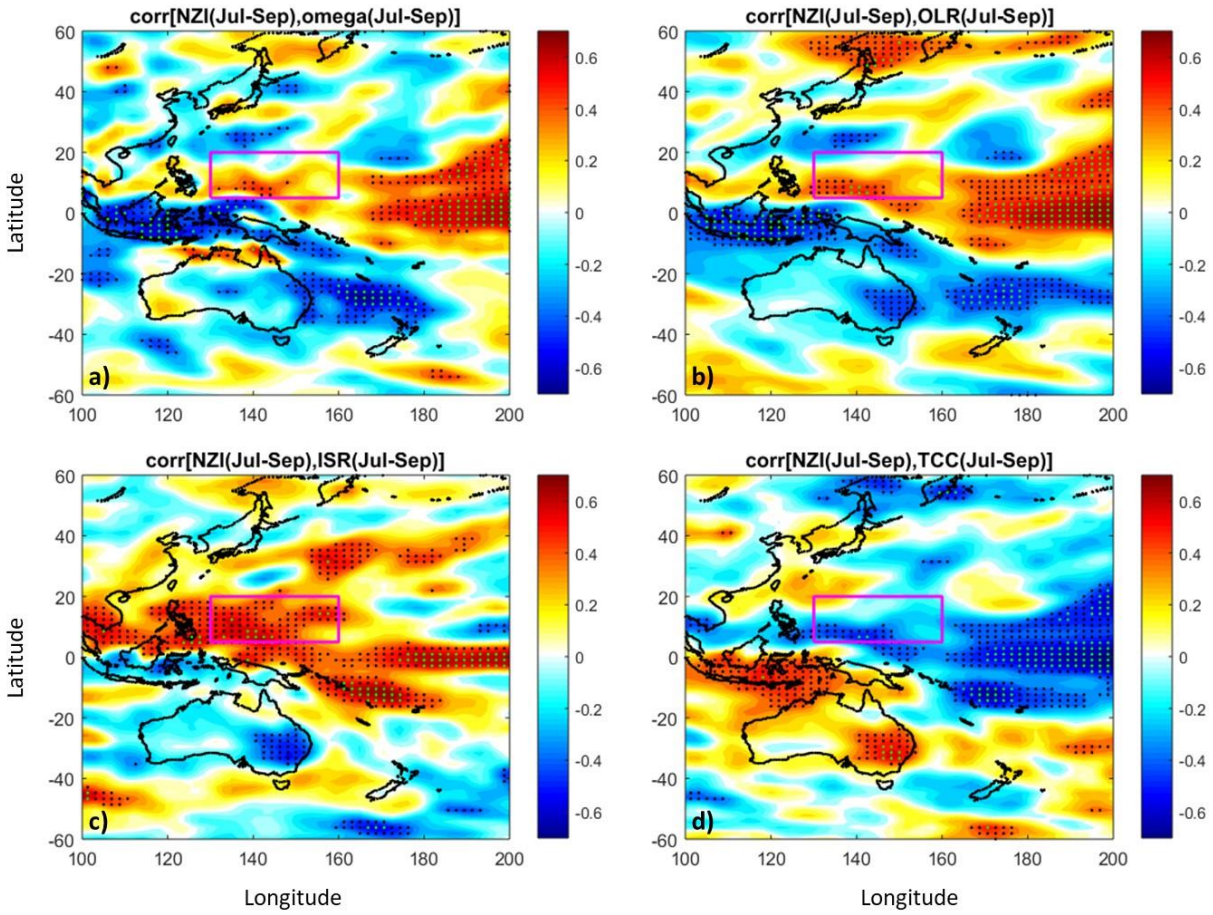

Figure 1.22: Jul-Sep correlation maps (1982-2014) between NZI and a) omega velocity at 500mb (positive sign corresponds to descending or decreased ascending motion), b) outgoing longwave radiation (OLR) at the top of the atmosphere, c) incoming solar radiation (ISR) at the surface, and d) total cloud cover (TCC). Before calculating correlations all series were detrended. Black dots indicate statistical significance at $a = 0.05$, while green dots indicate global significance at $a_{global} = 0.05$. For the latter, we have used the false discovery rate as in Gibson et al., with $a_{FDR} = 2a_{global} = 0.1$, to account for dependence of the local tests, as suggested by Wilks (2016). EPI region is indicated with a magenta box. NZI is calculated using the Optimum Interpolation SST, while other series are obtained from the 20th Century Reanalysis project. All results show that positive NZI is associated with decreased convective activity and increased ISR over the northwestern Pacific. Note also that a clear north-south dipole pattern is obtained over the western Pacific, which reveals the modulation effect of the NZI on the regional Hadley circulation.

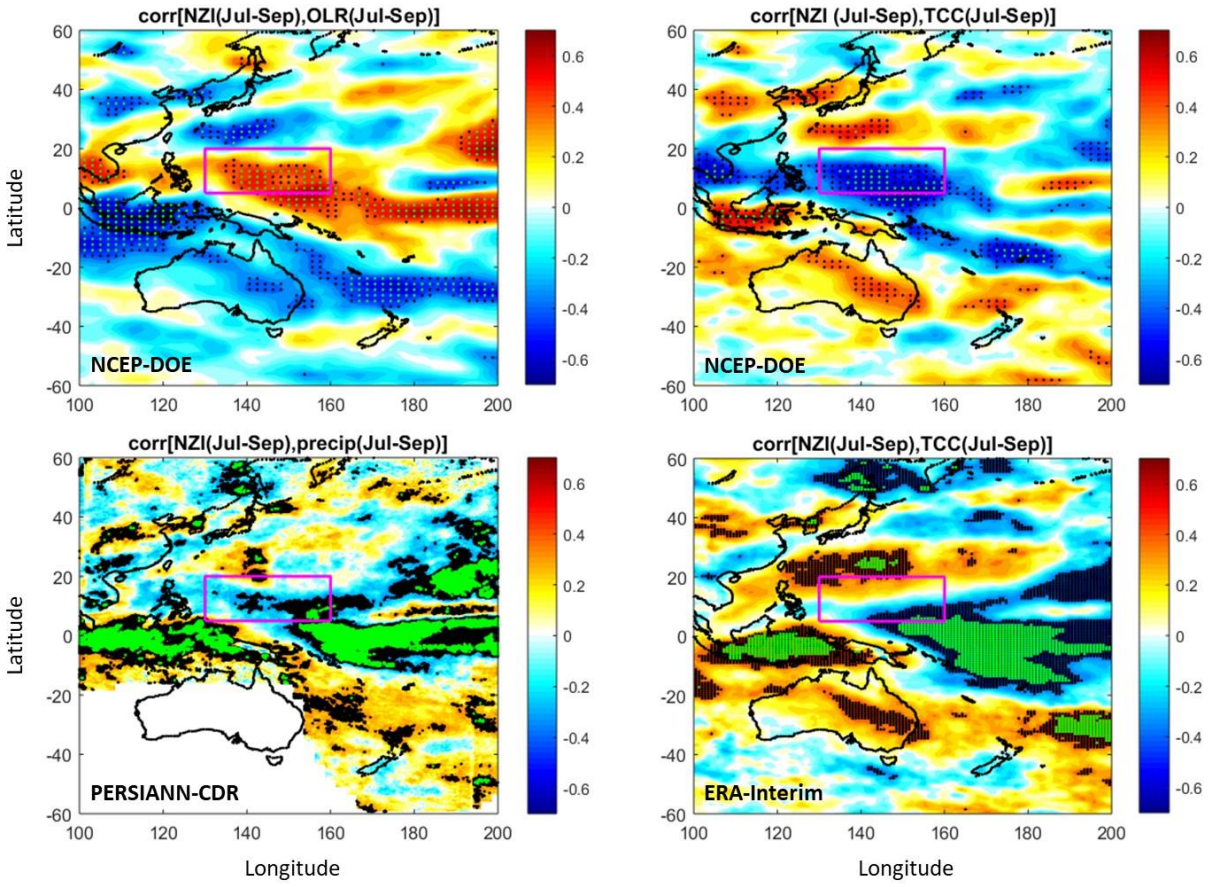

Figure 1.23: Same as in Figure 1.22, but TCC and OLR are obtained from the NCEP-DOE dataset in the top plots, while satellite precipitation is obtained from PERSIANN-CDR, and TCC is from the ERA-Interim project in the bottom plots. Relatively to results presented in other subplots and in Figure 1.22, results from the ERA-Interim project (used in Gibson et al.) are unclear as to the relationship between NZI and the convective activity over the EPI.

REFERENCES

Benjamini, Y. & Y. Hochberg (1995) Controlling the False Discovery Rate: a Practical and Powerful Approach to Multiple Testing, *J. R. Statist. Soc. B*, **57**(1), 289-300

Kay, JE, et al. (2015) The Community Earth System Model (CESM) large ensemble project: A community resource for studying climate change in the presence of internal climate variability. *Bulletin of the American Meteorological Society, 96*(8), 1333-1349.

Lindzen, R. S., and A. Y. Hou (1988) Hadley circulation for zonally averaged heating centered off the equator, *J. Atmos. Sci.*, **45**, 2416-2427.

Mamalakis, A., J.-Y. Yu, J. T. Randerson, A. AghaKouchak, & E. Foufoula-Georgiou, (2018) A new interhemispheric teleconnection increases predictability of winter precipitation in southwestern US. *Nature communications,* **9**(1), 2332.

Mamalakis, A., & Foufoula-Georgiou, E. (2018) A multivariate probabilistic framework for tracking the intertropical convergence zone: Analysis of recent climatology and past trends. *Geophysical Research Letters*, **45**. https://doi.org/10.1029/2018GL079865

Trenberth, K. E., Stepaniak, D. P., & Caron, J. M. (2000) The global monsoon as seen through the divergent atmospheric circulation, *Journal of Climate*, **13**, 3969–3993.

Wilks, D. S. (2016) "The stippling shows statistically significant grid points": How research results are routinely overstated and overinterpreted, and what to do about it. *Bulletin of the American Meteorological Society, 97*(12), 2263-2273.

1.3. Probabilistic assessment of predictive skill of extreme wet and dry years in southwestern US in observed and CMIP6 simulated climates

This chapter is currently in preparation for submission

Citation: Mamalakis, A., E. Foufoula-Georgiou, A. AghaKouchak and J.T. Randerson (2021) Probabilistic assessment of predictive skill of extreme wet and dry years in southwestern US in observed and CMIP6 simulated climates

Early and accurate seasonal prediction of winter precipitation totals in southwestern US (SWUS) is an exigent task of high practical and scientific interest, and has received great attention over the past three decades (Schonher and Nicholson, 1989; McCabe and Dettinger, 1999; Gershunov and Cayan 2003; Schubert et al., 2016; Madadgar et al., 2016; Liu et al., 2018; Hao et al., 2018; Zhang et al., 2018; Mamalakis et al., 2018; Pan et al., 2019; Stevens et al., 2020). From a practical and engineering point of view, failing to accurately predict winter precipitation totals limits the ability of practitioners to plan for sustainable water resources management and has caused considerable economic damage in the past, with the recent multi-year SWUS drought in 2012-2016 serving as a prominent example (Howitt et al., 2014; 2015; AghaKouchak et al., 2015; Medellín-Azuara et al., 2016).

From a science perspective, SWUS exhibits a highly variable hydroclimate on inter-annual scales (Dettinger et al., 2011), which makes precipitation prediction quite challenging. Specifically, the majority of the region's annual precipitation occurs during November to March, with most of the SWUS considered a dry region. This partially stems from the fact that SWUS lies within a transition zone, between the northern subtropics and mid-latitudes (i.e. 30°- 40°N) and is collocated with the descending branch of the Hadley circulation, where cool and dry air masses descend, reducing in relative humidity. However, SWUS is occasionally the area of landfall of powerful winter storms which carry their moisture from the Pacific basin. Some of them resemble long, narrow corridors of concentrated moisture in the atmosphere, known as atmospheric rivers (Ralph et al., 2006; Ralph et al., 2019; Gershunov et al., 2019; Huang et al., 2020). Just a small number of such winter storms is sufficient to bring more than twice the long-term average precipitation to

the SWUS, elevating the risk of flash flooding (Dettinger et al., 2011; Dettinger and Cayan, 2014; Corringham et al., 2019).

Despite the high variability and complexity of the precipitation-producing mechanisms in the SWUS, research has shown that precipitation in the region is associated with the presence of persistent anomalous patterns of atmospheric pressure over the Gulf of Alaska (Wang et al., 2014; Swain et al., 2014; Seager et al., 2015; Swain et al., 2016; 2017; Teng and Branstator, 2017; Gibson et al., 2019). Physically, these high-pressure or low-pressure patterns can weaken or strengthen the winter-time jet stream and storm tracks, causing dry or wet conditions, respectively. As a consequence of the relatively short-term memory of the atmosphere, however, early seasonal prediction of precipitation totals typically rely on sea surface temperatures (SSTs), either through deterministic models (i.e. SST-forced climate model simulations) or statistical models which aim to exploit physically- and historically- established teleconnections of precipitation with large-scale modes of climate variability. The latter typically include the El Niño-Southern Oscillation (ENSO), and modes of decadal or multi-decadal variability such as the Pacific Decadal Oscillation (PDO) and the Atlantic Multi-decadal Oscillation (AMO); see e.g., Schonher and Nicholson (1989), Redmond and Koch (1991), McCabe and Dettinger (1999), Enfield et al. (2001), McCabe et al. (2004), Dai (2013), Newman et al. (2016) and Lindsey (2016).

Although considerable progress has been made in the field of climate modelling, early and accurate seasonal precipitation prediction remains an important challenge (Wang et al., 2009; NASEM, 2016). Limits to predictive skill of dynamical models arise from incomplete knowledge of initial conditions, uncertainties in model physics, and limits on computational resources that place constraints on the grid resolution used in operational systems (Chang et al., 2000; Becker et al., 2014). Similarly, empirical statistical techniques exhibit limited predictive skill, arising primarily from the complex and changing nature of the relationship between large scale modes and regional hydroclimate. Notably, the relationship between ENSO and US climate variability has been shown to undergo multidecadal fluctuations (McCabe and Dettinger, 1999; Yu et al., 2012), with many recent studies pointing out that it has been losing strength in the recent decades, while the western Pacific climate variability (e.g. SST, sea level pressure, convection activity, etc.) appears to be gaining importance in driving SWUS precipitation and the atmospheric circulation over the Pacific (Wang et al.,

2014; Baxter and Nigam, 2015; Teng and Branstator, 2017; Seager et al., 2017; Swain et al., 2017; Myoung et al., 2018; Mamalakis et al., 2018; Johnson et al., 2019; Zhou et al., 2020). The relative contribution of anthropogenic forcing and natural variability to these multi-decadal changes is still not clear. For example, regarding the drivers of the recent multi-year (2012-2016) drought in California (Seager et al., 2017), some studies suggest that it had an anthropogenic component (Wang et al., 2014; Swain et al., 2014, Diffenbaugh et al., 2015), while other studies highlight the importance of natural variability and SST forcing (e.g. Seager et al., 2015; Seager and Henderson, 2016; Teng and Branstator, 2017).

Here, we revisit the problem of early seasonal precipitation prediction in the SWUS from a policy and decision making perspective, and we aim to explore the practical predictability of different classes of precipitation totals (i.e. dry, normal or wet), which are defined based on a range of probability levels. Specifically, we use copula modelling and a five-fold cross validation approach to avoid model overfitting and ensure robustness of the results, and we resolve the entire predictive distribution of precipitation for each year in the last five decades, conditioning on SST information. This allows us to assess each model's predictive performance in capturing different aspects of the historical probability distribution (e.g., mean, median, and high and low extremes), while also accounting for the prediction's uncertainty (i.e. going beyond point estimates), informative for planning and risk assessment. As predictors, we consider different combinations of widely used SST indices from all major ocean basins of the world (see Figure 1.24), principal components of SSTs, and we also perform a global-pattern significance analysis (e.g. Wilks, 2016) to assess predictability when thousands of null hypotheses (each per every grid point) are assessed simultaneously. Moreover, we design suitable metrics to statistically assess the null hypothesis of no predictive skill. The asymptotic, theoretical values of these statistics under the null hypothesis are presented and their finite-sample distributions are obtained using Monte Carlo simulations. Lastly, we repeat the analysis using outputs from state-of-the-art climate model simulations, in order to gain insight into how climate models simulate historical teleconnections between large scale SST modes and regional hydroclimate. We find that for normal precipitation totals, there is virtually no SST sources of predictability so that one can beat the climatology-based predictions. For extreme dry/wet precipitation totals, prediction skill is significant, with wet years being more predictable than dry years.

Such an asymmetry is known to exist in the ENSO climate teleconnections (Zhang et al., 2014), yet, here we show that wet conditions in SWUS are inherently more predictable even when using non-ENSO SST information. Regarding the latter, we find that state-of-the-art climate models might on average undermine the importance of non-ENSO SST variability in predicting extreme precipitation totals over SWUS.

The structure of the paper is the following. First, we describe the datasets used in this study, we outline the copula-based predictive model, and we propose some statistical metrics to assess the skill in predicting seasonal precipitation totals. Then, we apply the introduced probabilistic framework to retrospectively assess the practical predictability of winter (specifically Nov-Mar) precipitation totals over the SWUS, using observations and climate simulation outputs. Last, we state our conclusions and future research directions.

Data and Methods

Data Sets. For our analysis, we used observations of Nov-Mar precipitation amount in SWUS (see Figure 1.24), which are freely available at https://www.ncdc.noaa.gov/cag/time-series/us (Vose et al., 2014). Monthly SST on a 1º×1º grid were obtained from https://www.esrl.noaa.gov/psd/data/gridded/data.cobe2.html (Hirahara et al., 2014). Monthly time series of PDO was obtained from the NOAA website https://www.esrl.noaa.gov/psd/data/climateindices/list.

We used the 50-yr period from 1969-70 to 2018-19 to build and test our statistical models. We avoided considering earlier years in the record because the 1970s is roughly the time that many studies have pinpointed as the start of major changes in the atmospheric teleconnections (Wang et al., 2014; Swain et al., 2016; Mamalakis et al., 2018; Johnson et al., 2019). Both the precipitation and SST time series were linearly detrended before they were used in the analysis, so that long term trends do not impact our assessment.

Apart from observations, we repeated the analysis using monthly precipitation and SST outputs from each model in the sixth phase of the Coupled Model Intercomparison Project (CMIP6; see Eyring et al., 2016), focusing on the 50-yr historical period from 1965-66 to 2014-15 (note that for year 2015 and on, CMIP6 models are forced with climate change scenarios, and so, their outputs do not correspond to historical forcings).

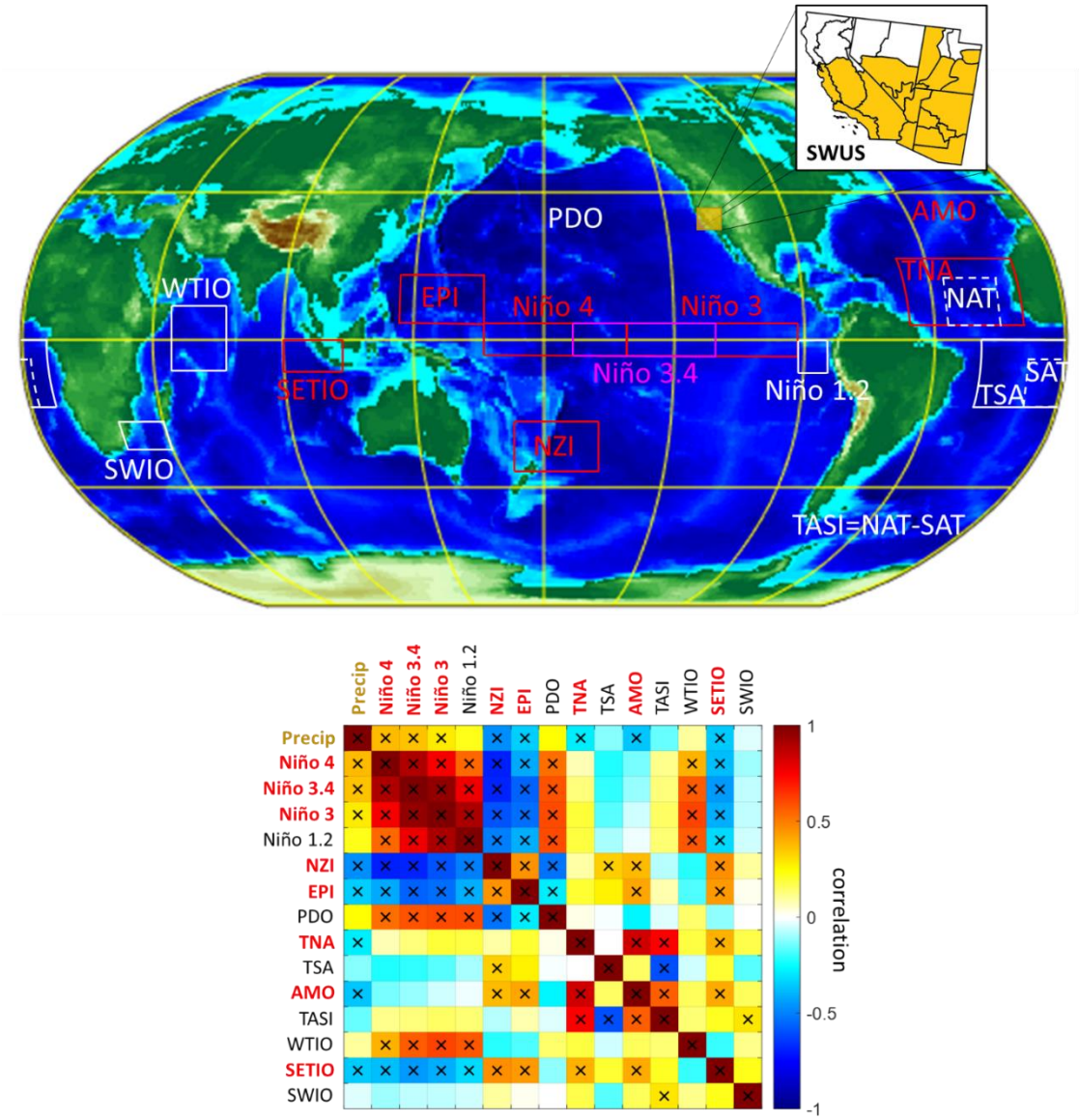

Figure 1.24. Correlation matrix for the 14 SST indices that were examined in this study (over the years from 1969-70 to 2018-2019). After considering their statistical significance with SWUS precipitation (highlighted with '**×**'), only eight of them were retained for prediction (see indices marked with red color). Here, winter precipitation over the SUWS corresponds to the Nov-Mar season and indices are averaged during the preceding Aug-Oct. All series are first linearly detrended.

a) Predictive distribution of SWUS total precipitation in Nov 1995 – Mar 1996

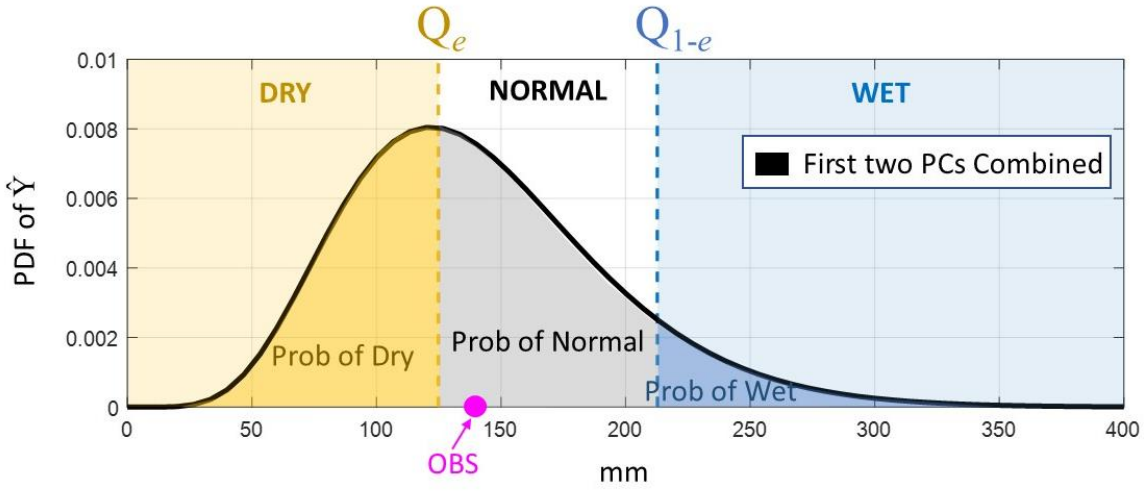

b) The Contingency Table

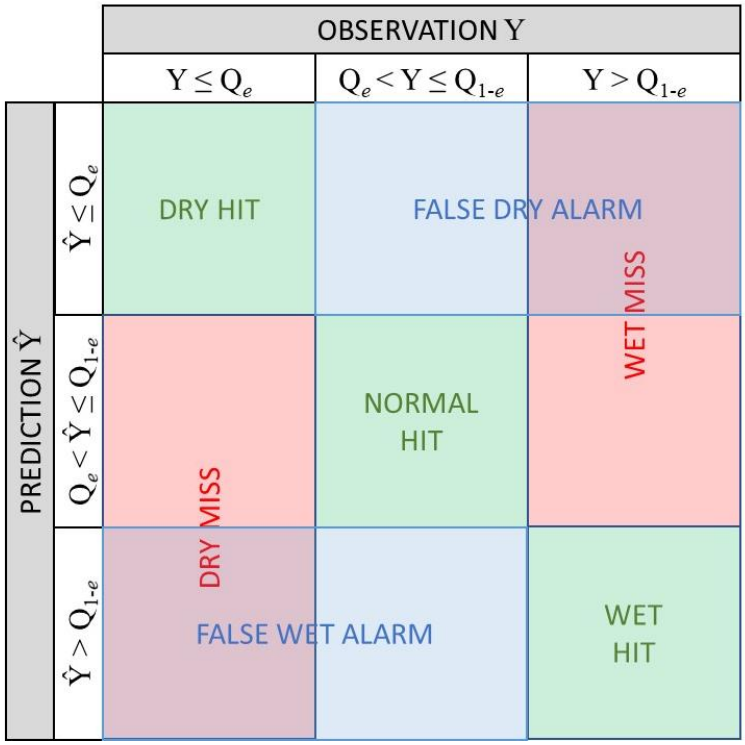

Figure 1.25. a) The predictive Probability Density Function (PDF) of SWUS precipitation for the year 1995-1996. The prediction is made using Equation 2, and conditioning on the first two principal components of the considered SST indices; see also lower panel of Figure 1.27. b) Summary of all possible outcomes when predicting precipitation. Q_e denotes the *e*-th quantile of the historical precipitation PDF.

Predictive Model. For each year $t = 1969-70, 1970-71, \ldots, 2018-19$, we used SST predictors averaged in Aug-Oct to estimate the predictive Probability Density Function (PDF) of SWUS precipitation in the following Nov-Mar season; see example in Figure 1.25a, for $t = 1995-96$. Specifically, if $f^t_{Y|\mathbf{X}}$ is the conditional predictive PDF of the random variable Y (in our case SWUS total precipitation in Nov-Mar season) in year t, given the random vector $\mathbf{X}$ (M predictors), then:

$$f^t_{Y|\mathbf{X}}(y) = \frac{f_{Y,\mathbf{X}}(y,\mathbf{x}^t)}{f_{\mathbf{X}}(\mathbf{x}^t)} \qquad (1)$$

where $f_{Y,\mathbf{X}}$ is the joint PDF of Y and $\mathbf{X}$, and $f_{\mathbf{X}}$ is the joint PDF of $\mathbf{X}$. Since the marginal PDFs of the predictor and the predictand variables are in principle different (e.g., SST vs. precipitation), simple theoretical multivariate distributions (like the multivariate Normal or Gamma distributions) cannot be used to model the joint distributions of Y and $\mathbf{X}$. To address this issue and to keep our approach simple, we used copula functions to represent the above joint distributions (see also Madadgar and Moradkhani, 2013; Madadgar et al., 2016). Equation (1) becomes (Nelsen, 1999):

$$f^t_{Y|\mathbf{X}}(y) = \frac{c_{Y,\mathbf{X}}(v,\mathbf{u}^t)}{c_{\mathbf{X}}(\mathbf{u}^t)}\, f_Y(y) \qquad (2)$$

where f_Y is the marginal PDF of Y, $c_{Y,\mathbf{X}}$ and $c_{\mathbf{X}}$ are the PDFs of the copulas, $v = \Pr[Y \le y]$ is the marginal cumulative distribution function (CDF) of Y evaluated at y, and $\mathbf{u}^t = [u^t_1, u^t_2, \ldots u^t_i, \ldots, u^t_M]^{\mathrm{T}}$, where $u^t_i = \Pr[X_i \le x^t_i]$ is the marginal CDF of the i^{th} predictor X_i evaluated at its value x^t_i. As previously described, to train this model we first linearly detrended all series and then fit parametric distributions to the historical precipitation totals and the predictor series, to model the marginal distributions. The fitted distributions were Gamma and Gaussian, respectively, both statistically significant at α = 0.05, based on the Kolmogorov-Smirnov test. To model the joint distributions, we chose to use Gaussian copulas in equation 2, because the Gaussian copula is radially symmetric (i.e. assigning the same probability to both the right and the left tail, Nelsen, 1999; this way our predictions were not systematically tilted towards either of the extremes), and it is among the simplest model to preserve high dimensional dependencies (Joe, 1997). Besides, as we have tested, our results were not sensitive to any of the above distributional choices.

As predictor variables, we examined various SST indices in the three oceans: Pacific, Atlantic and Indian Ocean (see Figure 1.24). Specifically, we examined the Pacific indices (Niño 4, Niño 3.4, Niño 3, Niño 1.2, PDO), the Atlantic indices (TNA, TSA, AMO, TASI) and the Indian Ocean indices (WTIO, SETIO, SWIO). More information about these indices is provided at NOAA's State of the Ocean website (http://stateoftheocean.osmc.noaa.gov/) and in Chen et al. (2016). We also considered two newly introduced Pacific indices, i.e., the New Zealand Index (NZI; 40ºS-25ºS and 170ºE-200ºE) and the East of the Philippines Index (EPI; 5ºN-20ºN and 130ºE-160ºE), which have been recently shown to exhibit strong statistical relationship with SWUS precipitation (Mamalakis et al., 2018; 2019). For our analysis, we disregarded indices that did not exhibit a statistically significant correlation (α = 0.05) with SWUS precipitation in the 50-yr period (see Figure 1.24), since the present predictive formula captures only linear dependencies. This led us to use eight SST indices in total (see red boxes in Figure 1.24a), considering them both individually and combined, while we also built a predictive model using their first two principal components (PCs), since this allows us to retain most of the indices information (the first and second PCs capture 51.1% and 26.1% of the variance of the 8 indices, respectively, i.e. yielding to a total of more than 75%), without dramatically increasing the complexity of the predictive model, and thus, avoiding overfitting (i.e. when thinking in terms of a linear regression model, using the first two PCs of eight indices requires the estimation of only two weights, rather than eight).

To ensure that our assessment of the prediction skill is robust, we adopted a five-fold cross validation approach. Under this setting, the 50-y period was separated into five, non-overlapping and continuous 10-yr sets (i.e. the first set included the years $[1969-70, 1970-71, \dots, 1978-79]$, the second set included the years $[1979-80, 1980-81, \dots, 1988-89]$, etc.), and for each year t in every set, prediction was made by fitting the predictive model (i.e. fitting the marginal and copula distributions) to the remaining 40 years. Note that the latter is a much stricter approach relatively to the leave-one-out cross validation, which can lead to unrealistically high predictive performance (usually from overfitting), especially as the complexity of the model increases (DelSole and Banerjee; 2017).

2.1. Statistical Metrics of Prediction Skill

For a probability of non-exceedance e, we define historical "dry years" as the years when the precipitation total did not exceed the e-quantile Q_e of the historical probability distribution. Similarly, historical "wet years" correspond to years when the precipitation total was above the historical Q_{1-e}; note that different values of e can be used to assess the prediction skill for a range of extremes. Based on these definitions, we can form a table with all possible outcomes with regard to correctly or incorrectly predicting an actual dry, normal, or wet year (see schematic in Figure 1.25b). The latter is known as "the contingency table" (Wilks, 2006), and has been widely used in many hydrologic and weather forecasting applications, to assess the skill of correctly predicting/monitoring events in different spatiotemporal scales (Behrangi et al., 2011; Haile et al., 2012; Hao et al., 2013). The typical contingency table consists of four possible outcomes (hit, miss, false alarm, and correct rejection), which originate from predicting two possible states: the occurrence or lack of occurrence of an event. In our case, the states (classes) are three, i.e. dry, normal, or wet totals of seasonal precipitation. Many different metrics to assess predictive skill can be defined, even when considering only two classes (Wilks, 2006; AghaKouchak and Mehran, 2013), however, the probabilities of hit (known as probability of detection; POD) and of false alarm (known as the false alarm ratio; FAR) are mostly used in the literature (Anagnostou et al., 2010; Gourley et al., 2012; Hao et al., 2013). To assess the predictive skill, we herein use different values of e (i.e. 0.15, 0.25, 0.333), and for each case, we calculate the following statistical metrics in the period from 1969-70 to 2018-19.

i) **Dry success**: The probability of observing a dry year, while predicting dry

$$DS = \Pr\left[Y \le Q_e \mid \hat{Y} \le Q_e\right] = \frac{\Pr[\hat{Y} \le Q_e \mid Y \le Q_e]\ \Pr[Y \le Q_e]}{\Pr[\hat{Y} \le Q_e]}, \qquad (3)$$

where Y is the observed value, $\hat{Y}$ is the prediction, and the above equation is known as the Bayes' theorem. The term $\Pr\left[Y \le Q_e \mid \hat{Y} \le Q_e\right]$ on the left cannot be calculated, since no single prediction values of $\hat{Y}$ are available, but rather entire predictive distributions. Yet, the term $\Pr\left[\hat{Y} \le Q_e \mid Y \le Q_e\right]$, in the numerator on the right, corresponds to the probability of the considered model detecting an actual drought (dry hit; similar to the POD), and it can be

easily calculated as the integral $\int_0^{Q_e} f_{Y|\mathbf{X}}^{Dry}(y)dy$, where $f_{Y|\mathbf{X}}^{Dry}$ is the composite PDF of all predictive PDFs during the actual dry years within the period from 1969-70 to 2018-19. Moreover, the probability of false dry alarm (similar to the FAR) is essentially embedded in the term in the denominator $\Pr[\hat{Y} \leq Q_e]$, i.e. how often the considered model predicts dry conditions. For example, if we imagine a trivial model which always predicts dry conditions (for all t years), then it is obvious that this model would exhibit a perfect dry hit score (i.e. $\Pr[\hat{Y} \leq Q_e \mid Y \leq Q_e] = 100\%$), however, it would also generate high levels of false dry alarms. Thus, by accounting for the overall probability of the model to predict dry, in the denominator, the proposed statistic combines, in a sense, the dry hit and false dry alarm scores. Lastly, note that the term $\Pr[Y \leq Q_e]$ is by definition equal to e.

The above statistical metric can be generalized in the form $\Pr[Y \in A \mid \hat{Y} \in A]$ which represents the probability that the observation belongs to a set of outcomes A (or generally satisfies a condition C), given that the model predicts so. Thus, we similarly define:

ii) Wet success: The probability of observing a wet year, while predicting wet

$$WS = \Pr[Y > Q_{1-e} \mid \hat{Y} > Q_{1-e}] = \frac{\Pr[\hat{Y}>Q_{1-e} \mid Y>Q_{1-e}]\ \Pr[Y>Q_{1-e}]}{\Pr[\hat{Y}>Q_{1-e}]} \quad (4)$$

iii) Normal success: The probability of observing a normal year, while predicting normal

$$NS = \Pr[Q_e < Y \leq Q_{1-e} \mid Q_e < \hat{Y} \leq Q_{1-e}] = \frac{\Pr[Q_e<\hat{Y}\leq Q_{1-e} \mid Q_e<Y\leq Q_{1-e}]\ \Pr[Q_e<Y\leq Q_{1-e}]}{\Pr[Q_e<\hat{Y}\leq Q_{1-e}]} \quad (5)$$

iv) No drought success: The probability of not observing a dry year, while predicting no dry

$$NDS = \Pr[Y > Q_e \mid \hat{Y} > Q_e] = \frac{\Pr[\hat{Y}>Q_e \mid Y>Q_e]\ \Pr[Y>Q_e]}{\Pr[\hat{Y}>Q_e]}, \quad (6)$$

The latter statistic may be especially useful for decision makers. Lastly, we use a summarizing statistical metric which combines the skill with regard to all classes (dry, normal, wet):

v) The categorical log-likelihood of the data:

$$LogL = \frac{1}{N}\text{Log}\left[\prod_t \left(I_D^t \int_0^{Q_e} f_{Y|\mathbf{X}}^t(y)dy + I_N^t \int_{Q_e}^{Q_{1-e}} f_{Y|\mathbf{X}}^t(y)dy + I_W^t \int_{Q_{1-e}}^{+\infty} f_{Y|\mathbf{X}}^t(y)dy\right)\right], \quad (7)$$

where N is the number of years (in our case $N = 50$). The above statistic represents, in logarithmic scale, the probability assigned by the considered model to the correct (observed) precipitation class per year, i.e. the likelihood of the observed class per year. The three integrals in Equation (7) represent the probability of dry, normal, and wet conditions in year t, as estimated from the model given $\mathbf{x}^t$. For any t, the coefficients (indicator functions) of the integrals indicate whether the year was actually dry, normal, or wet:

$$I_D^t = \begin{cases} 1, & 0 \le y_{obs}^t \le Q_e \\ 0, & otherwise \end{cases}, I_N^t = \begin{cases} 1, & Q_e < y_{obs}^t \le Q_{1-e} \\ 0, & otherwise \end{cases}, I_W^t = \begin{cases} 1, & y_{obs}^t > Q_{1-e} \\ 0, & otherwise \end{cases}$$

The above statistical metrics are used to assess the null hypothesis, H_0: *"The predictors **X** are independent of Y, and thus, non-informative for prediction"*.

Under H_0, the copula ratio in Equation (2) is equal to unity and the predictive distribution of precipitation for any t, is equal to the historical marginal PDF of precipitation (i.e. the climatology), $f_{Y|\mathbf{X}}^t(y) = f_Y(y)$. Based on this, the asymptotic ($N \to \infty$) values of the considered statistical metrics under H_0, can be easily derived:

$$DS_{H_0} = e$$

$$WS_{H_0} = e$$

$$NS_{H_0} = 1 - 2e$$

$$NDS_{H_0} = 1 - e$$

$$LogL_{H_0} = 2e\text{Log}[e] + (1 - 2e)\text{Log}[1 - 2e]$$

However, because of the limited sample size, $N = 50$, the asymptotic values cannot be used to assess significance, i.e., to reject the H_0. Thus, we use Monte Carlo simulations to obtain the critical values of the above statistics, for a significance level of α = 0.05.

Particularly, we simulate 5000 pairs of independent Y and X series (of sample size $N = 50$), and determine the empirical 95%-quantile for each of the above statistics and for different definitions of the extremes (e values), which we then use to assess significance (see Figure 1.26). For the sake of completeness, in Figure 1.26, we also present results for $N = 200$. As expected, for larger sample sizes, the sample variability decreases, and the distributions of the statistical metrics get narrower around the asymptotic values.

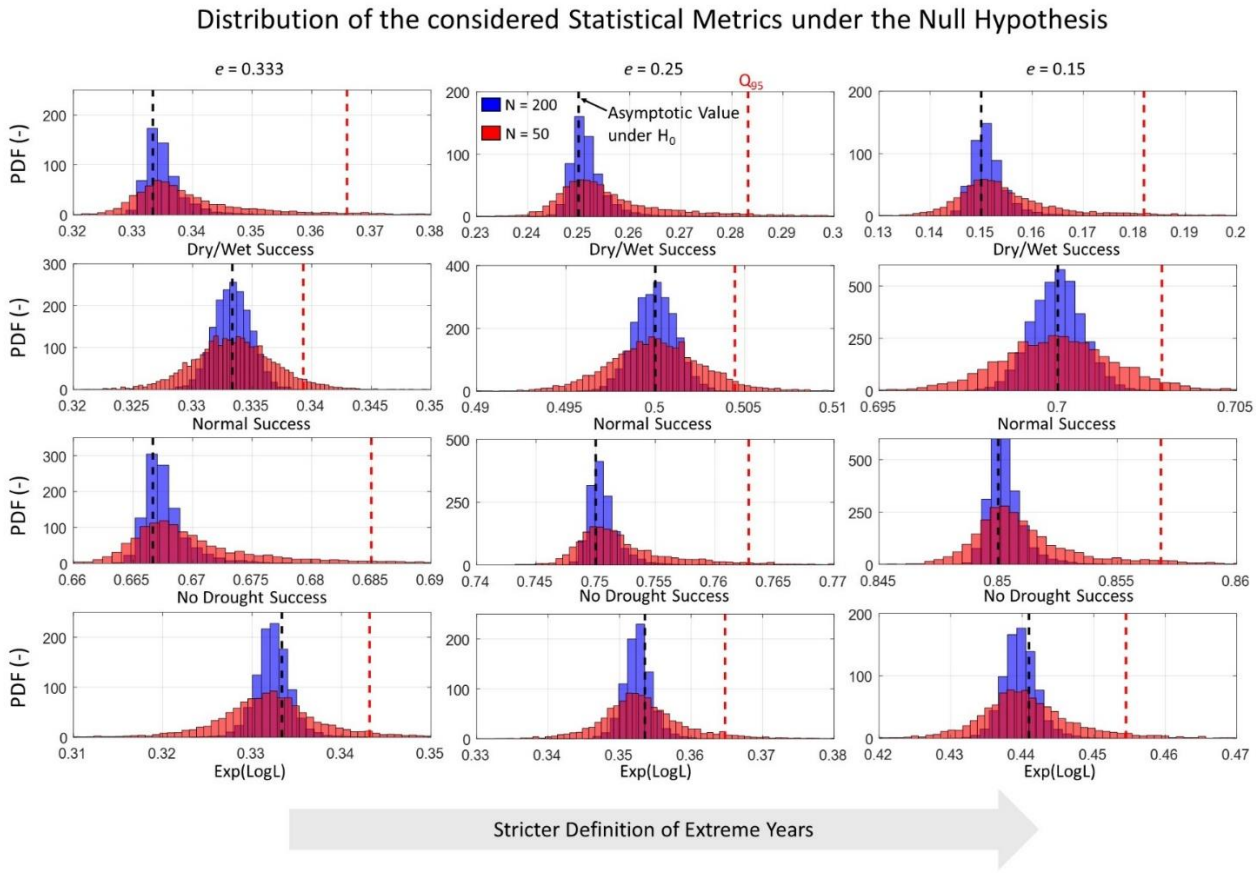

Figure 1.26. The empirical distribution of the considered statistical metrics under the null hypothesis H_0 of no predictive skill, for different sample sizes ($N = 200$, blue; $N = 50$, red) and for different definitions of extremes (e = 0.333, 0.25, 0.15). Dashed black lines correspond to the asymptotic ($N \to \infty$) values of the considered statistical metrics under H_0, while dashed red lines show the 95%-quantiles of the distributions of the metrics for $N = 50$, which are used in our analysis to assess significance at α = 0.05 significance level.

Results

Using observations. Figure 1.27 shows the series of the predictive distribution of precipitation for all years from 1969-70 to 2018-19 using different sets of climate indices. When using the traditional Niño 3.4 index, a small percentage of interannual precipitation variability is explained by the mean value of the predictive distribution (R^2 of only 7%), which corresponds to a non-significant linear correlation (at α = 0.05 significance level) between the prediction and the observations (see also Table 1.2). When adding NZI to the predictive model, the explained variance increases significantly, reaching 17%. Indeed, among all univariate predictive models NZI is the best performing one, according to all statistical metrics (Table 1.2). When we combine all the indices, the performance is lower than that of the Niño 3.4-NZI model (at least in terms of R^2). This implies that although additional information may be provided by adding many more predictors, the complexity of the model increases significantly, leading to a lower prediction skill due to overfitting (i.e. a known tradeoff between complexity and prediction skill). However, this is not the case when using the first two components of the indices as the predictors. Specifically, although roughly the same amount of information is used for prediction (i.e. the first two PCs collectively capture more than 75% of the variance of the eight indices), the model is much simpler (a bivariate model) yet the prediction skill improves, with R^2 = 24%. This is because the first two PCs provide a compressed representation of the eight indices. Note that if the above analysis is conducted without using the five-fold cross validation approach, results are much different, and one would mistakenly think that adding more predictors leads to better prediction skill, whereas the model is actually fitting noise (specifically, if the five-fold cross validation is not applied, R^2 = 13% when using only the Niño 3.4 index, R^2 = 24% when using both Niño 3.4 and NZI, and R^2 = 33% when using all indices).

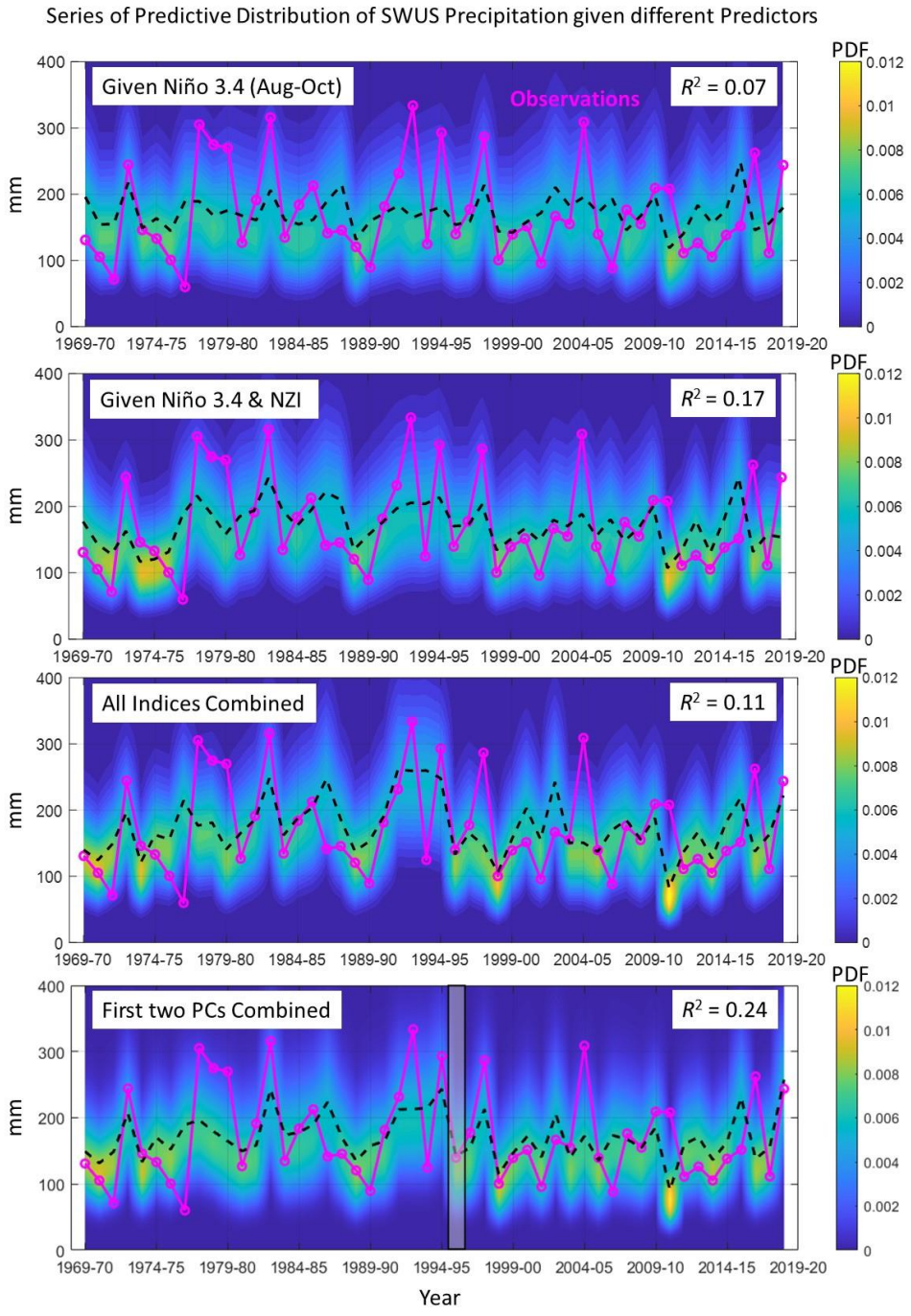

Figure 1.27. Series of the predictive PDF of SWUS winter precipitation from 1969-70 to 2018-19, using different predictive models. Observations of precipitation correspond to the Nov-Mar season, while predictors correspond to the Aug-Sep season. The observed precipitation variability that is explained by the mean value of the predictive PDF (broken black line) is also given (see R^2 values). In the lower panel, the grey rectangle highlights the prediction shown in Figure 1.25a.

Table 1.2. The skill scores based on the defined statistical metrics for different predictive models and for different extreme thresholds (i.e., probability of non exceedance e). **Bold** values of the statistics imply statistical significance at $\alpha = 0.05$ significance level.

Predictive Model	PACIFIC					ATLANTIC		INDIAN	MULTIVARIATE		
	Niño 4	Niño 3.4	Niño 3	NZI	EPI	TNA	AMO	SETIO	Niño 3.4 & NZI	All Indices	First two PCs
R^2	**0.081**	0.073	0.041	**0.181**	**0.080**	0.039	**0.109**	0.062	**0.170**	**0.112**	**0.241**
e = 0.333											
Dry Success	**0.367**	**0.373**	0.351	**0.426**	**0.366**	0.347	0.363	0.326	**0.426**	**0.423**	**0.404**
Wet Success	0.364	0.362	0.350	**0.407**	**0.387**	0.355	**0.381**	**0.377**	**0.400**	**0.412**	**0.448**
Normal Success	0.330	0.322	0.320	0.333	0.332	0.323	0.327	**0.342**	0.332	**0.348**	0.337
No Drought success	0.684	**0.688**	0.676	**0.716**	0.684	0.674	0.683	0.663	**0.716**	**0.712**	**0.704**
Exp[LogL]	0.332	0.335	0.329	**0.358**	0.343	0.331	0.342	0.328	**0.351**	0.326	**0.355**
e = 0.25											
Dry Success	**0.300**	**0.303**	0.282	**0.342**	0.271	0.252	0.262	0.247	**0.343**	**0.333**	**0.317**
Wet Success	**0.307**	**0.315**	**0.290**	**0.339**	**0.321**	**0.287**	**0.312**	**0.348**	**0.332**	**0.360**	**0.430**
Normal Success	0.488	0.489	0.492	**0.505**	0.497	0.491	0.488	0.498	0.502	**0.521**	**0.508**
No Drought success	**0.771**	**0.773**	**0.763**	**0.789**	0.759	0.751	0.755	0.749	**0.790**	**0.784**	**0.779**
Exp[LogL]	**0.371**	**0.375**	**0.365**	**0.385**	0.361	0.352	0.360	0.360	**0.380**	0.355	**0.396**
e = 0.15											
Dry Success	0.163	0.164	0.158	**0.229**	0.138	0.171	0.178	0.160	**0.225**	**0.207**	**0.199**
Wet Success	**0.198**	**0.217**	0.172	**0.330**	**0.199**	0.157	**0.185**	**0.230**	**0.315**	**0.284**	**0.325**
Normal Success	0.692	0.691	0.693	**0.704**	0.688	0.697	0.694	0.695	**0.703**	**0.704**	0.697
No Drought success	0.853	0.853	0.852	**0.869**	0.847	0.855	0.856	0.852	**0.867**	**0.863**	**0.861**
Exp[LogL]	0.435	0.445	0.431	**0.504**	0.415	0.431	0.434	0.442	**0.496**	0.429	**0.472**

Adding information from other climate indices to the Niño 3.4 model (or using the compression offered by principal components) also improves prediction of extreme precipitation totals (see Figure 1.28 and Table 1.2). For dry extremes, the Niño 3.4 index is on the edge of being a statistically significant predictor during the last five decades (Figure 1.28a), while wet years are more strongly associated with ENSO (Figure 1.28b). This asymmetry of the strength of the ENSO climate teleconnection (El Niño vs La Niña) has been previously reported (Zhang et al., 2014; Feng et al., 2017), and it has been attributed to the internal asymmetry of the ENSO dynamics, with El Niño events being typically more extreme and driving larger circulation anomalies than La Niña events (An and Jin 2004; Zhang et al., 2014). Overall, the Niño 3.4 index has not been a robust predictor in the last five decades, as indicated from the log-likelihood of the data (Figure 1.28e); see also remarks in recent studies (Wang et al., 2014; Baxter and Nigam, 2015; Teng and Branstator, 2017; Zhang et al., 2018).

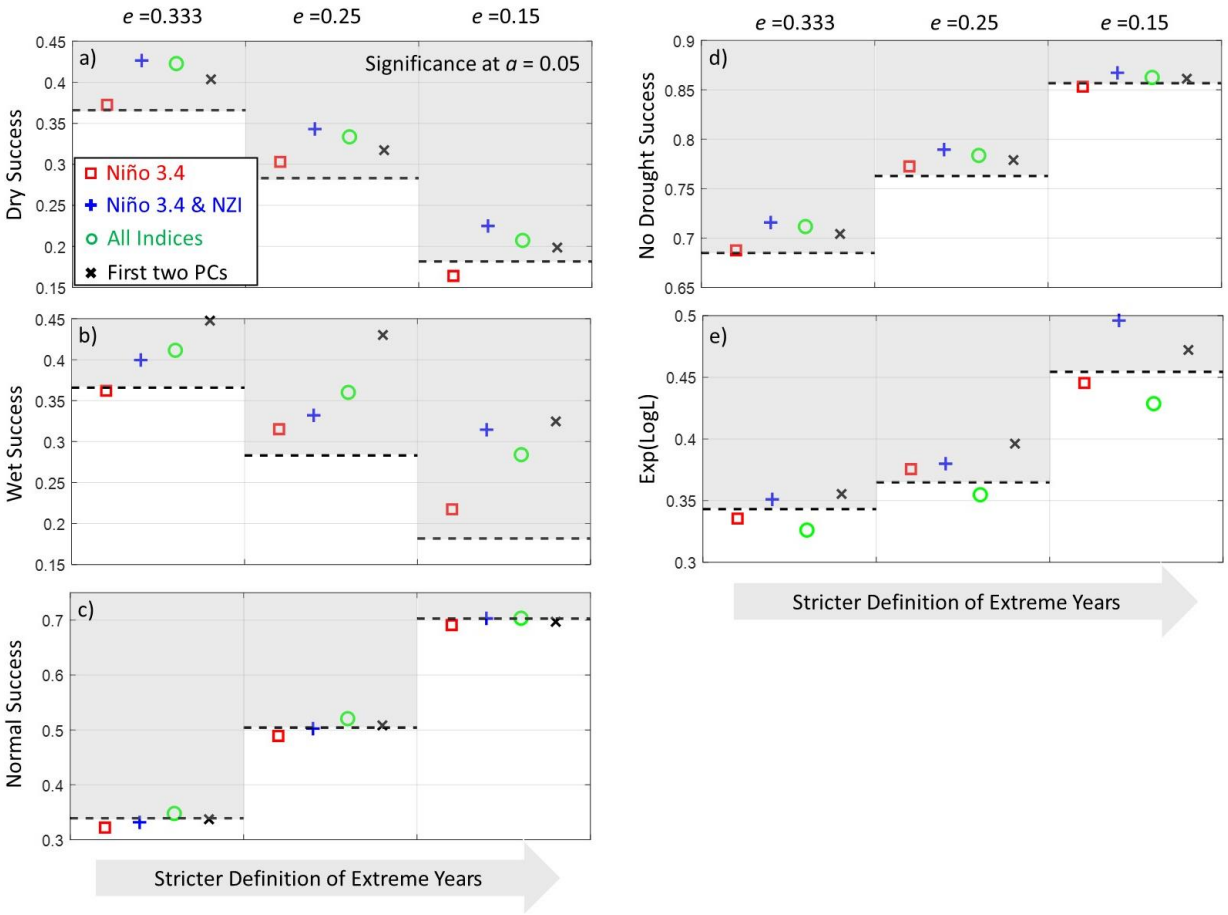

Figure 1.28. Performance of different predictive models, as evaluated using the introduced statistical metrics and different definition of extremes. Dashed black lines correspond to the critical values of the metrics under the null hypothesis H_0 of no predictive skill, at $\alpha = 0.05$ significance level. Values of the metrics above these limits are assessed as statistically significant (the shaded areas indicate significance). In most cases, models more efficiently predict wet than dry years (especially, that as the definition of extremes gets stricter), while normal years are virtually not predictable compared to extreme years.

When adding the NZI to the prediction, the skill increases and becomes statistically significant. This increase is especially the case for predicting dry years, which is consistent with recent reports that have shown SSTs over the western tropical and subtropical Pacific were an important driver of the recent multiyear drought in California from 2011-12 to 2015-16. Specifically, Wang et al. (2014) found that during the late boreal summer in 2013, increased convective activity eastward of the Philippines excited a cross-Pacific Rossby wave train, establishing a persistent high blocking ridge over the western coast of the U.S., resulting to a dry winter in 2013-2014 for the SWUS. In a more recent study, Mamalakis et al. (2018) found that the NZI is robustly associated with climate variability over the

Philippines (and SWUS precipitation), a connection which was has strengthened particularly in the last four decades, as climate models also show (Mamalakis et al., 2019). Similar remarks about the importance of western Pacific SSTs can be drawn when predicting non-drought conditions (see Figure 1.28d). Lastly, when using the first two PCs, the skill of predicting wet years increases even more. For example, wet precipitation totals corresponding to e =0.33 (average exceedance probability of 1 per 3 years) or e =0.25 (1 per 4 years) are successfully predicted more than 40% of the time. For extreme wet totals corresponding to e =0.15 (1 per 6-7 years), prediction skill exceeds 30%.

From Figure 1.28 and Table 1.2, it is also obvious that for most models, wet conditions are more predictable than dry conditions, especially as the definition of the extremes gets stricter (as e decreases). Moreover, all models show very limited, to virtually no skill in predicting normal conditions. In fact, for prediction of normal conditions, all models are on the edge of being statistically significant (see Figure 1.28 and Table 1.2). These results suggest that SST based predictions cannot beat the climatology-based predictions with regard to normal precipitation, and in other words, only extreme (dry/wet) precipitation years carry an early (late summer-early fall) ocean signature.

To further explore the above findings, we establish a global-pattern significance analysis (see e.g. Wilks 2016). We first repeat the prediction, but using as predictor the individual SST series over each grid point in the entire globe (first linearly detrending all the SST series and then applying the five-fold cross validation approach), and we present the maps of the statistical metrics in Figures 1.29-1.30. The purpose of this diagnostic approach is by no means to argue that SST variability in a single grid point can be used to predict SWUS precipitation, but rather to identify and extract coherent SST patterns that may be more or less effective for predicting different components of the precipitation distribution. These maps verify that wet years are more predictable than dry years based on SSTs. This is seen from the more robust and more coherent spatial pattern that wet years are associated with, especially as the definition of extremes becomes stricter (note that stippling indicates rejection of H_0 at $\alpha = 0.05$ significance level). Similarly, it is clear that normal conditions are virtually not predictable compared to extreme conditions, and as the analysis of the SST

indices concluded, only extreme precipitation years are associated with a statistically significant ocean signature.

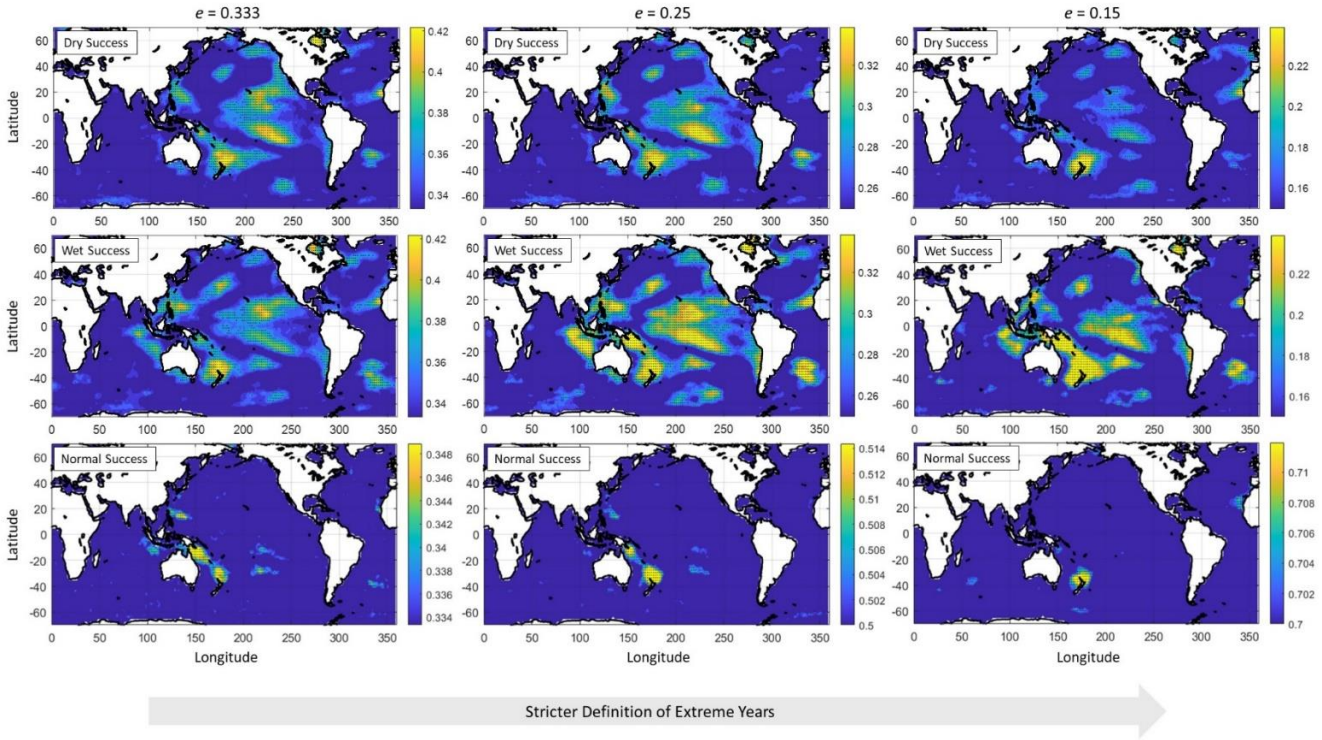

Figure 1.29. Same as in Figure 1.28, but when SST in each grid point was used separately as a predictor. The results for Dry, Wet and Normal Success are presented (top, middle and bottom panels, respectively). Dark blue color refers to the asymptotic values of the metrics under the null hypothesis H_0 (see Figure 1.26) indicating statistically insignificant prediction skill and stippling indicates significance (rejection of H_0) at $\alpha = 0.05$ significance level. It is shown that wet years are more predictable than dry years based on SST information, especially as the definition of extremes becomes stricter. Normal conditions are virtually not predictable compared to extreme conditions. Moreover, western Pacific SSTs are shown to be stronger predictors of extreme SWUS precipitation in the last five decades.

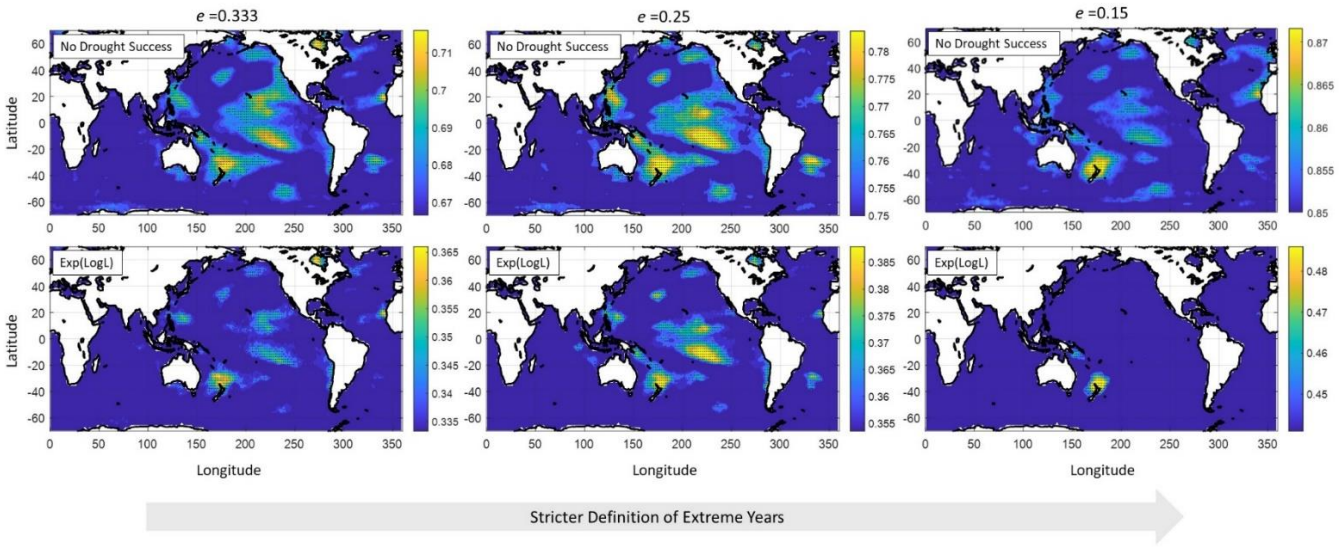

Figure 1.30. Same as in Figure 1.29, but the results for No Drought Success, and categorical Log-likelihood are presented (top and bottom panels, respectively).

Lastly, because in Figure 1.29, thousands of "local" null hypotheses are tested simultaneously, it is of importance to assess the so called global-pattern significance by controlling the false discovery rate (i.e. using the FDR method; see Wilks, 2016). Figure 1.31 shows the application of the FDR method for different significance levels (α_{FDR} = 0.20, 0.10, 0.05; see dashed lines), and for predicting different precipitation conditions (dry, wet, normal; see different colors of the curves). Specifically, in Figure 1.31, we sort all the "local" *p*-values of every grid point from each panel in Figure 1.29 (different colors correspond to different precipitation conditions, and different curves of the same color correspond to different definition of extremes, i.e. value of *e*). Based on the FDR method, the pattern significance is assessed by the number of *p*-values (see dots) being below the dashed lines in Figure 1.31 (see Wilks, 2016). It is shown that for all values of *e*, and all values of α_{FDR}, normal conditions are virtually not predictable. Wet conditions consistently carry a much larger significant SST pattern than dry conditions (consistently more blue points lie below the dashed lines than orange points), which verifies the higher predictability of wet conditions relatively to dry conditions, based on SSTs.

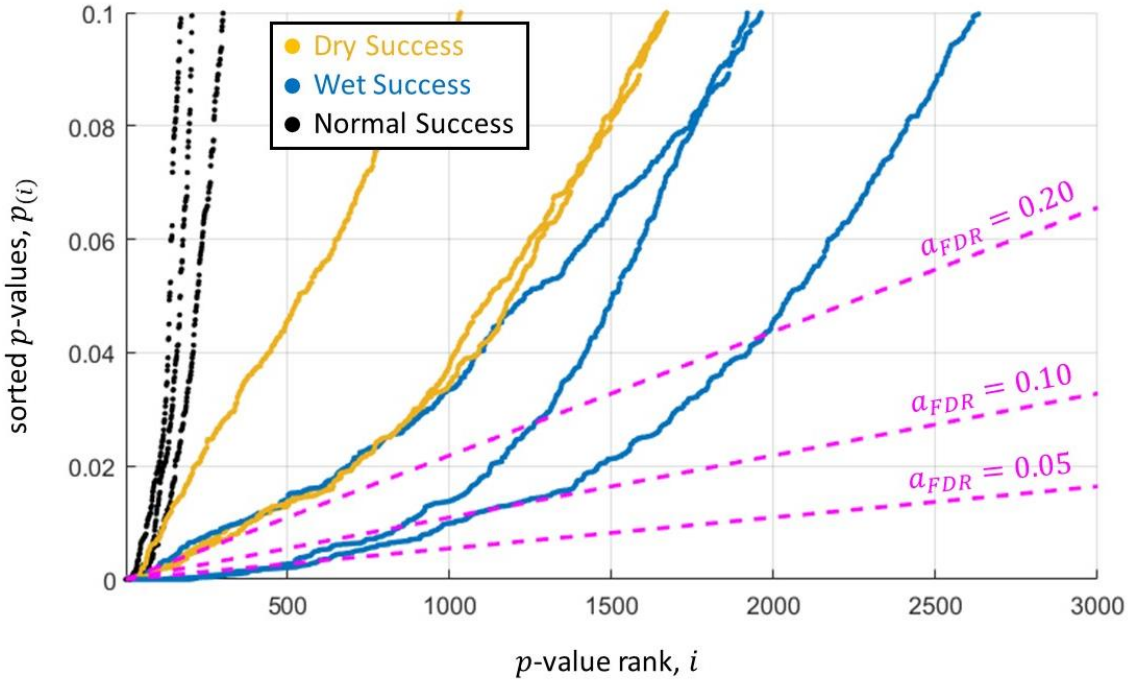

Figure 1.31. Application of the false discovery rate (FDR) method for different significance levels (dashed lines correspond to α_{FDR} = 0.20, α_{FDR} = 0.10, and α_{FDR} = 0.05), and for predicting different precipitation conditions (dry, orange dots; wet, blue dots; normal, black dots). Note that different curves of the same color correspond to predicting extremes of different *e* value. Each dot corresponds to a specific grid point of Figure 1.29 (orange, blue, and black dots correspond to the top, middle, and bottom panels in Figure 1.29, respectively), and to a specific *p*-value under the null hypothesis H_0 (see Figure 1.26). The pattern significance is assessed by the number of dots being below the dashed lines (see Wilks 2016). It is shown that for all values of *e*, normal conditions are virtually not predictable. Wet conditions consistently carry a much larger significant SST pattern than dry conditions (more blue points lie below the dashed lines than orange points).

Using CMIP6 model outputs. Here we repeat the analysis using precipitation and SST outputs from 27 CMIP6 models (see Table 1.3), for the period from 1965-66 to 2014-15. As shown in Figure 1.32, the majority of CMIP6 models significantly overestimate the multi-year average (Nor-Mar) precipitation in the SWUS, which indicates a systematic bias in reproducing regional precipitation. Because the copula-based predictive model in Equation (2) exploits multivariate relationships in the probability space and not in the real space, such systematic biases in the average first-order statistics of the predictand variable do not affect the assessment of predictability.

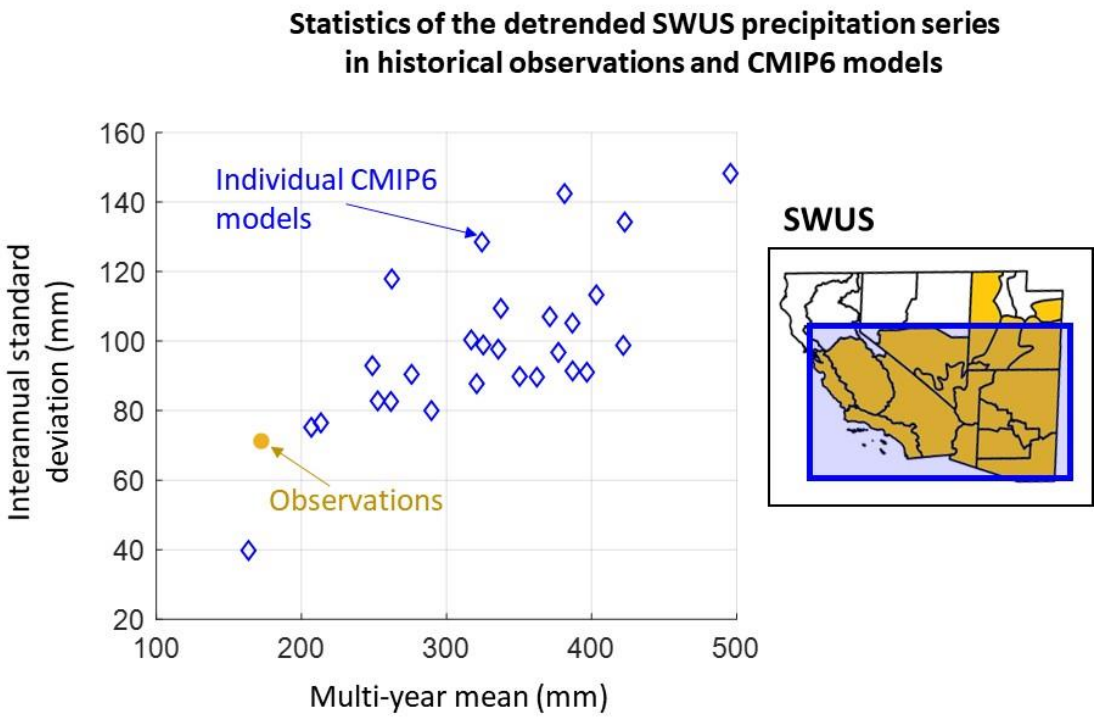

Figure 1.32. Multi-year mean and standard deviation of the winter (Nov-Mar) precipitation over the SWUS, as calculated using observations (from 1969-70 to 2018-2019) and individual CMIP6 model outputs (from 1965-66 to 2014-2015). The region of SWUS in each case is also shown on the right.

Table 1.3. CMIP6 models used in this study.

	Model	Number of ensembles
1	ACCESS-CM2	1
2	ACCESS-ESM1-5	3
3	BCC-CSM2-MR	1
4	CAMS-CSM1-0	2
5	CanESM5	20
6	CanESM5-CanOE	3
7	CESM2	6
8	CESM2-WACCM	1
9	CNRM-CM6-1	6
10	CNRM-CM6-1-HR	1
11	CNRM-ESM2-1	5
12	FGOALS-f3-L	1
13	FGOALS-g3	1
14	GFDL-ESM4	1
15	GISS-E2-1-G	1
16	INM-CM4-8	1
17	INM-CM5-0	5
18	IPSL-CM6A-LR	11
19	KACE-1-0-G	3
20	MIROC6	3
21	MIROC-ES2L	1
22	MPI-ESM1-2-HR	10
23	MPI-ESM1-2-LR	10
24	MRI-ESM2-0	1
25	NorESM2-LM	1
26	NorESM2-MM	1
27	UKESM1-0-LL	5

In Table 1.4 and Figure 1.33, we present the CMIP6 multi-model mean values of all statistical metrics based on different predictors, after predicting (in a 5-fold cross validation setting) precipitation in each CMIP6 model separately. With regard to ENSO, our results show that CMIP6 slightly overestimate its important as a source of precipitation predictability. This is shown from the higher values of R^2 and of most statistical metrics for all definitions of extremes that correspond to the ENSO indices (compare Tables 1.2 and 1.4). More importantly, it is surprising that all other indices over the western Pacific, Indian and

Atlantic Oceans seem to be unimportant sources of predictability according to CMIP6 models. Indeed, all the statical metrics show statistically insignificant connection between non-ENSO SST indices and SWUS precipitation. Consistently with the latter, when considering multiple indices together (see last three columns in Table 1.4), the performance is very similar to the one that individual ENSO indices exhibit. This means that adding non-ENSO indices does not improve the performance of predictions, and so, according to CMIP6 models, any non-ENSO index is not a robust source of SWUS precipitation predictability. The latter is in direct contradiction with the results from the analysis of observations and highlights a systematic bias in CMIP6 models in overestimating the ENSO effect to precipitation and, at the same time, underestimate the effect of non-ENSO SST variability. For similar conclusions referring to CMIP3 and CMIP5, see Langenbrunner and Neelin (2013), Polade et al., (2013). Nevertheless, results in Table 1.4 and Figure 1.33 show that, no matter the predictor used, normal years are not predictable based SST information, while wet years are inherently more predictable. This is in accordance to with the conclusions reached from the analysis of the observations.

Table 1.4. Same as Table 1.2, but using multi-model mean of 27 CMIP6 model simulations. **Bold** values of the statistics imply statistical significance at α = 0.05 significance level.

Predictive Model	PACIFIC					ATLANTIC		INDIAN	MULTIVARIATE		
	Niño 4	Niño 3.4	Niño 3	NZI	EPI	TNA	AMO	SETIO	Niño 3.4 & NZI	All Indices	First two PCs
R^2	**0.124**	**0.125**	**0.117**	0.070	0.061	0.052	0.045	0.060	**0.124**	**0.112**	**0.126**
e = **0.333**											
Dry Success	**0.383**	**0.382**	**0.377**	0.348	0.346	0.329	0.327	0.338	**0.381**	**0.383**	**0.382**
Wet Success	**0.395**	**0.396**	**0.391**	0.351	0.353	0.328	0.329	0.344	**0.394**	**0.404**	**0.399**
Normal Success	0.336	0.337	0.334	0.330	0.330	0.331	0.330	0.331	0.334	0.336	0.336
No Drought success	**0.691**	**0.692**	**0.689**	0.674	0.673	0.664	0.664	0.669	**0.691**	**0.692**	**0.692**
Exp[LogL]	**0.347**	**0.346**	0.343	0.328	0.328	0.322	0.320	0.324	0.341	0.309	0.342
e = **0.25**											
Dry Success	**0.294**	**0.294**	**0.289**	0.265	0.261	0.243	0.241	0.251	**0.294**	**0.295**	**0.294**
Wet Success	**0.304**	**0.310**	**0.306**	0.264	0.268	0.242	0.243	0.259	**0.309**	**0.312**	**0.312**
Normal Success	0.500	0.502	0.500	0.496	0.497	0.495	0.496	0.496	0.500	0.501	0.503
No Drought success	**0.765**	**0.766**	**0.764**	0.755	0.754	0.747	0.747	0.750	**0.766**	**0.766**	**0.766**
Exp[LogL]	0.363	0.363	0.360	0.347	0.348	0.340	0.338	0.343	0.359	0.320	0.358
e = **0.15**											
Dry Success	**0.184**	**0.183**	0.179	0.159	0.153	0.142	0.140	0.147	**0.184**	**0.185**	0.182
Wet Success	**0.189**	**0.195**	**0.194**	0.158	0.165	0.138	0.141	0.150	**0.192**	**0.203**	**0.195**
Normal Success	0.700	0.699	0.699	0.697	0.695	0.696	0.696	0.696	0.699	0.699	0.699
No Drought success	**0.858**	**0.857**	0.856	0.852	0.851	0.848	0.848	0.850	**0.857**	**0.858**	**0.857**
Exp[LogL]	0.445	0.444	0.442	0.430	0.432	0.423	0.422	0.424	0.439	0.393	0.437

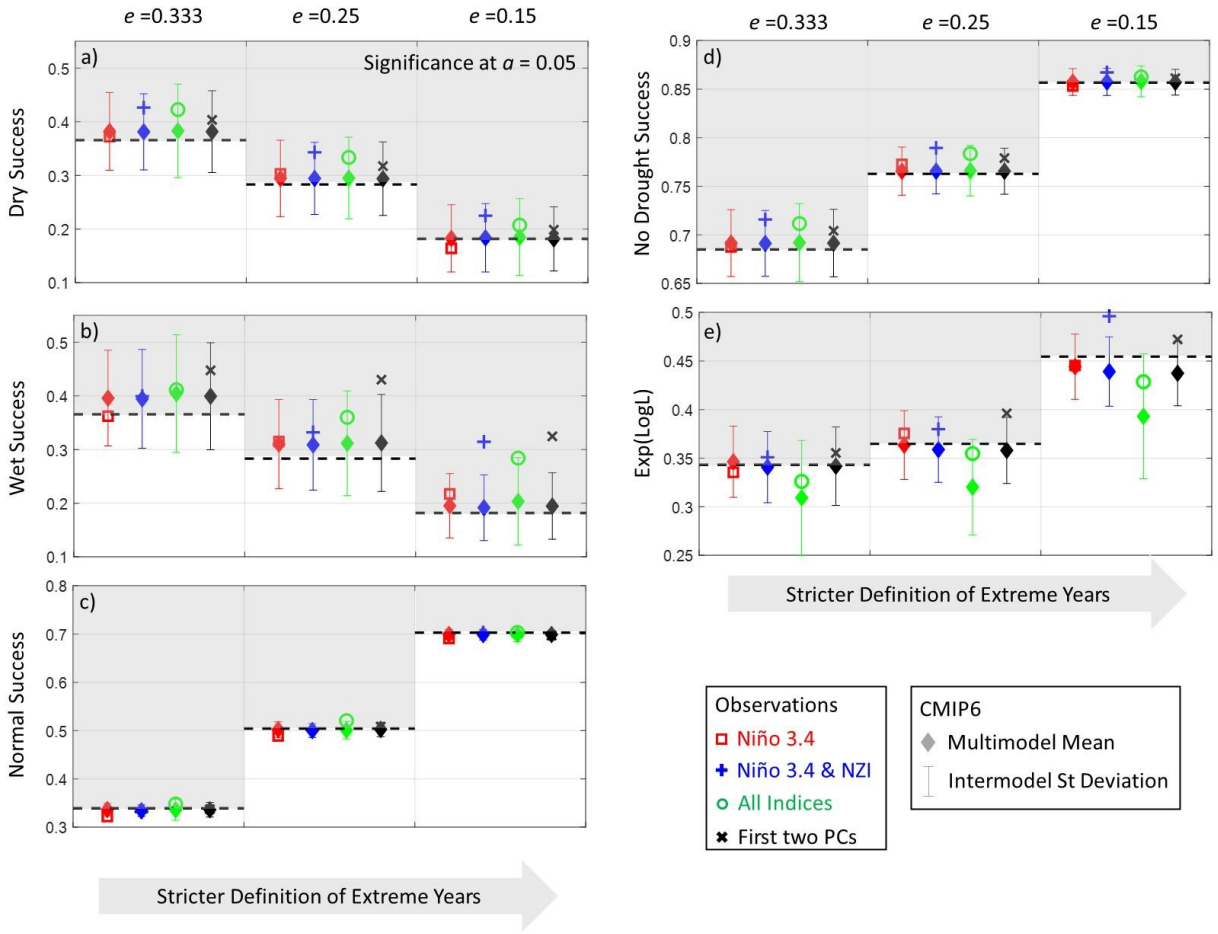

Figure 1.33. Same as in Figure 1.28, but results from CMIP6 model outputs (from 1965-66 to 2014-2015) are also presented.

Discussion and Concluding Remarks

In this study we have revisited the problem of seasonal prediction of winter precipitation totals over SWUS, focusing on extreme dry and wet conditions of different magnitude. We have presented a probabilistic framework, where prediction is made conditioning on SST information, and resolving the entire predictive precipitation distribution in each year. We have introduced statistical metrics which focus on assessing the models' ability in capturing different aspects of the precipitation distribution, also assessing the null hypothesis of no predictive skill, based on Monte Carlo simulations to account for the limited sample size.

After applying our framework to predict winter precipitation totals during the last five decades, we find that normal conditions are virtually not predictable relatively to

extreme conditions, and wet conditions are more predictable than dry conditions. We show that, for non-zero lead times, traditionally used indices based on central Pacific SST (like the Niño 3.4 index) have not been robust predictors of precipitation during the last five decades, especially with regard to dry conditions. In contrast, SSTs over the southwestern Pacific have been better predictors of precipitation totals. Although beyond the scope of this study, it is important to note that the exact physical mechanism of the latter connection remains unclear. On one hand, some studies support that climate variability (e.g. SST, sea level pressure, etc.) over the southwestern Pacific (i.e. in the proximity of the south Pacific convergence zone) leads by a few seasons the ENSO variability (Trenberth and Shea, 1987; van Loon and Shea, 1987; Stephens et al., 2007), and considering these dynamics, specific indices have been suggested to increase predictive skill of ENSO state (Hamlington et al., 2015). Given that ENSO is more robustly related to SWUS precipitation during winter (i.e. for zero lead time), the southwestern Pacific SSTs may provide important predictors of precipitation, by leading the ENSO state. More recent studies, however, suggest that western Pacific SSTs can affect precipitation not necessarily through ENSO teleconnections (e.g. Wang et al., 2014; Baxter and Nigam, 2015; Teng and Branstator, 2017; Mamalakis et al., 2018). The importance of this western Pacific pathway for driving SWUS precipitation has been increasing during the last 40 years, which is also the time when new, ENSO-independent SST patterns have been emerging and affecting tropical atmospheric circulation (Johnson et al., 2019). We note that the importance of the Indo-Pacific climate state in general, as a source of precipitation predictability, is increasingly acknowledged in the recent literature, and many studies focus on beyond ENSO indices to improve predictions and understanding of the variability of SWUS hydroclimate (Wang et al., 2014; Baxter and Nigam, 2015; Teng and Branstator, 2017; Seager et al., 2017; Swain et al., 2017; Myoung et al., 2018; Mamalakis et al., 2018; Johnson et al., 2019; Zhou et al., 2020; Stevens et al., 2020).

Our analysis of CMIP6 outputs verifies that copula-based models are not reliable when predicting normal years conditioned on SST information, but they are more reliable when predicting wet years. However, our results show that CMIP6 models seem to fail to reproduce non-ENSO SST indices to be important sources of predictability of SWUS precipitation, which contradicts the analysis of observations and the conclusions of the

recent literature, and it highlights that there are still standing important biases in climate models physics.

The framework introduced herein can be applied to any predictive model (beyond copula models) and allows to determine the predictive skill of precipitation not only in the past (retrospectively), but also in the future climate, by using climate model outputs to explore possible changes in the strength of climate teleconnections, highly important for assessment of climate change impacts on regional hydroclimate. It may be relatively straightforward to extend our approach to predict other aspects of the precipitation distribution, even beyond the ones considered here, e.g. by defining extremes based on specified magnitudes (instead of quantiles), and/or by using additional statistical metrics (e.g. probability of miss), important for risk quantification and water management decisions.

References

AghaKouchak, A. and A. Mehran (2013) Extended contingency table: Performance metrics for satellite observations and climate model simulations, *Water Resour. Res.*, **49**, 7144-7149, doi:10.1002/wrcr.20498.

AghaKouchak, A., D. Feldman, M. Hoerling, T. Huxman, and J. Lund (2015) Recognize Anthropogenic Drought, *Nature*, **524**(7566), 409-411.

An, S.-I. and F.-F. Jin (2004) Nonlinearity and asymmetry of ENSO, *J. Climate*, **17**, 2399–2412

Anagnostou, E.N., V. Maggioni, E.I. Nikolopoulos, T. Meskele, F. Hossain, and A. Papadopoulos (2010) Benchmarking high-resolution global satellite rainfall products to radar and rain-gauge rainfall esti-mates, *IEEE Trans. Geosci. Remote Sens.*, **48**(4), 1667–1683.

Azuara J.M., D. MacEwan, R.E. Howitt, D.A. Sumner, and J.R. Lund (2016) *Economic Analysis of the 2016 California Drought on Agriculture*, A report for the California Department of Food and Agriculture, Center for Watershed Sciences, University of California – Davis.

Baxter, S. and S. Nigam (2015) Key role of the North Pacific Oscillation-West Pacific Pattern in generating the extreme 2013/14 North American winter, *J. Climate*, **28**, 8109–8117.

Becker, E., H. van den Dool, and Q. Zhang (2014) Predictability and Forecast Skill in NMME, *J. Climate*, **27**, 5891–5906.

Behrangi, A., B. Khakbaz, T. Jaw, A. AghaKouchak, K. Hsu, and S. Sorooshian (2011) Hydrologic evaluation of satellite precipitation products at basin scale, *J. Hydrol.*, **397**, 225–237.

Chang, Y., S.D. Schubert, and M.J. Suarez (2000) Boreal winter predictions with the GEOS-2 GCM: The role of boundary forcing and initial conditions, *Quart. J. Roy. Meteor. Soc.*, **126**, 2293–2321, doi:10.1256/smsqj.56714.

Chen, Y., D.C. Morton, N. Andela, L. Giglio, and J.T. Randerson (2016) How much global burned area can be forecast on seasonal time scales using sea surface temperature?, *Environmental Research Letters*, **11**(4).

Corringham, T.W., F. M. Ralph, A. Gershunov, D.R. Cayan, and C.A. Talbot (2019) Atmospheric rivers drive flood damages in the western United States, *Science Advances*, **5**(12), DOI: 10.1126/sciadv.aax4631

Dai, A. (2013) The influence of the inter-decadal Pacific oscillation on US precipitation during 1923-2010, *Clim. Dyn*., **41**, 633 - 646.

DelSole, T. and A. Banerjee (2017) Statistical Seasonal Prediction Based on Regularized Regression. *J. Climate,* **30**, 1345–1361, https://doi.org/10.1175/JCLI-D-16-0249.1

Dettinger M.D., F.M. Ralph, T. Das, P.J. Neiman, and D. Cayan (2011) Atmospheric rivers, floods, and the water resources of California, *Water*, **3**(2), 455–478, https://doi.org/10.3390/w3020445

Dettinger, M.D. and D. Cayan (2014) Drought and the California Delta – A matter of extremes, *San Francisco Estuary and Watershed Sci*., **12**(2).

Diffenbaugh, N.S., D.L. Swain, and D. Touma (2015) Global warming increases California drought risk, *PNAS*, **112**(13), 3931-3936.

Enfield, D. B. and A. M. Mestas-Nuñez (2001) The Atlantic multidecadal oscillation and its relation to rainfall and river flows in the continental U.S., *Geophys. Res. Lett.*, **28**(10), 2077-2080.

Eyring et al. (2016) An overview of the Coupled Model Intercomparison Project Phase 6 (CMIP6) experimental design and organization, *Geosci. Model Dev.*, **9**, 1937–1958,, doi:10.5194/gmd-9-1937-2016

Feng, J., W. Chen, and Y. Li (2017) Asymmetry of the winter extra-tropical teleconnections in the Northern Hemisphere associated with two types of ENSO, *Clim Dyn*, **48** (2135). https://doi.org/10.1007/s00382-016-3196-2

Gershunov, A. and D.R. Cayan (2003) Heavy Daily Precipitation Frequency over the Contiguous United States: Sources of Climatic Variability and Seasonal Predictability, *J. Climate,* **16**, 2752–2765.

Gershunov, A., et al. (2019) Precipitation regime change in western north America: The role of atmospheric rivers, *Scientific Reports*, **9**(9944), https://doi.org/10.1038/s41598-019-46169-w

Gibson, P.B., D.E. Waliser, B. Guan, M.J. DeFlorio, F.M. Ralph, and D.L. Swain (2019) Ridging associated with drought across the western and southwestern United States: Characteristics, trends and predictability sources, *J. Climate*, DOI 10.1175/JCLI-D-19-0439.1.

Gourley, J.J., J.M. Erlingis, Y. Hong, and E.B. Wells (2012) Evaluation of tools used for monitoring and forecasting flash floods in the United States, *Weather Forecasting*, **27**(1), 158–173.

Haile, A.T., E. Habib, and T. Rientjes (2012) Evaluation of the Climate Prediction Center (CPC) Morphing technique (CMORPH) rainfall product on hourly time scales over the source of the Blue Nile River, *Hydrol. Processes*, **27**, 1829–1839.

Hamlington, B.D., R.F. Milliff, H. van Loon, and K.-Y. Kim (2015) A Southern Hemisphere sea level pressure-based precursor for ENSO warm and cold events, *J. Geophys. Res. Atmos.*, **120**, 2280–2292, doi:10.1002/2014JD022674.

Hao, Z., A. AghaKouchak, and T.J. Phillips (2013) Changes in concurrent monthly precipitation and temperature extremes, *Environ. Res. Lett.*, **8**(3), 034014, doi:10.1088/1748-9326/8/3/034014.

Hao, Z., Singh, V.P., and Xia, Y. (2018) Seasonal drought prediction: Advances, challenges, and future prospects, *Reviews of Geophysics*, **56**, 108– 141.

Hirahara, S., M. Ishii, and Y. Fukuda (2014) Centennial-scale sea surface temperature analysis and its uncertainty. *J. Climate* **27**, 57–75.

Howitt, R.E., J. Medellin-Azuara, D. MacEwan, J.R. Lund, and D.A. Sumner (2014) *Economic Analysis of the 2014 Drought for California Agriculture*, University of California, Davis, 2014.

Howitt, R.E., D. MacEwan, J. Medellín-Azuara, J.R. Lund, and D.A. Sumner (2015) *Economic Analysis of the 2015 Drought for California Agriculture*, Center for Watershed Sciences, University of California – Davis, Davis, CA, 16 pp.

Huang, X., D.L. Swain, D.B. Walton, S. Stevenson, and A.D. Hall (2020) Simulating and evaluating atmospheric river-induced precipitation extremes along the U.S. Pacific

Coast: Case studies from 1980–2017. *Journal of Geophysical Research: Atmospheres*, **125**, e2019JD031554. https://doi.org/10.1029/2019JD031554

Joe, H. (1997) *Multivariate Models and Dependence Concepts*, Chapman and Hall, London, U. K.

Johnson, N.C., M.L. L'Heureux, C.-H. Chang, and Z.-Z. Hu (2019) On the delayed coupling between ocean and atmosphere in recent weak El Niño episodes, *Geophysical Research Letters*, **46**, 11416– 11425. https://doi.org/10.1029/2019GL084021

Langenbrunner, B., and J. D. Neelin, 2013: Analyzing ENSO Teleconnections in CMIP Models as a Measure of Model Fidelity in Simulating Precipitation. *J. Climate*, **26**, 4431–4446, https://doi.org/10.1175/JCLI-D-12-00542.1.

Lindsey, R. (2016) How El Niño and La Niña affect the winter jet stream and U.S. climate. Climate.gov. https://www.climate.gov/news-features/featured-images/how-el-ni%C3%B1o- and-la-ni%C3%B1a-affect-winter-jet-stream-and-us-climate.

Liu, T., R.W. Schmitt, and L. Li (2018) Global search for autumn-lead sea surface salinity predictors of winter precipitation in southwestern United States, *Geophysical Research Letters*, **45**, 8445–8454. https://doi.org/10.1029/ 2018GL079293

Madadgar, S., and H. Moradkhani (2013) A Bayesian framework for probabilistic seasonal drought forecasting, *J. Hydrometeorol*., **14**, 1685–1705.

Madadgar, S., A. AghaKouchak, S. Shukla, A.W. Wood, L. Cheng, K.-L. Hsu, and M. Svoboda (2016) A hybrid statistical-dynamical framework for meteorological drought prediction: Application to southwestern United States, *Water Resour. Res.*, **52**, 5095-5110.

Mamalakis, A., J.-Y. Yu, J.T. Randerson, A. AghaKouchak, and E. Foufoula-Georgiou (2018) A new interhemispheric teleconnection increases predictability of winter precipitation in southwestern US. *Nature Communications*, **9**, https://doi.org/10.1038/s41467-018-04722-7

Mamalakis, A., J.-Y. Yu, J.T. Randerson, A. AghaKouchak, and E. Foufoula-Georgiou (2019) Reply: A critical examination of a newly proposed interhemispheric teleconnection to southwestern US winter precipitation. *Nature Communications*, **10**, https://doi.org/10.1038/s41467-019-10531-3.

McCabe, G.J. and M.D. Dettinger (1999) Decadal variations in the strength of ENSO teleconnections with precipitation in the western United States, *Int. J. Climatology*, **19**, 1399-1410.

McCabe, G.J., M.A. Palecki, and J.L. Betancourt (2004) Pacific and Atlantic ocean influences on multidecadal drought frequence in the United States, *Proc. Natl. Acad. Sci. U. S. A.*, **101**(12), 4136-4141.

Myoung, B., S.-W. Yeh, J. Kim, and M.C. Kafatos, (2018) Impacts of Pacific SSTs on atmospheric circulations leading to California winter precipitation variability: A diagnostic modeling, *Atmosphere*, **9**(455), https://doi.org/10.3390/atmos9110455

National Academies of Sciences, Engineering, and Medicine, NASEM (2016) *Next Generation Earth System Prediction: Strategies for Subseasonal to Seasonal Forecasts*, Washington, DC: The National Academies Press. doi:https://doi.org/10.17226/21873.

Nelsen, R.B. (1999) *An Introduction to Copulas*, Springer, N. Y.

Newman, M., et al. (2016) The Pacific Decadal Oscillation, Revisited, *J. Clim.*, 4399-4427.

Pan, B., K. Hsu, A. AghaKouchak, S. Sorooshian, and W. Higgins (2019) Precipitation prediction skill for the west coast United States: From short to extended range, *J. Climate,* **32**, 161–182, https://doi.org/10.1175/JCLI-D-18-0355.1

Polade, S. D., Gershunov, A., Cayan, D. R., Dettinger, M. D., and Pierce, D. W. (2013), Natural climate variability and teleconnections to precipitation over the Pacific-North American region in CMIP3 and CMIP5 models, *Geophys. Res. Lett.*, 40, 2296– 2301, doi:10.1002/grl.50491.

Ralph, F.M., P.J. Neiman, G.A. Wick, S.I. Gutman, M.D. Dettinger, D.R. Cayan, and A.B. White (2006) Flooding on California's Russian River: Role of atmospheric rivers. *Geophysical Research Letters*, **33**, L13801. https://doi.org/10.1029/2006GL026689

Ralph, F.M., et al. (2019) A scale to characterize the strength and impacts of atmospheric rivers, *Bulletin of the American Meteorological Society*, **100**(2), 269–289.

Redmond, K.T. and R.W. Koch (1991) Surface climate and streamflow variability in the Western United States and their relationship to large-scale circulation indices, *Water Resources Research,* **27**(9) 2381-2399.

Schonher, T. and S. E. Nicholson (1989) The relationship between rainfall and ENSO events, *J. Climate*, **2**, 1258–1269.

Schubert, S., Y. Chang, H. Wang, R. Koster, and M. Suarez (2016) A Modeling Study of the Causes and Predictability of the Spring 2011 Extreme US Weather Activity, *Journal of Climate*, 29(21), 7869-7887.

Seager, R., and N. Henderson (2016) On the role of tropical ocean forcing of the persistent North American West Coast ridge of winter 2013/14. *J. Climate*, **29**, 8027–8049, https://doi.org/10.1175/JCLI-D-16-0145.1.

Seager, R., N. Henderson, M.A. Cane, H. Liu, and J. Nakamura (2017) Is there a role for human-induced climate change in the precipitation decline that drove the California drought?, *J. Climate,* **30**, 10237–10258, https://doi.org/10.1175/JCLI-D-17-0192.1

Seager, R., et al. (2015) Causes of the 2011-2014 California drought, *J. Clim.*, **28**, 6997-7024.

Stephens, D.J., M.J. Meuleners, H. van Loon, M.H. Lamond, and N.P. Telcik (2007) Differences in atmospheric circulation between the development of weak and strong warm events in the Southern Oscillation, *J. Climate*, **20**, 2191–2209.

Stevens A., R., Willett, A. Mamalakis, E. Foufoula-Georgiou, A. Tejedor, J. Randerson, P. Smyth, and S. Wright (2020) Graph-guided regularized regression of Pacific Ocean climate variables to increase predictive skill of southwestern US winter precipitation, *J. Climate*, revised and under review.

Swain, D., M. Tsiang, M. Haugen, D. Singh, A. Charland, B. Rajaratnam, and N.S. Diffenbaugh, N. (2014) The extraordinary California drought of 2013/2014: Character, context, and the role of climate change, *Bulletin of the American Meteorological Society*, **95**(9), S3–S7.

Swain, D.L., D.E. Horton, D. Singh, and N.S. Diffenbaugh (2016) Trends in atmospheric patterns conducive to seasonal precipitation and temperature extremes in California, *Science Advances*, **2**(4), DOI: 10.1126/sciadv.1501344

Swain, D.L., D. Singh, D.E. Horton, J.S. Mankin, T.C. Ballard, and N.S. Diffenbaugh, (2017) Remote linkages to anomalous winter atmospheric ridging over the northeastern

Pacific, *Journal of Geophysical Research: Atmospheres*, **122**(12), 194–12,209. https://doi.org/10.1002/2017JD026575

Teng, H., and G. Branstator (2017) Causes of extreme ridges that induce California droughts, *J. Clim.*, doi: 10.1175/JCLI-D-16-0524.1.

Trenberth, K.E. and D. J. Shea (1987) On the evolution of the Southern Oscillation. *Mon. Wea. Rev.*, **115**, 3078–3096.

van Loon, H., and D.J. Shea (1987) The Southern Oscillation. Part VI: Anomalies of sea level pressure on the Southern Hemisphere and of Pacific sea surface temperature during the development of a warm event, *Mon. Weather Rev.*, **115**, 370–379.

Vose, R.S., et al. (2014) Improved historical temperature and precipitation time series for U.S. climate divisions, *J. Appl. Meteor. Climatol.*, **53**, 1232-1251.

Wang, B., et al. (2009) Advance and prospectus of seasonal prediction: Assessment of the APCC/CliPAS 14-model ensemble retrospective seasonal prediction (1980–2004), *Clim. Dyn.*, **33**(1), 93–117.

Wang, S.Y., L. Hipps, R.R. Gillies, and J.H. Yoon (2014) Probable causes of the abnormal ridge accompanying the 2013-2014 California drought: ENSO precursor and anthropogenic footprint, *Geophys. Res. Lett.*, **41**, 3220-3226.

Wilks, D. (2006) *Statistical Methods in the Atmospheric Sciences*, 2nd ed., 627 pp., Academic, Burlington, Mass.

Wilks, D.S. (2016) "The stippling shows statistically significant grid points": How research results are routinely overstated and overinterpreted, and what to do about it, *Bulletin of the American Meteorological Society*, **97**(12), 2263-2273.

Yu, J.-Y., Y. Zou, S.T. Kim, and T. Lee (2012) The Changing impact of El Niño on US winter temperatures, *Geophysical Research Letters*, **39**, doi:10.1029/2012GL052483.

Zhang, T., J. Perlwitz, and M.P. Hoerling (2014) What is responsible for the strong observed asymmetry in teleconnections between El Niño and La Niña?, *Geophys. Res. Lett.*, **41**, 1019–1025, doi:10.1002/2013GL058964.

Zhang, T., M.P. Hoerling, K. Wolter, J. Eischeid, L. Cheng, A. Hoell, J. Perlwitz, X. Quan, and J. Barsugli (2018) Predictability and prediction of southern California rains during strong El Niño events: A focus on the failed 2016 winter rains, *J. Climate,* **31**, 555–574, https://doi.org/10.1175/JCLI-D-17-0396.1

Zhou, W., Yang, D., Xie, S. *et al.* (2020) Amplified Madden–Julian oscillation impacts in the Pacific–North America region, *Nat. Clim. Chang.* **10,** 654–660. https://doi.org/10.1038/s41558-020-0814-0

CHAPTER 2

Future trends in the position of the Intertropical Convergence Zone

2.1. A multivariate probabilistic framework for tracking the intertropical convergence zone: Analysis of recent climatology and past trends

Part of this chapter has been published in Geophysical Research Letters

Citation: Mamalakis, A. and E. Foufoula-Georgiou (2018) A multivariate probabilistic framework for tracking the intertropical convergence zone: Analysis of recent climatology and past changes, Geophysical Research Letters, doi:10.1029/2018GL079865

The intertropical convergence zone (ITCZ) is the area where the northeasterly and southeasterly trade winds converge to the low-pressure zone on the equator. It is collocated with the ascending branch of the atmospheric meridional overturning circulation in the tropics (i.e. the Hadley circulation) and is characterized by deep convection and high amount of precipitation (Schneider et al., 2014), greatly affecting the tropical and subtropical hydroclimatic variability.

On seasonal timescales, the ITCZ migrates toward the warmer hemisphere, leading to the expansion of the Hadley cell and increasing the meridional heat transport toward the cooler hemisphere, which flattens the tropical temperature gradient (Donohoe et al., 2013; Schneider et al., 2014; Bischoff and Schneider, 2014; 2016; Adam et al., 2016a,b). The location and intra-annual variability of the ITCZ vary with longitude (Waliser and Gautier, 1993; Waliser and Somerville, 1994), and generally depend on the geometry and distribution of the continents, and the sea surface temperature (see e.g. Graham and Barnett, 1987; Philander et al., 1996; Chao and Chen, 2001; Trenberth, 2011; Schneider et al., 2014). In particular, the ITCZ migrates more over continental regions, where it collocates with the trough of the global monsoon (see Trenberth, 2000), and it is driven by the seasonal change of the solar heating. In contrast, over the Atlantic and eastern Pacific oceans, the ITCZ does not migrate seasonally between the two hemispheres and resides north of the equator during most of the year (Philander et al., 1996). In the western Pacific, apart from the northern ITCZ, the so-called south Pacific convergence zone (SPCZ) is also prominent from

the equatorial region north of Australia poleward and eastward toward 30°S in the central Pacific, with seasonally-varying strength, which picks during boreal winter (see Widlansky et al., 2011; Haffke and Magnusdottir, 2013; Berry and Reeder, 2014; Haffke and Magnusdottir, 2015). It should be also noted that although the ITCZ in the northern Pacific and Atlantic oceans is mainly a zonal feature, the SPCZ, as well as the south Indian ocean convergence zone (SICZ; Cook, 1998; 2000) and the south Atlantic convergence zone (SACZ; Carvalho et al., 2004) are diagonally oriented.

On decadal and longer scales, local features like the geometry of coastlines are not likely to be affecting the variability in the location of the ITCZ (Schneider et al., 2014). Instead, the ITCZ is influenced by the heating contrast between the two hemispheres, or more generally, the energetic asymmetry of the globe, and it tends to move toward the warmer hemisphere, mimicking its seasonal migration (Chiang and Bitz, 2005; Broccoli et al., 2006; Kang et al., 2008; Sachs et al., 2009; Arbuszewski, et al., 2013; Broecker and Putnam, 2013; Bischoff and Schneider, 2014; Schneider et al., 2014; Allen et al., 2015).

Due to its importance for efficient water resources management in tropical and subtropical regions, and for the sustainability of ecosystems and rainforests, efficient detection and tracking of the ITCZ on seasonal to decadal scales, as well as reliable assessment of changes in its dynamics are of high interest. Usually, the latter is based on tracking changes in the outgoing longwave radiation (OLR) or precipitation using global-zonal and annual averages (Hwang et al., 2013; Allen, 2015), thus not offering much insight into the changes of the intra-annual dynamics of the ITCZ, and not facilitating assessment of regional changes. Moreover, in particular seasons or regions of the Earth, the detection of ITCZ is rather subjective and the use of a single variable can be questionable (Nicholson, 2009; 2018). In the light of the above, more rigorous methods to objectively detect the ITCZ have been recently proposed (see method proposed by Bain et al., 2011), which consider multiple physical variables to assess the probability of any point to be part of the ITCZ using Bayesian inference. Although more insightful and theoretically consistent, these methods are computationally intensive, and require the use of manually-identified ITCZ points as training datasets, both of which limit their applicability only in specific longitudinal sectors and over short time periods, and are not offered for straightforward analysis of the extensive

observational, reanalysis or climate simulation products available, which is essential for climate change assessment studies.

Here, recognizing the fact that the ITCZ location has to be inferred based on physical variables (e.g., precipitation, OLR, cloud cover, etc.) which vary stochastically in space and time, we propose a new probabilistic approach for tracking the ITCZ. This approach allows for detailed analysis of the intra-annual dynamics in all longitudes of the globe, while being computationally efficient and flexible in its implementation. Our approach is based on the following principles:

i) The location of the ITCZ is longitudinally and seasonally explicit: at each longitude and in each month/season, there are latitudes at which the ITCZ is most likely to prevail.

ii) The ITCZ is a large-scale feature and isolated features of deep convection are not parts of it (Bain et al., 2011). Accordingly, we consider zonal means of the defining variables (e.g., precipitation or OLR) to reduce the likelihood of detecting small-scale, isolated patterns of convection as ITCZ points.

iii) In particular seasons or regions of the Earth, the definition of ITCZ based on the use of a single variable may be questionable (Nicholson, 2018), and thus, the joint consideration of multiple variables is necessary to increase robustness and physical causality.

Principles (i)-(ii) become less robust on finer than monthly/seasonal temporal scales, where tropical waves like the Madden-Julian Oscillation (MJO; Madden and Julian, 1971) can disturb the large-scale features of deep convection in the Indo-Pacific basin. Thus, our analysis is focused on seasonal to decadal scales. The proposed probabilistic framework is used to determine the recent climatology of the ITCZ, particularly its annual mean location as an explicit function of longitude, its intra-annual variability, and its overall probability distribution, i.e., the frequency at which every point within the ITCZ zone experiences the physical conditions used to define it, e.g., extreme precipitation, minimum OLR, etc. We also assess changes in ITCZ dynamics since the mid of the 20th century and report longitudinal trends.

Data. For our analysis, we use both observations and reanalysis products. Particularly, to study the recent climatology of the ITCZ, we use a high-resolution dataset of satellite precipitation (monthly precipitation series in 1983-2012 and on a 0.25º × 0.25º grid, see Ashouri et al., 2015) developed by the Center for Hydrometeorology and Remote Sensing (CHRS), and referred to as the PERSIANN-CDR dataset, and monthly records of OLR developed by the Physical Sciences Division of NOAA (monthly OLR series in 1983-2012 and on a 1º × 1º grid, see Lee, 2015) referred to as the PSD-CDR dataset. To study the ITCZ trends since the mid 20th century, we use reanalysis products obtained from the 20th Century Reanalysis V2c project (monthly series of precipitation, OLR, omega velocity, and cloud cover in 1948-2014 and on a 2º × 2º grid, see Compo et al., 2011), which is here referred to as the 20C dataset, and from the National Centers for Environmental Prediction–National Center for Atmospheric Research (monthly series of precipitation, OLR, omega velocity, and cloud cover in 1948-2014 and on a 2º × 2º grid, see Kalnay et al., 1996), which we here refer to as the NCEP/NCAR dataset. See Table S1 for more information on the data used.

Probabilistic tracking of the ITCZ. Many different variables have been used in the literature to define the location of the ITCZ, including pressure, surface wind convergence, precipitation, OLR, and cloudiness (see Nicholson, 2018 and references therein). Yet, the most commonly used variables are precipitation and OLR, since both are indicative of deep convection which takes place along the ITCZ (see for example Sachs et al., 2009; Bain et al., 2011; Donohoe et al., 2013; Schneider et al., 2014; Zhang and Wang, 2015; Bischoff and Schneider, 2014; 2016; Adam et al., 2016a,b, among others). Thus, we use here the latter two variables to track the ITCZ, but our framework is general and applicable in considering any single variable, and/or jointly distributed multiple variables to define the ITCZ.

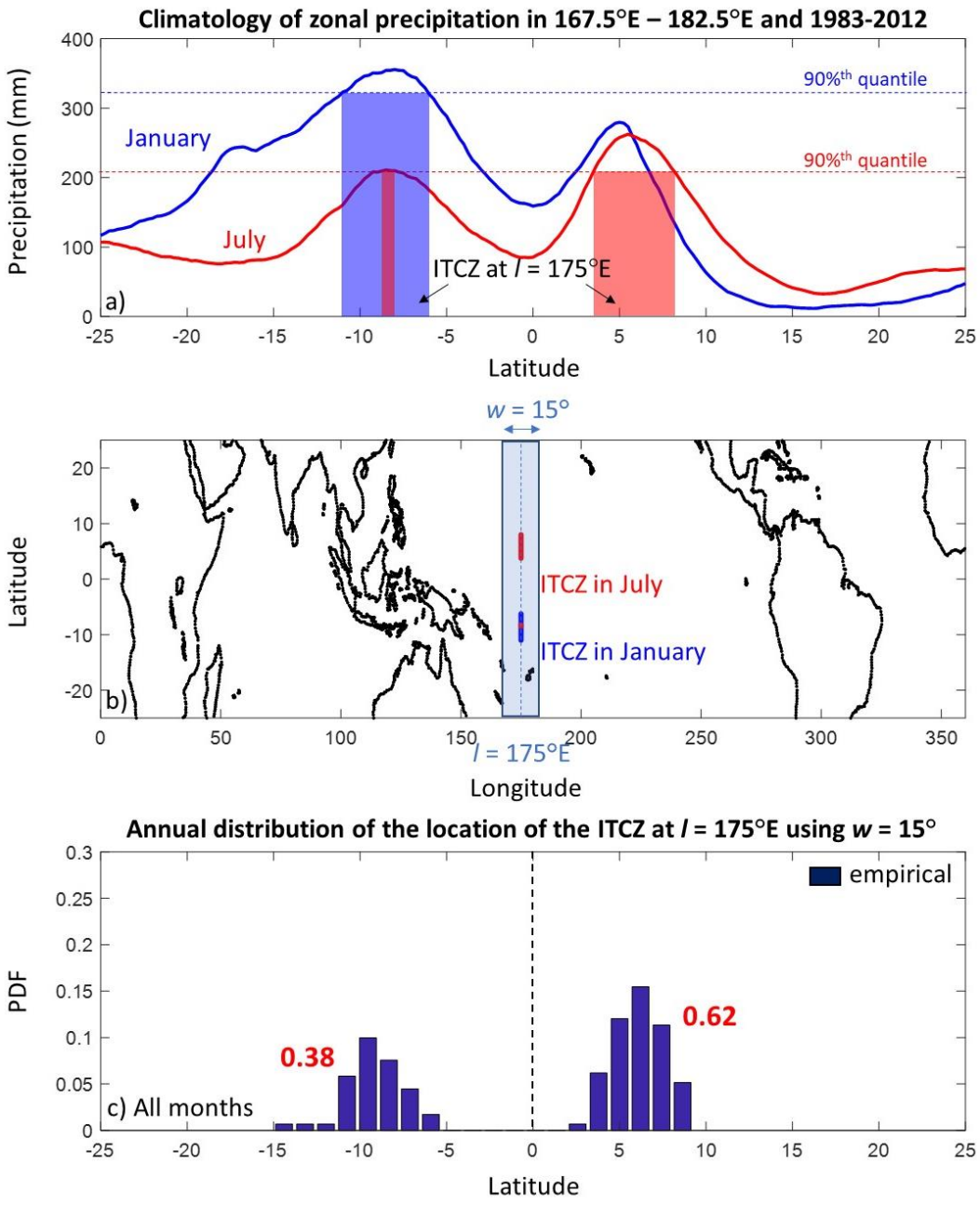

Figure 2.1. Probabilistic tracking of the ITCZ at longitude l = 175ºE, based on monthly precipitation (from PERSIANN-CDR). a) The zonal precipitation (167.5ºE – 182.5ºE) in January (blue curve) and July (red curve) for 1983-2012 (climatological means are presented). b) The location of the ITCZ in January (t = 1) and July (t = 7) at longitude l = 175º, using a longitudinal window of width w = 15º, and probability of non-exceedance a = 90%. It is shown that in July, the ITCZ is tracked in both hemispheres (double ITCZ). c) Annual probability density function (PDF) of the location of the ITCZ at longitude l = 175ºE, using "ITCZ points" obtained in each calendar month (t = 1, 2, ..., 12). The probability of ITCZ residing in the northern (southern) hemisphere during the year is 0.62 (0.38).

Let X denote the variable (e.g. precipitation) used for defining the ITCZ location, and $X_w^{l,t}$ the zonal average of X within the longitudinal window [l-w/2, l+w/2] of width w and during month/season t. The latitudinal distribution of $X_w^{l,t}$ can be obtained from observations or model outputs (see example in Figure 2.1a). For a specified probability of non-exceedance a, we define $x_{w,a}^{l,t}$ to be the a^{th} quantile of $X_w^{l,t}$, i.e.,

$$F\left(x_{w,a}^{l,t}\right) \equiv \Pr\left[X_w^{l,t} \le x_{w,a}^{l,t}\right] = a$$

where F is the cumulative distribution function (CDF) of $X_w^{l,t}$. We define the random variable $Y_{w,a}^{l,t}$to be the location (in degrees of latitude) at which the ITCZ is most likely to prevail, in longitude l, and in month/season t. A sample of $Y_{w,a}^{l,t}$ may then be the set of latitudinal points $y_{w,a}^{l,t}$(hereafter labeled as "ITCZ points") at which the value of $X_w^{l,t}$ exceeds the a^{th} quantile $x_{w,a}^{l,t}$, that is:

$$\left\{y_{w,a}^{l,t}\right\}:\ X_w^{l,t}\left(y_{w,a}^{l,t}\right) > x_{w,a}^{l,t} = F^{-1}(a) \qquad \text{or}$$

$$\left\{y_{w,a}^{l,t}\right\}:\ F\left(X_w^{l,t}\left(y_{w,a}^{l,t}\right)\right) > a \qquad (8)$$

In other words, we track the position of ITCZ based on the upper (1 - a)×100% of the zonal precipitation in longitude l and month/season t, using the points $y_{w,a}^{l,t}$ (see example in Figure 2.1a-b). When considering the OLR to track the ITCZ, the negative zonal OLR is used, since deep convection associates with minimum (not maximum) OLR. Such an approach is rather computationally efficient and allows the analysis of both the mean annual location and the intra-annual variability of the ITCZ, simply by obtaining the "ITCZ points", $y_{w,a}^{l,t}$, for each calendar month t = 1, 2, …, 12 (see Figure 2.1c) or each season.

When jointly considering multiple (e.g. $N \ge 2$) variables $\mathbf{X} = [X_1, X_2, \ldots, X_N]$ to track the ITCZ, the "ITCZ points", $y_{w,a}^{l,t}$, also satisfy Equation (8), but F is now the joint CDF of $\mathbf{X}_w^{l,t}$. This joint CDF can be estimated using copulas which offer the flexibility to express the joint distribution of multiple variables in terms of the quantiles of their marginal distributions (e.g., Nelsen, 1998; Salvadori and De Michele, 2007). Figure 2.2 illustrates an example where zonal precipitation and negative zonal OLR have been jointly used (i.e. N = 2) to detect the

location of the ITCZ during January (i.e. t = 1), at longitude l = 175ºE (and with w = 15º), in the period 1983-2012 (the latter is the period which all datasets cover; see Table S1). Note that in order to obtain results for the entire period, we have used the climatological mean precipitation and OLR (see also Figure 2.1). In this example, the zonal precipitation and –OLR are strongly correlated (r = 0.98) as indicated by the scatter plot and the copula function (see Figure 2.2b-c), which means that the ITCZ is well defined, and similar results would have been obtained by using the marginal distribution of either variable. Yet, this is not the case in all longitudes or seasons, and thus, the use of joint statistics becomes necessary. Using a = 90%, the ITCZ in January is located close to 10ºS (Figure 2.2d). By obtaining the samples $y_{15,90\%}^{175,t}$ for each calendar month t = 1, 2, …, 12, the annual distribution of the location of the ITCZ is obtained (see Figure 2.2e). It is shown that during the year, the ITCZ is more likely to be established in the northern hemisphere with probability 58%. Moreover, its annual average location is at 1ºN, while its intra-annual variability (defined here as twice the st. deviation of the distribution of the "ITCZ points", and measured in degrees of latitude) is about 15 degrees of latitude. The use of the st. deviation to quantify the intra-annual variability of ITCZ is preferred here against more complicated metrics (like the bimodal separation) which may be sensitive to outliers.

The proposed framework is physically motivated, straightforward, and flexible in its implementation. Moreover, by using different values of the parameters N, w, and a, the sensitivity of the results for a considered problem (regional analysis of ITCZ dynamics, analysis of trends, etc) can be investigated. Next we use the proposed framework to analyze the climatology of the ITCZ in the entire globe in the period 1983-2012, and the trends in the location of the ITCZ since the mid 20th century. For this purpose, we choose here to use N = 2 (precipitation and OLR), w = 15º and a = 90% (or in some cases a = 85%). The choice of w = 15º is important, since larger longitudinal windows (e.g. w > 30º) may not allow the tracking of non-zonal (diagonal) ITCZ features like the SPCZ, SICZ and SACZ. However, we note that depending on the region, season, scale, and scope of the investigation, future analysts may decide to use different/more variables (e.g. cloud cover, divergence, diabatic heating, pressure, vertical velocity, and/or a joint combination of them), different width of

the longitudinal window *w*, and different probability of non-exceedance *a*, to define the ITCZ, and no universally optimal values of these parameters exist.

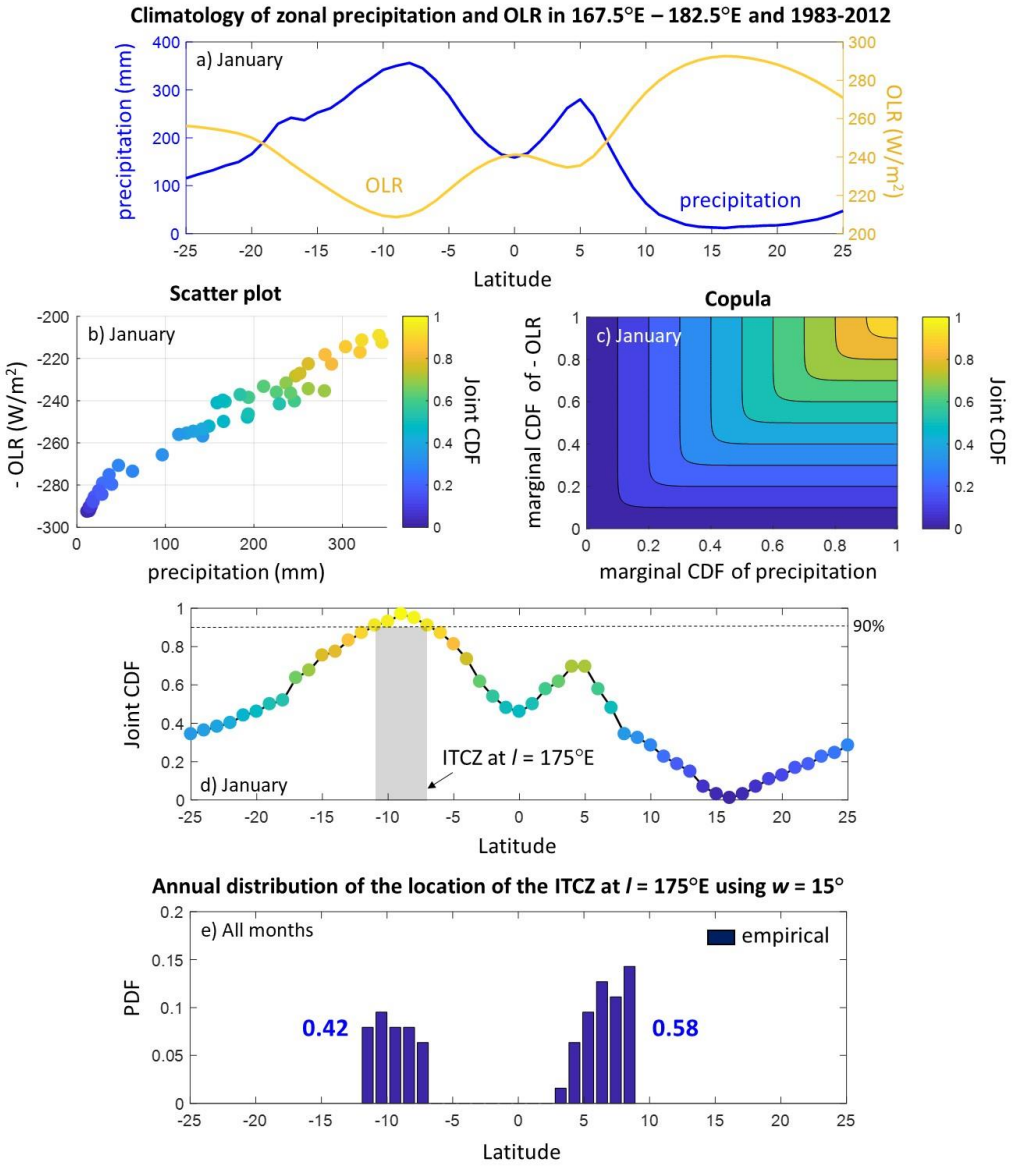

Figure 2.2. Probabilistic tracking of the ITCZ at longitude l = 175ºE, based on the joint distribution of the monthly precipitation and OLR. a) The zonally averaged (167.5ºE - 182.5ºE) precipitation (blue curve; from PERSIANN-CDR) and OLR (orange curve; from PSD-CDR) in January, 1983-2012 (climatological means are presented). b) Scatter plot of the points in (a). Coloring indicates the value of the joint cumulative distribution function (CDF) of precipitation and – OLR. c) The joint distribution is modelled using the Frank copula. d) The value of the joint CDF of precipitation and – OLR as a function of latitude. The location of the ITCZ is also indicated based on the probability of non-exceedance a = 90%. e) Annual probability density function (PDF) of the location of the ITCZ at longitude l = 175ºE, using "ITCZ points" obtained in each calendar month (t = 1, 2, …, 12). For a = 90%, five "ITCZ points" are tracked in each calendar month; see e.g. panel (d). The probability of ITCZ residing in the northern (southern) hemisphere during the year is 0.58 (0.42).

Recent climatology of the ITCZ. By obtaining the samples $y_{15,90\%}^{l,t}$ in all longitudes l = 0º, r_l, 2 r_l, …, 360º – r_l (r_l is the longitudinal resolution), and all calendar months t = 1, 2, …, 12 (we use climatological mean precipitation and OLR for each calendar month), the seasonal and annual distributions and basic statistics of the location of the ITCZ in the entire globe are obtained for the period 1983-2012 (Figures 2.3 and 2.4). Results are generally consistent using either precipitation or OLR, with slight discrepancies being apparent over the Indian ocean and east Asia (compare Figure 2.4a to 2.4b). When using OLR, some outliers are obtained over Mexico, and generally, the results when jointly considering both precipitation and OLR are more robust (see Figure 2.3).

Our results are consistent with the known physics of the ITCZ. Concerning the intra-annual variability, our framework shows that the ITCZ is more migratory over continental regions (compare Figures 2.3a-b and see Adam et al., 2016a,b), with the deep convection zone being mostly evident in the northern hemisphere during Apr-Sep (Figure 2.3a), and migrating to the south mainly over Africa and America, during Oct-Mar (Figure 2.3b). Also, the SPCZ is shown to increase in strength during Oct-Mar; note for example, that during Apr-Sep, the subtropical part of the SPCZ is not tracked (see also Figure 1 in Waliser and Gautier, 1993; Figures 2, 4, 5 and 8 in Trenberth, 2000; Figure 1 in Widlansky et al., 2011; and Figure 1 in Adam et al., 2016a,b). Both these remarks are in accordance with the suggestion that the ITCZ collocates with the trough of global monsoon, which seasonally follows solar heating (Trenberth, 2000).

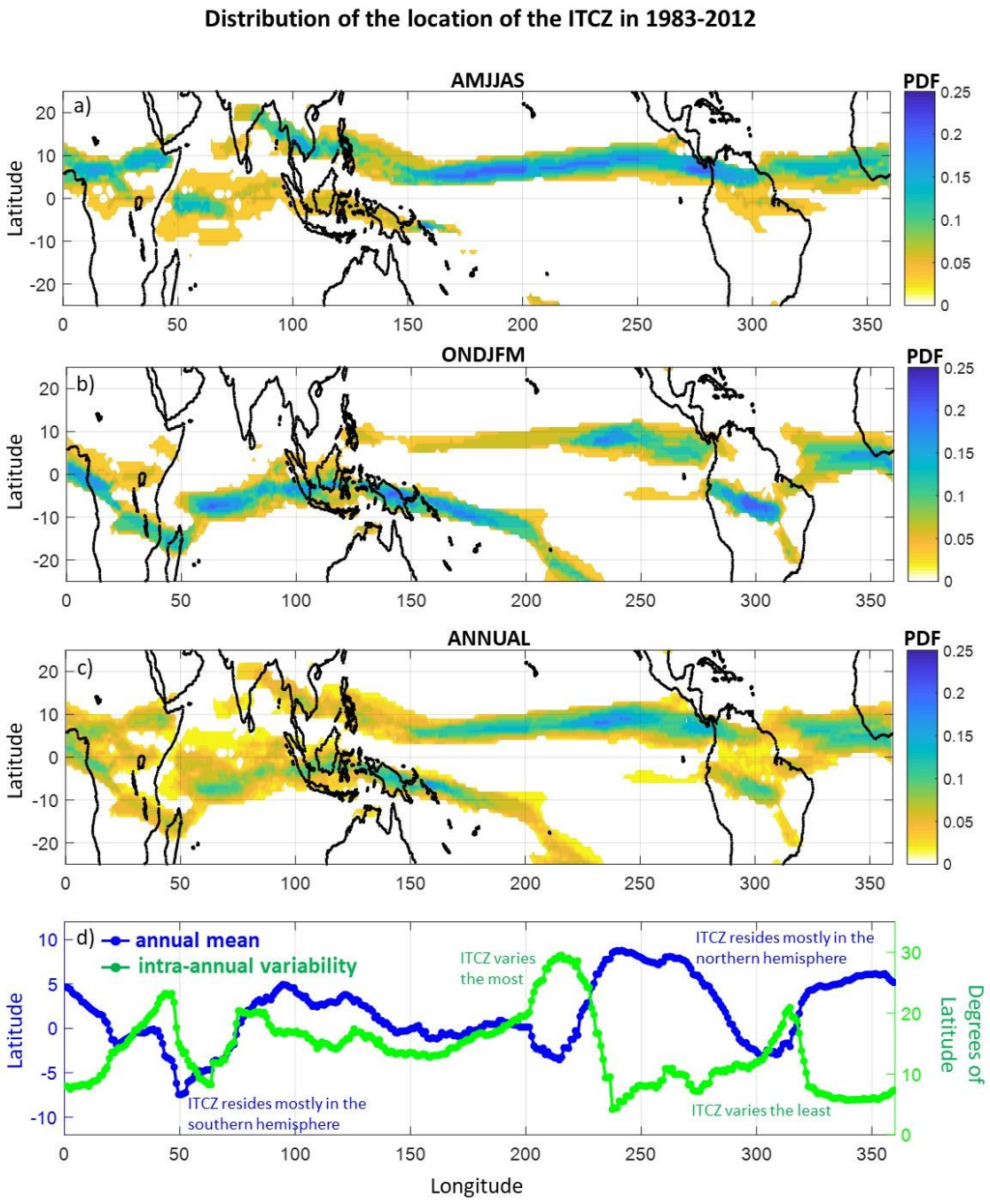

Figure 2.3. The location of the ITCZ around the globe in 1983-2012. a) The empirical probability density function (PDF) of the location of the ITCZ during Apr-Sep, as computed in overlapping longitudinal windows of width w = 15º, based on the upper 10% (probability of non-exceedance a = 90%) of the joint distribution of zonal precipitation (from PERSIANN-CDR) and zonal – OLR (from PSD-CDR); we use the long-term climatology of precipitation and OLR in each month, see also Figure 2.2. b) Same as in (a), but for Oct-Mar. c) Same as in (a), but the annual distribution is presented. d) The annual mean (blue color) and the intra-annual variability (twice the st. deviation of the distribution of the "ITCZ points"; green color) of the location of the ITCZ as a function of longitude.

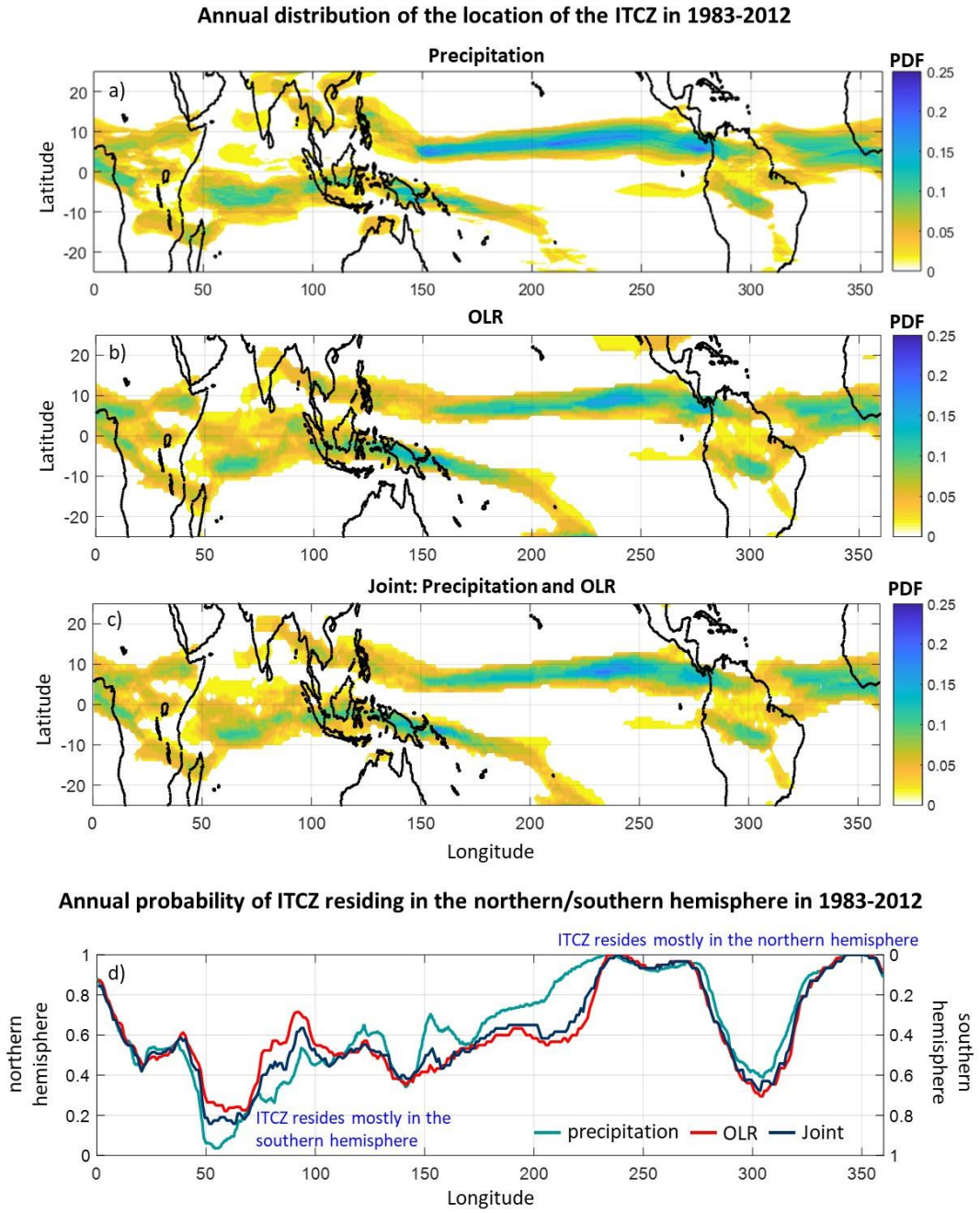

Figure 2.4. Location of the ITCZ in 1983-2012 as defined using multiple physical variables. a) The empirical annual probability density function (PDF) of the location of the ITCZ computed in overlapping longitudinal windows of width w = 15º and probability of non-exceedance a = 90%, using zonal precipitation (from PERSIANN-CDR). b) Same as in (a), but using zonal – OLR (from PSD-CDR). c) Same as in (a), but using the joint distribution of precipitation and – OLR. d) The probability of ITCZ residing in the northern/southern hemisphere as a function of longitude, in 1983-2012, based on satellite observations of precipitation (green color; data from PERSIANN-CDR), OLR (red color; data from PSD-CDR) and their joint distribution (dark blue color).

Concerning the longitudinal variability, the ITCZ resides in the northern hemisphere (Philander et al., 1996), apart from the area of the Indian and the western Pacific Oceans, and the Amazon (see Figures 2.3 and 2.4). Over Indian Ocean, the ITCZ is positioned in the southern hemisphere during most of the year (see Figures 2.3d, 2.4d and Waliser and Gautier, 1993), while in boreal summer, it is difficult to define, as its interaction with the Indian monsoon is still under debate (note the noisy patterns over India in Figure 2.3a and S2.a). Particularly, although the traditional view is that the Indian monsoon is driven by land-sea thermal contrast, recent studies support that it is a manifestation of the seasonal migration of the ITCZ towards India (Chao and Chen, 2001; Gadgil, 2003; Fleitmann, et al., 2007; Bordoni and Schneider, 2008). In the western and central Pacific, the ITCZ consists of two distinct and much distant zones, the northern ITCZ and the SPCZ, which co-exist almost year-round, however, with high intra-annual variability in their strengths (see Figure 2.3d and Waliser and Gautier, 1993). As proposed recently by Mamalakis et al. (2018), the large intra-annual variability of the ITCZ and of the overturning meridional circulation (see Figures 2, 5 and 8 in Trenberth, 2000) over the western and central Pacific can establish interhemispheric connections through the accompanied expansion of the regional Hadley cell (atmospheric bridge; see also Alexander et al., 2002 and Liu et al., 2010). Accordingly, studies suggest that the longitudinal zone around the globe where the most significant interhemispheric interaction occurs is the region of east Australia to east Asia (Tao and Xu, 1962; Wang and Zhao, 1987; Liu et al., 2010). Over the eastern Pacific and Atlantic Oceans, observations suggest that the ITCZ is least variable (Figure 2.3d), tending to stay in the northern hemisphere during the whole year (see Figure 2.4d and Waliser and Gautier, 1993), although a double ITCZ may form during boreal spring in the eastern Pacific (see Figure 2.3 and Haffke et al., 2016; Yang and Magnusdottir; 2016; Bischoff and Schneider, 2016; Adam et al., 2016b).

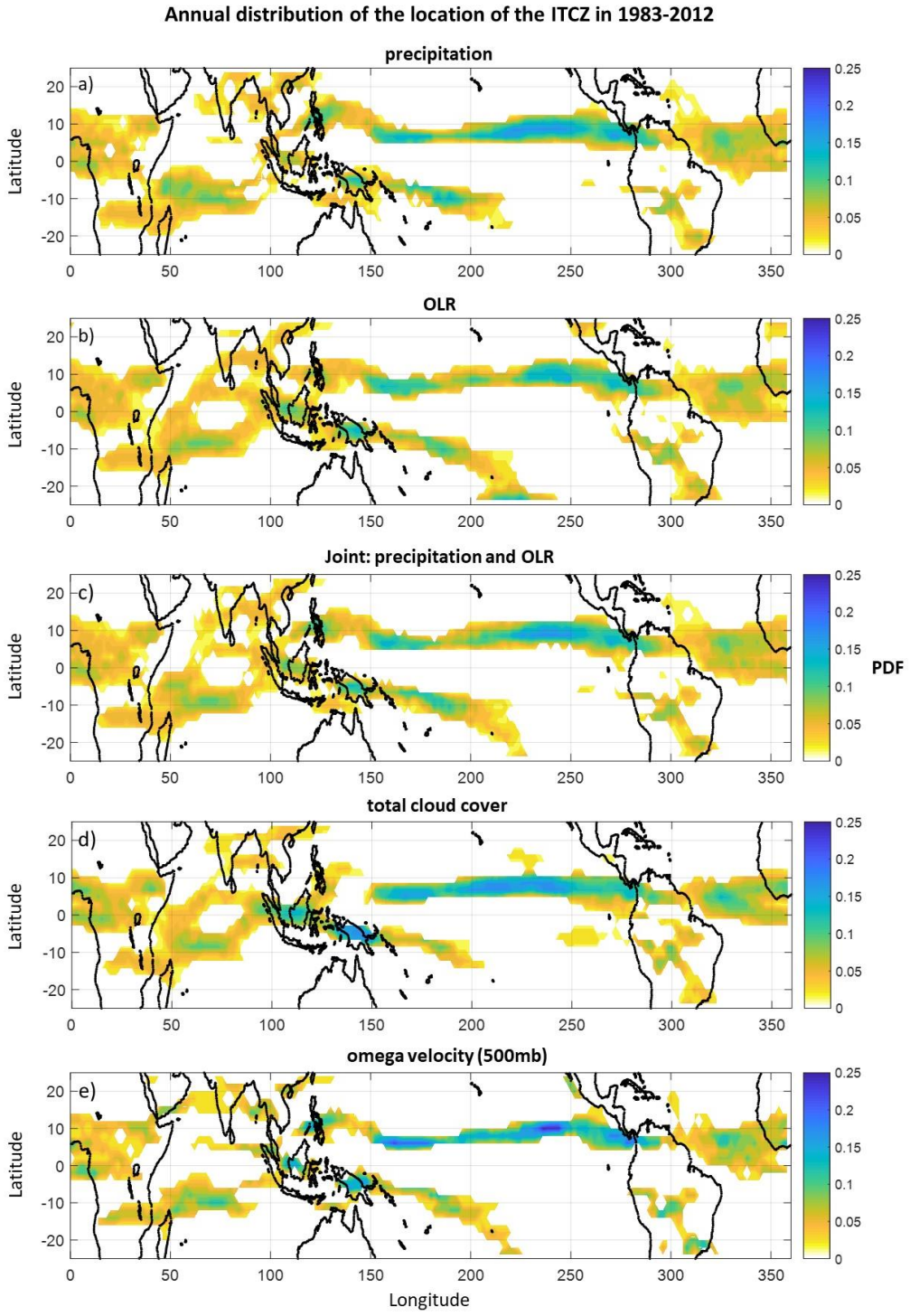

Figure 2.5. Same as Figure 2.4, but using monthly products from the 20CR dataset; w = 15º, a = 90%. a-e) The location of ITCZ is defined using precipitation, OLR, the joint distribution of precipitation and – OLR, total cloud cover, and omega velocity at the 500 mb level (upward motion corresponds to negative omega velocity), respectively. The cloud cover is obtained by considering the entire atmosphere as a single layer.

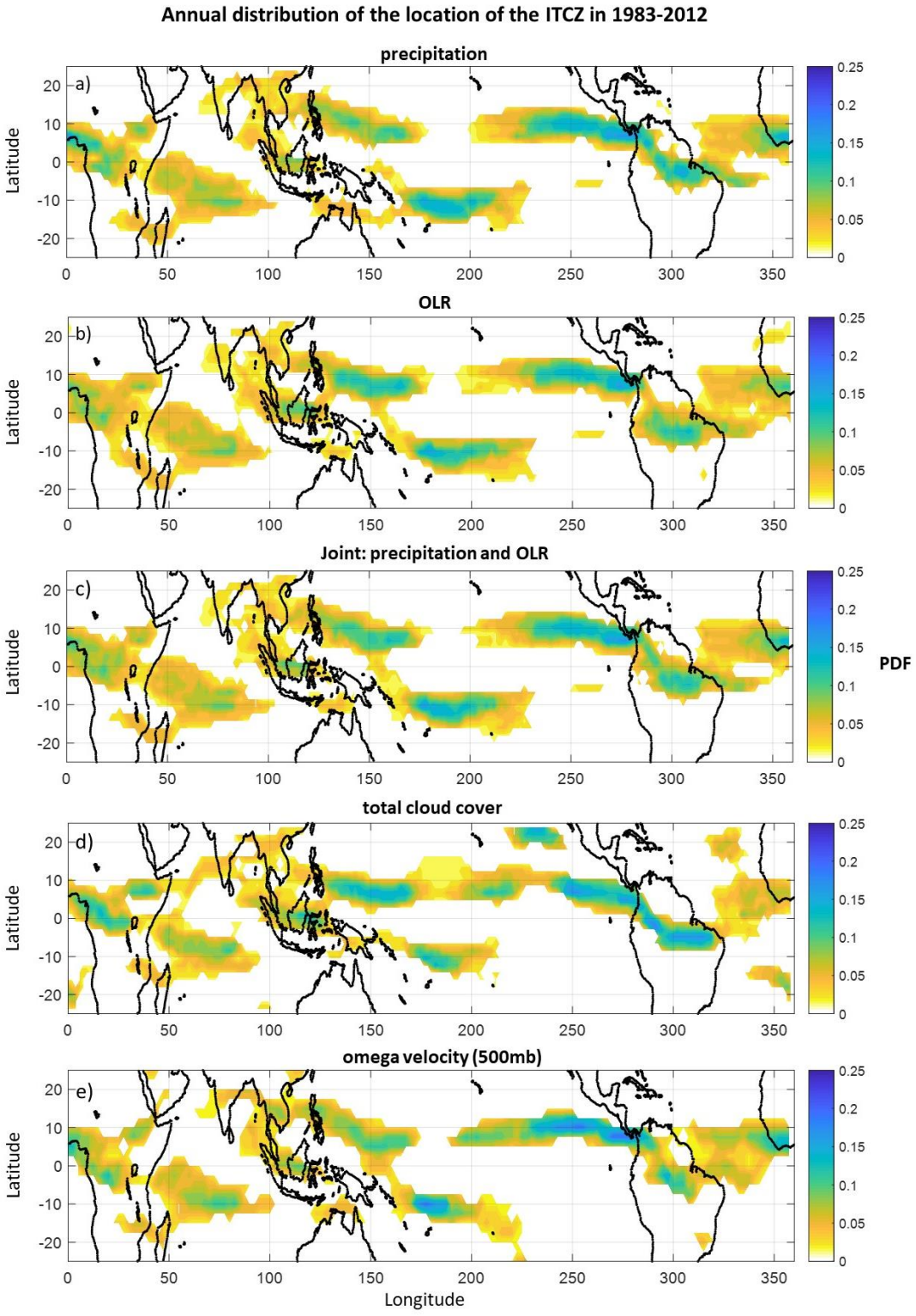

Figure 2.6. Same as Figure 2.5, but using monthly products from the NCEP/NCAR dataset.

The ITCZ climatology has also been obtained based on monthly products from the 20CR and the NCEP/NCAR datasets (see Figure 2.5 and 2.6, respectively). Particularly, to illustrate the generality of our framework, we have used many different variables to track the ITCZ (i.e. precipitation, OLR, joint statistics of precipitation and OLR, total cloud cover and omega velocity), and the corresponding distributions of the location of ITCZ are shown to be very similar with that presented in Figure 2.3, especially when using products from the 20CR dataset. The general agreement of the results in Figures 2.3-2.6, indicates the effectiveness of the reanalysis datasets in capturing the ITCZ dynamics, and thus, their suitability to be used in assessing decadal changes in the ITCZ location.

Another important result is that when one investigates the annual distribution of the ITCZ based on season by season analysis in 1983-2012 (i.e. t = 1, 2, …, 119), or month by month analysis (i.e. t = 1, 2, …, 320), results are very similar (see Figure 2.7a-b and 2.8, respectively) to the case of using monthly climatology of precipitation and OLR (Figure 2.3), indicating the robustness and consistency of our framework. However, we note that in months when the MJO is active, it may introduce biases in the tracking of the ITCZ, thus, the seasonal tracking is more accurate.

The physical consistency of the tracking framework is also illustrated by exploring the effect of El Niño-Southern Oscillation (ENSO) on the ITCZ location. As an example, Figure 2.7c presents the sampled "ITCZ points" in all seasons in 1983-1992, at l = 175ºE. Our results show that in almost all seasons two ITCZs are tracked (one in each hemisphere; the northern ITCZ and the SPCZ), and reveal a dependence between the ENSO and the location of the SPCZ in the central/western Pacific (here at l = 175ºE), as shown by the co-variation of the latter with the series of the Niño 3.4 index. It is shown that during El Niño (La Nina) years, the derived "ITCZ points" are located northern (southern) than average (see for example Trenberth and Shea, 1987; Widlansky et al., 2011; Berry and Reeder, 2014; Adam et al., 2016a,b).

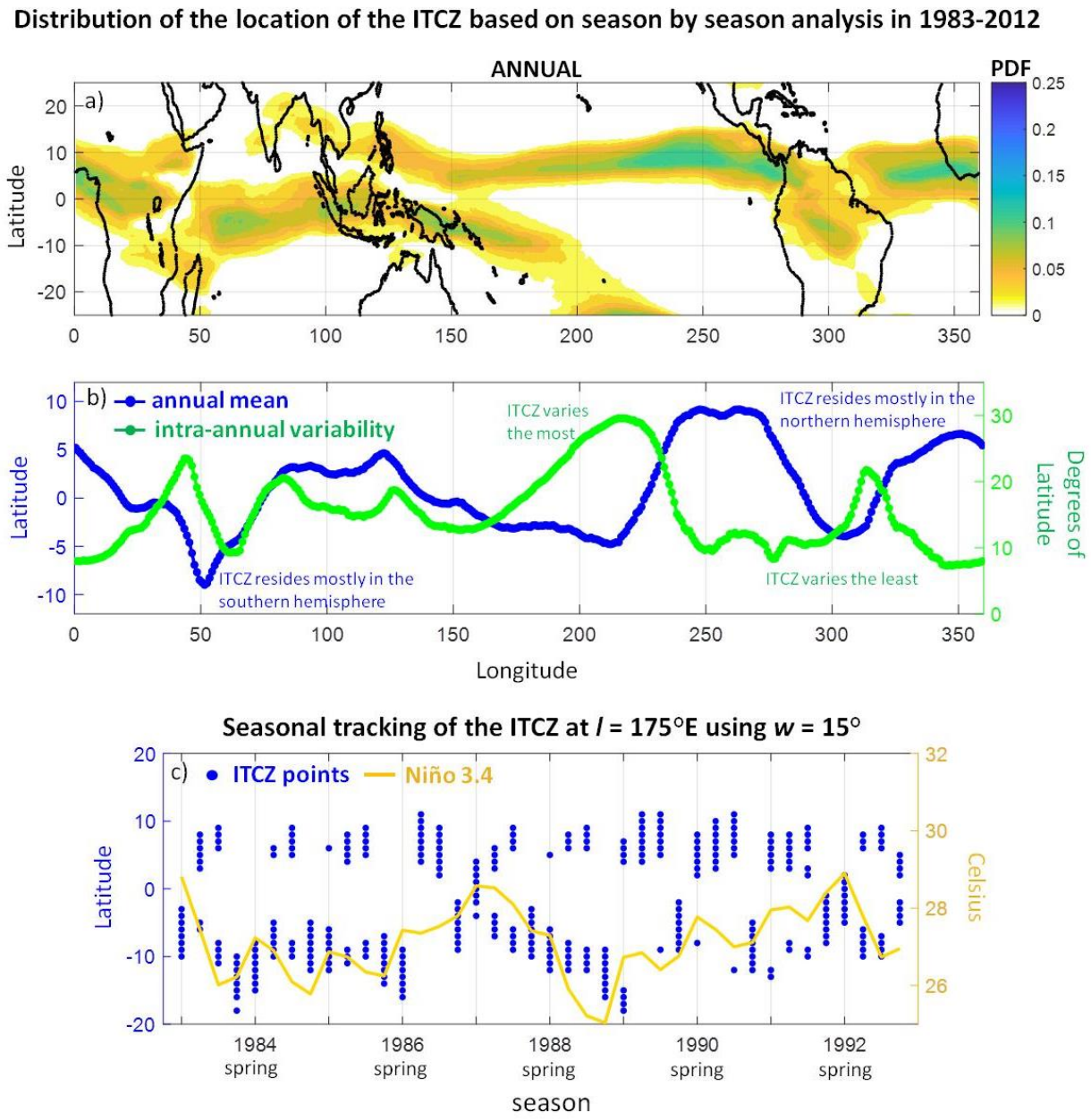

Figure 2.7. Seasonal tracking of the ITCZ. a-b) Same as in Figure 2.3c-d, but using all 119 seasons in 1983-2012 (winter of 1983 is excluded); w = 15°, a = 85%. c) The sampled "ITCZ points" (blue points) in all seasons of 1983-1992, based on the upper 15% (probability of non-exceedance a = 85%) of the joint distribution of zonal precipitation and – OLR, at longitude l = 175ºE (using w = 15º). To indicate the effect of the El Niño-Southern Oscillation on the location of the SPCZ (here corresponding to the "ITCZ points" in the southern hemisphere), we also present seasonal series of Niño 3.4 (the scale in the right vertical axis was chosen so that the series of Niño 3.4 can be co-displayed with the "ITCZ points").

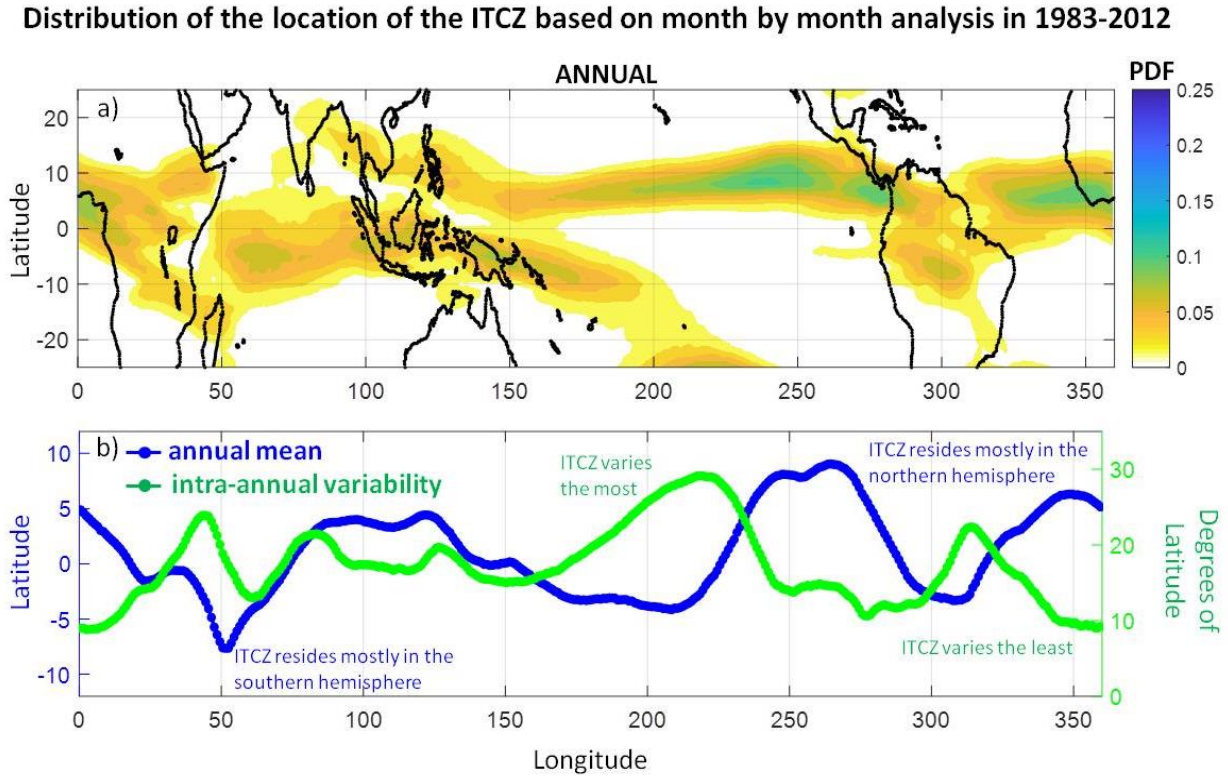

Figure 2.8. Same as Figure 2.7a-b, but using all 320 months in 1983-2012.

ITCZ trends. Time series (2-yr averages of the seasonal series) of the location of the ITCZ for the entire globe and for the period 1948-2014 are presented in Figure 2.9, based on reanalysis products from the 20C dataset (Figure 2.9a) and the NCEPNCAR dataset (Figure 2.9b). Generally, there are evident changes in several regions, with the most prominent and consistent (i.e. identified in both reanalysis products) change being a southward shift/trend of ITCZ in the central and western Pacific Ocean (see also Berry and Reeder, 2014). Specifically, differences in the distribution of the location of the ITCZ in the period 1991-2010 relative to the period 1951-1970 clearly indicate the southward shift, which is more profound in the results of NCEP/NCAR (see Figure 2.9c-d). In terms of annual precipitation, a similar southward shift has been reported and studied in the literature. Particularly, during the late 20th century, the tropical rainbelt shifted southward, due to the decrease of the interhemispheric temperature gradient (Friedman et al.,2013; Hwang et al., 2013; Polson et al., 2014; Allen et al., 2015; Chung and Soden, 2017). The latter was mainly driven by the increased anthropogenic release of sulfate aerosols in the northern hemisphere, which

counteracted the effect of the greenhouse gases (Friedman et al., 2013) and altered the cloud radiative properties (Hwang et al., 2013; Chung and Soden, 2017), making the north-to-south temperature difference decrease. Our results clearly support these precipitation trends, but we additionally report similar changes when the ITCZ is defined using OLR and/or multiple variables (note that similar trends are obtained when using total cloud cover and omega velocity to define the ITCZ from either reanalysis dataset; not shown here). More particularly, over the region of 150º E - 220º E, results derived from the 20CR dataset indicate southward trends from -0.5 to -1 degrees of latitude per decade, while the NCEP/NCAR results indicate trends from -1 to -1.5 degrees of latitude per decade (see Figure 2.10a). Time series for a specific longitude l = 200º E are also presented (see Figure 2.9e), and results from applying a simple linear regression (considering also the autocorrelation of the series) confirm the statistical significance of the trends.

Conclusions. Due to its high importance in water resources management and sustainability of ecosystems in tropical and subtropical regions, efficient tracking of the changes in the seasonal and decadal dynamics of the ITCZ at different longitudes is necessary. In the light of the limitations of existing approaches, here we proposed and applied a new probabilistic framework which facilitates detailed analysis of changes in the seasonal dynamics of the ITCZ, and offers the ability to use multiple variables to define it, which adds to its physical rigor. Moreover, it is rather computationally efficient and flexible in its implementation, which makes it useful for the analysis of multi-model ensembles in climate change assessment studies.

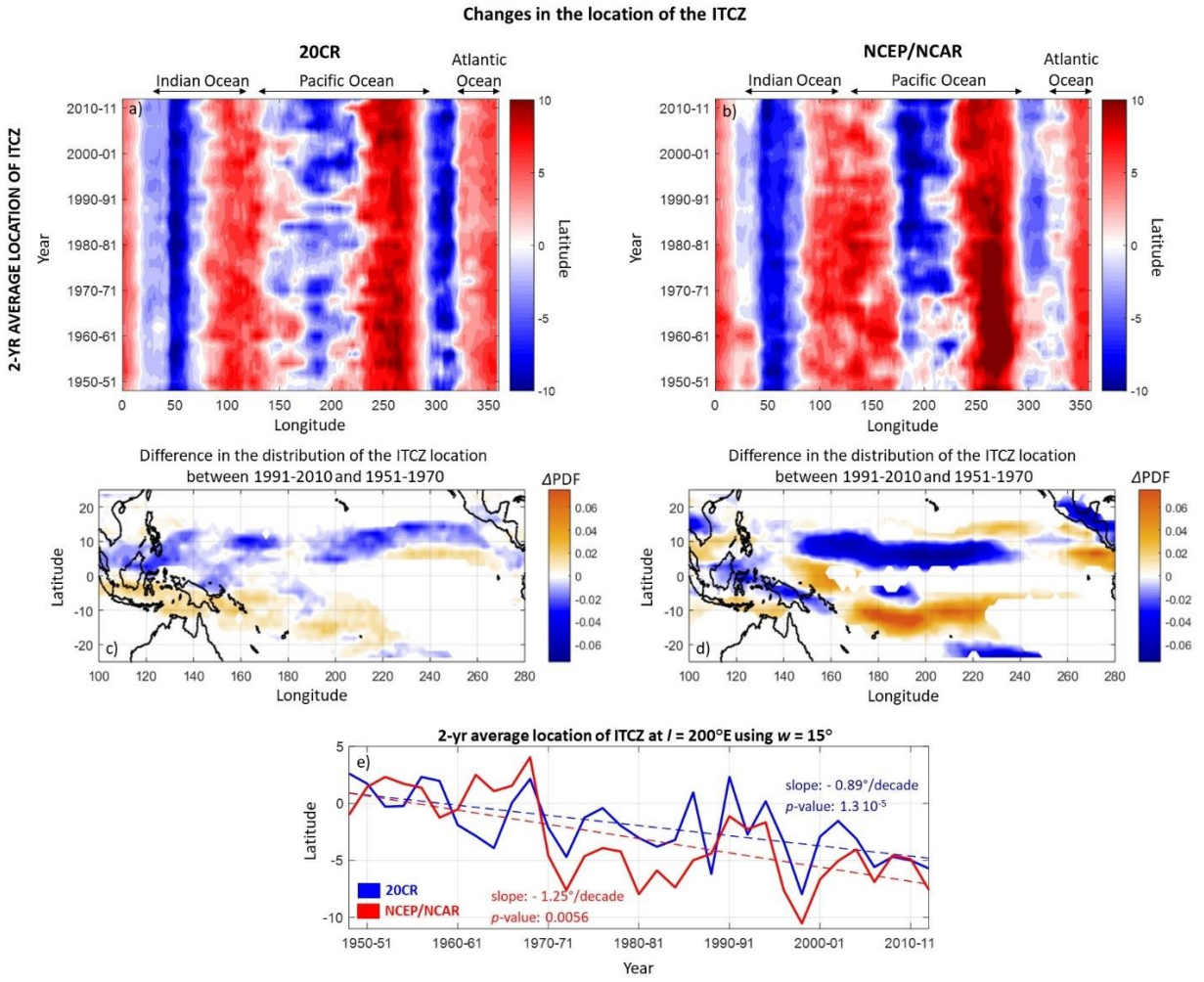

Figure 2.9. Changes in the location of the ITCZ. a) 2-yr average of the seasonal series of the location of the ITCZ as a function of longitude, for 1948-2014. The location of the ITCZ is obtained in each season using overlapping longitudinal windows of length w = 15°, based on the upper 15% of the joint distribution of zonal precipitation and – OLR. Data are from the 20CR dataset. b) Same as in (a), but data are from the NCEP/NCAR dataset. c) Difference in the probability distribution of the location of the ITCZ (*Δ*PDF) between the periods 1991-2010 and 1951-1970. Data are from the 20CR dataset. d) Same as in (c), but data are from the NCEP/NCAR dataset. The central Pacific region is where results from the two datasets show the most prominent trends, indicating a southward shift of the ITCZ. e) The ITCZ series at l = 200ºE (using w = 15º) and the corresponding linear trends.

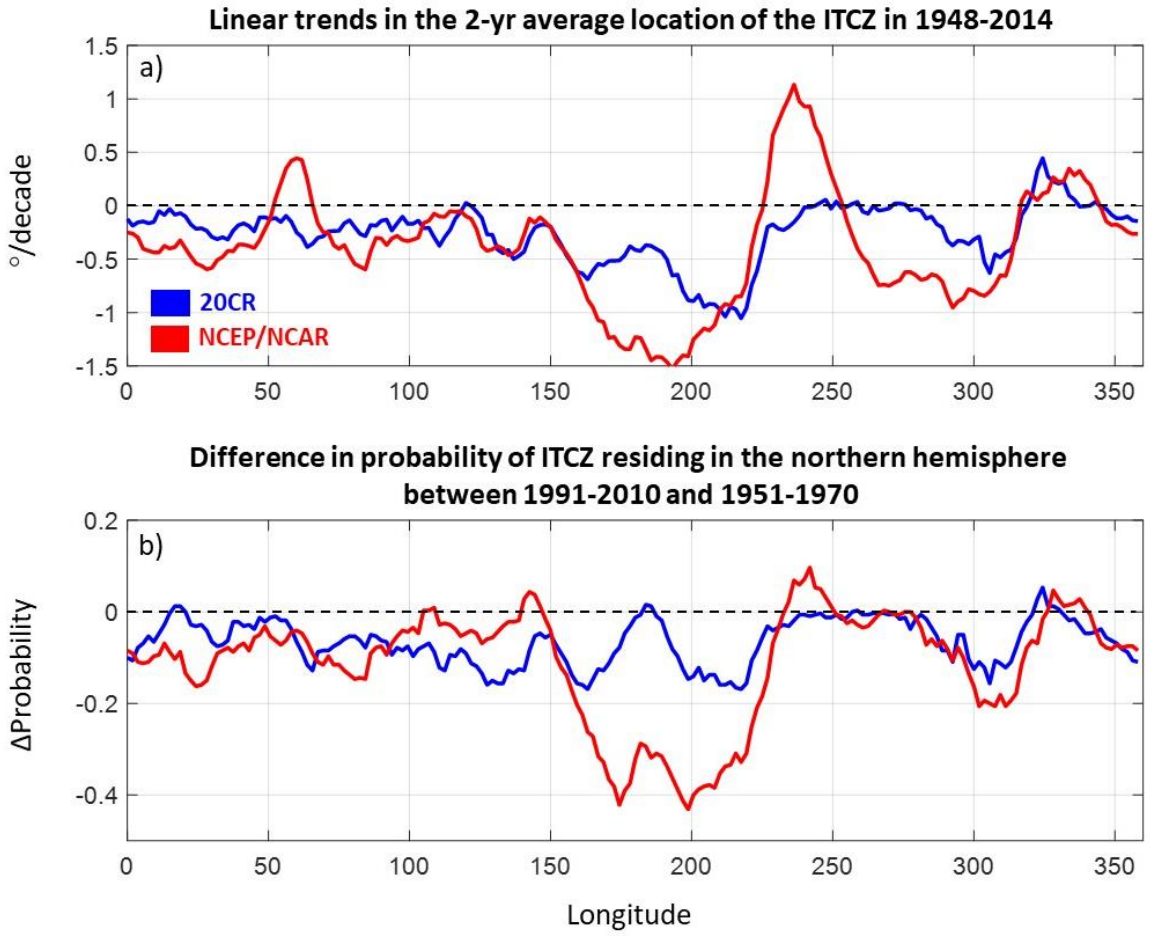

Figure 2.10. Trends and changes in the distribution of the location of the ITCZ. a) Linear trends of the 2-yr average location of the ITCZ in 1948-2014 as a function of longitude, using simple linear regression. b) The difference in probability of the ITCZ residing in the northern hemisphere, between periods 1991-2010 and 1951-1970. The central Pacific region is where results from the two datasets show the most prominent trends, indicating a southward shift of the ITCZ.

References

Adam O., T. Bischoff, T. Schneider (2016a) Seasonal and interannual variations of the energy flux equator and ITCZ. Part I: Zonally averaged ITCZ position, *J. Clim.*, **29**, 3219-3230. doi:10.1175/JCLI-D-15-0512.1

Adam O., T. Bischoff, T. Schneider (2016b) Seasonal and interannual variations of the energy flux equator and ITCZ. Part II: Zonally varying shifts of the ITCZ, *J. Clim.*, **29**, 7281-7293. doi:10.1175/JCLI-D-15-0710.1

Alexander, M. A., I. Blade, M. Newman, J.R. Lanzante, N.-C. Lau, J.D. Scott (2002) The Atmospheric Bridge: The Influence of ENSO Teleconnection on Air-Sea Interaction over the Global Oceans, *J. Clim.*, **15**, 2205-2231.

Allen, R. J. (2015) A 21st century northward tropical precipitation shift caused by future anthropogenic aerosol reductions, *J. Geophys. Res. Atmos.*, **120**, 9087–9102, doi:10.1002/2015JD023623.

Allen, R. J., A.T. Evan, B.B.B. Booth (2015) Interhemispheric aerosol radiative forcing and tropical precipitation shifts during the late twentieth century, *J. Clim.*, **28**, doi: 10.1175/JCLI-D-15-0148.1

Arbuszewski, J.A., P.B. deMenocal, C.Cléroux, L. Bradtmiller, A. Mix (2013) Meridional shifts of the Atlantic intertropical convergence zone since the Last Glacial Maximum, *Nature Geoscience*, **6**, doi: 10.1038/NGEO1961

Ashouri, H., K.L. Hsu, S. Sorooshian, D.K. Braithwaite, K.R. Knapp, L.D. Cecil, B.R. Nelson, and O.P. Prat (2015) PERSIANN-CDR: Daily Precipitation Climate Studies Data Record from Multisatellite Observations for /Hydrological and Climate Studies, *Bull. Amer. Meteor. Soc.*, **96**, 69-83, doi: http://dx.doi.org/10.1175/BAMS-D-13-00068.1.

Bain, C.L., et al (2011) Detecting the ITCZ in instantaneous satellite data using spatiotemporal statistical modeling: ITCZ climatology in the east Pacific, *J. Climate*, **24**, doi: 10.1175/2010JCLI3716.1

Berry, G., and M.J. Reeder (2014) Objective Identification of the Intertropical Convergence Zone: Climatology and Trends from the ERA-Interim *J. Climate*, **27**, DOI: 10.1175/JCLI-D-13-00339.1

Bordoni, S. and T. Schneider, (2008) Monsoons as eddy-mediated regime transitions of the tropical overturning circulation. *Nature Geosci.*, **1**, 515-519.

Bischoff, T. and T. Schneider (2014) Energetic constraints on the position of the intertropical convergence zone, *J. Clim.*, **27**, doi: 10.1175/JCLI-D-13-00650.1

Bischoff, T. and T. Schneider (2016) The equatorial energy balance, ITCZ position, and double-ITCZ bifurcations, *J. Clim.*, **29**, doi: 10.1175/JCLI-D-15-0328.1

Broccoli, A. J., K. A. Dahl, and R. J. Stouffer, 2006: Response of the ITCZ to Northern Hemisphere cooling. *Geophys. Res. Lett.,* **33,** L01702, doi:10.1029/2005GL024546.

Broecker, W.S., and A. E. Putnam (2013) Hydrologic impacts of past shifts of Earth's thermal equator offer insight into those to be produced by fossil fuel CO_2, *PNAS*, 110(42).

Carvalho, L.M., C. Jones, B. Liebmann (2004) The South Atlantic Convergence Zone: Intensity, Form, Persistence, and Relationships with Intraseasonal to Interannual Activity and Extreme Rainfall, *J. Climate*, **17**, 88-108.

Chao, W.C., and Chen, B. (2001) The origin of monsoons, *Journal of the Atmospheric Sciences*, **58**, 3497–3507.

Chiang, J. C. H. & Bitz, C. M. (2005) Influence of high latitude ice cover on the marine Intertropical Convergence Zone. *Clim. Dyn.*, **25**, 477–496

Chung, E.-S. and B.J. Soden (2017) Hemispheric climate shifts driven by anthropogenic aerosol-cloud interactions, *Nature Geoscience*, **10**, doi: 10.1038/NGEO2988

Compo, G. P., *et al.* (2011) Review Article, The twentieth century reanalysis project, *Q. J. R. Meteorol. Soc.* **137**, 1–28.

Cook, K.H. (1998) On the response of the Southern Hemisphere to ENSO. Proc 23rd Climate Diagnostics and Prediction Workshop, Miami, FL. American Meteorological Society, 323–326.

Cook, K.H. (2000) The South Indian Convergence Zone and interannual rainfall variability over southern Africa. J. Climate, 13, 3789-3804.

Donohoe, A., J. Marshall, D. Ferreira, and D. McGee (2013) The relationship between ITCZ location and cross-equatorial atmospheric heat transport: from the seasonal cycle to the last glacial maximum, *J. Clim.*, **26**, doi: 10.1175/JCLI-D-12-00467.1

Fleitmann, D., et al. (2007) Holocene ITCZ and Indian monsoon dynamics recorded in stalagmites from Oman and Yemen (Socotra), *Quaternary Science Reviews*, **26**, 170–188

Friedman, A.R., Y.-T. Hwang, J.C.H. Chiang, D.M.W. Frierson (2013) Interhemispheric temperature asymmetry over the twentieth century and in future projections, *J. Clim.*, **26**, doi: 10.1175/JCLI-D-12-00525.1

Gadgil, S., (2003) The Indian monsoon and its variability, *Annual Reviews of Earth and Planetary Sciences*, **31**, 429–467.

Graham, N.E., and T.P. Barnett (1987) Sea Surface Temperature, Surface Wind Divergence, and Convection over Tropical Oceans, *Science*, **238** (4827), 657-659.

Haffke, C., and G. Magnusdottir (2013) The South Pacific Convergence Zone in three decades of satellite images, *J. Geophys. Res. Atmos.*, **118**, doi:10.1002/jgrd.50838.

Haffke, C. and G. Magnusdottir (2015) Diurnal cycle of the South Pacific Convergence Zone in 30 years of satellite images, *J. Geophys. Res. Atmos.*, **120**, 9059-9070

Haffke, C., G. Magnusdottir, D. Henke, P. Smyth, Y. Peings (2016) Daily states of the March-April east Pacific ITCZ in three decades of high-resolution satellite data, *J. Clim.*, 29, doi: 10.1175/JCLI-D-15-0224.1

Hwang, Y.-T, D.M.W. Frierson, and S.M. Kang (2013) Anthropogenic sulfate aerosol and the southward shift of tropical precipitation in the late 20th century, *Geoph. Res. Lett.*, **40**, doi:10.1002/grl.50502

Kalnay et al., (1996), The NCEP/NCAR 40-Year Reanalysis Project, *BAMS*, **77**(3), 437-471

Kang, S. M., Held, I. M., Frierson, D. M. W. & Zhao, M. (2008) The response of the ITCZ to extratropical thermal forcing: idealized slab-ocean experiments with a GCM. J. Clim. 21, 3521–3532.Lee, H.-T., (2014) Climate Algorithm Theoretical Basis Document (C-ATBD): Outgoing Longwave Radiation (OLR) - Daily. NOAA's Climate Data Record (CDR) Program, CDRP-ATBD-0526, 46 pp.

Liu, G., L. Ji, S. Sun, and Q. Zhang (2010) An inter-hemispheric teleconnection and a possible mechanism for its formation, *Advances in Atmospheric Sciences*, **27**(3), 629-638.

Madden, R. A., and P. R. Julian (1971) Detection of a 40 – 50 day oscillation in the zonal wind in the tropical Pacific, *J. Atmos. Sci.*, **28**, 702 – 708.

Mamalakis, A., J.-Y. Yu, J.T. Randerson, A. AghaKouchak, and E. Foufoula-Georgiou (2018) A new interhemispheric teleconnection increases predictability of winter precipitation in southwestern US, *Nature Communications*, DOI: 10.1038/s41467-018-04722-7.

Nelsen, R.B. (1998) An Introduction to Copulas, Lecture Notes in Statistics, 139, Spinger-Verlag, New York.

Nicholson, S. E. (2009) A revised picture of the structure of the "monsoon" and land ITCZ over west Africa, *Clim Dyn*, **32**, 1155–1171

Nicholson, S. E. (2018) The ITCZ and the seasonal cycle over equatorial Africa, *BAMS*, doi: 10.1175/BAMS-D-16-0287.1

Philander, S. et al. (1996) Why the ITCZ is mostly north of the equator, *J. Clim.*, **9**, 2958–2972.

Polson, D., M. Bollasina, G. C. Hegerl, and L. J. Wilcox (2014), Decreased monsoon precipitation in the Northern Hemisphere due to anthropogenic aerosols, *Geophys. Res. Lett.*, **41**, 6023–6029, doi:10.1002/2014GL060811.

Sachs, J.P., D. Sachse, R.H. Smittenberg, Z. Zhang, D.S. Battisti, and S. Golubic (2009) Southward movement of the Pacific intertropical convergence zone AD 1400-1850, *Nature Geoscience*, **2**, doi: 10.1038/NGEO554

Salvadori, G., C. De Michele (2007) On the use of copulas in hydrology: theory and practice, *J. Hydrol. Eng.*, **12**(4), 369-380.

Schneider, T., T. Bischoff, and G. H. Haug (2014) Migrations and dynamics of the intertopical convergence zone, *Nature*, **513**, doi:10/nature13636

Tao, S. Y., and S. Y. Xu (1962) The characteristics of the zonal and meridional circulation over tropical and subtropical regions in eastern Asia in summer. *Acta Meteorologica Sinica*, **32**, 91–103. (in Chinese)

Trenberth, K.E., D.J. Shea (1987) On the evolution of the Southern Oscillation, *Mon. Weater Rev.*, **115**, 3078-3096

Trenberth, K. E., D. P. Stepaniak and J. M. Caron (2000) The global monsoon as seen through the divergent atmospheric circulation, *J. Climate*, **13**, 3969-3993.

Trenberth, K. E., (2011) Changes in precipitation with climate change, *Climate Research*, **47**, 123-138, doi: 10.3354/cr00953

Waliser, D.E., and C. Gautier (1993) A Satellite-derived Climatology of the ITCZ, *J. Clim.,* **6**, 2162–2174

Waliser, D.E. and R. C. J. Somerville (1994) Preferred Latitudes of the Intertropical Convergence Zone, *Journal of the Atmospheric Sciences*, **51**(12), 1619-1639.

Wang, S. W., and Z. C. Zhao (1987) The interaction between the two hemispheres and long-term forecasting, *Foundation of Long-term Weather Forecasting*, Shanghai Science & Technology Press, Shanghai, 116–130. (in Chinese)

Widlansky, M. J., P. J. Webster, C. D. Hoyas (2011) On the location and orientation of the South Pacific Convergence Zone. *Clim. Dyn.*, DOI: 10.1007/s00382-010-0871-6.

Yang, W. and G. Magnusdottir (2016) Interannual signature in daily ITCZ states in the east Pacific in boreal spring, *J. Clim.*, 29, doi: 10.1175/JCLI-D-16-0395.1

Zhang, G., and Z. Wang (2015), Interannual variability of tropical cyclone activity and regional Hadley circulation over the Northeastern Pacific, *Geophys. Res. Lett.*, **42**, 2473–2481, doi:10.1002/2015GL063318.

2.2. Zonally contrasting shifts of the intertropical convergence zone in response to climate change

This chapter is currently under review

Citation: Mamalakis, A., J.T. Randerson, J.-Y. Yu, M.S. Pritchard, G. Magnusdottir, P. Smyth, P.A. Levine, S. Yu and E. Foufoula-Georgiou (2020) Zonally contrasting shifts of the tropical rainbelt in response to climate change

The intertropical convergence zone (ITCZ) and its dynamics[63] play a vital role in the tropical atmospheric circulation and hydroclimate, affecting the vulnerability of tropical forest ecosystems, and influencing the food security and property of billions of people. As such, intense research has been focused on identifying the physical mechanisms that determine the climatology and variability of the ITCZ position across seasonal and interannual scales[63-71], and its long-term response to large scale natural climate variability and external anthropogenic forcing[63,67,72-83]. Evidently, this research topic has been highlighted in the literature as one of a few scientific questions of prime importance, towards accelerating the progress and filling in gaps in our knowledge of climate science[84].

From a local perspective, the ITCZ has been shown to be controlled by tropical mechanisms impacting near-equatorial sea surface temperature (SST) gradients[85]. From an energetic perspective, analysis of paleoclimate records, reanalysis data, and idealized climate simulations all indicate that the ITCZ variability can be influenced by differences in atmospheric heating between the two hemispheres (in the zonal mean, such hemispheric energy asymmetries determine the cross-equatorial atmospheric energy transport; AET_0), with the ITCZ tending to shift toward the more heated hemisphere, mimicking its seasonal behavior[63]. Hemispheric energy asymmetries can be the result of natural climate variability (shifts of the Interdecadal Pacific Oscillation, the Atlantic Multi-decadal Oscillation, or volcanic eruptions[86]) or external anthropogenic forcing (e.g., changes in emissions of sulfate aerosols[77,80,87]). Many studies have also highlighted the importance of extratropical energy sources/disturbances in altering tropical dynamics[88-96]. In the case of a northern atmospheric cooling, the ITCZ is displaced southward, increasing the northward AET_0 to

maintain the atmospheric energy balance[91] (a recent example of a southward ITCZ shift occurred during the late 20th century[97] likely because of increasing emissions of sulfate aerosols in the northern hemisphere, which decreased the hemispheric temperature difference[77,80,82,98]). Apart from AET_0, ITCZ variations have been also linked to the equatorial net energy input (NEI_0) into the atmosphere, with ITCZ shifting equatorward when NEI_0 increases (e.g. during an El Niño event)[**63**,68,70]. More generally, the ITCZ has been shown to covary with the energy flux equator (EFE; a zone where the meridional AET vanishes[91]), the latitude of which can be (to a first order) approximated by the ratio of AET_0 and NEI_0[**63**,68,70], a proxy that combines in a sense both local (mostly reflected in NEI_0) and non-local (reflected in AET_0) energy sources/disturbances. The close link between the ITCZ and the EFE holds not only in the zonal mean[**63**,70], but also over large longitudinal sectors (e.g. over a whole continent or ocean basin)[71], which has motivated recent studies to try to explain sector-mean ITCZ variability under a "2D energetic framework", i.e. where both zonal and meridional fluxes are taken into account[71,99-102].

Regarding the response of the ITCZ to future climate change in particular, past research has mostly focused on zonal-mean changes, and it shows that many different factors (greenhouse gases, aerosols, albedo, clouds, ocean heat transport or storage, regional ocean circulation, etc.) can affect the geographic pattern of tropical SSTs and/or the energy balance, and consequently the ITCZ location[79,83,92]. For example, future reduction in aerosol emissions[87,98,103], as well as Arctic sea-ice loss (closely related to Arctic amplification[104]) and glacier melting in the Himalayas[105,106] are expected to reduce the hemispheric albedo significantly more in the northern hemisphere than in the southern hemisphere, resulting in a northern warming and an ITCZ shift to the north[79,83,94]. On the other hand, the Atlantic Meridional Overturning Circulation (AMOC) is expected to weaken in the future[107-109] (new results indicate that it has already been weakening[110]), which will result in a reduction of the northward oceanic heat transport from the tropics to the northern Atlantic and a northern cooling, leading to a southward shift of the ITCZ[83,89,94,111].

Despite the relative consensus in the literature with regard to the ITCZ response to individual forcing agents and processes as discussed above, there is still uncertainty about the ITCZ response to the integrated effect of all these processes under climate change. This

uncertainty mainly stems from model inaccuracies and biases, and high inter-model variability due to different conceptualization and modelling of the subgrid processes impacting relevant radiative and dynamical processes. Particularly, although a future narrowing of the ITCZ is a robust projection under climate change[81], results significantly differ across models regarding the future ITCZ position, leading to an almost zero zonal-mean ITCZ shift when considering the multi-model mean[83]. Another reason for this uncertainty is that, as mentioned earlier, most studies have focused on zonal-mean changes of the ITCZ, possibly masking model agreements over particular areas. Indeed, because of the compensating effects of the relevant radiative and dynamical processes influencing the ITCZ position (e.g. the northward ITCZ shift caused by snow and ice albedo feedbacks and reduction of aerosols in the northern hemisphere will be compensated by a weaker AMOC[83]), and since most of these processes are not expected to be equally influential in different longitudinal sectors of the globe, the integrated ITCZ response to climate change should not be expected to be homogeneous in longitude[79]. Thus, more explicit analysis, focusing on the regional ITCZ and EFE changes (rather than zonal-mean changes) is necessary to gain insight into the future response of the ITCZ to climate change, and the associated inter-model uncertainty/consensus.

In light of the above, here we explored the ITCZ responses to climate change from the present through 2100 using Earth system model simulations from the sixth phase of the Coupled Model Intercomparison Project[112] (CMIP6; see Table 2.1), forced with a combined SSP3/RCP7.0 scenario[113,114] (that is, the combination of the shared socioeconomic pathway 3 and the representative concentration pathway 7.0). In our analysis, we explicitly explored seasonal and annual-mean ITCZ trends as a function of longitude, while also taking into account the present-day ITCZ biases of each model. In this way, we aimed to identify model consensus over particular areas, elucidate the regional responses of the ITCZ to climate change, and gain insight into the processes that influence the ITCZ location in different longitudinal sectors.

With regard to regionally tracking the ITCZ, we acknowledge that there is ambiguity in the literature as to a precise regional definition of the ITCZ and/or which is the optimal variable/method to use for its tracking[115]. For example, past studies have variously used the

surface pressure minimum, surface wind convergence, precipitation maximum, minimum outgoing longwave radiation (OLR) or cloudiness maximum to track the ITCZ[115]. The justification for using so many different variables to track the ITCZ is the assumption that the above minima/maxima collocate with each other (i.e. pressure minima roughly collocate with convergence maxima, etc.); yet, this assumption may not be true over specific regions or in specific seasons[115], and so, this ambiguity in the regional ITCZ definition is problematic. For the purposes of this study, to address the latter ambiguity, we have used a newly proposed probabilistic framework[97], which tracks the ITCZ over different longitudes and seasons by simultaneously assessing the statistics of multiple variables, and thus increasing the robustness of the tracking approach (see [116] for other probabilistic methods which use multiple variables to track the ITCZ). In particular, we considered overlapping longitudinal windows, and used the window-mean precipitation and OLR (two most common variables in the ITCZ literature) to track the ITCZ. For each window and season, ITCZ points were defined as those which correspond to the maximum (above a certain threshold) joint probability of non-exceedance of the two window-mean variables (note that in cases where precipitation and OLR extrema collocate, the latter definition falls back to simply tracking the points of the extrema; see [97] for more information). The end product of the method is to provide the probability of every grid point in the tropics to be part of the ITCZ in a longitudinally-explicit manner (see Figure 2.11). The resulted probability distribution of ITCZ position is used to compare the climatology and interannual variability of the ITCZ between observations and CMIP6 models during the base period, as well as to assess future ITCZ changes, while in specific cases, we also present results based on simple precipitation or OLR maps/indices, for the shake of completeness.

In our analysis, we used satellite precipitation data[117] and OLR time series[118] as our refence datasets in the base period 1983-2005, and outputs from 27 different CMIP6 models (totally 105 runs) to explore the effect of climate change on ITCZ location by 2100; see Table 2.1. The revealed ITCZ shifts were also assessed as to their physical consistency with future changes in equatorial SSTs and AET_0, and EFE shifts.

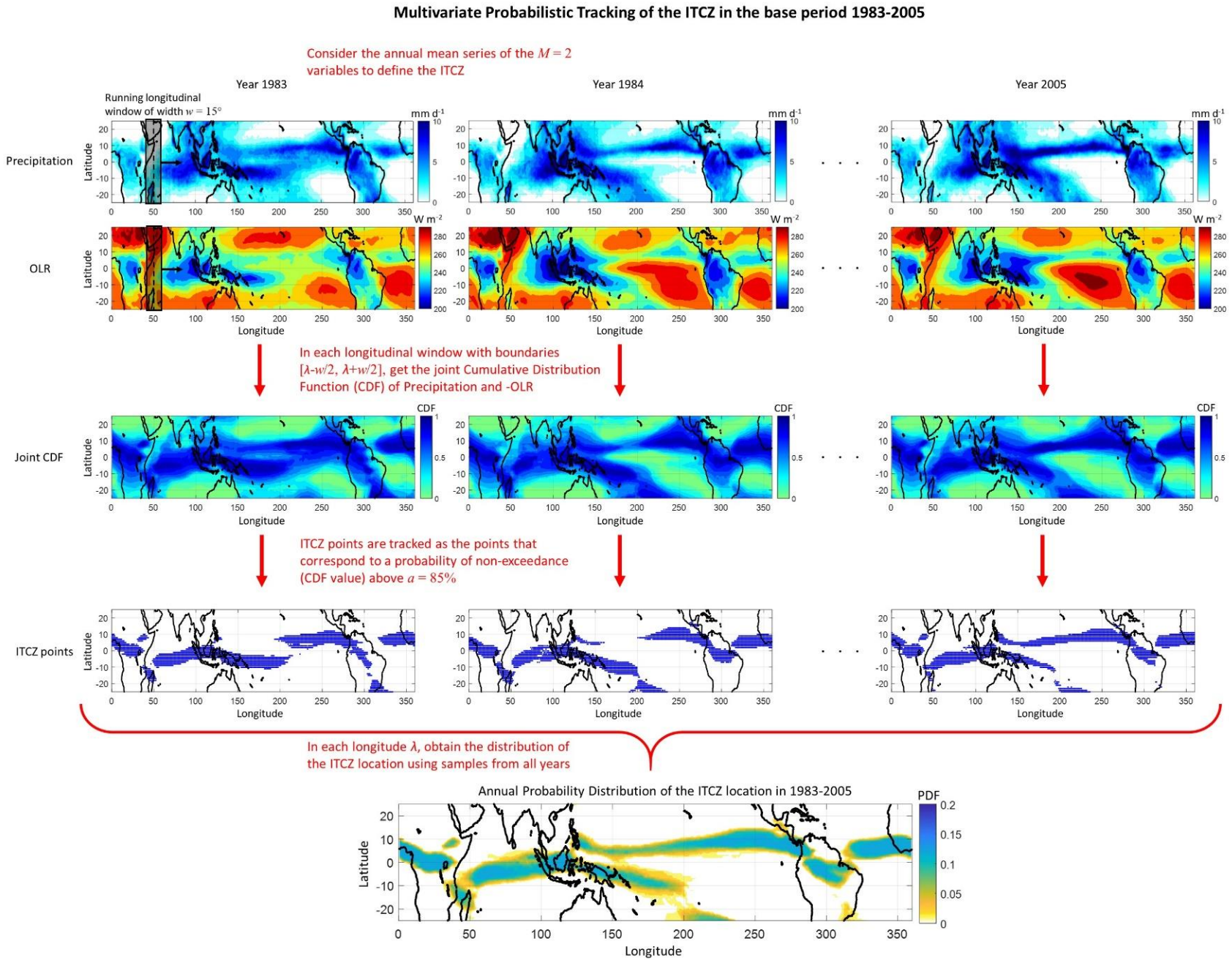
Multivariate Probabilistic Tracking of the ITCZ in the base period 1983-2005
Consider the annual mean series of the $M = 2$ variables to define the ITCZ
Year 1983
Year 1984
Year 2005
Running longitudinal window of width $w = 15°$
Precipitation
OLR
mm d-1
W m-2
Latitude
Longitude
In each longitudinal window with boundaries [λ-w/2, λ+w/2], get the joint Cumulative Distribution Function (CDF) of Precipitation and -OLR
Joint CDF
CDF
ITCZ points are tracked as the points that correspond to a probability of non-exceedance (CDF value) above $a = 85\%$
ITCZ points
In each longitude λ, obtain the distribution of the ITCZ location using samples from all years
Annual Probability Distribution of the ITCZ location in 1983-2005
PDF

Figure 2.11: Application of a longitudinally explicit, multivariate probabilistic approach to track the ITCZ on annual scales. The approach is shown here for the case when the defining variables are $M = 2$, i.e. precipitation and OLR (we use satellite data; see data availability statement), and the tracking probability threshold is $a = 85\%$. When aiming to track the ITCZ on seasonal scales, only the season of interest is used from each year. For more information, please see Mamalakis and Foufoula-Georgiou (2018).

Table 2.1: CMIP6 models used in this study and their double-ITCZ biases. For models with multiple runs, the average value of bias across all runs is presented.

	Model	Number of ensembles	East Pacific double-ITCZ Bias	Atlantic double-ITCZ Bias	Average Bias
1	ACCESS-CM2	1	0.48	0.54	0.50
2	ACCESS-ESM1-5	3	0.36	0.20	0.31
3	BCC-CSM2-MR	1	0.53	0.60	0.55
4	CAMS-CSM1-0	2	0.53	0.85	0.64
5	CanESM5	20	0.35	0.70	0.46
6	CanESM5-CanOE	3	0.36	0.71	0.47
7	CESM2	6	0.23	0.40	0.29
8	CESM2-WACCM	1	0.22	0.46	0.30
9	CNRM-CM6-1	6	0.32	0.51	0.38
10	CNRM-CM6-1-HR	1	0.28	0.50	0.35
11	CNRM-ESM2-1	5	0.35	0.51	0.40
12	FGOALS-f3-L	1	0.22	0.37	0.27
13	FGOALS-g3	1	0.31	0.42	0.34
14	GFDL-ESM4	1	0.49	0.72	0.57
15	GISS-E2-1-G	1	0.53	0.78	0.61
16	INM-CM4-8	1	0.44	0.77	0.55
17	INM-CM5-0	5	0.43	0.67	0.51
18	IPSL-CM6A-LR	11	0.19	0.74	0.38
19	KACE-1-0-G	3	0.47	0.39	0.45
20	MIROC6	3	0.16	0.38	0.24
21	MIROC-ES2L	1	0.22	0.53	0.32
22	MPI-ESM1-2-HR	10	0.34	0.83	0.50
23	MPI-ESM1-2-LR	10	0.29	0.85	0.48
24	MRI-ESM2-0	1	0.26	0.58	0.36
25	NorESM2-LM	1	0.39	0.51	0.43
26	NorESM2-MM	1	0.21	0.29	0.23
27	UKESM1-0-LL	5	0.30	0.48	0.36

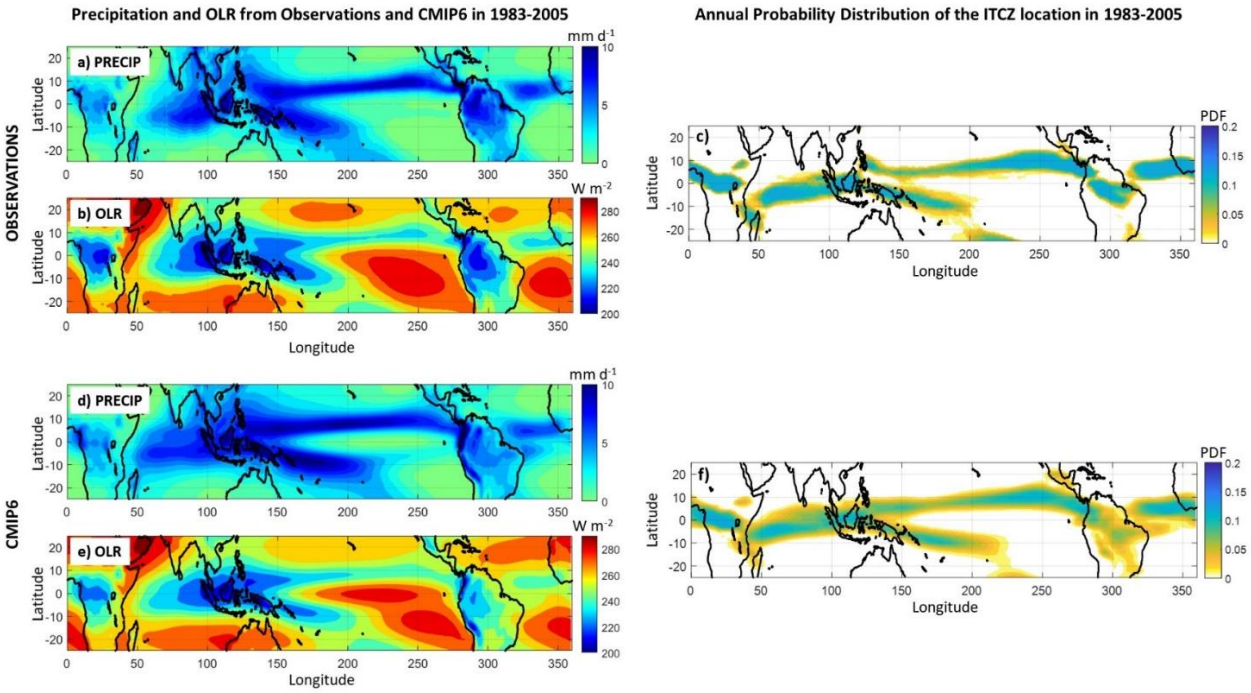

Figure 2.12: The baseline climatology of the ITCZ in observations and CMIP6, as shown in average precipitation and OLR maps, and using a multivariate probabilistic tracking framework. a) Observed tropical precipitation in 1983-2005. b) Same as in (a), but for OLR. c) Probability density function (PDF) of the location of the ITCZ on annual scales and in all longitudes. The ITCZ tracking is performed based on the joint statistics of the observed window-mean precipitation and outgoing longwave radiation (OLR) in overlapping longitudinal windows (see Figure 2.11); this panel is the identical with Figure 2.13e. d-f) Same as in (a-c), but results are obtained from the CMIP6 output. The multi-model mean across 27 CMIP6 is presented.

Results

Model simulation of contemporary ITCZ position. Here, we explore the ability of the considered CMIP6 climate models in accurately reproducing the recent ITCZ climatology and interannual variability. In doing so, we compare the distributions of the location of the ITCZ in May-Oct and Nov-Apr (during the base period 1983-2005) as derived by using satellite observations with those derived by using model outputs (for information on the ITCZ tracking approach, see Figures 2.11-2.12). The analysis of observations indicates that during May-Oct, the ITCZ is a zonally oriented feature located mainly in the Northern Hemisphere, apart from the Indian Ocean (see Figure 2.13a), where a secondary ITCZ also prevails in the equator, and the western Pacific, where the tropical part of the south Pacific convergence zone (SPCZ) is also tracked by our method. In the Nov-Apr period, the ITCZ migrates to the

south (mainly over land; see Figure 2.13c), and three southern convergence features strengthen: the SPCZ, the south Atlantic convergence zone, and the south Indian ocean convergence zone, which, in contrast to the summer ITCZ, are diagonally oriented. The highest intra-annual variability of the ITCZ location is found in the western and central Pacific, where the ITCZ consists of two distinct and much distant zones, the SPCZ and the northern ITCZ. These two bands coexist for most of the year, with the SPCZ strengthening during boreal winter and the northern ITCZ strengthening during boreal summer. The smallest intra-annual variability of the ITCZ location is found in the eastern Pacific and Atlantic oceans, where the ITCZ tends to stay in the northern hemisphere during most of the year; however a double ITCZ may form in the eastern Pacific during boreal spring.

Although CMIP6 models are mostly consistent in simulating the location of the ITCZ during May-Oct, they exhibit important biases in the Pacific and Atlantic oceans during Nov-Apr (see Figures 2.13-2.14). Particularly, models tend to overestimate the probability of the ITCZ migrating to the southern hemisphere over the eastern Pacific and Atlantic Oceans. These biases have been well documented in the literature (the so-called "double-ITCZ biases" [119,120]) and explored as to their linkage with other systematic biases in simulated equatorial sea surface temperatures and the atmospheric energy input/transport[119-125].

Due to these biases, projections of future ITCZ shifts, which are usually obtained as the difference between the simulated future and baseline averages, need to be cautiously interpreted and analyzed. Particularly, including information about the present-day ITCZ model biases in the analysis may lead to a better understanding of future ITCZ shifts, as recent literature suggests[121,122]. In order to assess the impact of these present-day model biases on our interpretation of the future ITCZ trends more quantitatively, we calculated the average difference in the (Nov-Apr) probability distribution of the ITCZ location between models and observations over specific boxes (see Figure 2.14a). Specifically, The double-ITCZ bias of each CMIP6 model over the eastern Pacific or Atlantic Ocean is defined as the average (over the considered longitudinal sector) difference in the Nov-Apr probability distribution of the ITCZ location between the model and the observations:

$$\Delta P = \frac{1}{\frac{(\lambda_2-\lambda_1)}{r_\lambda}+1} \sum_{\lambda=\lambda_1}^{\lambda_2} \left(\frac{1}{2} \int_{\varphi_1}^{\varphi_2} \left| \Delta \mathrm{PDF}_{\lambda,\varphi} \right| d\varphi \right)$$

where $\Delta PDF_{\lambda,\varphi}$ is the difference in the Nov-Apr probability distribution function (PDF) of the ITCZ location between the model and the observations at latitude φ and longitude λ, and r_λ is the model's longitudinal resolution. For calculating the bias over the Atlantic ocean, [φ_1, φ_2] = [15°S, 10°N] and [λ_1, λ_2] = [310°E, 360°N], while for the eastern Pacific bias, [φ_1, φ_2] = [10°S, 15°N] and [λ_1, λ_2] = [200°E, 300°N]. The ITCZ biases of all models are presented in Table 2.1. The average bias (weighted by the longitudinal width of each sector) is also presented.

Our results indicated that CMIP6 models simulate a more frequent southward migration of the Atlantic ITCZ than what is observed, by ΔP = 57 ± 17.8% (that is the spatially-averaged difference in probability between models and observations over tropical Atlantic), and likewise in the Pacific toward the southeastern sector of the basin, by ΔP = 34 ± 11.3% (see Figure 2.14b and Table 2.1). These numbers show that the Atlantic bias is more severe, and as such, the signature of the seasonal double-ITCZ biases on annual scales is apparent mainly over the Atlantic and not so much over the eastern Pacific basin (see Figure 2.13f). Note that when we used the average tropical precipitation and/or OLR difference between models and observations to assess the systematic double-ITCZ biases (i.e. not the probabilistic method), we obtain similar results (see Figure 2.12). Moreover, our analysis shows that there is a statistically significant ($p < 0.05$) positive correlation of eastern Pacific and Atlantic biases across the CMIP6 models on the order of 0.42, which indicates that it may be unlikely for a model to exhibit relatively important biases only in one of the two basins. Apart from the double-ITCZ bias, climate models from both projects are also shown to produce a more zonally oriented SPCZ than what observations suggest[120].

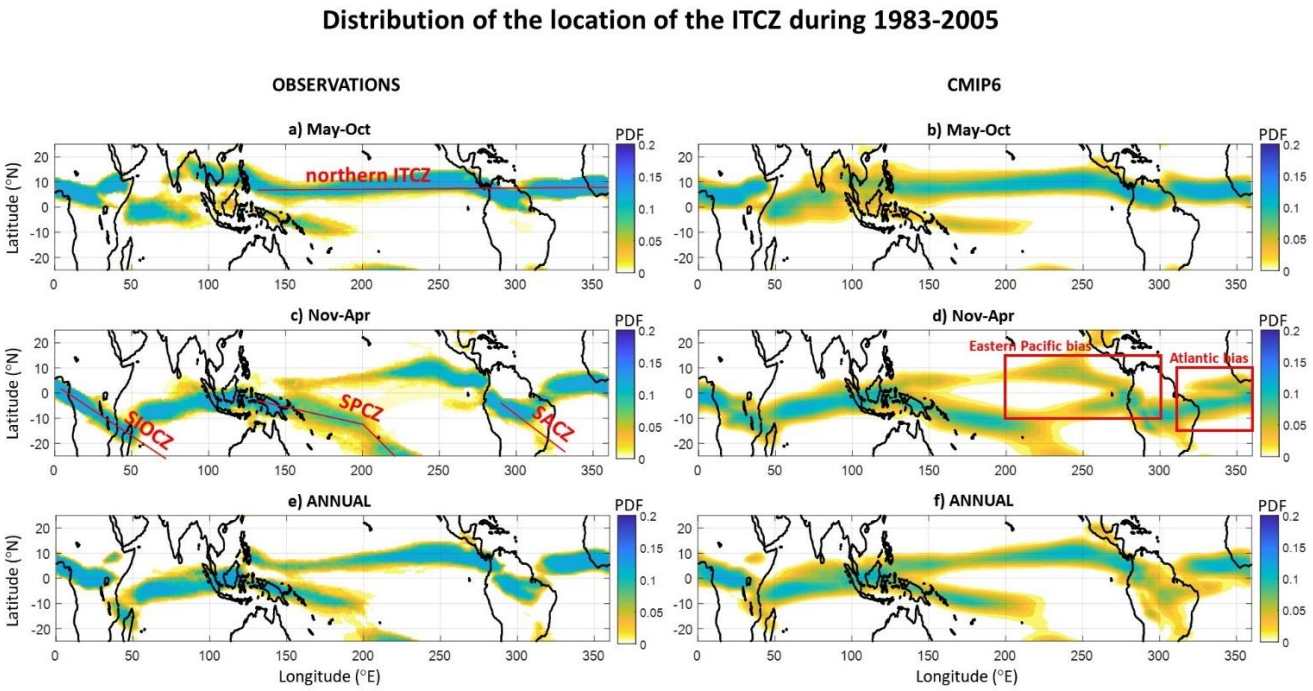

Figure 2.13: Climatological location of the ITCZ during 1983-2005 based on observations and CMIP6 models. a-b) Probability density function (PDF) of the location of the ITCZ in all longitudes during season May-Oct. The ITCZ tracking is performed based on the joint statistics of the observed (panel (a)) or the simulated (panel (b)) window-mean precipitation and outgoing longwave radiation (OLR) in overlapping longitudinal windows (see Figure 2.11). c-d) Same as in (a)-(b), but for season Nov-Apr. e-f) Same as in (a)-(b), but tracking is performed on an annual scale. In (b), (d), and (f), the multi-model mean across all 27 CMIP6 models is presented. Some well-known distinct ITCZ features are highlighted in the results from the observations, while the double-ITCZ biases in the eastern Pacific and Atlantic basins are apparent in the CMIP6 results (season Nov-Apr). The areas over which the double-ITCZ biases are quantified are shown as red boxes in panel (d).

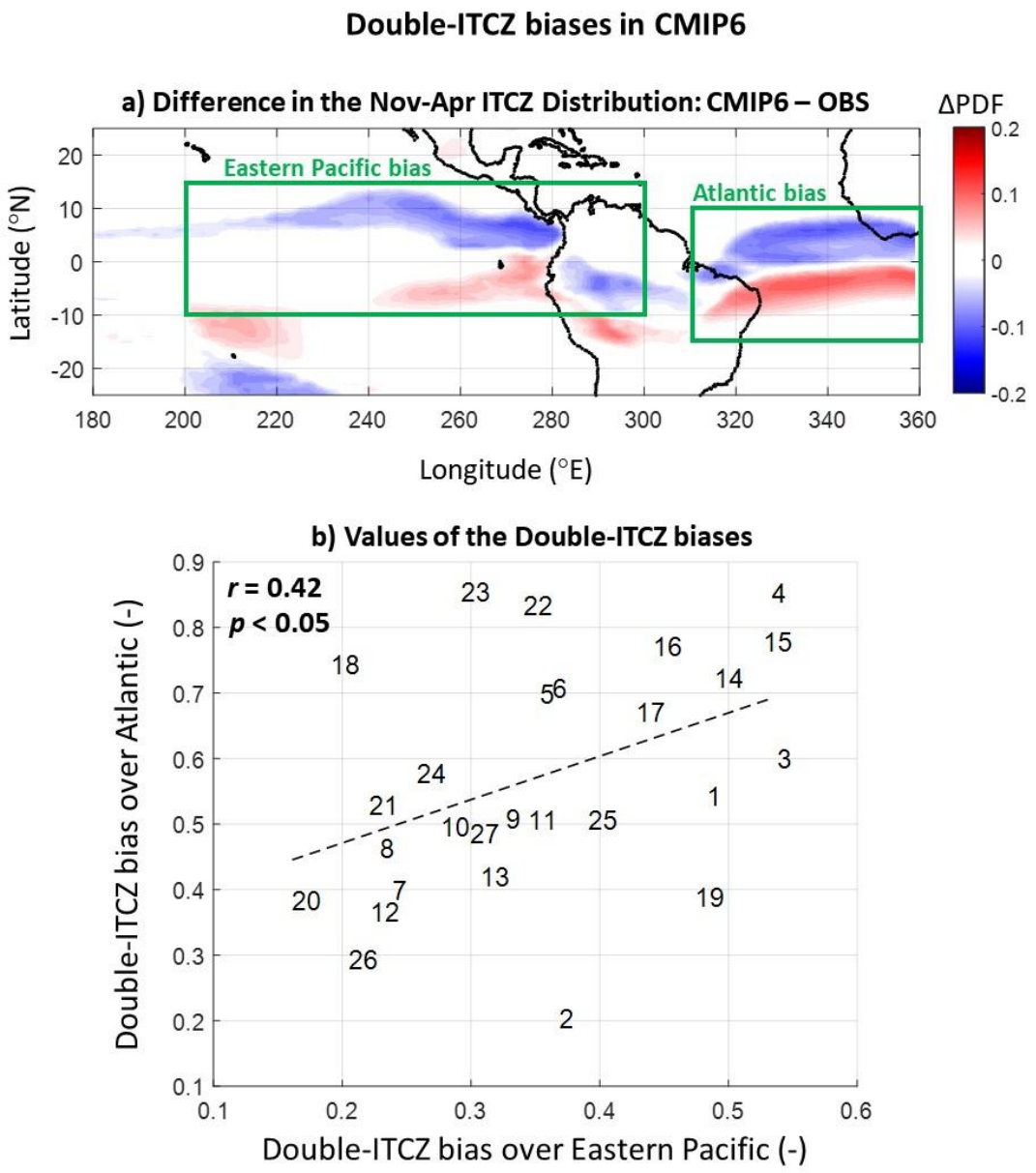

Figure 2.14: Double-ITCZ biases in CMIP6. a) Difference in the distribution of ITCZ location (Nov-Apr) between CMIP6 and observations. The multi-model mean across 27 CMIP6 models is presented. b) Scatter plot of the double-ITCZ biases in CMIP6 models (measured in probability; that is we calculated the average difference in the probability distribution of the ITCZ location between models and observations over the green boxes in panel (a)). Each model is labeled according to Table 2.1. For models with multiple runs, the average value of bias across all runs is presented. Based on both panels, CMIP6 models are shown to exhibit higher bias over the Atlantic basin than eastern Pacific, while a statistically significant ($p < 0.05$) positive dependence ($r = 0.42$) of these biases is apparent in panel (b). The latter indicates that it may be unlikely for a model to exhibit relatively important bias only in one of the two ocean basins.

To explore the ability of the models to accurately simulate the ITCZ on interannual time scales, we compared the effect of the El Niño – Southern Oscillation (ENSO) on the location of the ITCZ, as determined by satellite data and model outputs (not shown). Specifically, we calculated the difference in the distribution of the ITCZ location between years corresponding to the four strongest El Niño events and the four strongest La Niña events during the 23-yr base period 1983-2005. In models runs, El Niño and La Niña events do not correspond to the same years with reality, thus, we used the Niño 3.4 index to define ENSO events. Results showed that CMIP6 models are mostly consistent in reproducing the effect of ENSO on the location of the ITCZ during Nov-Apr (the period when ENSO typically peaks). Results from both the observations and the models indicate that during El Niño conditions, the ITCZ is displaced more equatorward in the Pacific relative to La Niña conditions, due to the anomalous heating in the tropical Pacific Ocean which favors deep convection[69,71].

Future ITCZ change. Our analysis of annual and zonal-mean changes indicated that the ITCZ shift under future climate change for the CMIP6 models is -0.5 ±1.2° N (slightly southward; see Table 2.2). The inter-model uncertainty within the CMIP6 models is very large (the standard deviation is more than twice the mean shift), which leads to the multi-model mean shift not being statistically distinguishable from zero (Table 2.2), and confirming the results of [83].

One of the most important findings of this study is that despite the high inter-model uncertainty regarding the zonal-mean ITCZ shift, models exhibit greater agreement in ITCZ changes as a function of longitude (see Figure 2.15). Particularly, in the May-Oct season, CMIP6 models indicate a robust northward shift of the ITCZ over Africa and the Indian Ocean[126], and a southward shift over most of the Pacific and Atlantic Oceans (in the Atlantic basin the shift is less statistically robust relative to the one in the Pacific; see Figure 2.15a). In the Nov-Apr season, the south Indian Ocean convergence zone and the south Pacific convergence zone both shift northward[121], while the eastern Pacific ITCZ is shown to shift southward. In the Atlantic basin, most models predict a higher probability of the ITCZ to prevail over the equator in the future relative to the base period, revealing a pattern of an

equatorward ITCZ shift. In general, an interesting zonally contrasting ITCZ response to climate change is revealed in both seasons and even more clearly on the annual scale (see Figure 2.15c and Table 2.2), which consists of a robust northward ITCZ shift over the eastern Africa/Indian ocean region, and a robust southward ITCZ shift over the eastern Pacific Ocean, south America, and the Atlantic Ocean. This zonally contrasting response is also apparent when calculating the future change in annual-mean precipitation or OLR (see Figure 2.16).

To more precisely quantify this zonally contrasting ITCZ response to climate change, we tracked the temporal evolution of the ITCZ location as a function of longitude and over two different longitudinal sectors, i.e. the Eurasian sector (20°E-130°E) and the eastern Pacific and Atlantic sector (250°E-360°E); the boundaries of the two sectors were chosen based on Figure 2.17a, but following results are quite robust if the boundaries are moderately changed (i.e. ±10°). A clear northward ITCZ shift is observed over the Eurasian sector, while a southward shift is apparent in the eastern Pacific and Atlantic Oceans (Figure 2.17a). Over the western Pacific, the ITCZ shifts southward during May-Oct and northward during Nov-Apr (as was shown in Figure 2.15), which translates into a decreased seasonal ITCZ migration in the future, and an annual-mean shift that is close to zero. When comparing the 2075-2100 and 1983-2005 periods, a statistically significant (based on the *t*-test; $p < 0.01$) northward shift on the order of 0.8 ± 0.6° N was obtained over the Eurasian sector (see Table 2.2). In contrast, over the eastern Pacific and Atlantic sector, CMIP6 models indicate a statistically significant southward shift on the order of -0.7 ± 0.9° N. The future ITCZ shift and the change in precipitation asymmetry (i.e. the change in the quantity: $\text{Precip}_{0^\circ\text{-}20^\circ\text{N}} - \text{Precip}_{0^\circ\text{-}20^\circ\text{S}}$) between 2075-2100 and 1983-2005 for every CMIP6 model are shown in Figure 2.17b, indicating that the majority of models predict a future increase in precipitation in the northern subtropics relative to the south over the Eurasian sector (red color). The opposite is true for most CMIP6 models over the east Pacific and Atlantic sector (blue color).

Table 2.2: Mean and standard deviation of the future ITCZ and EFE shifts (2075-2100 minus 1983-2005, positive values indicate northward movement) and changes of the hemispheric energetic asymmetry over different longitudinal sectors, as obtained from 27 CMIP6 models outputs. The baseline values (i.e. referring to 1983-2005) are also provided. Values with **bold** font correspond to a multi-model mean which is statistically distinguishable from zero, based on the *t*-test ($p < 0.01$). It is shown that there is a robust consensus across models regarding future changes in the Eurasian and E. Pacific – Atlantic sectors, but such a consensus is not apparent in the zonal mean.

27 CMIP6 Models		Global zonal mean	Eurasian Sector [20ºE-130ºE]	E Pacific & Atlantic Sector [250ºE-360ºE]
ITCZ latitude (degrees North)	Base Period	**3.6 ±2.0**	**-1.0 ±1.1**	**4.1 ±2.3**
	Future Shift	-0.5 ±1.2	**0.8 ±0.6**	**-0.7 ±0.9**
Q_S - Q_N (PW)	Base Period	-0.03 ±0.37	**0.93 ±0.21**	**-0.96 ±0.23**
	Future Change	-0.05 ±0.21	**-0.24 ±0.10**	**0.31 ±0.16**
EFE latitude (degrees North)	Base Period	-0.4 ±0.8	**-3.2 ±0.9**	**4.9 ±1.9**
	Future Shift	0.2 ±0.5	**0.7 ±0.4**	**-1.4 ±1.1**

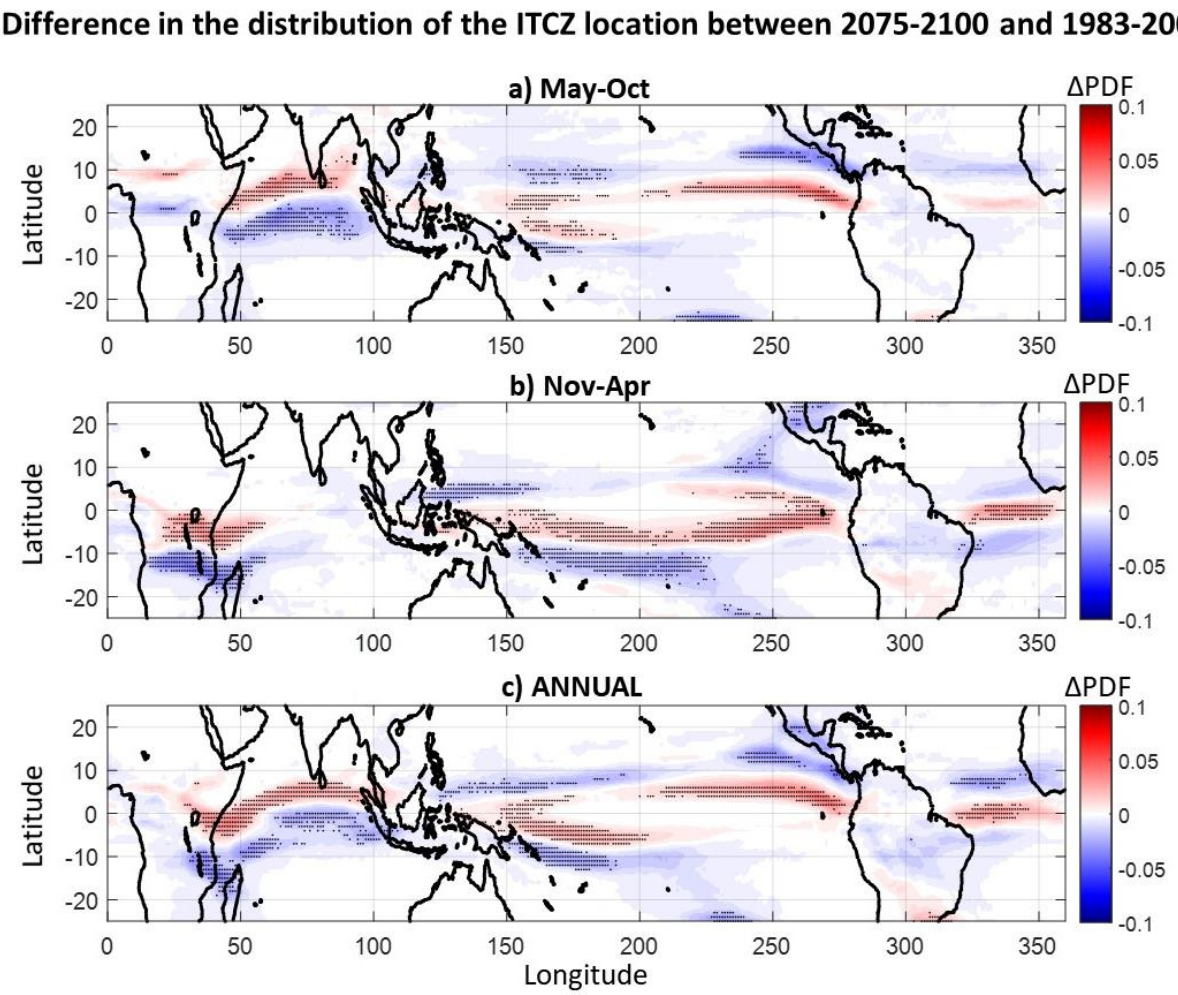

Figure 2.15: Future changes in the ITCZ location under climate change as predicted in CMIP6. a) Difference in the probability density function (ΔPDF) of the location of the ITCZ in May-Oct between 2075-2100 and 1983-2005. b) Same as in (a), but for Nov-Apr. c) Same as in (a), but the changes in the annual distribution are shown. In all plots the multi-model mean across 27 CMIP6 models is presented, while stippling indicates agreement (in the sign of the change) in more than ¾ of the models considered. Results indicate a robust northward ITCZ shift over eastern Africa and Indian Ocean and a southward ITCZ shift over eastern Pacific and Atlantic Oceans.

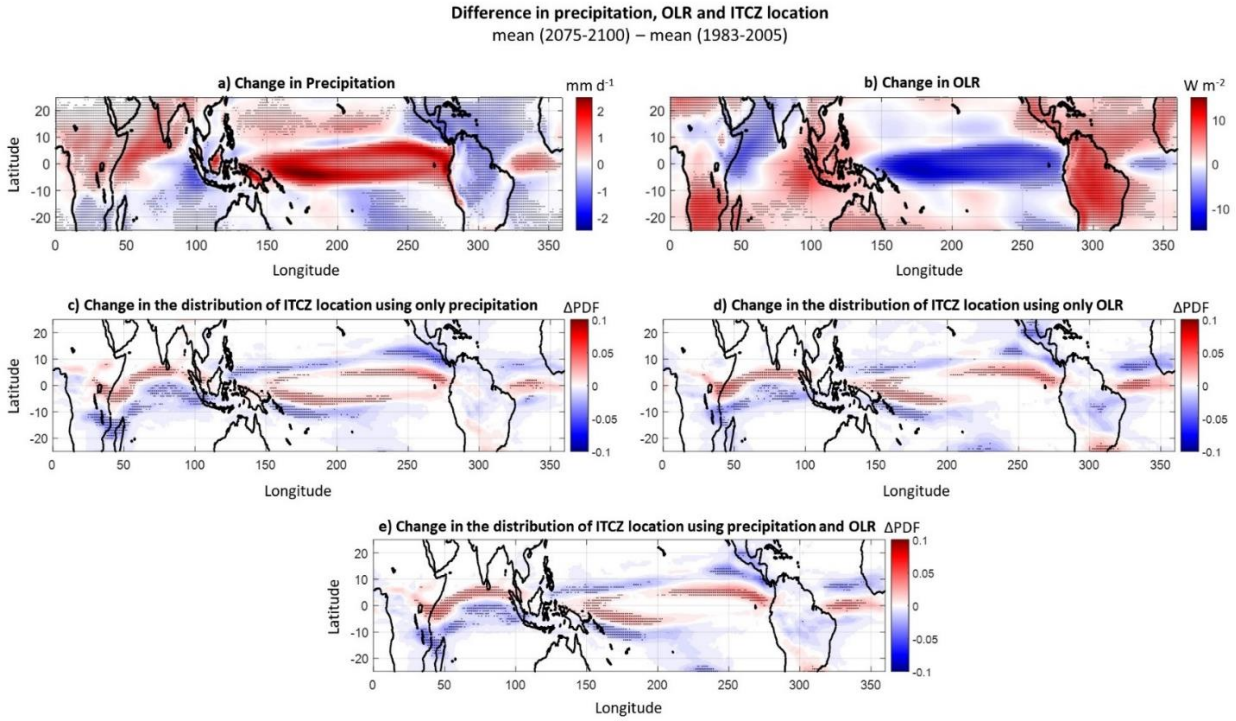

Figure 2.16: Future changes in the ITCZ location in CMIP6, as shown in changes of average precipitation and OLR maps, and using a multivariate probabilistic tracking framework. a) Difference of mean precipitation (mm/d) between 2075-2100 and 1983-2005. b) Same as in (a), bur for OLR (W/m^2). c) Difference in the annual probability density function (ΔPDF) of the location of the ITCZ between 2075-2100 and 1983-2005. The ITCZ tracking is performed using only precipitation. d) Same as in (c), but OLR is used to track the ITCZ. e) Same as in (c), but both precipitation and OLR are jointly used to track the ITCZ; this panel is the identical with Figure 2.15c. In all plots the multi-model mean across 27 CMIP6 models is presented, while stippling indicates agreement (in the sign of the change) in more than ¾ of the models considered. All plots show (to a greater or lesser extend) a northward ITCZ shift over eastern Africa and Indian Ocean and a southward ITCZ shift over eastern Pacific and Atlantic Oceans.

With regard to the effect of the double-ITCZ biases on the revealed ITCZ response, we found that the results over the Eurasian sector are not sensitive to the performance of the models in the base period. That is to say that there is no statistically significant relationship between the bias of a model and the projected shift over the Eurasian sector (not shown). However, over the eastern Pacific and Atlantic sector (i.e. where the double-ITCZ biases occur), ITCZ biases seem to be affecting the sign of the predicted ITCZ shift to some extent. In particular, our analysis showed that the smaller the bias of a model over the southern Atlantic, the more likely it is to predict a southward shift of the Atlantic ITCZ in the future (see Figure 2.18). This means that the pattern of the ITCZ contraction over the Atlantic Ocean that is depicted in Figure 2.15b-c is likely a spurious result, originating from some of the models being highly biased in the base period. Since in reality the Atlantic ITCZ remains in the northern hemisphere for most of the year and there is very little to zero precipitation over the southern Atlantic (see Figures 2.12-2.13), a future southward Atlantic ITCZ shift as indicated by the models with lower bias is more likely (a future negative ITCZ-pattern over the southern Atlantic Ocean as shown in Figure 2.15b is an artifact from the high bias in some models and will be an algebraic impossibility in reality). In consistency with the above, we found that the small fraction of CMIP6 models that predict a northward ITCZ shift over the east Pacific and Atlantic sector (i.e. in contrast to the majority of the models which predict a southward ITCZ shift; see Figure 2.17b) exhibit relatively high double-ITCZ biases in the base period. Thus, we argue that the double-ITCZ biases, if anything, are undermining the extend of the southward ITCZ shift over the eastern Pacific and Atlantic sector that will actually happen, and thus, our claims about the robustness of the zonally contrasting response of the ITCZ to climate change fall, if anything, on the conservative side.

Overall, the robust agreement between climate models over these two large sectors (Table 2.2 and Figures 2.15-2.17) provides confidence that global warming will lead to opposite meridional shifts of the ITCZ in the Eurasian vs. E. Pacific/Atlantic sectors. As already mentioned, this zonally contrasting response leads to almost zero ITCZ shift from a zonal-mean perspective (Table 2.2), confirming the recent literature[83,127].

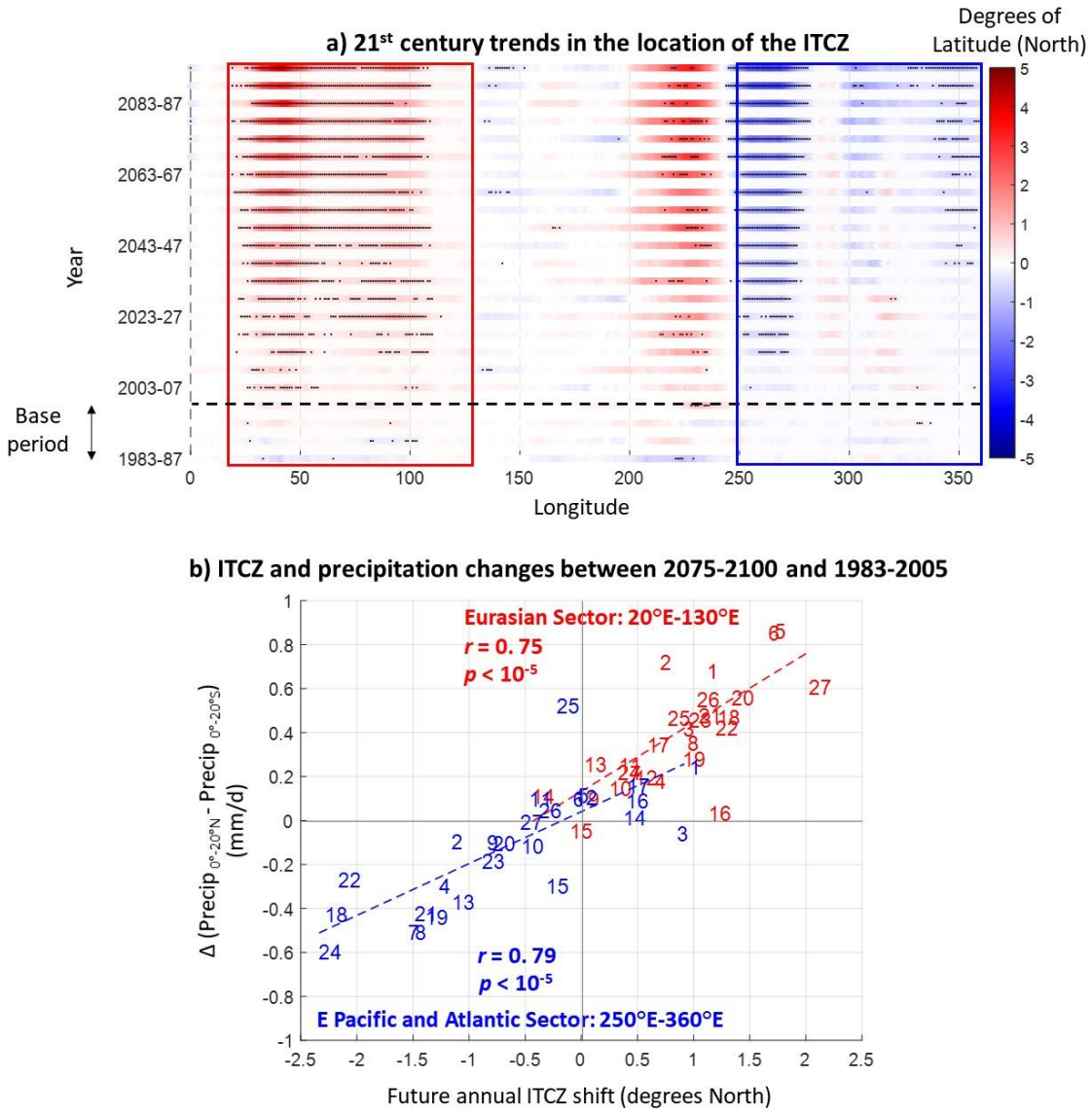

Figure 2.17: 21st century series of ITCZ location as predicted in CMIP6. a) Series of the 5yr-mean ITCZ location relative to the base period as a function of longitude. The multi-model mean across 27 CMIP6 models is presented, while stippling indicates agreement (in the sign of the change) in more than ¾ of the models considered. b) Scatter plot of the projected ITCZ shift (horizontal axis) and change of tropical precipitation asymmetry (vertical axis) between the periods 2075-2100 and 1983-2005, using all 27 CMIP6 models zonally averaged over the Eurasian sector (20ºE-130ºE; red color) and the eastern Pacific and Atlantic sector (250ºE-360ºE; blue color). Each model is labeled according to Table 2.1. Based on either index (shift or precipitation asymmetry), a robust contrasting ITCZ response between the two sectors is revealed, whereby the ITCZ shifts northward over the Eurasian sector and southward over eastern Pacific and Atlantic Oceans.

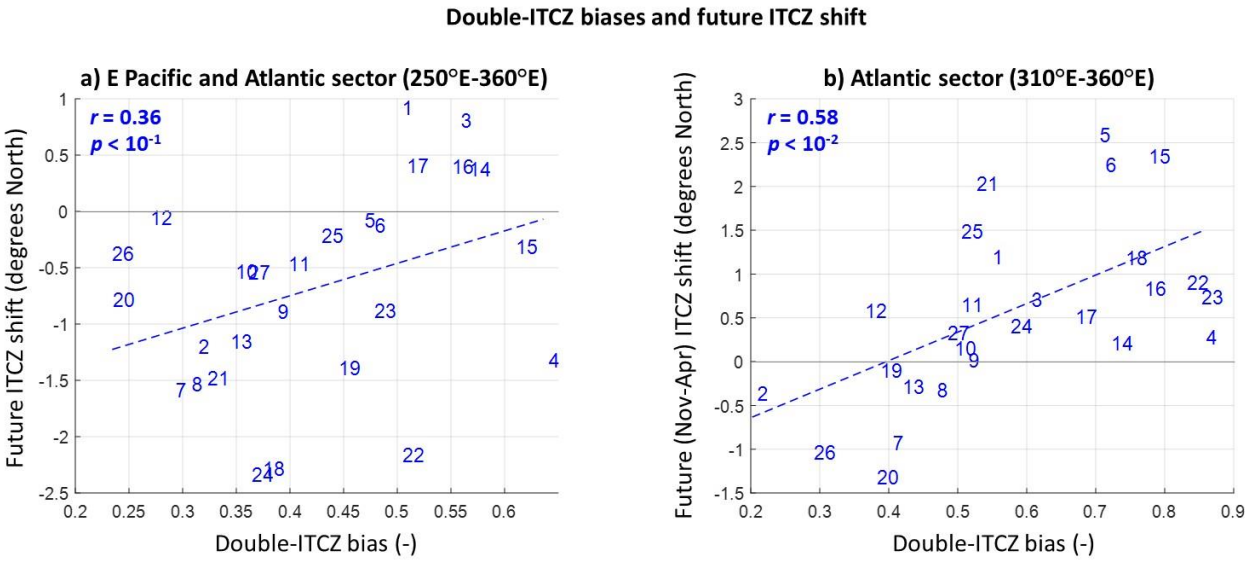

Figure 2.18: The effect of the double-ITCZ bias on the sign of the projected ITCZ shift over the east Pacific and Atlantic Oceans. a) The ITCZ shift (in degrees of latitude) over the east Pacific and Atlantic Oceans between 2075-2100 and 1983-2005 is shown as a function of the double-ITCZ bias (measured in probability; that is we calculated the average difference in the probability distribution of the ITCZ location between models and observations over the green boxes in Figure 2.14a) for all CMIP6 models (each model is labeled according to Table 2.1). b) Same as in (a), but results refer to the Atlantic Ocean. In both cases, a statistically significant positive dependence is apparent. This illustrated positive dependence indicates that the lower the double-ITCZ bias of the model over the east Pacific and Atlantic Oceans is in the base period, the more likely it is for the model to produce a southward shift of the ITCZ in the future.

Link to sea surface temperature changes. Many different tropical explanations/mechanisms contributing to future and past regional ITCZ and precipitation shifts have been proposed in the literature (e.g. the wet-get-wetter mechanism[128], feedbacks affecting near-equatorial sea surface temperatures[126], plant physiological responses[129], changes in monsoonal dynamics[130], etc.). Motivated by the known close coupling between sea surface temperature and precipitation in the tropics[126,131,132], we explored the consistency of the revealed contrasting response of the ITCZ with the changes in the SST. We found that, globally, the SST warming is more pronounced in the northern hemisphere than the southern hemisphere (Figure 2.19). This is a known and robust result under climate change and is partially due to the strengthening of the southeast trade winds which favor sea surface evaporation[126]. Another important contributor to this hemispheric asymmetry is the muted warming over the Southern Ocean (Figure 2.19), which has been attributed to the

intense vertical mixing which occurs in this area, resulting in considerable ocean heat uptake[133]. In fact, models and observations suggest that more than half of the historical excess heat due to the increased radiative forcing has been stored in the Southern Ocean over the last decades[133-135]. Muted warming is also observed over the north Atlantic Ocean, which is a result of the weakening of the AMOC, another robust feature under climate warming[109].

Regarding the tropics, we found that over the Pacific Ocean, SST warming is more pronounced in the east than the west, which is a consistent result with the anticipated weakening of the Walker circulation under climate change[126,136]. In both eastern Pacific and Atlantic Oceans, higher SST warming occurs in low latitudes between 10°S and 5°N, which is consistent with this region serving as an attractor for a southward shift of the ITCZ from its current baseline position at 4.1 ± 2.3°N for this sector (see Figure 2.19c). In contrast, over the Indian Ocean in the Eurasian sector, higher SST warming in the northern subtropics is consistent with the predicted shift of the ITCZ to the north from its current baseline position (Figure 2.19b). The pattern of SST change in the Indian Ocean resembles a positive Indian Ocean Dipole (IOD) pattern (with a more pronounced warming over the northwestern Indian Ocean and a less pronounced warming over southeastern Indian Ocean), which is linked to locally developed Bjerknes feedbacks between SST gradients, and wind and thermocline changes in the basin[126,136,137].

Despite the fact that the predicted changes in tropical north-south SST gradients are consistent with the zonally contrasting ITCZ response, more insight is needed as to why these SST changes occur. Both local and non-local process chains are relevant. For example, the positive IOD pattern in the Indian Ocean has been argued to be a result of the weakening of the Walker circulation locally, but also influenced at its southern margin by the oceanic lateral advection of relatively weak warming signatures from the remote Southern Ocean[126]. Other causatively relevant non-local possibilities include extratropics-to-tropics teleconnections within the atmosphere, which are usually based on energetic arguments[91,126]. Indeed, as noted in the introduction, to get more insight into past or future ITCZ shifts, recent studies have utilized atmospheric energetic constraints to explain tropical climatic changes, and in some cases attributed them to extratropical factors, even if these

changes were longitudinally confined, i.e. not referring to the zonal mean[71,99-102,111]. Motivated by this, we looked into the future changes in the atmospheric heat budget and further investigated whether the zonally contrasting ITCZ response could be related to similar zonally contrasting changes in the hemispheric heating and EFE shifts.

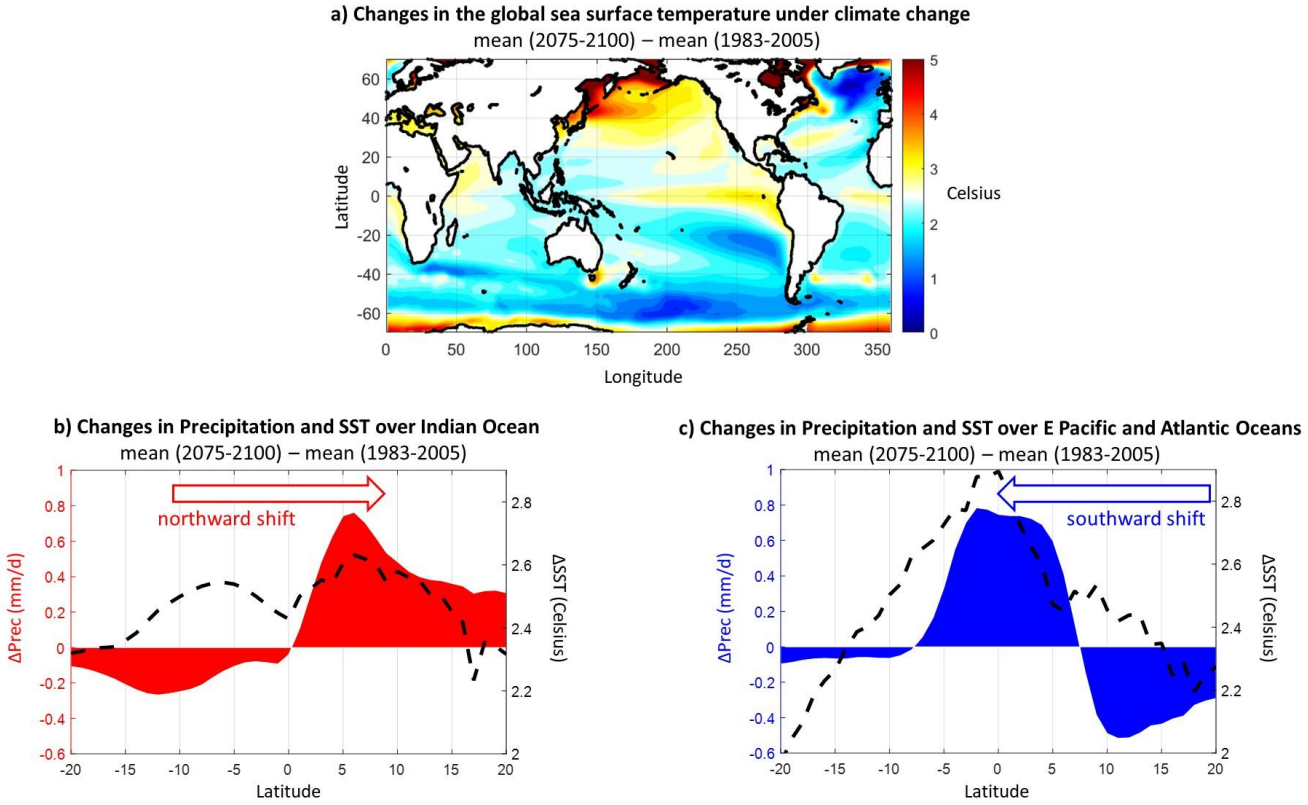

Figure 2.19: Future changes in sea surface temperature and precipitation under climate change as predicted in CMIP6. a) Global changes in sea surface temperature (SST) between future 2075-2100 and base period 1983-2005. b) Zonal mean over the Indian Ocean (50ºE-100ºE) of the changes of precipitation (in mm/d) and SST (in Celsius). c) Same as in (b), but for the eastern Pacific and Atlantic Oceans (250ºE-360ºE); land changes are not considered in the zonal mean. All results refer to the multi-model mean across 27 CMIP6 models.

Atmospheric Energetic constraints. Considering a long enough period (e.g. 1983-2005) so that the energy storage in the atmosphere is negligible[63,138], and assuming that the system is in equilibrium, the atmospheric energy budget is [68,138]:

$$\nabla \cdot \mathbf{F} = R^{\mathrm{TOA}} - O = Q \qquad (9)$$

where **F** is the vector of vertically-integrated atmospheric moist static energy flux, R^{TOA} is the net energy input at the top of the atmosphere (TOA; i.e. net downward shortwave minus the outgoing longwave radiation) and O is the ocean energy uptake (O can be further partitioned to latent/sensible heat and radiative surface components) and represents the heating from the surface (note that the energy storage in the land is negligible on timescales greater than a season[63]). Q is the net energy input into the atmospheric column of unit horizontal area (see Figure 2.20a-b for the distribution of Q in the base period, and schematic in Figure 2.21a), and Equation (9) states that it is equal to the horizontal divergence of the AET. Thus, future changes in Q under climate change are related to changes in the horizontal AET, which can in principle be related to the future ITCZ shifts.

In response to climate change, models indicate that the energy input into the atmosphere will increase in the tropics and decrease at high latitudes 50º-70º, especially over the ocean (see Figure 2.21b for the change in the total energy input, and its partitioning into TOA and surface components[139] in Figure 2.21c-d, according to Equation (9)). Particularly, over the Atlantic Ocean, a pattern of northern atmospheric cooling and southern heating is revealed, which is consistent with a weakening in the AMOC (i.e. the see-saw response[83,89,109,140-142]), while over the Southern Ocean, atmospheric cooling is consistent with increased heat flux from the atmosphere to the ocean in response to increasing emissions of greenhouse gases[143]. Moreover, we find an increase in atmospheric heating over the tropics, which is mostly a result of the TOA component of the budget (Figure 2.21c), and is associated with cloud radiative effect; i.e., the OLR escaping to space is reduced in the future (see partitioning of TOA energy change in Figure 2.22c, and [83]). Over land, the effect of processes like snow and ice albedo feedbacks (see Figure 2.22d and studies regarding climate change-induced glacier melting over the Himalayas[105,106], climate change-induced sea ice loss in the Arctic[94,104,144]) and reduction of anthropogenic aerosols, which are more pronounced over the northern hemisphere[83,103], are partially compensated by increases in OLR cooling (see Figure 2.22c). As a result, we find that the net effect of all these processes is that more energy is being added into the atmosphere over land in the northern hemisphere and specifically over Europe, Southeast Asia, North America, and the Arctic (see Figure

2.21b), which contrasts the important heat loss in the northern Atlantic region due to the weakening of the AMOC.

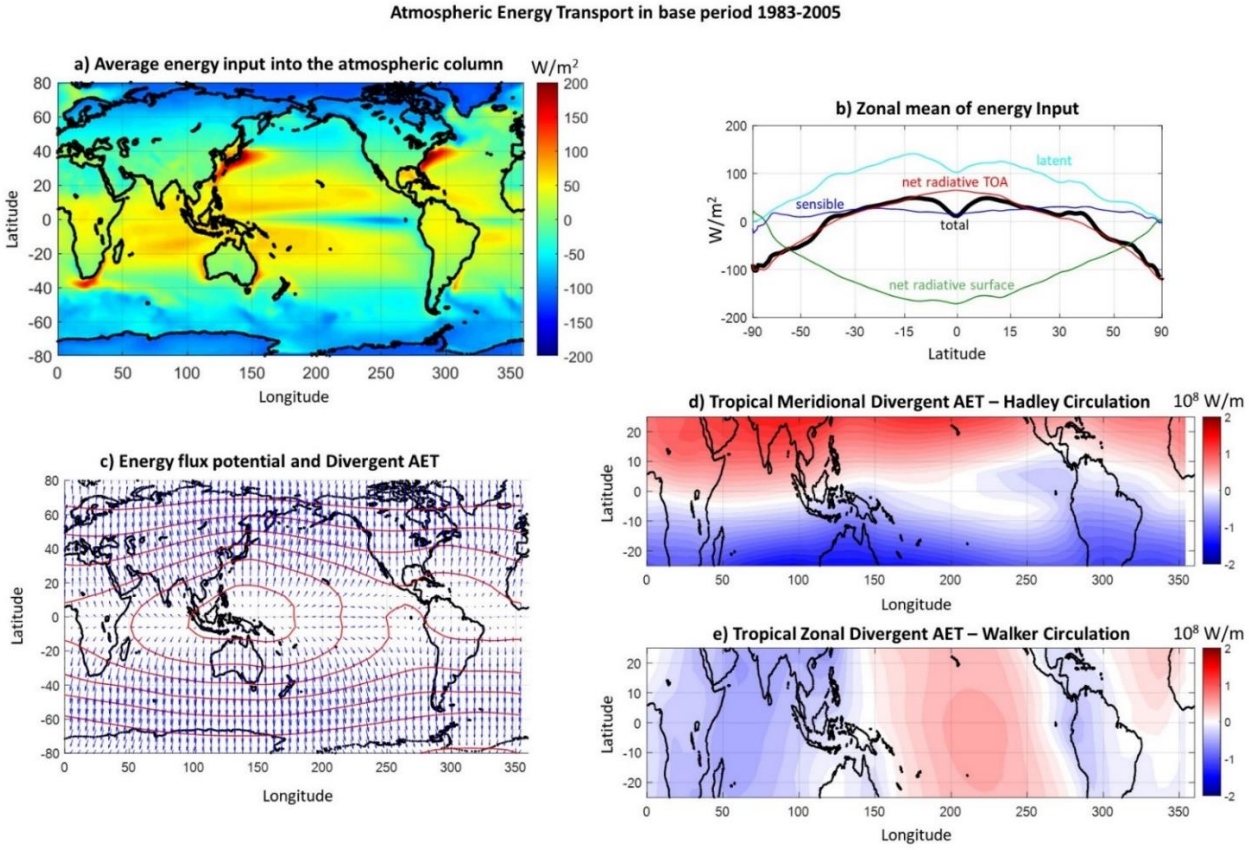

Figure 2.20: Atmospheric energy transport in base period 1983-2005, as predicted in CMIP6. a) The average energy input (W/m^2) into the atmospheric column in the base period 1983-2005. b) Zonal mean of (a). The horizonal axis is scaled as $\sin(\varphi)$. c) Energy flux potential (red contours; contouring interval is 0.2 PW, with equatorial extrema being minima), and divergent atmospheric energy transport (blue vectors). Vectors are on the order of 10^8 W/m; see panels (d) and (e) for specific values. d) Divergent meridional component of the atmospheric energy transport over the tropics in 1983-2005, most of which is due to the mean meridional atmospheric circulation (Hadley circulation). e) Same as in (d), but the divergent zonal component is presented (it reflects the Walker circulation). In all plots, the multi-model mean across 27 CMIP6 models is presented.

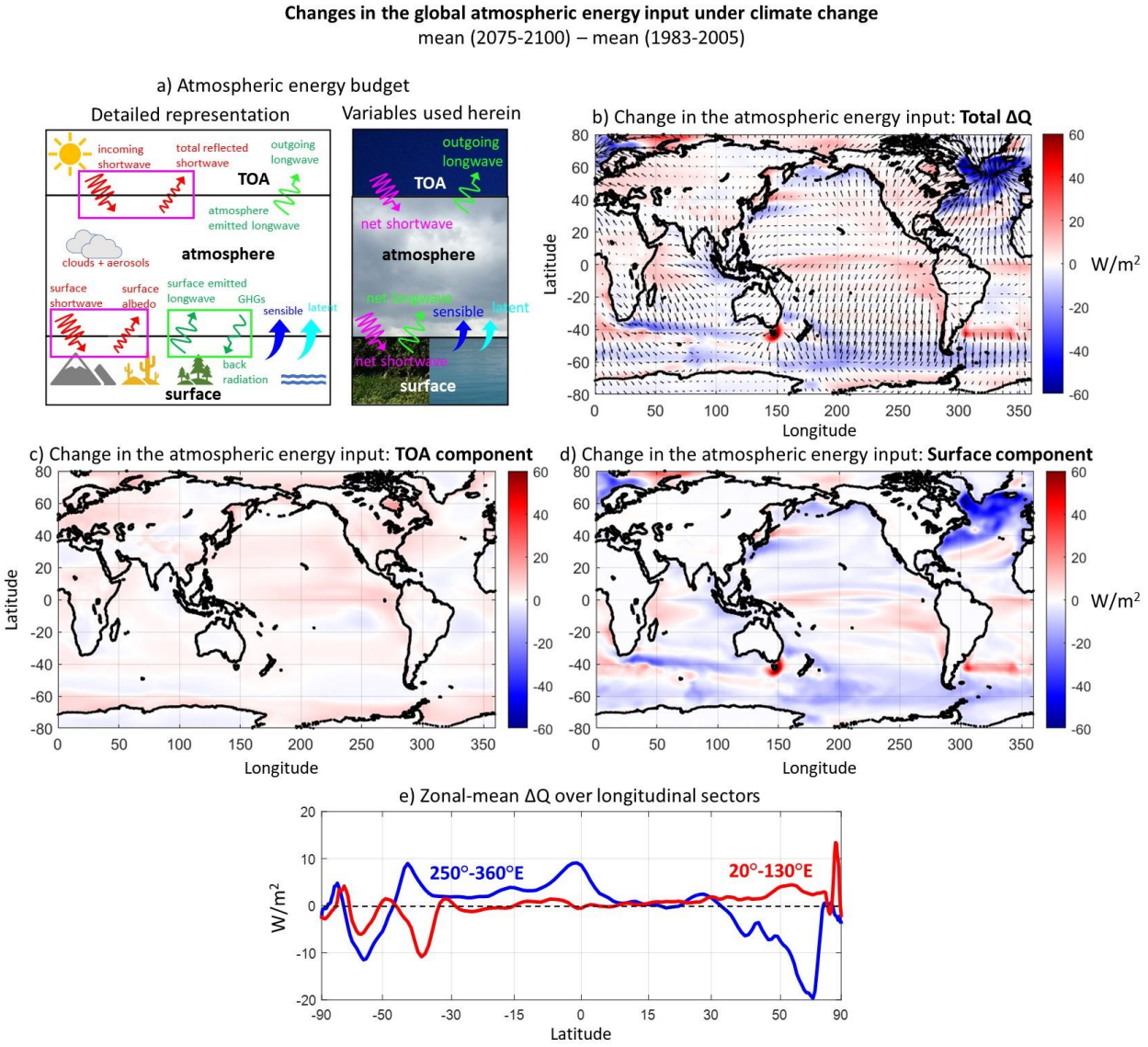

Figure 2.21: Future changes in the atmospheric energy input under climate change as predicted in CMIP6. a) Graphic representation of the atmospheric energy budget. b) Difference of the average energy atmospheric input between 2075-2100 and 1983-2005 periods (shading), while vectors show the change in the divergent component of the atmospheric energy transport; vectors are on the order of 10^7 W/m (see Figure 2.23 for specific values). c) Same as in (b), but only the top of the atmosphere (TOA) component is shown. d) Same as in (b), but only the surface component is shown. This panel highlights the contribution of the ocean to the future atmospheric heating/cooling. e) Zonal mean of (b) over the Eurasian sector (20ºE-130ºE; red curve) and the eastern Pacific and Atlantic sector (250ºE-360ºE; blue curve). The horizontal axis is scaled as $\sin(\varphi)$. In all plots, the multi-model mean across 27 CMIP6 models is presented. Results show that under global climate change, more energy is added in the atmosphere over the northern hemisphere than the southern hemisphere in the Eurasian sector, while the opposite is true in the eastern Pacific and Atlantic Oceans.

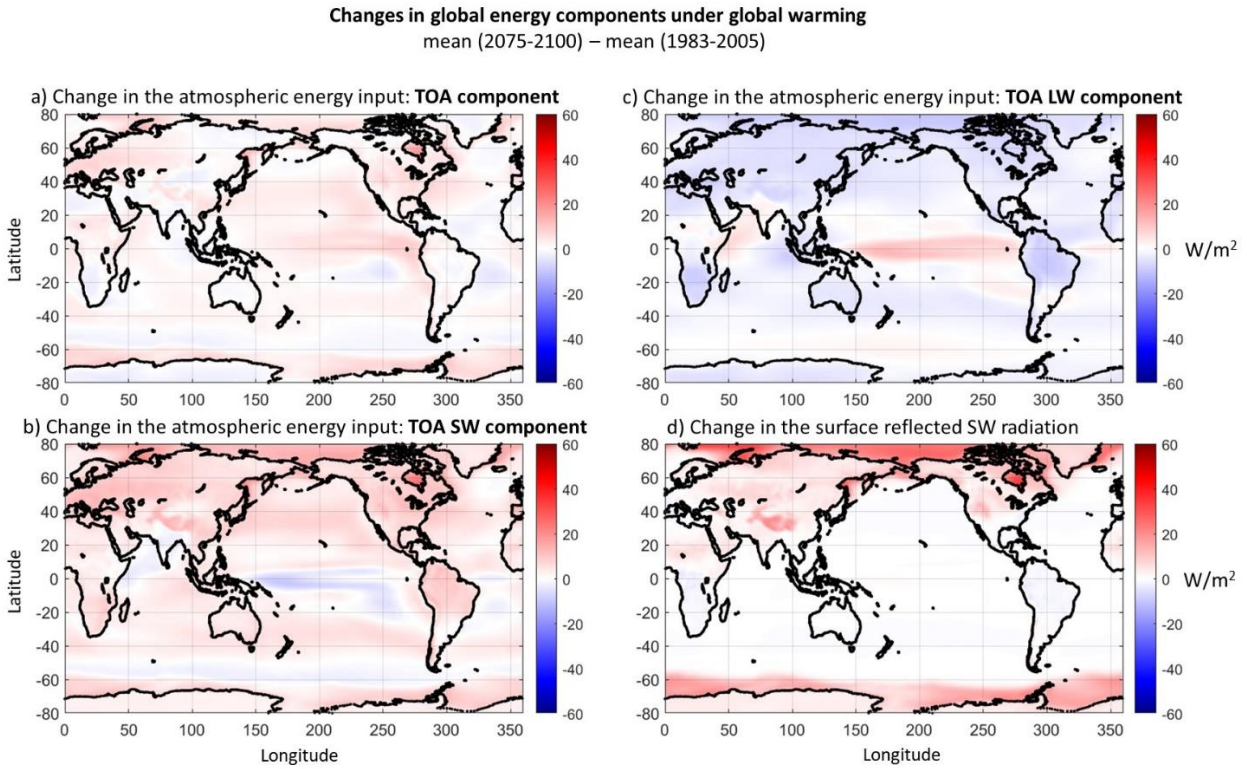

Figure 2.22: Future changes in the components of the atmospheric energy budget as predicted in CMIP6. a) Projected change in the top of the atmosphere (TOA) atmospheric energy input between 2075-2100 and 1983-2005. The multi-model mean across 27 CMIP6 models is presented. b) Same as in (a), but only the TOA shortwave component is presented. c) Same as in (a), but only the TOA longwave component is presented. d) Same as in (a), but the change in the shortwave radiation reaching the surface due to surface albedo changes is presented.

In terms of the zonal mean, the compensating effects of all these processes lead to an almost zero net change in the hemispheric energy asymmetry. Particularly, CMIP6 models predict a change on the order of $\Delta\ (Q_S - Q_N)$ = -0.05 ± 0.21PW (Q_S and Q_N refer to the hemisperically integrated energy input over the southern and northern hemisphere, respectively) consistent with the negligible zonal-mean ITCZ shift (see Table 2.2). However, when considering the Eurasian sector and the eastern Pacific and Atlantic sector separately, significant differences emerged (Table 2.2), with models showing a higher level of consensus in terms of the sign of the change in the energy asymmetry (changes were assessed to be statistically significant; $p < 0.01$). Over the Eurasian sector, most models predict that more energy is added into the northern hemisphere than the southern hemisphere under climate change (Figure 2.21e), which reduces the baseline hemispheric energy asymmetry; i.e. Δ

($Q_S - Q_N$) = -0.24 ± 0.10 PW (see Table 2.2). In contrast, over the eastern Pacific and Atlantic Oceans, the northern hemisphere atmosphere receives less energy in the future (Figure 2.21e) probably due to the weakening of the AMOC, which contributes to a northern hemisphere atmospheric cooling; i.e. Δ ($Q_S - Q_N$) = 0.31 ± 0.16 PW. These results highlight contrasting changes of the hemispheric energy asymmetry to global climate change between the two considered sectors, which is statistically consistent with the revealed zonally contrasting response of the ITCZ (we have established statistically significant dependence between changes in hemispheric heating and precipitation asymmetries; not shown), i.e. our results suggest that the ITCZ shifts towards the more heated hemisphere in each of the two sectors. However, such a suggestion is generally physically grounded only in the zonal mean perspective. Since these results do not refer to the zonal mean, more extensive analysis (e.g. considering the zonal energy fluxes at the sectors' boundaries as well as the NEI_0[**63**,68,70]) is needed in order to gain more insight into the quantitative link between future sector-mean ITCZ shifts and their regional energetic constraints. In doing so, we used a 2D theoretical energetic framework (where both zonal and meridional fluxes are taken into account)[71,99], which has only recently been used to explain sector-mean ITCZ shifts[71,99-102] and to the best of our knowledge, it has not yet been applied in any climate change scenario.

The energy flux **F** in Equation (9) can be decomposed into the divergent and rotational components ($\mathbf{F}_\chi$ and $\mathbf{F}_\psi$, respectively), and since the divergence of the rotational component is identically zero (i.e. $\boldsymbol{\nabla} \cdot \mathbf{F}_\psi = 0$), Equation (9) takes the form of Poisson's equation:

$$\boldsymbol{\nabla} \cdot \mathbf{F}_\chi = \boldsymbol{\nabla}^2 \chi = Q \qquad (10)$$

where χ is the energy flux potential (an arbitrary scalar function)[71,99], such that its gradient is equal to the divergent component of AET, i.e. $(\partial_x \chi, \partial_y \chi) = \boldsymbol{\nabla}\chi = \mathbf{F}_\chi = (u_\chi, v_\chi)$. By solving Equation (10), the potential χ (also $\mathbf{F}_\chi$) can be obtained; all derivatives are evaluated in spherical coordinates but written here in Cartesian coordinates for simplicity. In accordance to previous studies[71,99,100], outside from the tropics, the zonal component of the divergent AET is negligible compared to the meridional component in the base period (i.e. $v_\chi \gg u_\chi$; see Figure 2.20c), while in the tropics, they are of the same magnitude (i.e. both the Walker

and Hadley circulations contribute to the divergence of heat; Figure 2.20d-e). The changes of $\mathbf{F}_{\chi}$ in response to climate change are presented in Figure 2.21b, and they are shown to be consistent with changes in Q. Noticeable features in these changes are the patterns of divergence over increased heating in the tropics and Eurasia, and the patterns of convergence over increased cooling of the atmosphere in the Southern and north Atlantic Oceans.

With regard to the changes of $\mathbf{F}_{\chi}$ specifically in the tropics (where the mean circulation and thus the ITCZ control AET), the results are insightful. Over the tropics of the Eurasian sector, a robust increase of southward energy transport is apparent in the future (see Figure 2.23a), which is consistent with the revealed northward shift of the ITCZ. In contrast, the future cooling over the Atlantic Ocean (Figure 2.21b) is compensated by changes in the extratropical $\mathbf{F}_{\chi}$ (controlled by extratropical eddies; see Figure 2.21b), but also by a robust increase in the northward energy transport over the tropics of the eastern Pacific and Atlantic (see Figure 2.23a), which is consistent with the revealed southward shift of the ITCZ in this sector. Similarly to the changes in the ITCZ location and in Q, these results highlight zonally contrasting changes in the meridional component of $\mathbf{F}_{\chi}$, providing more confidence regarding the contrasting ITCZ shifts over the two considered sectors. Note also that future changes in the zonal energy fluxes roughly resemble the opposite of the baseline pattern (i.e. opposite in sign and about 10% smaller in magnitude), which signifies the weakening of the Walker circulation under climate change[126,136].

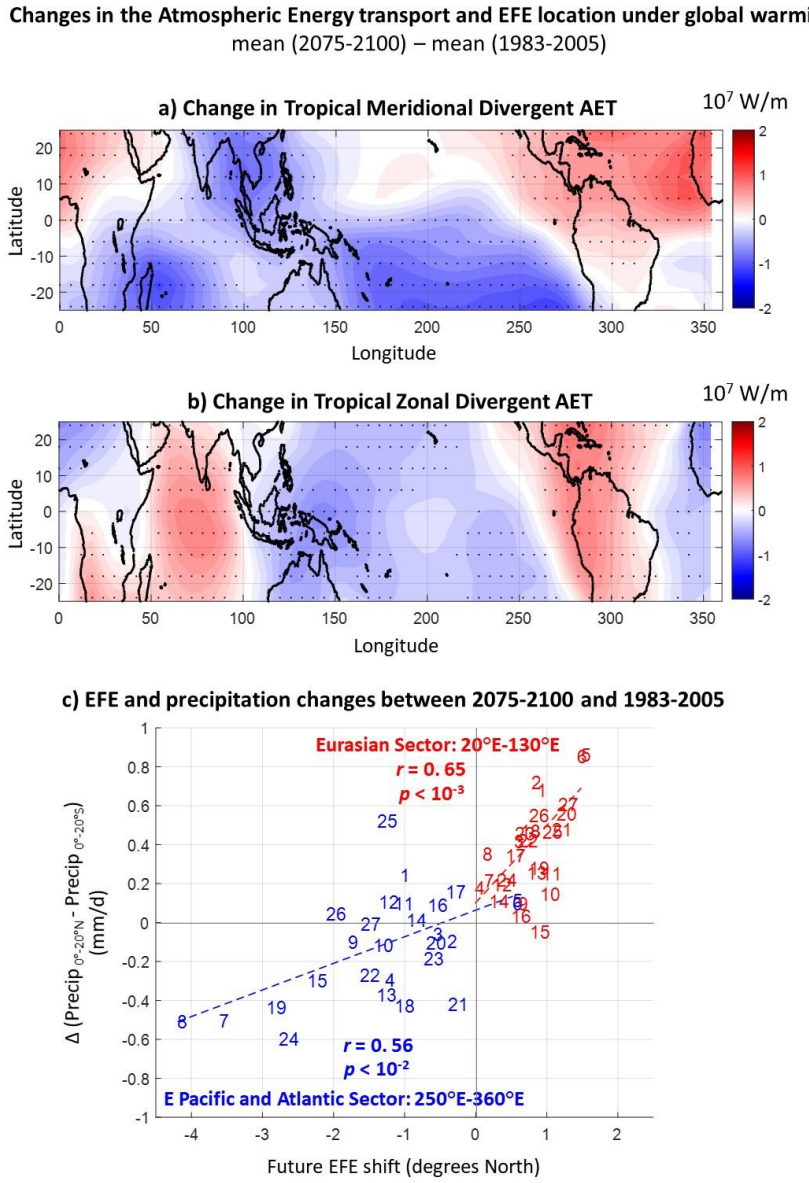

Figure 2.23: Future changes in the atmospheric energy transport (AET) over the tropics and the energy flux equator (EFE) under climate change, as predicted in CMIP6. a) Change is the divergent meridional component of the atmospheric energy transport over the tropics between 2075-2100 and 1983-2005. The multi-model mean across 27 CMIP6 models is presented, while stippling indicates agreement (in the sign of the change) in more than ¾ of the models considered. b) Same as in (a), but for the divergent zonal component. c) Change in the precipitation asymmetry (between 2075-2100 and 1983-2005) as a function of the EFE shift, using all 27 CMIP6 models zonally averaged over the Eurasian sector (20ºE-130ºE; red color) and the eastern Pacific and Atlantic sector (250ºE-360ºE; blue color). Each model is labeled according to Table 2.1. Results show that under global climate change, the future state of the atmospheric energy transport will be characterized by an increased southward transport (divergent component) over the Eurasian sector, which implies a northward shift of EFE (see Equation 11), and it is statistically consistent with a northward shift of the ITCZ. The opposite (i.e. increased northward energy transport and southward shift of EFE) is true in the eastern Pacific and Atlantic Oceans.

Finally, to further verify the consistency of the zonally contrasting ITCZ shifts with regional energetics, we evaluated the future EFE shifts over the two sectors (see Table 2.2 and Figure 2.23c). Note that the EFE variability has been shown to be linked with the ITCZ variability, not only in the zonal mean[63,70], but also over large longitudinal sectors (the ITCZ – EFE link breaks down only over the western and central Pacific)[71]. For a sector with longitudinal boundaries λ_1 and λ_2, the sector-mean position of the EFE (or equivalently of the ITCZ), can be approximated to a first order by meridionally expanding (Taylor series) Equation (10) at the equator[71]:

$$[\varphi_{\mathrm{EFE}}]_{\lambda_1}^{\lambda_2} = -\frac{1}{a}\frac{\left[v_{\chi_0}\right]_{\lambda_1}^{\lambda_2}}{[Q_0]_{\lambda_1}^{\lambda_2} - \frac{1}{\lambda_2-\lambda_1}u_{\chi_0}\Big|_{\lambda_1}^{\lambda_2}} \qquad (11)$$

where $[\cdot]_{\lambda_1}^{\lambda_2}$ represents the zonal mean over the sector. Our results showed that although CMIP6 models do not predict a robust future EFE shift in the zonal mean (on the order of 0.2 ± 0.5° N; see Table 2.2), over the Eurasian sector a robust norward shift is revealed on the order of 0.7 ±0.4° N, while over the Eastern Pacific and Atlantic sector the EFE shifts to the south by -1.4 ±1.1° N. Both these shifts are statistically significant ($p < 0.01$), and they explain 30-40% of the inter-model variance of the projected precipitation change (see Figure 2.23c).

Overall, results show that the revealed ITCZ shifts show a robust statistical and physical link with the future changes in the regional energy balance. It can be also concluded that CMIP6 models do exhibit a consensus over the two considered sectors, highlighting contrasting ITCZ shifts, contrasting changes in Q, and contrasting EFE shifts. This contrasting response of all these quantities and the corresponding models' consensus have been hidden in the zonal-mean analysis of past work.

Discussion

In this study, the future ITCZ shifts under global climate change were explored as a function of longitude and season using climate model simulations. A zonally contrasting response of the ITCZ has been revealed, which was found to be robust across different climate models, and different seasons, and to be of large longitudinal extent, covering about two thirds of the globe. The contrasting ITCZ pattern has been masked in the analysis of zonal-mean ITCZ

shifts in previous literature, as well as due to the presence of model biases in the present-day climatology of the ITCZ. The contrasting ITCZ response can be summarized as a northward shift over the eastern Africa and Indian Ocean and a southward shift over the eastern Pacific, south America and the Atlantic.

We found that the revealed ITCZ response is driven by a positive IOD-like pattern over the Indian Ocean, and high SST warming in low latitudes over the eastern Pacific and Atlantic Oceans. This is consistent with the known coupling between tropical SST and precipitation changes. From an atmospheric energetic perspective, our analysis showed that future climate change induces a zonally contrasting change in the hemispheric heating of the atmosphere, as a result of the combined effect of radiative and dynamical processes. These included snow and ice-albedo feedbacks, forcing from reductions of the aerosols, cloud radiative effects, OLR cooling, an AMOC weakening, and increases in Southern Ocean heat uptake. Independent of the physical approximations to simulate these processes, most models revealed that future changes in the atmospheric energy budget consist of increases in atmospheric heating over Eurasia and cooling over the Southern Ocean, which contrast with atmospheric cooling over the North Atlantic Ocean as a consequence of an AMOC weakening. These changes in the atmospheric heating induce an increase in the southward energy transport over the tropics of eastern Africa and Indian Ocean (and an northward EFE shift), and an increase in the northward energy transport over the tropical eastern Pacific and Atlantic Oceans (and a southward EFE shift), both of which are physically and statistically consistent with the zonally contrasting ITCZ response. We note that further analysis based on careful design of idealized climate experiments is needed to determine the relative contribution of extratropical and tropical mechanisms/forcing (causality investigation) to the revealed ITCZ shifts in each sector.

Based on our results, we can simultaneously explain anticipated future increases of drought stress in southeastern Africa and Madagascar, intensifying flooding in southern India[130], and greater drought stress in Central America[111] – large hydrological hotspots of global change[145,146] that will affect the livelihood and food security of billions of people.

References

63. Schneider, T., T. Bischoff, and G. H. Haug (2014) Migrations and dynamics of the intertopical convergence zone, *Nature*, **513**, doi:10/nature13636

64. Waliser, D. E. & Gautier, C. (1993) A satellite-derived climatology of the ITCZ. *J. Clim.* **6**, 2162–2174.

65. Trenberth, K. E., Stepaniak, D. P., & Caron, J. M. (2000) The global monsoon as seen through the divergent atmospheric circulation. *Journal of Climate*, **13**, 3969–3993. https://doi.org/10.1175/1520-0442(2000)013<3969:TGMAST>2.0.CO;2

66. Adler, R. F., and Coauthors, 2003: The Version-2 Global Precipitation Climatology Project (GPCP) monthly precipitation analysis (1979–present). *J. Hydrometeor.*, **4**, 1147–1167, doi:10.1175/1525-7541(2003)004,1147:TVGPCP.2.0.CO;2

67. Donohoe, A., J. Marshall, D. Ferreira, and D. McGee (2013) The relationship between ITCZ location and cross-equatorial atmospheric heat transport: from the seasonal cycle to the last glacial maximum, *Journal of Climate*, **26**, doi: 10.1175/JCLI-D-12-00467.1

68. Bischoff, T. and T. Schneider (2014) Energetic constraints on the position of the intertropical convergence zone, *Journal of Climate*, **27**, doi: 10.1175/JCLI-D-13-00650.1

69. Berry, G., & Reeder, M. J. (2014). Objective identification of the intertropical convergence zone: Climatology and trends from the ERA-interim. *Journal of Climate*, **27**, 1894–1909. https://doi.org/10.1175/JCLI-D-13-00339.1

70. Adam, O., Bischoff, T., & Schneider, T. (2016a). Seasonal and interannual variations of the energy flux equator and ITCZ. Part I: Zonally averaged ITCZ position. *Journal of Climate*, *29*, 3219–3230. https://doi.org/10.1175/JCLI-D-15-0512.1

71. Adam, O., Bischoff, T., & Schneider, T. (2016b). Seasonal and interannual variations of the energy flux equator and ITCZ. Part II: Zonally varying shifts of the ITCZ. *Journal of Climate*, *29*, 7281–7293. https://doi.org/10.1175/JCLI-D-15-0710.1

72. Chou, C., J.-Y. Tu, and P.-H. Tan (2007) Asymmetry of tropical precipitation change under global warming, *Geoph. Res. Let.*, **34**, doi: 10.1029/2007GL030327

73. Sachs, J.P., D. Sachse, R.H. Smittenberg, Z. Zhang, D.S. Battisti, and S. Golubic (2009) Southward movement of the Pacific intertropical convergence zone AD 1400-1850, *Nature Geoscience*, **2**, doi: 10.1038/NGEO554

74. Cai, W. *et al.* (2012) *More extreme swings of the South Pacific convergence zone due to greenhouse warming*. *Nature* **488**, 365–369.

75. Broecker, W.S., and A. E. Putnam (2013) Hydrologic impacts of past shifts of Earth's thermal equator offer insight into those to be produced by fossil fuel CO_2, *PNAS*, 110(42)

76. Arbuszewski, J.A., P.B. deMenocal, C.Cléroux, L. Bradtmiller, A. Mix (2013) Meridional shifts of the Atlantic intertropical convergence zone since the Last Glacial Maximum, *Nature Geoscience*, **6**, doi: 10.1038/NGEO1961

77. Hwang, Y.-T, D.M.W. Frierson, and S.M. Kang (2013) Anthropogenic sulfate aerosol and the southward shift of tropical precipitation in the late 20th century, *Geoph. Res. Lett.*, **40**, doi:10.1002/grl.50502

78. Lau, W. K. M., and K.-M. Kim (2015), Robust Hadley circulation changes and increasing global dryness due to CO2 warming from CMIP5 model projections, *Proc. Natl. Acad. Sci. U.S.A.*, *112*, 3630–3635.
79. Allen, R. J. (2015), A 21st century northward tropical precipitation shift caused by future anthropogenic aerosol reductions, *J. Geophys. Res. Atmos.*, **120**, 9087–9102, doi:10.1002/2015JD023623.
80. Allen, R. J., A.T. Evan, B.B.B. Booth (2015) Interhemispheric aerosol radiative forcing and tropical precipitation shifts during the late twentieth century, *Journal of Climate*, **28**, doi: 10.1175/JCLI-D-15-0148.1
81. Byrne, M. P., and T. Schneider (2016), Narrowing of the ITCZ in a warming climate: Physical mechanisms, *Geophys.Res. Lett.*, **43**, 11,350–11,357, doi:10.1002/2016GL070396.
82. Chung, E.-S. and B.J. Soden (2017) Hemispheric climate shifts driven by anthropogenic aerosol-cloud interactions, *Nature Geoscience*, **10**, doi: 10.1038/NGEO2988
83. McFarlane, A. A., and D. M. W. Frierson (2017), The role of ocean fluxes and radiative forcings in determining tropical rainfall shifts in RCP8.5 simulations, *Geophys. Res. Lett.*, **44**, 8656–8664, doi:10.1002/2017GL074473.
84. Bony, S. et al., (2015) Clouds, circulation and climate sensitivity, *Nature Geoscience*, **8**, 261-268.
85. Xie, S.-P., 2004: The shape of continents, air–sea interaction, and the rising branch of the Hadley circulation. *The Hadley Circulation: Present, Past, and Future,* H. F. Diaz and R. S. Bradley, Eds., Springer, 121–152.
86. Haywood, J. M., A. Jones, N. Bellouin, and D. Stephenson, (2013) Asymmetric forcing from stratospheric aerosols impacts Sahelian rainfall. *Nat. Climate Change*, **3**, 660–665, doi:10.1038/nclimate1857.
87. Cox, P. M., P. P. Harris, C. Huntingford, R. A. Betts, M. Collins, C. D. Jones, T.E. Jupp, J. A. Marengo, and C. A. Nobre. (2008) Increasing risk of Amazonian drought due to decreasing aerosol pollution, *Nature* 453, no. 7192: 212.
88. Chiang, J. C. H., & Bitz, C. M. (2005). Influence of high latitude ice cover on the marine intertropical convergence zone. *Climate Dynamics*, *25*, 477–496. https://doi.org/10.1007/s00382-005-0040-5
89. Zhang, R. and T.L. Delworth (2005) Simulated topical response to a substantial weakening of the Atlantic thermohaline circulation, *Journal of Climate*, **18**, 1853-1860
90. Broccoli, A. J., Dahl, K. A., & Stouffer, R. J. (2006). Response of the ITCZ to Northern Hemisphere cooling. *Geophysical Research Letters*, *33*, L01702. https://doi.org/10.1029/2005GL024546
91. Kang, S. M., Held, I. M., Frierson, D. M. W., & Zhao, M. (2008). The response of the ITCZ to extratropical thermal forcing: Idealized slab-ocean experiments with a GCM. *Journal of Climate*, **21**, 3521–3532. https://doi.org/10.1175/2007JCLI2146.1
92. Frierson, D. M. W., and Y.-T. Hwang (2012), Extratropical influence on ITCZ shifts in slab ocean simulations of global warming, *J. Clim.*, **25**, 720–733.
93. Hwang, Y., and D. Frierson (2013) Link between the double-intertropical convergence zone problem and cloud biases over the Southern Ocean. *Proc. Natl. Acad. Sci. USA*, **110**, 4935–4940.

94. Tomas, R. A., C. Deser, and L. Sun, 2016: The role of ocean heat transport in the global climate response to projected Arctic sea ice loss. J. Climate, 29, 6841–6859, doi:10.1175/ JCLI-D-15-0651.1.
95. Green, B., and J. Marshall (2017) Coupling of trade winds with ocean circulation damps ITCZ shifts. *J. Climate*, **30**, 4395–4411.
96. Yu, S. and M.S. Pritchard, 2019: A strong role for the AMOC in partitioning global energy transport and shifting ITCZ position in response to latitudinally discrete solar forcing in the CESM1.2., *J. Climate,* https://doi.org/10.1175/JCLI-D-18-0360.1
97. Mamalakis, A., & Foufoula-Georgiou, E. (2018). A multivariate probabilistic framework for tracking the intertropical convergence zone: Analysis of recent climatology and past trends. *Geophysical Research Letters*, **45**. https://doi.org/10.1029/2018GL079865
98. Rotstayn, L., M. Collier, and J. Luo (2015) Effects of declining aerosols on projections of zonally averaged tropical precipitation. *Environ. Res.*, **10**, 044018.
99. Boos, W. R. & Korty, R. L. Regional energy budget control of the intertropical convergence zone and application to mid-Holocene rainfall. *Nat. Geosci.* **9**, 892–897 (2016).
100. Adam, O., Schneider, T. & Brient, F. (2018) Regional and seasonal variations of the double-ITCZ bias in CMIP 5 models, *Clim. Dyn*., **51** (101). https://doi.org/10.1007/s00382-017-3909-1
101. Adam, O., T. Schneider, Y. Enzel and J. Quade (2019) Both differential and equatorial heating contributed to African monsoon variations during mid-Holocene, *Earth and Planetary Science Letters,* **522**, 20-29.
102. Lintner, B., and W. Boos (2019) Using atmospheric energy transport to quantitatively constrain South Pacific Convergence Zone shifts during ENSO, *J. Climate*, **32**, 1839–1855.
103. Lamarque, J. M., G. Kyle, M. Meinshausen, K. Riahi, S. Smith, D. van Vuuren, A. Conley, and F. Vitt (2011), Global and regional evolution of shortlived radiatively-active gases and aerosols in the representative concentration pathways, *Clim. Change*, **109**, 191–212.
104. Serreze, M. C., and R. G. Barry, 2011: Processes and impacts of arctic amplification: A research synthesis. *Global Planet. Change*, **77**, 85–96, doi:10.1016/j.gloplacha.2011.03.004.
105. Immerzeel W. W., Pellicciotti F. and Bierkens M. F. P. (2013) Rising river flows throughout the twenty-first century in two Himalayan glacierized watersheds, *Nat. Geosci.*, **6**, 742–5
106. Chaturvedi R. K., Kulkarni A., Karyakarte Y., Joshi J. and Bala G. (2014) Glacial mass balance changes in the Karakoram and Himalaya based on CMIP5 multi-model climate projections, *Clim. Change*, **123**, 315–28
107. Weaver, A. J. et al. (2012) Stability of the Atlantic meridional overturning circulation: A model intercomparison. *Geophys. Res. Lett.*, **39**, L20709.
108. Cheng, W., J. C. H. Chiang, and D. Zhang (2013) Atlantic meridional overturning circulation (AMOC) in CMIP5 models: RCP and historical simulations. *J. Climate*, **26**, 7187–7197.
109. Rahmstorf, S., Box, J. E., Feulner, G., Mann, M. E., Robinson, A., Rutherford, S., & Schaffernicht, E. J. (2015). Exceptional twentieth-century slowdown in Atlantic Ocean

overturning circulation. *Nature Climate Change*, **5**(5), 475–480. https://doi.org/10.1038/nclimate2554

110. Caesar, L., Rahmstorf, S., Robinson, A., Feulner, G., & Saba, V. (2018). Observed fingerprint of a weakening Atlantic Ocean overturning circulation. *Nature*, **556**(7700), 191–196. https://doi.org/10.1038/s41586-018-0006-5

111. Chen, Y., Langenbrunner, B., & Randerson, J. T. (2018). Future drying in Central America and northern South America linked with Atlantic meridional overturning circulation. *Geophysical Research Letters*, **45**, 9226–9235. https://doi.org/10.1029/2018GL077953

112. Eyring et al. (2016) An overview of the Coupled Model Intercomparison Project Phase 6 (CMIP6) experimental design and organization, *Geosci. Model Dev.*, **9**, 1937–1958,, doi:10.5194/gmd-9-1937-2016

113. O'Neill, B.C. et al. (2017) The roads ahead: Narratives for shared socioeconomic pathways describing world futures in the first 21st century, *Global Environmental Change*, **42**, 169–180.

114. Van Vuuren D.P., et al., (2011) Representative concentration pathways: An overview, *Climatic Change*, 109, 5-31, doi:10.1007/s10584-011-0148-z

115. Nicholson, S. E. (2018) The ITCZ and the seasonal cycle over equatorial Africa, *BAMS*, **99**, 337–348.

116. Bain, C.L., et al (2011) Detecting the ITCZ in instantaneous satellite data using spatiotemporal statistical modeling: ITCZ climatology in the east Pacific, *J. Climate*, **24**, doi: 10.1175/2010JCLI3716.1

117. Ashouri, H., K.L. Hsu, S. Sorooshian, D.K. Braithwaite, K.R. Knapp, L.D. Cecil, B.R. Nelson, and O.P. Prat (2015) PERSIANN-CDR: Daily Precipitation Climate Studies Data Record from Multisatellite Observations for /Hydrological and Climate Studies, *Bull. Amer. Meteor. Soc.*, **96**, 69-83, doi: http://dx.doi.org/10.1175/BAMS-D-13-00068.1.

118. Lee, H.-T. (2014). Climate algorithm theoretical basis document (C-ATBD): Outgoing longwave radiation (OLR)—Daily. NOAA's Climate Data Record (CDR) Program, CDRP-ATBD-0526 (46 pp.)

119. Mechoso, C., and Coauthors (1995) The seasonal cycle over the tropical Pacific in coupled ocean–atmosphere general circulation models. *Mon. Wea. Rev.*, **123**, 2825–2838.

120. Oueslati, B. and Bellon, G., (2015) The double ITCZ bias in CMIP5 models: interaction between SST, large-scale circulation and precipitation, *Clim. Dynam.*, **44**, 585–607, doi:10.1007/s00382-015- 2468-6.

121. Dutheil, C., et al., (2019) Impact of temperature biases on climate change projections of the South Pacific Convergence Zone, *Clim. Dyn.*, https://doi.org/10.1007/s00382-019-04692-6.

122. Samanta, D., Karnauskas, K. B., & Goodkin, N. F. (2019). Tropical Pacific SST and ITCZ biases in climate models: Double trouble for future rainfall projections?. *Geophysical Research Letters*, **46**. https://doi.org/10.1029/2018GL081363

123. Adam, O., T. Schneider, F. Brient, and T. Bischoff (2016) Relation of the double-ITCZ bias to the atmospheric energy budget in climate models, *Geophys. Res. Lett.*, **43**, 7670–7677, doi:10.1002/2016GL069465.

124. Li, G., and Xie, S.-P. (2014) Tropical Biases in CMIP5 Multimodel Ensemble: The Excessive Equatorial Pacific Cold Tongue and Double ITCZ Problems, *J. Clim.*, **27**, 1765–1780.
125. Tian, B., & Dong, X. (2020) The double-ITCZ Bias in CMIP3, CMIP5 and CMIP6 models based on annual mean precipitation, *Geophysical Research Letters*, **47**, e2020GL087232. https://doi.org/10.1029/2020GL087232
126. Xie, S.-P. et al. (2010) Global warming pattern formation: sea surface temperature and rainfall, *J. Clim.* **23**, 966–986.
127. Byrne, M. P., A. G. Pendergrass, A. D. Rapp, K.R. Wodzicki (2018) Response of the Intertropical Convergence Zone to Climate Change: Location, Width, and Strength, *Current Climate Change Reports*, **4**, 355–370.
128. Held, I. M. & Soden, B. J. (2006) Robust responses of the hydrological cycle to global warming. *J. Clim.* **19**, 5686–5699.
129. Kooperman GJ, Chen Y, Hoffman FM, Koven CD, Lindsay K, et al. **2018**. Forest response to rising CO_2 drives zonally asymmetric rainfall change over tropical land. *Nat. Clim. Change*, **8**: 434–40.
130. D'Agostino, R., Bader, J., Bordoni, S., Ferreira, D., & Jungclaus, J. (2019). Northern Hemisphere monsoon response to mid-Holocene orbital forcing and greenhouse gas-induced global warming. *Geophysical Research Letters*, **46**, 1591–601. https://doi.org/10.1029/2018GL081589
131. Kang S.M. and I.M. Held (2012) Tropical precipitation, SSTs and the surface energy budget: a zonally symmetric perspective, *Clim. Dyn.*, **38**, 1917-1924.
132. Xiang, B., M. Zhao, Y. Ming, W. Yu, and S.M. Kang (2018) Contrasting Impacts of Radiative Forcing in the Southern Ocean versus Southern Tropics on ITCZ Position and Energy Transport in One GFDL Climate Model, *J. Clim.* **31**, 5609–5628.
133. Hwang, Y.-T., S.-P. Xie, C. Deser, and S. M. Kang (2017), Connecting tropical climate change with Southern Ocean heat uptake, Geophys. Res. Lett., 44, 9449–9457, doi:10.1002/2017GL074972.
134. Frölicher, T. L., J. L. Sarmiento, D. J. Paynter, J. P. Dunne, J. P. Krasting, and M. Winton (2015), Dominance of the Southern Ocean in anthropogenic carbon and heat uptake in CMIP5 models, *J. Clim.*, **28**, 862–886.
135. Roemmich, D., J. Church, J. Gilson, D. Monselesan, P. Sutton, and S. Wjiffels (2015), Unabated planetary warming and its ocean structure since 2006, *Nat. Clim. Change*, **5**, 240–254.
136. Vecchi, G.A. and B.J. Soden (2007) Global Warming and the Weakening of the Tropical Circulation, *J. Clim.*, **20**, 4316–4340.
137. Saji, N. H., B. N. Goswami, P. N. Vinayachandran, and T. Yamagata (1999) A dipole mode in the tropical Indian Ocean. Nature, 401, 360–363.
138. Hartmann D.L. (2016) Global Physical Climatology (Elsevier, Amsterdam), 2nd Ed.
139. Feldl, N. and S. Bordoni (2016) Characterizing the Hadley circulation through regional climate feedbacks, *J. Clim.*, **29**, 613–622.
140. Rahmstorf, S., (2002) Ocean circulation and climate during the past 120,000 years, Nature, **419**, 207-214.
141. Cheng, W., C. M. Bitz, and J. C. H. Chiang (2007), Adjustment of the global climate system to abrupt changes in the Atlantic meridional overturning circulation, in Ocean

Circulation: Mechanisms and Impacts, Geophys. Monogr. Ser., vol. 173, edited by A. Schmittner, J. Chiang, and S. Hemming, pp. 295–314, AGU, Washington, D. C.

142. Drijfhout, S., van Oldenborgh, G. J. & Cimatoribus, A. (2012) Is a decline of AMOC causing the warming hole above the North Atlantic in observed and modeled warming patterns? J. Clim. **25,** 8373-8379.

143. Swart, N. C., S. T. Gille, J.C. Fyfe, and N.P. Gillet (2018) Recent Southern Ocean warming and freshening driven by greenhouse gas emissions and ozone depletion, *Nature Geoscience*, 11, 836-841.

144. Deser, C., R. A. Tomas, and L. Sun, (2015) The role of ocean-atmosphere coupling in the zonal-mean atmospheric response to Arctic Sea ice loss. *Journal of Climate*, **28**, 2168-2186, doi:10.1175/JCLI-D-14-00325.1.

145. Diffenbaugh, N. S., & Giorgi, F. (2012). Climate change hotspots in the CMIP5 global climate model ensemble. Climatic Change, 114(3–4), 813–822. https://doi.org/10.1007/s10584-012-0570-x

146. Xu, L., Wang, A., Wang, D., & Wang, H. (2019). Hot spots of climate extremes in the future. Journal of Geophysical Research: Atmospheres, 124, 3035–3049. https://doi.org/10.1029/2018JD029980

CONCLUSIONS

In this dissertation we aimed to gain insight into a) the physical teleconnections and predictability of winter precipitation variability over the southwestern US (SWUS), and b) the future shifts in the position of the tropical rainbelt/intertropical convergence zone (ITCZ) in response to climate change.

We found that traditional climatic drivers of SWUS precipitation like the El Niño-Southern Oscillation (ENSO) have decreased in importance while new emerging modes of sea surface temperature (SST) over the southwestern Pacific have been more robust predictors in the last decades. We introduced a new SST mode, termed the New Zealand Index (NZI), which was found to correlate significantly with SWUS precipitation (correlation coefficient on the order of 0.7), also corresponding to non-zero lead times of prediction. We have suggested that the revealed teleconnection depends on a western Pacific ocean-atmosphere pathway, whereby SST anomalies propagate from the southern to the northern hemisphere during boreal summer and early fall, through an atmospheric bridge that materializes via the mean atmospheric meridional circulation (Hadley circulation). Our analysis also showed an amplification of this new teleconnection over the past four decades.

To test more quantitatively the traditional and the revealed teleconnections as to their importance for prediction skill, we presented a comprehensive probabilistic framework to assess the predictability of dry/wet and normal precipitation years in the SWUS. Based on newly proposed statistical metrics to assess the null hypothesis that there is no predictive skill, we confirmed that the NZI has been a stronger predictor of SWUS precipitation in the last decades than ENSO. Our results also highlighted that predictive models are more reliable when predicting wet years compared to dry years, and they lack skill in predicting normal years. By repeating the analysis using CMIP6 climate model outputs, we found that, with respect to its relevance to SWUS precipitation, climate models might on average undermine the importance of non-ENSO SST variability.

Our results highlight the need to understand the dynamic nature of the coupled ocean-atmosphere system and exploit climate information that goes beyond the traditionally used indices for improving future prediction skill of regional precipitation in a changing climate. Future research should focus on the development of new, data-driven methodologies that aim to integrate physics and machine learning, and predict seasonal precipitation variability in a setting where the predictors are not prescribed a priori, but rather emerge from the

model fit to the data. An important challenge of such methods would be addressing overfitting and non-stationarity, as well as quantifying prediction uncertainty. Lastly, the physical mechanisms of the NZI teleconnection need further exploration, beyond statistical analysis, and based on carefully-designed idealized climate experiments.

Regarding the ITCZ response to climate change, our results document a robust zonally contrasting response of the ITCZ, with a northward shift over eastern Africa and the Indian Ocean, and a southward shift in the eastern Pacific and Atlantic Ocean by 2100, for the SSP3-7.0 scenario. By using a two-dimensional horizontal energetics framework, we found that the revealed ITCZ response is consistent with future changes in the divergent atmospheric energy transport over the tropics, and sector-mean shifts of the energy flux equator (EFE). The changes in the EFE appear to be the result of zonally contrasting imbalances in the inter-hemispheric atmospheric heating over the two sectors, consisting of increases in atmospheric heating over Eurasia and cooling over the Southern Ocean, which contrast with atmospheric cooling over the North Atlantic Ocean due to a model-projected weakening of the Atlantic meridional overturning circulation.

Our results provide new insights about the mechanisms that will influence the future position of the tropical rainbelt, and may allow for more robust projections of climate change impacts. Particularly, although our results establish consistency between the energetics framework and projected changes in tropical precipitation, only about 40% of the inter-model variance of precipitation change is explained based on energetic arguments. This highlights the important limitations of the energetics framework, and the need to further explore mechanisms involving ocean-atmosphere-land coupling at a regional scale. As future work, to further infer causality, carefully designed idealized climate experiments are needed, as a complement to analyses like this one that attempt to understand mechanisms contributing to robust future changes in the hydrological cycle within and across different Earth system models. Another important dimension of our results that needs further investigation is how the revealed ITCZ shifts are projected to alter the frequency and magnitude of precipitation extremes over the tropics and subtropics. Future studies should quantify the socio-economic effects of these changes, in a setting where no new adaptation policies are in place versus where climate-informed preparedness guides adaptation and

management. This would help to highlight the importance and potential damage these changes might have, if no adaptation policies are adopted. Also, from an engineering perspective, new designing methods need to be developed for practitioners to implement, which will take into account the risk of climate change-induced intensification of extreme events and natural hazards.